Escorcia Carranza, Ivonne (2015) Metamaterial based CMOS terahertz
focal plane array. PhD thesis/

http://theses.gla.ac.uk/6955/

# Metamaterial based CMOS Terahertz Focal Plane Array

## Ivonne Escorcia Carranza

A Thesis submitted to

School of Engineering

University of Glasgow

in fulfilment of the requirements for the degree of

*Doctor of Philosophy*

December 2015

# Abstract

The distinctive properties of terahertz radiation have driven an increase in interest to develop applications in the imaging field. The non-ionising radiation properties and transparency to common non-conductive materials have led research into developing a number of important applications including security screening, medical imaging, explosive detection and wireless communications. The proliferation of these applications into everyday life has been hindered by the lack of inexpensive, compact and room-temperature terahertz sources and detectors. These issues are addressed in this work by developing an innovative, uncooled, compact, scalable and low-cost terahertz detector able to target single frequency imaging applications such as stand-off imaging and non-invasive package inspection.

The development of two types of metamaterial (MM) based terahertz focal plane arrays (FPAs) monolithically integrated in a standard complementary metal-oxide semiconductor (CMOS) technology are presented in this Thesis. The room temperature FPAs are composed of periodic cross-shaped resonant MM absorbers, microbolometer sensors in every pixel and front-end readout electronics fabricated in a 180 nm six metal layer CMOS process from Texas Instruments (TI). The MM absorbers are used due to the lack of natural selective absorbing materials of terahertz radiation. These subwavelength structures are made directly in the metallic and insulating layers available in the CMOS foundry process. When the MM structures are distributed in a periodic fashion, they behave as a frequency-selective material and are able to absorb at the required frequency. The electromagnetic (EM) properties are determined by the MM absorber geometry rather than their composition, thus being completely customisable for different frequencies. Single band and broadband absorbers were designed and implemented in the FPAs to absorb at 2.5 THz where a natural atmospheric transmission window is found, thus reducing the signal loss in the imaging system.

The new approach of terahertz imaging presented in this Thesis is based in coupling a MM absorber with a suitable microbolometer sensor. The MM structure absorbs the terahertz wave while the microbolometer sensor detects the localised temperature change, depending on the magnitude of the radiation. Two widely used microbolometer sensors are investigated to compare the sensitivity of the detectors. The two materials are Vanadium

Oxide (VOx) and p-n silicon diodes both of which are widely used in infrared (IR) imaging systems. The VOx microbolometers are patterned above the MM absorber and the p-n diode microbolometers are already present in the CMOS process. The design and fabrication of four prototypes of FPAs with VOx microbolometers demonstrate the scalability properties to create high resolution arrays. The first prototype consists of a 5 x 5 array with a pixel size of 30 μm x 30 μm. An 8 x 8 array, a 64 x 64 array with serial readout and a 64 x 64 array with parallel readout are also presented. Additionally, a 64 x 64 array with parallel output readout electronics with p-n diode microbolometers was fabricated.

The design, simulation, characterisation and fabrication of single circuit blocks and a complete 64 x 64 readout integrated circuit is thoroughly discussed in this Thesis. The absorption characteristics of the MMs absorbers, single VOx and p-n diode pixels, 5 x 5 VOx FPA and a 64 x 64 array for both microbolometer types demonstrate the concept of CMOS integration of a monolithic MM based terahertz FPA. The imaging performance using both transmission and reflection mode is demonstrated by scanning a metallic object hidden in a manila envelope and using a single pixel of the array as a terahertz detector. This new approach to make a terahertz imager has the advantages of creating a high sensitivity room temperature technology that is capable of scaling and low-cost manufacture.

# Acknowledgments

I would like to thank my supervisor, Prof. David Cumming for giving me the invaluable opportunity to be part of the Microsystem Technology Group (MST) and for allowing me to work on such a fascinating and challenging project. I am thankful for his guidance and great support throughout my PhD. I would also like to thank CONACyT-Mexico for their financial support.

I am also deeply thankful to my second supervisor Dr. James Grant for being such an inspiring person, working alongside him has been an honour and true privilege. I want to thank him for introducing me to the world of terahertz, for his willingness to always share his wealth of knowledge, for being very patient with me and being my greatest encourager from day one of my PhD. I am extremely thankful to him for checking and correcting this Thesis in great detail.

I would also like to thank John Gough and his team at Texas Instruments Greenock for their constant help and support especially during tapeout deadlines. I am grateful to them for allowing us to be part of the 'University Support' scheme which helped us fabricate all our chips. This project would not have been possible without their support. Thanks to the staff at James Watt Nanofabrication Centre for assisting Dr. James Grant during the post-processing of all our chips and the Electronics Workshop staff for always providing electronics components and for fabricating all our printed circuit boards.

I am thankful to everyone in the MST group, I have thoroughly enjoyed working alongside such intelligent, dedicated and creative people. A special acknowledgment goes to my very good friend Angelos for making every day in the office interesting and fun especially during the very long nights of chip layout. Thanks for all the conversations, for introducing me to the Mediterranean cuisine and for creating our band 'Tamarin'. I want to thank Kirsty for being my first Scottish pal, for introducing me to all kinds of new music and for always being so supportive. Thanks to Lourdes and Boon for being the best gym buddies and such special friends, I really appreciate you all. It is such a comfort to know that I can always count on you.

Special thanks to my parents for believing in me and for supporting me through every season of my life. *Gracias a mi padres por siempre creer en mi y por apoyarme en cada etapa de mi vida, ¡los amo!* Thanks to my sister for being the person I look up to

# Publications

## Peer-reviewed Journals

**Carranza, I. E.**, Grant, J., Gough, J., and Cumming, D.R.S., (2015) "Metamaterial Based Terahertz Imaging" *IEEE Transactions on Terahertz Science and Technology*, vol. 5, no. 6, pp. 892-901. (doi: 10.1109/TTHZ.2015.2463673)

Grant, J., **Escorcia Carranza, I.**, Li, C., McCrindle, I., Gough, J., and Cumming, D. (2013) *"A monolithic resonant terahertz sensor element comprising a metamaterial absorber and micro-bolometer"* *Laser and Photonics Reviews*, 7 (6). pp. 1043-1048. (doi:10.1002/lpor.201300087)

## International Conference Proceedings

**Carranza, I. E.**, Grant, J., and Cumming, D. R. S., "Terahertz Imaging Using a Monolithic Metamaterial Based Detector," in *39th International Conference in Infrared, Millimeter and Terahertz Waves (IRMMW-THz)*, 14-19 September 2014, Tucson, Arizona. (doi: 10.1109/IRMMW-THz.2014.6956016)

Grant, J., **Escorcia-Carranza, I.**, Li, C., McCrindle, I.J., and Cumming, D. R. S., "Terahertz Image Sensor Comprising a Metamaterial Absorber and Micro-bolometer," in *11th International Symposium on Photonic and Electromagnetic Crystal Structures (PECS-XI)*, 11-15 May 2014, Shanghai, China.

## Poster Presentations

**Escorcia Carranza, I.**, Grant, J., and Cumming, D. R. S., "Metamaterial based Terahertz Focal Plane Array," *IEEE Electron Devices Society Scotland: Mini-Colloquium on Microsystems (IEEE- EDS)*, 19 April 2013, Edinburgh, United Kingdom.

## Advanced Training Schools

**Escorcia Carranza, I.**, Grant, J., and Cumming, D. R. S., "Metamaterial based Terahertz Focal Plane Array," (Poster) in *22$^{nd}$ European Doctoral School on Metamaterials entitled Fabrication of Metamaterials*, 17-21 June 2013, Glasgow, United Kingdom.

# Table of Contents

# List of Figures

# List of Tables

# Glossary of Terms

| | |
|---|---|
| α-Si | amorphous silicon |
| AC | alternating current |
| BNC | bayonet neill–concelman |
| BW | bandwidth |
| CMOS | complementary metal-oxide semiconductor |
| CPGA | ceramic pin grid array |
| CW | continuous wave |
| DAC | digital-to-analogue converter |
| DC | direct current |
| DFG | difference-frequency generation |
| DRC | design rule check |
| EAGLE | easily applicable graphical layout editor |
| EM | electromagnetic |
| eV | electronVolt |
| ERR | electric ring resonator |
| ESD | electrostatic discharge |
| FDTD | finite-difference time-domain |
| FET | field effect transistor |
| FIB | focused ion beam |
| FIR | far infrared |
| FOM | figures of merit |
| FPA | focal plane array |
| FTIR | Fourier transform infrared |
| FWHM | full width at half maximum |
| IR | infrared |
| JWNC | James Watt Nanofabrication Centre |
| KNT | Kelvin Nanotechnology |
| LC | inductor-capacitor |
| LHM | left-handed materials |
| LO | local oscillator |

| | |
|---|---|
| MM | metamaterial |
| NEP | noise equivalent power |
| NIM | negative index material |
| NSD | noise spectral density |
| OLG | open loop gain |
| PCB | printed circuit board |
| PCA | photo-conductive antenna |
| PCD | photo-conductive detector |
| PECVD | plasma-enhanced chemical vapour deposition |
| PMMA | polymethyl methacrylate |
| PTD | pulsed time domain |
| QCL | quantum cascade laser |
| RH | relative humidity |
| rms | root-mean-square |
| ROIC | readout integrated circuit |
| $R_{ON}$ | on resistance |
| $R_v$ | responsivity |
| S | scattering (parameters) |
| SBD | schottky barrier diode |
| SEM | scanning electron micrograph |
| SMA | subMiniature version A |
| SMU | source measure unit |
| SNR | signal to noise ratio |
| SR | set-reset |
| SRR | split ring resonator |
| T | thermal time constant |
| TCC | temperature coefficient of current |
| TCR | temperature coefficient of resistance |
| TCV | temperature coefficient of voltage |
| TG | transmission gate |
| TSMC | Taiwan Semiconductor Manufacturing Company |
| THz-TDS | terahertz time domain spectroscopy |
| TI | Texas Instruments |
| TPX | polymethylpentene |
| VGA | voltage gain amplifier |
| VOx | vanadium oxide |

# Chapter 1 Introduction

## 1.1 Motivation

Terahertz technology has unique characteristics in the scope of sensing and imaging fields allowing the technology to be at the forefront of research developing applications such as stand-off security imaging. The most impressive attributes of terahertz radiation are its absorption characteristics and its non-ionising radiation nature. Terahertz radiation can penetrate common non-conductive materials such as clothing, paper and plastics. Additionally, its non-ionising nature makes it non-hazardous to human tissue. The combination of these unique properties makes terahertz technology ideal for non-invasive imaging applications ranging from airport security, medical imaging and package inspection. Furthermore, the unique terahertz spectroscopic fingerprints of many materials allow for identification of explosives, hazardous substances and illicit drugs.

Terahertz technology is currently in its nascent stages much as infrared (IR) in the early 1800's and microwave in the late 1800's. Due to the existing limitations in terahertz technology it is as yet to make the same impact as its electromagnetic (EM) neighbours. This situation is widely known as "Terahertz gap". In order to bring terahertz technology to maturity on par with that of the IR and microwave, the development of compact, portable, continuous high power, cost-effective and room temperature sources as well as high responsivity, sensitivity and fast terahertz detectors operating at room temperature is required. Currently, terahertz imaging technology has encountered obstacles such as the use of bulky and expensive equipment, the necessity for cryogenic cooling, slow read out speed, and the challenge of scaling to array formats required for high resolution focal plane arrays (FPAs).

The development of FPAs using cheap silicon-based technology for visible light imaging revolutionised imaging systems. It is anticipated that the realisation of high sensitivity, real-time, room temperature and low-cost terahertz FPAs would rapidly promote the exploitations of terahertz imaging systems in many applications and result in the closing of the "Terahertz gap".

The objective for this project is to develop a terahertz detector that overcomes the current obstacles in terahertz imaging technology by employing concepts used in IR imaging systems such as the implementation of bolometric sensors and high resolution FPAs. Due to the lack of natural selective terahertz absorptive materials, metamaterial (MM) absorbers are investigated to selectively absorb the radiation. These MM structures are scalable, consist of subwavelength unit cells and can be designed to absorb at any desired frequency by modifying the size and shape which tunes the electric and magnetic response.

This Thesis demonstrates the monolithic integration of two types of microbolometer sensors with MM absorbers into a complementary metal-oxide semiconductor (CMOS) process to develop a FPA with front-end readout integrated circuit (ROIC). The electronics were designed in a 180 nm process from Texas Instruments (TI). The CMOS integration of the FPA with minimal post-processing steps provides a low-cost terahertz detector able to function at room temperature with the great advantage of being easily incorporated into high resolution imaging systems. The imaging application is demonstrated by capturing images in reflection and transmission mode. Images are produced of a covered and uncovered object demonstrating the ability of terahertz radiation of penetrating non-conductive materials. This system demonstrates the ultimate application of non-invasive imaging for security screening purposes which can be widely used in package inspection, airport security and medical imaging.

## 1.2 Aims and Objectives

The aim of this Thesis is to describe the design and characterisation of an innovative and unique FPA for terahertz imaging applications. The work focuses on the integration of a microbolometer sensor with a terahertz MM absorber into a commercial CMOS process to create a monolithic terahertz FPA. Dr. James Grant designed, simulated and tested the MM absorbers on their own to corroborate absorption at the required frequency. Once the MM shape was decided, the cross-shaped absorbers were integrated in the metallic and insulating layers of the CMOS process. Different designs based on cross shapes were investigated to achieve single and broadband absorption centred at 2.5 THz. In addition to this, two uncooled microbolometers were investigated to compare their sensitivity once they were integrated in each pixel of the terahertz FPA. The design of the ROIC was also integrated in the CMOS process to read each pixel of the FPA in a serial and parallel mode.

The work from Dr. James Grant is described and referenced in this Thesis to show a complete picture of the project. His work can be described as follows:

- The design and characterisation of cross-shaped terahertz MM absorbers with an absorption frequency at 2.5 THz to be integrated in the metal and insulating layers of a CMOS process.
- Post-processing of the CMOS chips to monolithically integrate the microbolometer sensors to create a MM based terahertz FPA.

My activity in the project consisted in the design and simulation of the readout electronics and the electrical and optical characterisation of all the fabricated chips to determine the performance of the terahertz detectors in transmission and reflection mode imaging. My specific objectives of this project can be described as follows:

- The design, layout, simulation and testing of readout integrated circuits fully customised to work in serial and parallel mode using a six layer 180 nm CMOS process from TI.
- Monolithic integration of the MM cross-shaped structures and readout electronics into the CMOS process.
- Characterisation of the FPA with terahertz laser radiation to derive the respective figures of merit (FOMs) such as responsivity ($R_v$), noise spectral density (NSD), noise equivalent power (NEP), temperature coefficient of resistance or voltage (TCR or TCV) and thermal time constant ($\tau$).
- The characterisation of two uncooled microbolometer sensors used for imaging applications: p-n diode and Vanadium Oxide (VOx) patterned by Dr. James Grant in each pixel of the CMOS FPA.
- Transmission and reflection mode imaging to demonstrate non-invasive imaging capabilities in the terahertz regime by imaging covered and uncovered metallic objects.

# 1.3 Thesis Outline

The organisation and contents of this Thesis are outlined in this section:

Chapter 2 provides an introduction to terahertz technology, its properties, current terahertz sources and detectors, and possible applications in the imaging field. A comparison of current terahertz imaging technologies is explained with a focus on thermal detectors and FPAs. This chapter concludes with an introduction to single band and broadband MM absorbers, negative index materials (NIMs) and their applications in terahertz technology.

Chapter 3 explains the characteristics and most important FOMs used to evaluate the performance of terahertz thermal detectors. The theory and equations to define $R_v$, NEP, TCR, and $\tau$ are discussed for further understanding in the characterisation of terahertz detectors. Atmospheric absorption in the terahertz spectrum is described to explain the reason of working with the specific frequency of 2.5 THz. Additionally, the proposed theory behind the MM structure absorption and the characterisation of scattering (S) parameters to extract the effective electric and magnetic properties is explained.

Chapter 4 focuses on the design of the MM absorber and readout electronics for the FPA. The original MM structures are described as a background of the original idea used to design the terahertz absorbers and their integration into a CMOS process. The work in this chapter is presented in chronological order as the CMOS chips were fabricated. Each of the six chips fabricated is described to detail their main characteristics. The circuit blocks used to design the readout electronics are described with their respective simulation results. The designs include a 5 x 5 VOx array, an 8 x 8 VOx array, a 64 x 64 VOx array-serial readout and a 64 x 64 array-parallel readout with VOx microbolometers and a 64 x 64 array with parallel output readout electronics with p-n diode microbolometers. The characterisation of both microbolometers started from single pixels and then moved towards array formats.

Chapter 5 describes the experimental characterisation of the fabricated FPAs. The experimental results were compared to the simulation results presented in Chapter 4. The characterisation of single circuit blocks is presented as well as the full readout electronics circuits. The single pixel characterisation for both types of microbolometers is presented and compared. The post-processing steps that were needed to add the respective VOx microbolometers and to create membranes in the FPAs are also detailed. The comparison between different membrane thicknesses in both microbolometers and their effect in $R_v$ and NEP is presented. After all the chips were characterised, the chip with the best performance was used for the imaging experiments in both transmission and reflection mode. The experiments show the possible application for non-invasive terahertz imaging by hiding a metallic object in a manila envelope and successfully obtaining an image of the hidden object.

Chapter 6 summarises the results and suggests future work to be undertaken with the fabricated chips containing the high resolution 64 x 64 FPAs.

# Chapter 2 Literature Review

## 2.1 Terahertz Spectrum

Terahertz radiation is located in between IR and millimetre wave radiation in the EM spectrum as shown in Figure 2.1. Terahertz radiation lies in the frequency range of 100 GHz to 10 THz with respective wavelengths of 3 mm to 30 μm corresponding to a quantum energy of 0.4 meV to 0.04 eV [1]. This frequency range, known as the 'terahertz gap', has been a relatively  unexplored region of the EM spectrum in the past due to the limitations encountered in the performance of optical equipment along with conventional semiconductors being incapable of generating and detecting terahertz radiation. As a consequence, the design of terahertz detectors and sources has been slow compared to the advanced imaging technologies developed in the neighbouring spectrums. Although terahertz technology development has been hindered in the past, terahertz waves have very unique characteristics that make it a promising candidate for imaging applications. Its short wavelengths can provide up to ten times better spatial resolution than millimetre wave radiation and better resolution in imaging applications, since the resolution of an image increases with the decrease in the wavelength [2].
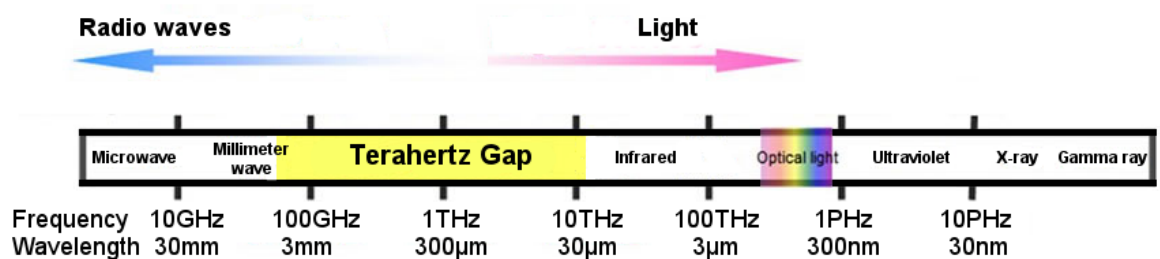


**Figure 2.1 – Electromagnetic spectrum showing the location of the "Terahertz Gap" located in the frequency range of 100 GHz to 10 THz.**

One important characteristic of terahertz waves is its non-ionising attribute since it operates at low energy levels in contrast to X-rays that have energies in the range of thousands of electron volts (eV) [3]. According to Xiaoxia *et. al.* when terahertz pulses interact with biological tissue during the absorption process, the energy in the terahertz light beam is insufficient to drive chemical reactions and therefore is not harmful to the tissue which is a major asset for medical imaging research [4]. It has been demonstrated

that abnormalities in biological tissue can be detected by terahertz waves which provide a better contrast than X-rays for soft tissues [3]. Skin, mouth, and other surface cancers can be detected by monitoring the contrast in tissue composition and water absorption information, used as a molecular marker; the diseased tissue showed an increase in water absorption [5]. For now, medical imaging applications are limited to the detection of surface cancers due to the limited penetration of terahertz waves into deeper layers of biological tissue. Terahertz waves are appropriate for medical imaging due to their minimum scattering while passing through the first layers of the skin [6]. According to the Rayleigh criterion, the spatial resolution is inversely proportional to the wavelength and the intensity is proportional to $f^4$. Given that cell sizes are shorter than the wavelength, Terahertz waves scatter in proportion to Mie or Tyndall scattering ($f^2$) in contrary to Rayleigh scattering which dominates in the IR and visible spectrum [7].

Many common non-conductive materials can be imaged, identified and analysed due to their transparency to terahertz waves and their unique spectral terahertz fingerprints. The unique responses of materials within the terahertz range provide spectroscopic information that is generally absent in optical and X-ray images [3]. Specific gaseous and solid materials such as drugs and explosives also have unique fingerprints, especially in the 2 THz to 4 THz range, which allow them to be identified with terahertz waves [8]. An example of drug identification via terahertz spectroscopy is shown in Figure 2.2a where three different drugs were imaged while placed inside an envelope [9]. The drugs identified by their terahertz absorption levels at different frequencies were methamphetamine, MDMA (ecstasy) and aspirin. Different frequencies were used to compare and provide better contrast in the substances as shown in Figure 2.2b. This allows for applications such as detection of hazardous materials and drug identification.

Perhaps the most attractive application for terahertz radiation is in the field of security imaging due to terahertz radiation being transparent to many non-conductive materials that are opaque in the visible and IR regions. Bjarnason *et. al.* experimentally demonstrated the ability of terahertz waves to be transmitted through common fabrics [10].

Due to the increased events of weapon threats in public places like airports, fast and effective detection of harmful objects is urgently needed. Terahertz stand-off imaging is a promising emerging candidate for new real-time scanning detectors due to the capability of detecting weapons made of metals and even ceramic hidden inside clothes, packages and luggage made of non-conductive materials. This important property allows for non-invasive package inspection and airport security screenings without the harm of the being exposed to ubiquitous x-ray scanners.
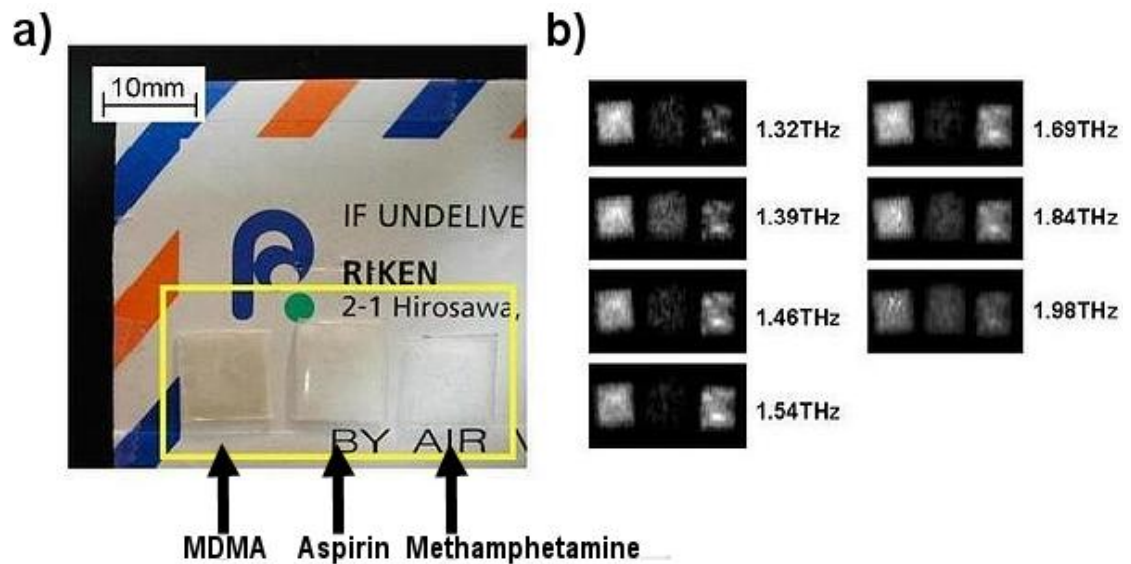
**Figure 2.2 – Identification of drugs done by terahertz imaging. a) Image of the sample drugs inside the envelope MDMA (ecstasy), aspirin and methamphetamine. b) Images showing different absorption depending on the terahertz wave. Reproduced with permission: [K. Kawase, Y. Ogawa, Y. Watanabe, and H. Inoue, "Non-destructive terahertz imaging of illicit drugs using spectral fingerprints," Optics Express, vol. 11, no. 20, pp. 2549–2554 © 2003 The Optical Society [9]].**

# 2.2 Terahertz Imaging Systems

Terahertz imaging exists in two modalities: active and passive. Active imaging needs a source to radiate the scene while the detector collects the information of the transmitted or reflected light from the scene. Passive imaging systems use naturally occurring sources of radiation such as a black body object and detect the contrast in the temperature within a scene.

## 2.2.1 Passive Imaging Systems

Passive systems are ground based systems that have been created with heterodyne receivers and cryogenic sensors operating at 4 K with very low NEP to achieve high sensitivity [11]. They are mainly used for space imaging where cold sky illumination is available. Natural terahertz sources are offered in the universe where the energy is radiated by the emissivity of objects such as interstellar dust [12]. These types of systems can achieve long stand-off imaging in the range of metres with resolutions in the range of centimetres. Another advantage is the lack of exposure radiation which has better public acceptance when used for security imaging. Their drawbacks are size, weight, power and high-cost due to the required cooling [13]. Their operation at room temperature is very limited because they do not have a large dynamic range compared to active systems

7

meaning that the temperature difference between the receiver, the target and the ambient is minor and hardly detectable.

## 2.2.2 Active Imaging Systems

The most common form of terahertz imaging is active imaging systems which has two main non-invasive imaging categories: Pulsed Time Domain (PTD) and Continuous Wave (CW). An example schematic of both modalities is shown in Figure 2.3a and b respectively.
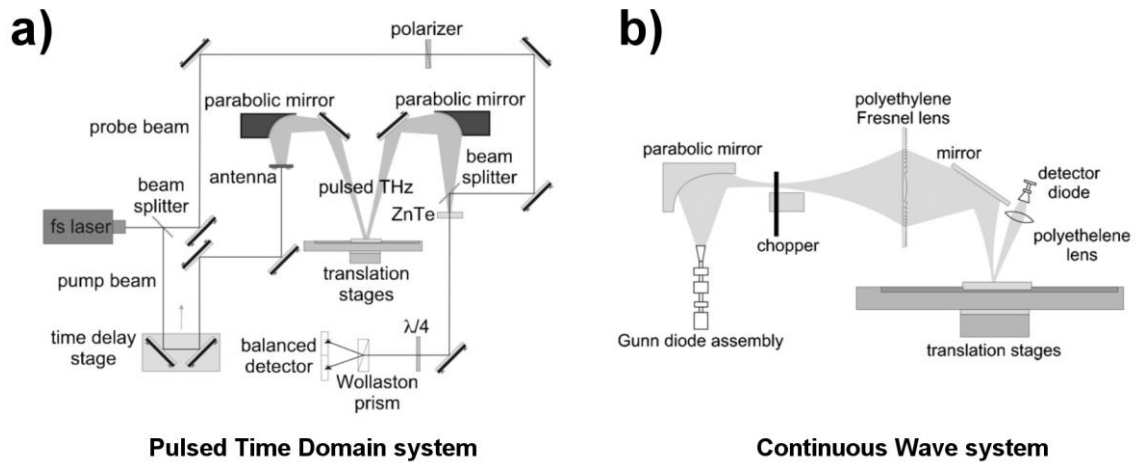


**Figure 2.3 – Active terahertz imaging systems: a) Pulsed Time Domain system and b) Continuous Wave system. Reproduced with permission: [N. Karpowicz, H. Zhong, J. Xu, K.-I. Lin, J.-S. Hwang, and X.-C. Zhang, "Comparison between pulsed terahertz time-domain imaging and continuous wave terahertz imaging," Semiconductor Science and Technology, vol. 20, no. 7, pp. S293–S299 © 2005 IOP Publishing** [14]**].**

The main form of PTD imaging is the terahertz time-domain spectroscopy (THz-TDS) technique. An ultra-fast laser that produces optical pulses e.g. femtosecond Ti-sapphire laser is separated into two optical paths using a beam splitter [15]. One is directed through a time delay stage and is then focussed onto a photoconductive antenna. The antenna is fabricated on top of a low temperature GaAs substrate and emits pulses of terahertz radiation which are directed using a focussed lens onto the object. The reflected or transmitted terahertz radiation is then directed onto the detector. The second pulse from the femtosecond laser is directed to the terahertz detector and effectively 'samples' the electric field of the terahertz wave incident on the detector. The terahertz pulse interacts in the detector with a much-shorter laser pulse (e.g. 0.1 picoseconds) in a way that produces an electrical signal that is proportional to the electric field of the terahertz pulse at the time the laser pulse gates the detector on. By repeating this procedure and varying the timing of the gating laser pulse, it is possible to scan the terahertz pulse and construct its electric field as a function of time. A Fourier transform is then used to extract the frequency

spectrum from the time-domain data [1] and the transmission, reflection and absorption can be determined for the object under test [14]. Moreover, since the waveform contains both amplitude and phase information it is possible to calculate the complex refractive index of the object. The cost (dominated by the femtosecond laser), extensive and bulky component requirement and complexity of this technique have significantly hindered its opportunities as a portable imaging system, despite this there has been recent advancements in scaling down these systems.

CW imaging systems use narrow-linewidth, single frequency terahertz sources. In the imaging experiments, the beam is focused into the object under test or reflected with the necessary optical lenses. Since there is no necessity for a time delay stage and femtosecond laser, the optics required and complexity of the test set up is reduced. CW imaging systems provide information by measuring the change in signal amplitude to the detector after being transmitted or reflected by the object. Although CW imaging systems do not give information regarding time-domain and frequency-domain, they offer compact, simple, fast and relatively low-cost systems that could lead to portable imaging systems.

# 2.3 Terahertz Sources

The difficulty of creating terahertz sources with high power is due to the limitations in traditional silicon electronic and semiconductor devices. These essential building blocks are limited by reactive parasitics, transit times that cause high-frequency roll-off or resistive losses that dominate the device impedances at these wavelengths [12].

## 2.3.1  Schottky-Based Frequency Multipliers

Sources based on frequency multiplication offer many advantages for generating terahertz radiation. Fundamental local oscillators (LOs) are a mature technology offering high output power and efficiency, low noise, electronic tuning and compact design. This common technique uses multiplication of lower frequency oscillators which are composed of planar GaAs Schottky barrier diodes (SBDs) [16]. These diodes have high electron mobility, compared to silicon, enabling them to be used for terahertz applications. An even number of diodes is used in an anti-series configuration placed in an aluminium nitride or quartz substrate. The advantage of the aluminium nitride substrate is that it provides very low dielectric loss while the quartz substrate provides high thermal conductivity. The advantage is the reduction in signal attenuation and low temperature rise of the diodes. They are fixed via a flip-chip bonding approach in a split-block waveguide configuration

[17]. Terahertz sources built with this technique can operate at 1.2 THz with an output power of 80 µW at room temperature and when operated cold (120 K) they can reach over 250 µW [18]. Although these sources can operate without the use of cryogenic systems, their performance is limited by their low output power.

## 2.3.2  Quantum Cascade Lasers (QCLs)

Lasers for visible and near-infrared frequencies have been designed with semiconductor devices such as p-n diode junctions where the emission of a wavelength depends on the bandgap of the material used. This technique is done by emitting EM radiation through the recombination of a conduction band electron with a valence band hole across the active material bandgap [19]. Although this process is very common, it cannot be directly translated to terahertz frequencies due to the lack of bulk semiconductor materials with a suitable bandgap making it difficult to translate the widely used technique to terahertz lasers. The reason is that the terahertz radiation has long wavelengths and a very small energy gap of approximately 0.4 meV to 0.04 eV making it very difficult to grow, process and fabricate such narrow bandgap materials into heterostructure materials [20].

The solution implemented to overcome this problem is the use of QCLs. They are created in repetitive stacks of quantum semiconductor thin layers of varying material composition. This periodic stack of materials forms a superlattice. In regular semiconductor laser diodes, only a single recombination of electron-hole pairs is allowed, once the photon is generated the electron that produced it stays in the valence band. In QCLs this is not the case; the electrons are free to tunnel into the next period of the structure where another photon can be emitted from a single electron-hole recombination. This recombination happens in the inter-subband of these heterostructures and is used for laser emission [21].

The use of quantum semiconductor materials and the fact that photons can freely transverse through other bands of the structure gives them the name "quantum cascade". This process increases the laser's efficiency leading to higher output powers than semiconductor laser diodes. The emission wavelength is tuned by the layer thicknesses of the semiconductor materials. The disadvantage of QCLs is their operation at cryogenic temperatures and their limited frequency tuning [22].

Recent research is focused on designing room temperature QCLs without limiting output power. Lu *et. al.* presented a room temperature continuous emission 3.6 THz source with an output power of 3 µW and when operated in pulsed mode the output power can

achieve 1.4 mW [23]. An alternative form to produce terahertz QCLs at room temperature based on intracavity difference-frequency generation (DFG) was presented by Belkin *et. al.*[24]. The technology is based in generating a terahertz beam out of the difference of two IR pump beams created in a nonlinear optical crystal. The terahertz DFG QCL source operates with mid-IR wavelengths at 8.9 μm and 10.5 μm resulting in a terahertz wavelength of 60 μm with an output power of 300 nW at room temperature. Because of their small size, room temperature operated QCLs are very promising for active imaging and integration with hand held terahertz detectors to form portable terahertz imaging systems.

### 2.3.3 Photo-conductive Generation

Dr. David Auston and his colleagues were the pioneers of the design of photoconductive antennas (PCAs) which subsequently led to the development of THz-TDS [25]. A PCA has two important features: an antenna structure and a photoconductive substrate. The antenna structure is used to radiate sub-millimetre wavelength EM pulses into free space [26]. The approach of generating and detecting extremely fast ultra-short electronic pulses by combining high speed optical sources, microwave transmission line techniques and photoconductive properties of semiconductor materials led to the creation of the "Auston switch" [27].

Terahertz radiation is created using this method by applying a large electric field between an antenna comprising two electrodes deposited onto a highly resistive semiconductor thin film. When a photon with energy greater than the material bandgap interacts with an electron in the valence band, a free electron is excited in the conduction band and a hole is left behind in the valence band of the film. The photocarriers in the conduction band of the semiconductor are generated by the incident ultra-short laser pulses focused between the electrodes [19].

The excited electron-hole pairs in the semiconductor are accelerated by the electric field during the optical pulse breaking down an electron switch, which shorts out an applied voltage to produce high-voltage pulses and a broadband EM pulse in the terahertz region [15]. A second optical pulse is introduced to terminate the initial pulse by creating a short-circuit in the transmission line [27]. The semiconductor physical parameters and the laser ultra-short pulse intensity and duration define the output power and bandwidth of the radiation. Modular PCA terahertz sources are available in 0.1 THz to 4 THz with up to several tens of microwatts average output power radiation [15]. The PCA acts as both the

source and the detector in a typical THz-TDS system. The detection process will be explained in section 2.4.1.

### 2.3.4 Optically Pumped Lasers

Optically pumped lasers provide the largest output power of all the terahertz sources; powers in excess of 100 mW are readily attainable. A typical laser system consists of two waveguide cavities: a $CO_2$ pump laser and an optically pumped far infrared (FIR) laser. They operate using the principle of molecular rotational transition of gases. A grating-tuned $CO_2$ laser, with emission in the 9 μm to 11 μm range, is typically used to pump the gas in the FIR cavity. In the FIR molecular laser, vibrational transitions of molecules displaying a permanent electric dipole moment are excited by the $CO_2$ pump laser and subsequently emitted [28]. The pump radiation is often admitted into the terahertz cavity through a small input-coupling-hole in one end mirror. The terahertz radiation produced in the laser is then typically emitted through either an output-coupling-hole or some sort of uniform output couple [29]. The wide gain profile makes it possible to tune the FIR laser emission by sweeping the cavity length. The disadvantages of using FIR lasers is that they are not continuously tuneable and require large cavities as well as high power supplies, although they have a frequency output range from 0.25 THz to 8.0 THz, depending on the gas molecule used in the FIR cavity [28], [30].

## 2.4 Terahertz Detectors

Originally, terahertz imaging systems required sources and detectors to operate at cryogenic temperatures. Cryogenic detectors operate with liquid helium at temperatures of 4 K (-269 °C) and below. The detectors were cooled to reduce the surrounding noise hence maximising the signal to be measured, thus increasing sensitivity. This approach requires bulky and expensive equipment that limit the potential of terahertz imaging systems. Therefore, present research in terahertz technology focuses on the development of low-cost, uncooled detectors where uncooled refers to not employing artificial means of reducing the temperature of the detector and its operation is at ambient temperature. Uncooled imaging systems detect the localised heating using thermal sensors and were first used on IR imaging systems. The most common cooled and uncooled sensors for terahertz applications will be explained throughout this section.

### 2.4.1   Photo-conductive Detectors (PCDs)

Dr. David Auston designed PCDs in 1984 based on the PCA design explained in the section 2.3.3 [27], [31]. PCDs were the first devices used to detect pulsed terahertz radiation and now they are primarily used in THz-TDS. In the PCA structure, there are two metal contacts evaporated onto a semiconductor substrate. A voltage is connected to the electrical contacts and the excited photo-carriers are accelerated by the electric field during the optical pulse resulting in the generation of terahertz waves. This same structure is used as a PCD, contrary to PCAs, a current input is connected to the two metal contacts. During the optical pulse the excited photo-carriers are accelerated by the electric field component of the incident terahertz pulse shone at the gap between the electrodes. This process closes the circuit and the generated current can be measured and is proportional to the terahertz field [32].

### 2.4.2  Golay Cells

Golay cells are thermal terahertz sensors classified as opto-acoustic detectors that have been widely used by astronomers. The concept and design of Golay cells was first proposed by Marcel J. E. Golay [33]. In a Golay cell, heat is transferred to a small volume of gas in a sealed chamber behind the absorber. As the gas expands, the deformation of a membrane caused by the pressure increase is translated as the terahertz response by an optical reflectivity measurement [34]. These devices are designed for operation in the spectral range of 20 GHz to 20 THz. They report a reasonable performance with an approximate NEP of 10 nW/$\sqrt{Hz}$ reaching a responsivity of 10 kV/W with 12.5 Hz modulation [35].

Although Golay cells have been widely used, their performance is degraded by mechanical vibrations, therefore they need to be mounted on vibration-isolating benches increasing their size and cost. Also, they need high voltage power supplies in the range of ±15 V. These detectors suffer from slow response times in the range of 25 ms and require input windows for high transparency, e.g. polyethylene window, which lowers their transmission characteristics [36].

### 2.4.3  Schottky Barrier Diodes

Schottky barrier diodes (SBDs) are named after Walter H. Schottky for his pioneering work in the field of metal-semiconductor interfaces [37]. They have been widely used for the detection of millimetre and sub-millimetre wavelengths. They are used

both in direct detection and as nonlinear elements in heterodyne receiver mixers operating in the temperature range of 4 K to 300 K. For this function, planar Schottky diodes are usually fabricated on a highly doped GaAs substrate. GaAs offers high mobility and a sufficiently large bandgap, thus barrier height to reduce leakage currents and cost-effective post-processing [38]. They are composed of a metal-semiconductor barrier having fast switching properties (around 1 ns), can reach very low NEP and high responsivity at terahertz waves. However, their responsivity drops orders of magnitude at frequencies greater than 1 THz and are not tuneable [1]. The company Virginia Diodes, Inc. has reported SBD detectors with a responsivity of 400 V/W at 900 GHz, with a thermal time constant of less than 1 ns and NEP of 20 pW/√Hz at 800 GHz [39].

## 2.4.4 Field Effect Transistors (FETs)

Research has demonstrated CMOS-based devices, such as FETs, can operate as broadband detectors of sub-Terahertz radiation. Dyakonov *et. al.* predicted that a steady current flow in an asymmetric FET channel could lead to instability and spontaneous generation of plasma waves. This would lead to the emission of EM radiation at the plasma wave frequency [40].

Therefore, the channel of a FET can act as a resonator for plasma waves propagating in the channel which are generated from the modulation of the electron concentration. An excess of positive charges decreases the electron concentration and in consequence creates an excess of positive charges attracting electrons nearby. The detectable plasma frequency is dependent on the gate lengths, for example, if the length is in the dimension of a micron or sub-micron it can reach sub-terahertz or terahertz range [41]. Radiation detection is a result of the rectified alternating current (AC) current induced by the nonlinear properties of the transistor channel [42]. The photoresponse appears in the form of direct current (DC) voltage between source and drain and is proportional to the radiation power (photovoltaic effect). Asymmetry between the source and drain is needed to induce the photovoltaic effect. Dyakonov presented three causes of asymmetry [43]:

- Difference in the source and drain boundary conditions due to external parasitic capacitances
- Asymmetric design of the source and drain contact pads causing an AC voltage between the source and the gate (or drain and gate) from the incoming radiation
- Asymmetry from a DC current passed between the source and drain creating a depletion of the electron density on the drain side of the channel

Theoretically, it is assumed that the incoming radiation creates the AC voltage between the source and the gate and there is no DC current between the source and drain.

Unfortunately, as the radiation frequency increases, the responsivity decreases rapidly beyond 1 THz. This is because the photovoltaic signal decreases due to the reduction in coupling efficiency and larger transistor parasitics at higher frequencies resulting in increased noise [41]. The response can increase if the device is cooled or a non-silicon high mobility material FET is used such as a GaAs FET [44]. Furthermore, individual pixels, each of which require an antenna, are physically large at sub 1 THz wavelengths [45]. R. A. Hadi *et. al.* have reported a broadband (0.6-1 THz) detector implemented in a 65 nm bulk CMOS process with an integrated lens. At 1.027 THz the responsivity is 800 V/W and the minimum NEP is 66 pW/$\sqrt{Hz}$ (without lens) [46].

## 2.4.5 Pyroelectric detectors

Pyroelectric sensors are made from a very unique crystal that becomes electrically polarised when there is a temperature change. When the sensor is radiated by an EM wave, it absorbs the radiation and transforms it into an electrical charge. Pyroelectric detectors are AC sources whose current output is inversely proportional to the thickness of the material and rate of change of temperature [36]. The company Spiricon has created high performance pyroelectric cameras with an FPA of 124 x 124 pixels with a 100 μm pitch where the active area is 12.4 mm x 12.4 mm. The camera is called Pyrocam III [47]. Each detector is composed of a rugged $LiTaO_3$ pyroelectric crystal mounted with indium bumps to a solid-state readout multiplexer. The camera has a wavelength range of 0.3 THz to 300 THz. In order to work in the terahertz range, a polyethylene window is installed to avoid visible and near-IR waves. If the camera is operated with a CW laser, an internal chopper must be used with a 48 Hz chop rate [48].

The disadvantage is that pyroelectric sensors require modulation as the sensor will not create a current at constant temperatures [49]. Although, pyroelectric sensors suffer from slow response times; the speed can be increased by either employing a small area detector or by using fast laser pulse detection, at the expense of sensitivity [44]. Despite having found solutions to the aforementioned limitations, these sensors unfortunately lack the attractive potential for efficient integration offered by CMOS because the pyroelectric material is difficult to process.

### 2.4.6  Microbolometers

Microbolometers are uncooled thermal detectors composed of an element that measures the incident EM power by detecting a response to a temperature change [50]. As the sensors are struck by incident radiation the temperature increase is measured by an electric signal (e.g. resistance change). The sensing material chosen for the microbolometer has a large influence in the sensitivity of the detector. It is important to have a material with a high TCR to detect signal changes per degree of temperature. Resistive microbolometers have been widely used to detect wavelengths in the IR spectrum and they are implemented in a suspended bridge configuration for better thermal isolation [51]. The most common materials used in uncooled detectors are VOx, amorphous silicon ($\alpha$-Si) and P+/Nwell silicon diodes [52]. The use of microbolometers has now evolved into terahertz detection as well. The successful implementation of microbolometers is due to their ability to be integrated with a CMOS process giving opportunity to create FPAs with their respective readout circuit.

#### 2.4.6.1  Vanadium Oxide

VOx uncooled detectors were originally used in IR imaging systems [53]. VOx is a thermally sensitive resistive material with high TCR properties (-2 %/K to -3 %/K) at room temperature, low 1/f noise and relatively mature deposition technology compatible with basic silicon micro-machining techniques [54]. The challenge with VOx is to find an adequate deposition process and as a result film properties that obtain a balance between high TCR and low sheet resistance for good low noise performance at room temperature. In order to make the bolometer layer compatible with the CMOS technology, the processing temperature has to be kept as low as possible [55]. VOx films are deposited as microbolometers above every pixel of the FPA. The variability introduced by the minimal difference in the VOx film properties throughout all the pixels is typically taken into account in the data acquisition process by having reference pixels. The readout techniques compensate for any minor non-uniformity introduced by the VOx.

#### 2.4.6.2  Diode Sensor – P+/Nwell

Diodes have been widely use as sensors in imaging systems due to their temperature sensing characteristics and existing integration in the standard CMOS process. The major advantage of the diode is that the p-n junction can be used for temperature sensing therefore they have a lower cost of production and smaller pixel size [56]. In contrast to the VOx sensor presented previously, the sensing layers are in the bottom layer of the CMOS process where the diodes reside. The diodes have a forward voltage of about

0.7 V and a voltage change with temperature in the range of -1 mV/K to -2 mV/K resulting in a TCV of -0.2 %/K which is low compared to the VOx, but having more diodes in series can increase the TCV for better sensitivity [52]. The benefits of investigating the p-n diode sensor are its simple post-processing etching steps consisting in creating a thin silicon membrane and pixel isolation, better sensor uniformity, lower noise compared to VOx and reduced self-heating.

### 2.4.6.3  Amorphous silicon

Amorphous silicon is a material widely used for a variety of devices such as the active layer in thin-film transistors for liquid crystal displays, small area solar powered photovoltaic devices for consumer products and large area power solar cells [52]. Amorphous silicon microbolometers have the advantage of high TCR, high optical absorption coefficient and mainly, the low-cost of fabrication since they can be manufactured using silicon compatible processes. The films can only be produced by plasma-enhanced chemical vapour deposition (PECVD) or sputtering [52]. The TCR and sheet resistance characteristics depend on the doping concentration, deposition temperature and annealing. TCRs up to 2.5 %/K have been achieved at room temperature [57]. The fact that α-Si can be deposited at low temperatures (75°C) makes the material suitable for cheaper production and high-volume applications [58]. Amorphous silicon is comparable to VOx but it has the slight disadvantage of high impedance, thus higher thermal noise. This type of noise is the main contributor to uncooled detectors and it affects the sensitivity of the detector. Due to the higher noise, the image quality is affected by not being able to detect the smallest of temperature differences [59].

# 2.5 Room Temperature CMOS Compatible Terahertz Imaging Systems

Thermal imaging systems originated with IR technology around 200 years ago when IR (calorific) rays were discovered by Sir W. Herschel in 1800 [60]. Thermal imaging was based on creating an electronic picture of the scene by creating a map of thermal energy representing different levels of radiant energy called a "thermogram" [60]. In the late 1870s, S. P. Langley developed the "bolometer" as part of his studies of the IR portion of the solar spectrum. The bolometer was able to measure thermal radiation and detected it from a cow standing at a distance of 400 m [61]. In 1897, H. Rubens and E.F. Nichols published the existence of the "terahertz gap" by saying that there was a wide region of separation between electrical waves and light waves in the EM spectrum and that more had

to be done to study them [62]. Between 1894-1898, J. C. Bose created the galena crystal detector and developed the first terahertz experiments. This was the beginning of terahertz detection and generation, and where the term "terahertz" was applied to sub-millimetre/FIR EM radiation that occupies the wavelength range between 300 GHz to 3 THz [63].

Thermal imaging is now the focus of terahertz imaging systems. This removes the necessity for cryogenic cooling, thus reducing component size and cost. In order to make this possible, CMOS compatibility is essential for the integration of uncooled sensors and terahertz absorbers able to detect terahertz waves at room temperature reducing the fabrication cost. CMOS integration also overcomes the challenge of scaling two dimensional array sensors (FPAs) required for high resolution imaging. The development of FPAs started in the 1970s and has revolutionized imaging systems since then. This section will mention examples of room temperature FPAs.

## 2.5.1  Field Effect Transistor Focal Plane Array

A room-temperature 3 x 5 pixel FPA operating at 0.65 THz has been presented using FETs as differential on-chip patch antennas [64]. The FPA was fully integrated in a 250 nm BiCMOS process. The 3 x 5 FPA is shown in Figure 2.4 illustrating the pixels with an area of 150 x 200 $\mu m^2$. The FPA reports a responsivity of 80 kV/W at a gate voltage of around 0.35 V and minimum NEP of 300 pW/$\sqrt{Hz}$ at 0.45 V. Each pixel consisted of a narrow-band patch antenna including an integrated ground plane, a differential NMOS FET pair, and a 43-dB voltage amplifier with a 1.6 MHz bandwidth. The maximum cutoff frequency of the NMOS transistors was 35 GHz. The image was obtained in transmission mode by simultaneously scanning four pixel lines in parallel at a frequency of 30 KHz.

Another example of a room temperature FET FPA was designed by STMicroelectronics. Their prototype consists of a 32 x 32 pixel array built in a 65 nm CMOS bulk process technology and operates in a CW mode. The array is also based on differential on-chip ring antennas coupled to NMOS FET detectors. The camera operates at a frequency of 856 GHz achieving a responsivity of 115 kV/W when using a 5 dB VGA gain. The minimum NEP is 12 nW integrated over a 500 kHz video bandwidth, operating in a video-mode at a maximum of 500 fps [65]. Unfortunately the responsivity of FETs decreases rapidly beyond 1 THz  and the individual antennas required in every pixel are physically large at sub 1 THz wavelength [66].
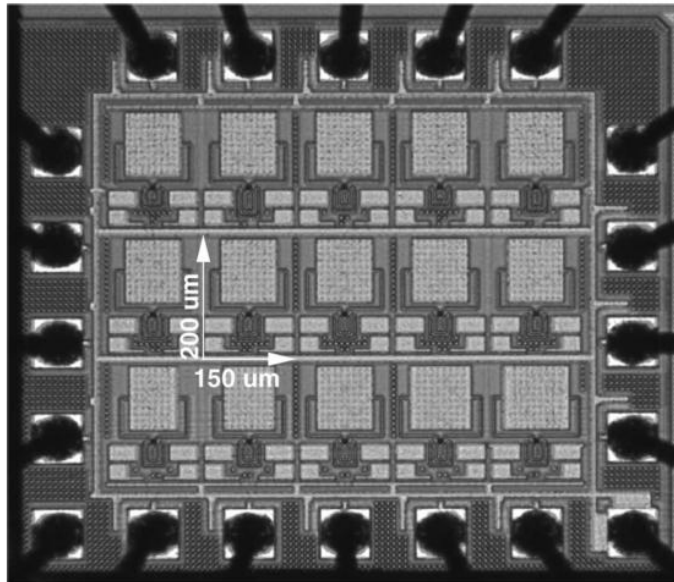
**Figure 2.4 – Room temperature Field Effect Transistor Focal Plane Array containing a 3 x 5 pixel array. Reproduced with permission: [E. Öjefors, U. R. Pfeiffer, A. Lisauskas, and H. G. Roskos, "A 0.65 THz Focal-Plane Array in a Quarter-Micron," Journal of Solid-State Circuits, vol. 44, no. 7, pp. 1968–1976 © 2009 IEEE** [64]**].**

## 2.5.2 Infrared based Focal Plane Array

Traditional quarter wavelength absorption techniques have been widely used to detect wavelengths in the IR spectrum. The thermal imagers consist of antenna coupled microbolometers integrated into CMOS technology. Microbolometers are used to absorb the IR radiation in a resonant cavity where either the bolometer membrane is placed at a distance of $\lambda/4$ ($\lambda$ is the targeted wavelength) from the mirror surface in the substrate (Figure 2.5a) or the thickness of the bolometer membrane is $\lambda/4$ (Figure 2.5b) [67]-[68]. In the second case, the reflective layer or mirror is placed directly below the membrane. The mirrors are used to reflect the IR radiation back into the bolometer to be absorbed. Resistive microbolometers (e.g. VOx) are the most common thermal sensing materials due to their high temperature coefficient. The devices are implemented in a suspended bridge configuration for better thermal isolation, they have thin membranes to minimise thermal conduction between pixels and are compatible with CMOS technology. The bolometer bridge is then connected to the readout electronics by narrow metallic legs and vias.
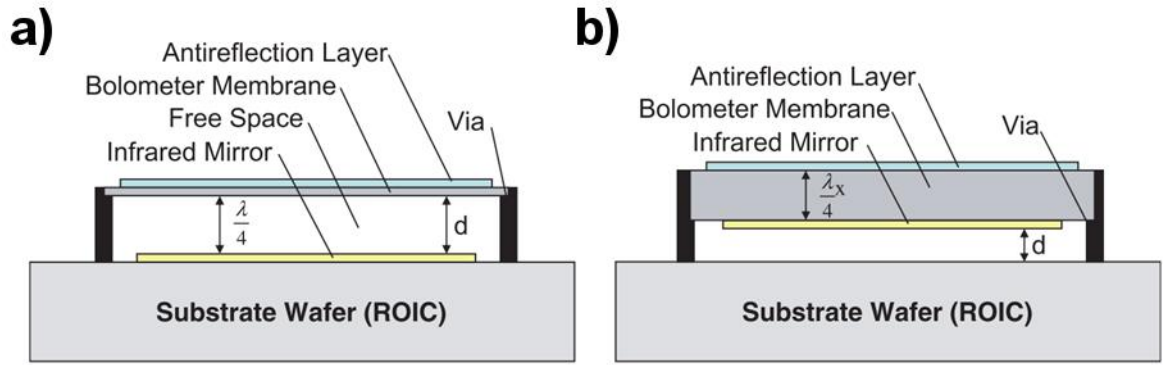
**Figure 2.5 – Cross-sectional view of traditional quarter wavelength devices. a) The thin membrane is separated by λ/4 and b) the membrane thickness is λ/4 where λ is the wavelength of the targeted radiation. Reproduced with permission: [F. Niklaus, A. Decharat, C. Jansson, and G. Stemme, "Performance model for uncooled infrared bolometer arrays and performance predictions of bolometers operating at atmospheric pressure," Infrared Physics & Technology, vol. 51,  pp. 168–177 © 2008 Elsevier [67]].**

CEA-Leti has designed a 320 x 240 FPA composed of 50 μm pitch pixels able to operate as a broadband detector in the 2 THz to 4 THz range. Their technology is based on traditional quarter wavelength thermal imagers. At terahertz frequencies, the quarter wavelength absorption approach seems unfeasible due to the requirement to have such large cavities. For example at 1 THz, a traditional quarter wavelength absorber, such as those used in the mid IR, would have to be positioned a distance 75 μm away from the underlying substrate. This is unfeasible in practice due to the extremely challenging fabrication requirements.

But a new approach is given for this challenge: there is a separation between the EM absorption and the thermometer (sensor) as shown in Figure 2.6. Each pixel is composed of a broadband antenna and a resonant quarter wavelength cavity designed to couple efficiently with terahertz radiation [2]. The reported thermal time constant is between 20 ms and 40 ms. At 2.5 THz the NEP is 32 pW with a video rate of 25 Hz and a responsivity of 12.6 MV/W. The major disadvantage of this method of detection is the extensive fabrication process that increases the production cost.
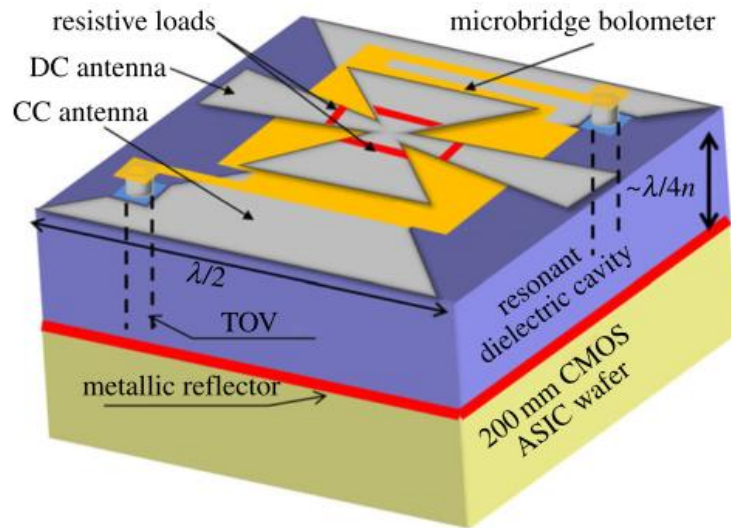
**Figure 2.6 - CEA Leti bolometer pixel structure based on quarter wavelength resonant cavity. Reproduced with permission: [F. Simoens and J. Meilhan, "Terahertz real-time imaging uncooled array based on antenna and cavity-coupled bolometers," Philosophical Transactions A Mathematical, Physical & Engineering Sciences, vol. 372, no. 2012, pp. 1–12 © 2014 Royal Society Publishing** [2]**].**

### 2.5.3 Diode based Microbolometer Focal Plane Array

Another approach for CMOS terahertz FPAs is the integration of highly sensitive microbolometers using silicon diode p-n junctions as the temperature sensitive element instead of resistive microbolometers. This technique has been very successful for IR imaging providing very cost effective devices. Perenzoni *et. al.* created a polysilicon diode-based microbolometer with metal antennas connected to each pixel as shown in Figure 2.7. These microbolometers are multiple diodes connected in series suspended above the substrate implemented in a 350 nm CMOS technology [69]. The chip includes different antenna sizes that can be individually selected to operate at 0.5 THz, 1.0 THz and 2.0 THz. The device is composed of an antenna connected to a matched load which heats up proportionally to the incident EM radiation and the heat is transferred by conduction to the polysilicon diodes. The polysilicon diodes are placed near the antenna load and a set of reference diodes is used to track temperature variations. The air gap underneath the oxide membrane is created by removing the silicon underneath and is needed to reduce the thermal losses travelling towards the substrate. The diode array has an estimated NEP of 100 pW/$\sqrt{\text{Hz}}$ at a bias voltage of 0.65 V. Due to the configuration of diodes in series the temperature coefficient of current (TCC) is in the range of 5 % to 15 % meaning that the diode current will change at this percentage rate per every degree of temperature, depending also in the bias voltage.
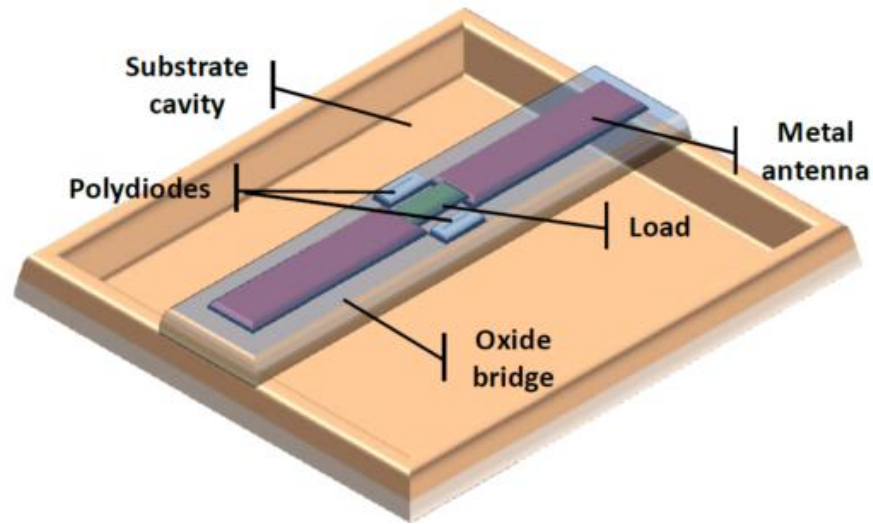
**Figure 2.7 - Polysilicon diode-based microbolometer with metal antennas connected to each pixel of the focal plane array. Reproduced with permission: [M. Perenzoni and S. Domingues, "A diode-based bolometer implemented on micromachined CMOS technology for terahertz radiation detection," Proceedings of SPIE, Silicon Photonics and Photonic Integrated Circuits III, vol. 8431, pp. 84311T–1–6 © 2012 SPIE** [69]**].**

SBDs fabricated in CMOS without any post-processing steps have been reported by Han *et. al*. The investigators created a 4 x 4 passive-pixel array architecture functioning at 280 GHz with DC biased SBDs. The term passive-pixel means that the terahertz sensors have the diodes forward biased to achieve a small dynamic resistance of approximately 50Ω, therefore no in-pixel buffers are needed to drive the bus for multiplexing properties. This technique also helps to reduce the NEP due to the noise contribution coming from the in-pixel amplifier. The pixel pitch is 500 μm as shown in Figure 2.8. When the input modulation is 1 MHz, the measured peak responsivity is 5.1 kV/W at 282 GHz and NEP of 29 pW/√Hz for a bias current of 50 μA [70]. The peak responsivity reduces to 336 V/W after de-embedding the on-chip amplifier gain of 24 dB. They also demonstrate an array with only 4 SBDs working at 860 GHz. They reduce the number of cells to compensate for NEP degradation. The responsivity peak at 860 GHz is 273 V/W with a NEP of 42 pW/√Hz for a bias current of 20 μA.
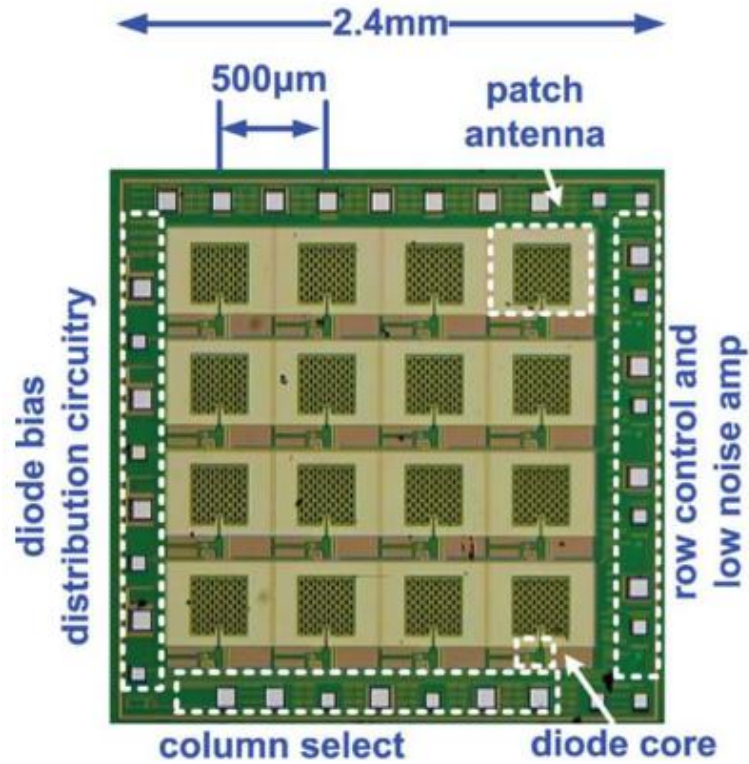
**Figure 2.8 - Schottky-barrier diode based focal plane array. Reproduced with permission: [Ruonan Han; Yaming Zhang; Youngwan Kim; Dae Yeon Kim; Shichijo, H.; Afshari, E.; Kenneth, K.O., "Active Terahertz Imaging Using Schottky Diodes in CMOS: Array and 860-GHz Pixel," IEEE Journal of Solid-State Circuits, vol.48, no.10, pp.2296-2308 © 2013 IEEE** [70]**].**

## 2.5.4 VOx Microbolometer Focal Plane Array

Uncooled microbolometer technology has enabled low-cost FPAs with a high number of pixels with reliable performance. FPAs with thermal microbolometers made with VOx thin film material have been reported using thermally isolated microbridges with high TCRs. The advantage of VOx microbolometers is their reduced complexity, low-cost, no cooling and no scanner technology with high reliability, lightweight and complete integration with silicon integrated circuits.

Chevalier *et. al.* presented a broadband terahertz camera based on VOx microbolometers shown in Figure 2.9. The camera is has 384 x 288 pixels with at 35 µm pitch and is called IRXCAM-THz-384 [71]. They operate a real-time camera with a video rate of 50 Hz. The NEP reported at two different frequencies is: 24.7 pW at 4.25 THz and 76.4 pW at 2.54 THz. The camera is equipped with a custom F/0.94 THz refractive lens barrel used for high quality images in real-time at 50 Hz.
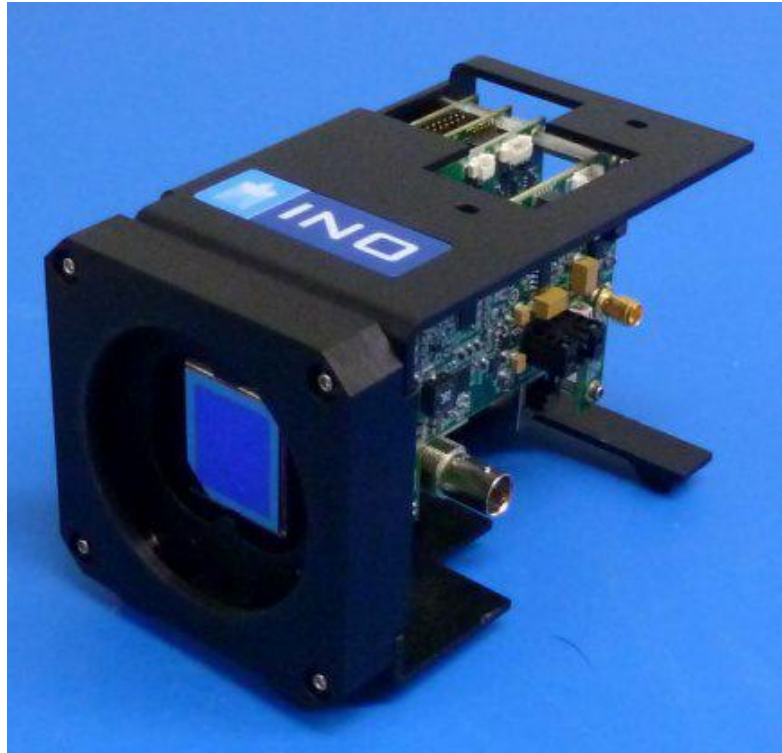
**Figure 2.9 - VOx bolometer 384 x 288 pixels with 35 μm pitch from the National Optics Institute. Reproduced with permission: [C. Chevalier, L. Mercier, F. Duchesne, L. Gagnon, B. Tremblay, M. Terroux, F. Généreux, J.-E. Paultre, F. Provençal, Y. Desroches, L. Marchese, H. Jerominek, C. Alain, and A. Bergeron, "Introducing a 384x288 pixel terahertz camera core," Proceedings SPIE, Terahertz, RF, Millimeter, Submillimeter-Wave Technology and Applications VI, vol. 8624, pp. 86240F–1–8 © 2013 SPIE** [71]**].**

# 2.6 Metamaterials

The classification of materials with regards to their EM properties is shown in the ε-μ, four-field, diagram in Figure 2.10. It indicates the combinations of positive and negative values for the permittivity and permeability of materials. Ordinary materials or dielectric materials with positive permittivity and permeability, such as air with ε=μ=1, are found in the first quadrant. Electric and magnetic plasma are found in the second and fourth quadrant respectively. Materials with negative permittivity and negative permeability, non-existent in nature, are found in the third quadrant. These are called left-handed materials (LHMs) or negative index materials (NIM) and were first proposed by Veselago in 1968 where he proved theoretically that the index of refraction between an ordinary medium with ε, μ > 0 and one with ε, μ < 0 would be negative. In his explanation, he quoted Snell's law to explain the possibility of a material with a negative index of refraction [72]. He introduced the terms $p_1$ and $p_2$ to give a more precise 'law of refraction' expression shown in Equation 2.1:

$$\frac{\sin \varphi}{\sin \psi} = n_{1,2} = \frac{p_2}{p_1} \left| \sqrt{\frac{\varepsilon_2 \mu_2}{\varepsilon_1 \mu_1}} \right| \qquad \textbf{2.1}$$

where $p_1$ and $p_2$ represent the characteristics of the first and second media, if these two are different in sign, the index of refraction will be negative [73]. Figure 2.11a shows Veselago's example of how the rays passing through lenses made out of LHMs change their paths inversely in contrast to their normal path. The convex lens has a diverging effect and the concave lens a converging effect. Figure 2.11b shows a representation of a liquid with a positive index of refraction 1.3 (left) and a negative index of refraction -1.3 (right) indicating the light bending properties of a left-handed medium [74].

Around thirty years later, John Pendry realised the artificially electric plasma using the wire medium showing a negative permittivity [75]. In 1999, Pendry *et. al.* proposed the creation of materials with negative effective permeability $\mu_{eff}$. His work consisted in split-ring resonators where he showed that the periodic array of this particular structure resulted in a negative permeability and magnetic response produced by the circulating current on the resonators [76]. His discovery revolutionised the concept of non-existent materials and new materials made from artificial objects were investigated. The first experimentally demonstrated artificial LHM was made by R.A. Shelby, D.R. Smith and S. Schultz in 2001 where he combined the wire medium with SRRs to produce a material with a negative index of refraction [77]. These new materials exhibit properties not available in nature which led to the creation of MM structures.
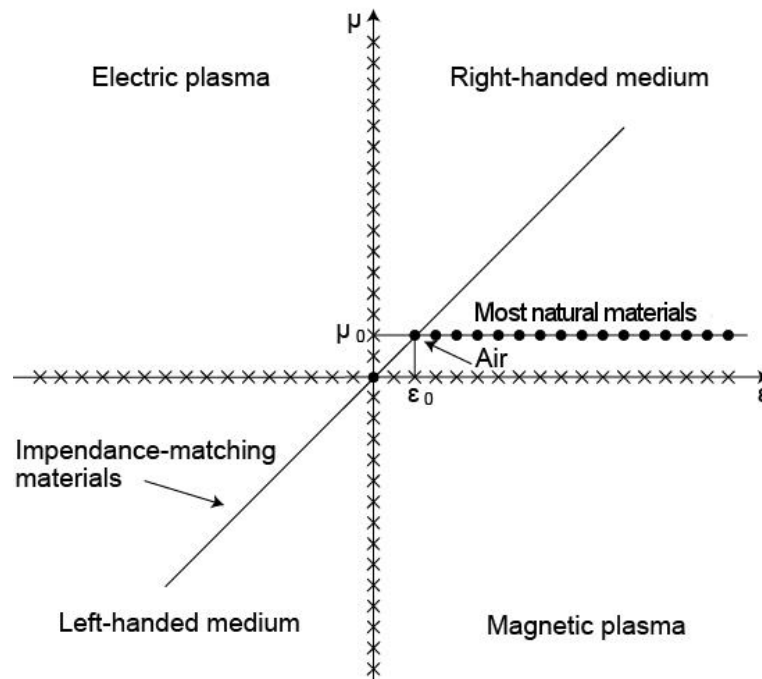


**Figure 2.10 – Classification of materials with regards to their electromagnetic properties in the *εμ*-plane. Image adapted with permission: [Cui, T. J., Smith, D. R. & Liu, R. editors. Metamaterials: Theory, Design, and Applications © 2009 Springer [78]].**
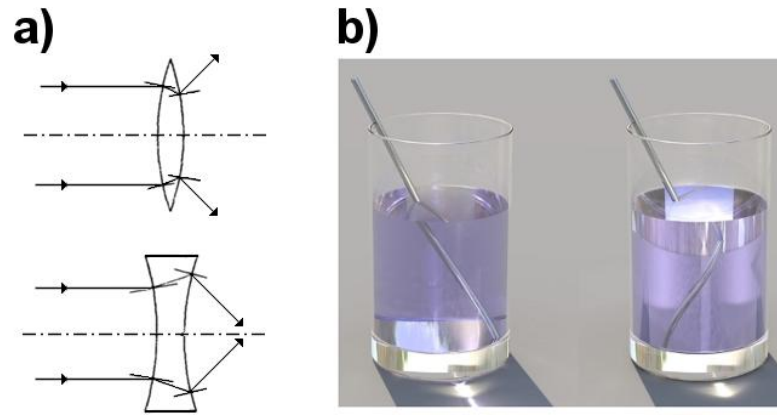
**Figure 2.11 – Negative index materials: a) Veselago's example of the ray paths passing through lenses of materials with negative index of refraction** [73] **and b) liquid with a positive index of refraction 1.3 (left) and a negative index of refraction -1.3 (right)** [74].

The term MM was derived from the Greek prefix -*meta* meaning beyond or after because of the new engineered properties presented by these man-made materials. MMs are engineered structures designed to mimic the EM response that occurs naturally in many materials at shorter wavelengths and can be used to manipulate EM radiation [79]. MM arrays are composed of repetitive unit cells smaller than the wavelength of the spectral domain of interest [80]. These sub-wavelength element arrays determine their EM properties by the size, shape and structure of the unit cell layout rather than their material composition and can be used to image at the diffraction limit [81]-[82].

One important characteristic of MMs is their ability to absorb EM waves uniformly with absorption close to unity depending on the design [83]. They were originally created to absorb at microwave frequencies [76], but now the structures can be designed to absorb at any EM wave ranging from microwave to the optical spectrum, depending on the geometry.

Typical MM pixels have symmetric shapes in the form of electric ring resonators (ERRs) or magnetic split ring resonators (SRRs) shown in Figure 2.12a and b respectively [84]. The resonators are typically made of highly conductive metals such as copper, gold, or silver and can be paired with a metallic ground plane separated by an insulator as shown in Figure 2.12c. SRRs and ERRs when placed in parallel with a conducting ground plane offer a high impedance surface. When the MM structures are distributed in a periodic fashion on a flat surface they behave as a frequency-selective surface when an incident EM wave interacts with them. Furthermore, the advantage of pairing the resonators with ground planes is to exhibit independent control over effective permittivity $\varepsilon_{eff}$ and permeability $\mu_{eff}$. This allows for the electric response to be tuned independently by changing the shape/geometry of the resonators, and the magnetic response by changing the spacing between the resonator and the ground plane.
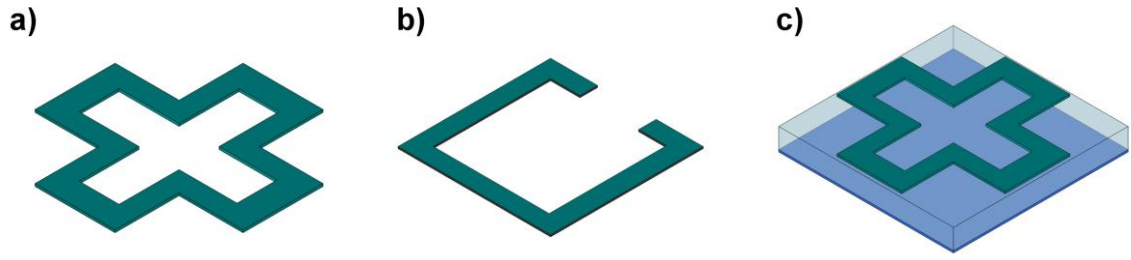
**Figure 2.12 - a) ERR, b) SRR c) ERR with ground plane separated with an insulator.**

One application of MMs is the creation of cloaking devices that allow the concealing of objects from external observers by deflecting certain parts of the EM spectrum [85]. Superlensing is another application, it allows a perfect lens to reconstruct an object in the image plane with unprecedented resolution [86]. This could be widely used for super-resolution in medical imaging and optical imaging, although more work has to be done to overcome the challenge of loss.

For this project we utilised the ability of MMs to absorb terahertz radiation where there is a lack of natural selective absorbing materials [83]. The use of MMs has made possible the design and implementation of strong terahertz absorbers that has resulted in the implementation of good terahertz detectors. Not only that, but their available integration in CMOS metallic/insulating layers has converted them in a strong candidate for compact, low cost terahertz imaging.

## 2.6.1 Single Band

Single band MM absorbers have two metallic layers separated by an insulating layer. The top metallic layer is either a SRR or an ERR and the bottom metallic layer is a continuous ground plane. This type of MM relies on the characteristics of the material shapes interacting with the incident radiation absorbing at one specific frequency [84]. Single band MMs are narrow band by nature; they absorb the incident light and consequently the bandwidth of this resonant absorption is narrow, typically their full width at half maximum (FWHM) is no more than 20% of the centre frequency. Figure 2.12c shows an example of a single band MM absorber.

## 2.6.2 Broadband

Broadband MMs are created by stacking metal-insulator layers with shapes of slightly different sizes that change the resonant peaks depending on the number of the layers. The individual resonant peaks from each structure merge into one broad absorption spectrum. Single layer structures are narrowband as mentioned before, but broadband structures can increase their FWHM by two and half times changing from 20% to 48%. An

example of a broadband MM structure is shown in Figure 2.13 a and b; it consists in alternating stacks of metal crosses and dielectric layers on top of a continuous ground plane or substrate.
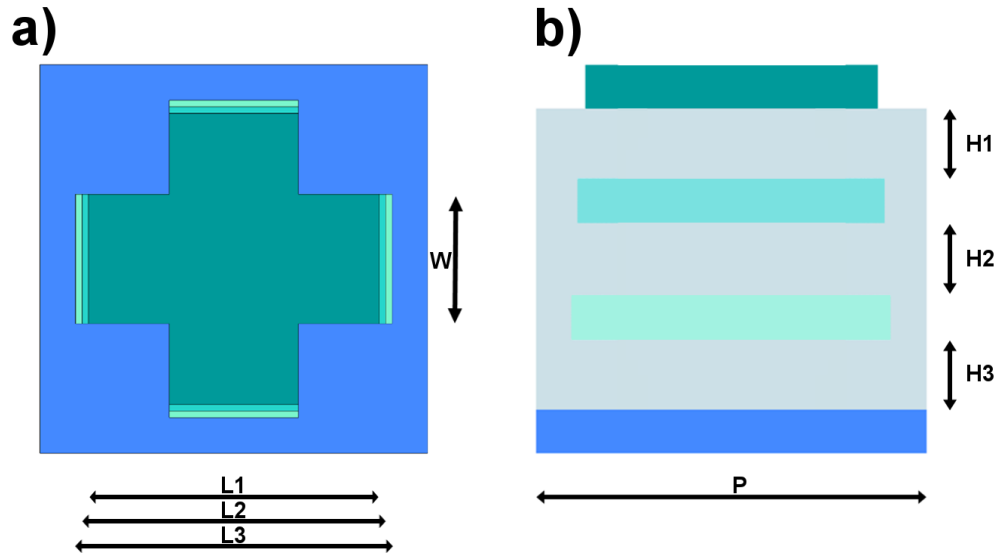


**Figure 2.13 - Broadband metamaterial a) top view and b) side view.**

## 2.7 Summary

The terahertz region of the EM spectrum has proven to be one of the most elusive. Being situated between IR light and microwave radiation, terahertz radiation is resistant to the techniques commonly employed in these well-established neighbouring bands. The interest of terahertz applications started with astronomers due to availability of passive terahertz radiation in space. Now, the potential use in medical and security applications, due to the transparency of common materials to terahertz waves, have led to increased activity in terahertz research to mature imaging technologies to the levels of the neighbouring spectrums. The past 20 years have seen an innovative creation of terahertz imaging systems although the need for expensive sources and detectors is still required for this technology. Terahertz research is now focusing on the development of uncooled, low-cost imaging systems based on technology ranging from SBDs, FETs and bolometers. The integration of uncooled sensors into a CMOS process is the main priority to create a low-cost technology. Furthermore, operation at frequencies above 1 THz is desirable as the shorter wavelength enables better spatial resolution. For this reason, MMs play an important role in the development of imaging technology due to their excellent terahertz absorption at any desired frequency as well as their ability to be monolithically integrated into small single pixels thus creating FPAs in the terahertz frequency range.

# Chapter 3 Detector Figures of Merit

The performance of thermal detectors, specifically microbolometers, is evaluated by the following figures of merit (FOM): $R_v$, NEP, TCR, and $\tau$ [87]-[88]. These FOM were originally used to characterise IR uncooled detectors but can be directly applied to characterise terahertz thermal detectors. The unique characteristics of MMs and their use as terahertz absorbers is investigated by proposing a design theory based on common inductor-capacitor (LC) circuits and the retrieval methods of EM parameters.

## 3.1  Responsivity

A detector's responsivity is defined as the ratio of the output signal voltage (or current) of a microbolometer per incident power on the area of one pixel detector; therefore, $R_v$ units are expressed in Volts per Watt or Amperes per Watt [88]. The units are defined according to the biasing and the readout technique employed. In this Thesis the responsivity will be measured in Volts per Watt. The responsivity is dependent on the ability of the microbolometer sensor to absorb incident terahertz radiation in the form of heat and change its resistance proportionally to the temperature change. Since the resistance of the microbolometer changes according to its TCR value, the change in the output voltage signal ($V_s$) is proportional to the incident power. In an array context, the pixels will be at different temperatures due to different incident power depending on the object being imaged. These settings will give a voltage map of the particular object based on the different voltages of every pixel.

Microbolometers are characterised by using a simple model of the heat flow equation where temperature change ($\Delta T$) is introduced by the modulation of the incoming terahertz radiation and is characterised by Equation 3.1 [89]. If the radiation is frequency modulated, the amplitude of the temperature signal varies as $1/\sqrt{1 + \omega^2 \tau^2}$ creating a pole with a 3 dB frequency ($f_{3dB}$) of $1/2\pi\tau$ [90]

$$\Delta T = \frac{\eta A_D P_0}{G_{th}\sqrt{1 + \omega^2 \tau^2}} \qquad \textbf{3.1}$$

where $\eta$ is the absorption magnitude, $A_D$ is the pixel area, $P_0$ is the incident power upon the pixel, $G_{th}$ is the thermal conductance, $\omega$ is the angular modulation frequency and $\tau$ is the thermal time constant. For simplicity in explaining the theory, it is assumed that there is no Joule heating caused by the bias current. Therefore, the output voltage signal, $V_s$, from the microbolometer biased with a constant current is expressed as Equation 3.2:

$$V_s = \alpha R I_B \Delta T \qquad \qquad \textbf{3.2}$$

where $\alpha$ is the TCR, $R$ is the resistance of the microbolometer, and $I_B$ is the bias current. Since $V_s$ is proportional to the material's TCR, it is ideal to use a sensor material with a very large temperature coefficient to measure a larger output voltage range. The sensor's TCR is defined by Equation 3.3 [91]:

$$\alpha = \frac{1}{R}\frac{dR}{dT} \qquad \qquad \textbf{3.3}$$

The resulting output voltage signal for a resistive microbolometer is expressed as Equation 3.4 by combining Equations 3.1 and 3.2:

$$V_s = \frac{\alpha R I_B \eta A_D P_0}{G_{th}\sqrt{1 + \omega^2 \tau^2}} \qquad \qquad \textbf{3.4}$$

For a diode sensor the output voltage signal is expressed as Equation 3.5:

$$V_{s\_diode} = \frac{TC_D \eta A_D P_0}{G_{th}\sqrt{1 + \omega^2 \tau^2}} \qquad \qquad \textbf{3.5}$$

where $TC_D$ is the temperature coefficient for the diode forward voltage, $\eta$ is the absorption magnitude, $A_D$ is the pixel area, $P_0$ is the incident power upon the pixel, $G_{th}$ is the thermal conductance, $\omega$ is the angular modulation frequency and $\tau$ is the thermal time constant.

Since $R_v$ is the ratio of the microbolometer's output voltage signal per incident power on the area of one pixel detector and is expressed in Volts per Watt, the resulting expression is obtained by dividing Equations 3.4 and 3.5 by $A_D P_0$. Therefore, $R_v$ for a resistive microbolometer can be expressed as Equation 3.6 [92] and the responsivity for a diode microbolometer, $R_{v\_diode}$, can be expressed as Equation 3.7 [93]:

$$R_V = \frac{\alpha \eta R I_B}{G_{th}\sqrt{1 + \omega^2 \tau^2}} \qquad \qquad \textbf{3.6}$$

$$R_{V\_diode} = \frac{TC_D \eta}{G_{th}\sqrt{1 + \omega^2 \tau^2}} \qquad \qquad \textbf{3.7}$$

The value of responsivity in both cases is directly proportional to the temperature coefficients of the sensor materials and inversely proportional to the thermal conductance where the principal heat loss mechanism originates from the supporting arm structure made to connect the electronic tracks and to support the pixel from array structure. Clearly a

large responsivity is desired for better detector's performance. The largest responsivity is obtained at a DC measurement ($f = 0$ Hz) and it will decrease as the modulation frequency increases, an example of this behaviour is shown in Figure 3.1. Thermal detectors can be designed to trade lower responsivity for a faster response.
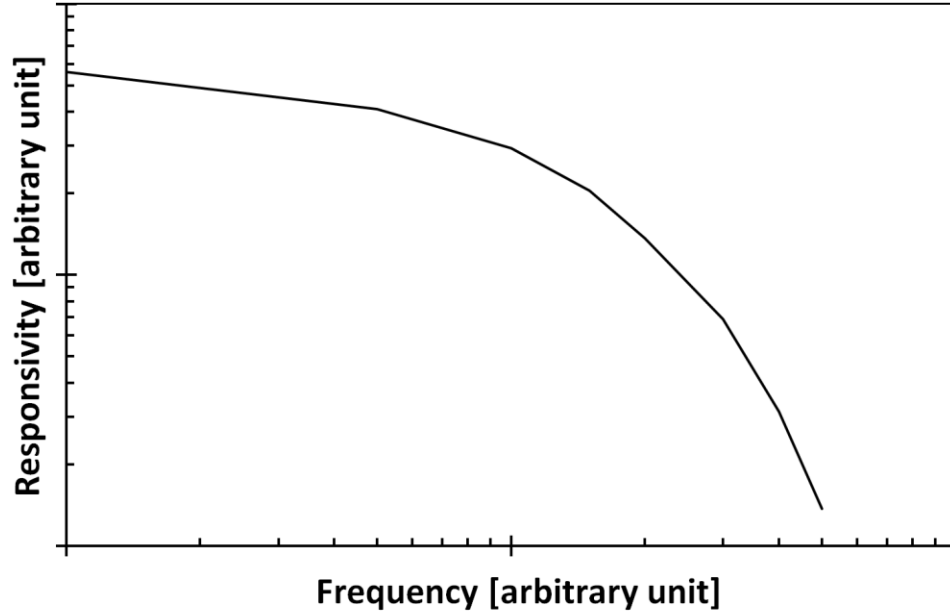


**Figure 3.1 – Responsivity, R$_v$, as a function of modulation frequency showing the largest R$_v$ occurring at DC ($f = 0$ Hz) and decreasing as the frequency increases.**

# 3.2 Thermal Time Constant

The pixel's temperature increases and decreases as the laser's input radiant power is modulated; therefore, a FOM to determine the time it takes the detector to respond to changes in temperature is needed. The detector's response time is characterised by the FOM known as thermal time constant, $\tau$, and is expressed by Equation 3.8 [94]. It is defined as the time it takes the output signal to reach 63% of its final value when the detector is exposed to a change in input power modulation.

$$\tau = \frac{C_{th}}{G_{th}} \qquad \textbf{3.8}$$

where $C_{th}$ is the heat capacity of a single detector and $G_{th}$ is the thermal conductance of the supporting arm structure. Figure 3.2 shows an example of a detector's response to an input power pulse indicating the $\tau$.
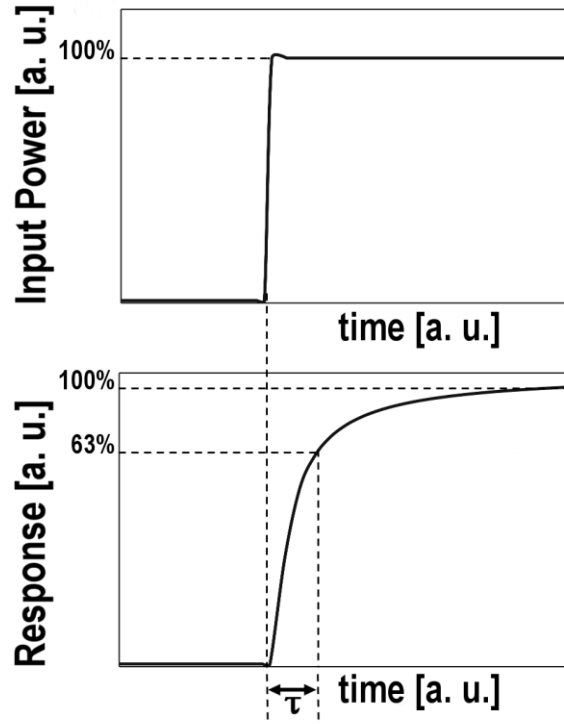
**Figure 3.2 – Example of the response of a detector to an input power pulse showing the respective thermal time constant, τ, measured from 0% to 63% of the final response signal.**

In a resistive and diode microbolometer, the heat capacity is determined by the volume of one pixel, therefore thinner pixel membranes are desired to minimise $\tau$ and achieve fast detection. Shorter response times will make the detector to follow rapid changes of the incoming terahertz radiation and could result in a detector with real-time operation characteristics. $C_{th}$ is calculated as [95]:

$$C_{th} = V\rho c \qquad \textbf{3.9}$$

where $V$ is the volume of the detector, $\rho$ is the density and $c$ is the mass specific heat of each of the microbolometer materials. The total thermal conductance, $G_{th}$, is estimated as the sum of the four heat paths between the microbolometer and its surroundings and is dominated by the heat loss through the supporting arms from the microbolometer to the substrate [67]:

$$G_{th} = G_{leg-conduction} + G_{radiation} + G_{gas-conduction} + G_{convection} \qquad \textbf{3.10}$$

where $G_{leg\text{-}conduction}$ is the thermal conductance through the legs supporting the membrane, $G_{radiation}$ is the thermal conduction between the microbolometer and the EM radiation, $G_{gas\text{-}conduction}$ is the thermal conduction between the bolometer and its surrounding gas and $G_{convection}$ is the thermal conduction between the microbolometer and its surroundings by gas convection.

According to Equation 3.8, $\tau$ is dependent of $1/G_{th}$, therefore in order to reduce it, $G_{th}$ would have to be large, but this would affect $R_v$ as they are inversely proportional. A

compromise between $G_{th}$ and $\tau$ has to be taken in consideration when designing the detector.

# 3.3 Noise

The detection capability of any imaging system is limited by fluctuations of a random nature, known as "noise". Noise is an important factor to consider when characterising a detector since it limits the precision of measured signals depending on the signal-to-noise (SNR) ratio. SNR measures the peak signal voltage divided by the root-mean-square (rms) noise voltage. The sensor's detection performance is limited by different noise sources such as noise from the sensor material, noise from the integrated readout electronics or external noise from biasing equipment. The three major sources of noise in microbolometers are the Johnson noise, phonon noise and the 1/f noise according to Nemarich [96]. These noise sources are expressed as *rms* noise voltages per the square root of Hertz and will be explained in this section.

## 3.3.1 Johnson Noise

Johnson noise is also known as Nyquist noise or thermal noise because it is generated by the thermal agitation of the charge carriers in conductive materials at equilibrium. This type of noise is intrinsic to semiconductors including resistors. It is present even without any type of biasing and it is also known as white noise because of the constant power distribution with frequency [97]. It was discovered by J. B. Johnson [98] and later explained theoretically by H. Nyquist in 1928 [99] where he showed that the thermal agitation of the charge carriers in any circuit causes a small fluctuating *rms* noise or current to flow through a resistor [100]. The *rms* value of the Johnson noise voltage ($V_J$) for a resistor is defined in Equation 3.11 and is usually represented by a Thevenin circuit model where the Johnson voltage source is in series with a noise-free resistance ($R_{ideal}$) (Figure 3.3a). If the terminals of the resistor are shorted, the equivalent circuit with a Johnson noise current ($I_J$) is represented by a Norton circuit model with an *rms* current source in parallel with $R_{ideal}$ as shown in Figure 3.3b and is defined by Equation 3.12:

$$V_J = \sqrt{4kTR} \qquad \textbf{3.11}$$

$$I_J = \sqrt{\frac{4kT}{R}} \qquad \textbf{3.12}$$

where $k$ is Boltzmann's constant (1.381 x $10^{-23}$ J/K), $T$ is the temperature in K, and $R$ is the electrical resistance of the material in $\Omega$. Johnson noise is a function of bandwidth but not

of frequency and it is dependent on the electrical resistance, $R$, therefore a lower value of $R$ is ideal to decrease the $V_J$ noise figure.
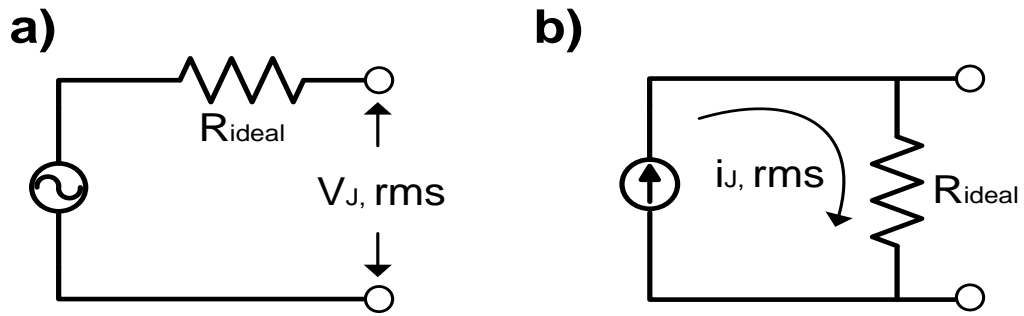


**Figure 3.3 – Equivalent circuit models for a) Johnson voltage source in series with an ideal resistor represented with a Thevenin circuit and b) Johnson current source in parallel with an ideal resistor represented with a Norton circuit.**

### 3.3.2  1/f Noise

The first spectral density measurement of 1/f noise was published by J.B. Johnson in 1925 where he showed that at lower frequencies the noise was larger than the expected Johnson noise and the spectral density behaviour was proportional to 1/f [101]. Although, the phenomenon was present in the experiments, the actual reason of the behaviour was not investigated. A few years later, it was proposed by Brillouin and Bernamont that the 1/f noise was inversely proportional to the total number of charge carriers in the sample. Around the same time, the excess noise was being studied at Bells Labs; Pearson showed that the noise was proportional to current squared and attributed it to resistance fluctuations at the contacts caused by mobility fluctuations of the carriers. He called this behaviour 'contact noise'. Another theory was established by Hooge where he said that only scattering of charge carriers by phonons contributed to the 1/f noise [102].

Two main theories of 1/f noise have been developed: carrier number fluctuation theory and the mobility fluctuation theory [103]. The 1/f noise may be due to the trapping of charge carriers at special energy levels occurring in atoms near the surface of the material [104]. This could be caused by traps due to crystal defects, such as dislocations, and contaminants in electronic devices. These traps randomly capture and release carriers causing carrier number fluctuation. As a result, it is associated with DC current flow in both resistive and depletion regions. The noise is present when a bias current flows through the resistive microbolometer. This current is caused by fluctuating mobility of minority carriers which disappear at the surface causing a current flow through the device [105].

The 1/f noise receives its name from the particular characteristics of the power spectrum which varies as the reciprocal of frequency thus having a 1/f-type roll-off. This noise source, also known as flicker noise, is dominant at low frequencies whereas the

Johnson noise is dominant at higher frequencies. The behaviour of the 1/f noise and Johnson noise as a function of frequency is shown in Figure 3.4.
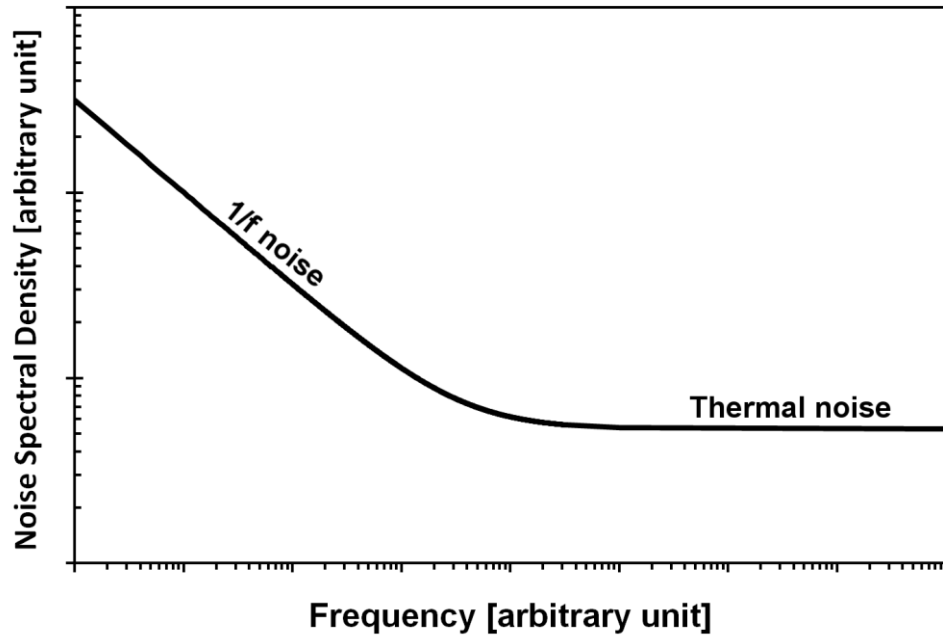


**Figure 3.4 - Representation of noise sources versus frequency where the 1/f noise is dominant at low frequencies and the constant thermal noise dominates at higher frequencies.**

The 1/f noise in a microbolometer is expressed as Equation 3.13 [106]:

$$V_{1/f} = I_B R\sqrt{n/f_m} \qquad\qquad \textbf{3.13}$$

where $I_B$ is the bias current in A, $n$ is an empirical *1/f* parameter and $f_m$ is the modulation frequency in Hz. The 1/f noise is the only noise that is dependent on the bias current, the higher the bias current, the higher the noise.

### 3.3.3 Phonon Noise

Phonon noise, also known as thermal fluctuation noise, is caused due to fluctuations in the rate at which heat is transferred from the sensor (thermal mass) to its surrounding environment. In the case of a microbolometer the thermal exchange is between the microbolometer and the heat sink, such as the substrate, with the respective conductance across the supporting legs. The thermodynamic fluctuations associated with thermal impedance are called phonon noise because the quantization of the heat flow is quantized in the form of phonons with energy of order $kT$ [107]-[108]. Phonon noise is expressed by Equation 3.14:

$$V_{ph} = R_v\sqrt{4kT^2 G_{th}} \qquad\qquad \textbf{3.14}$$

where $R_v$ is the responsivity in V/W, $k$ is the Boltzmann's constant (1.381 x 10$^{-23}$ J/K), $T$ is the temperature in K and $G_{th}$ is the thermal conductance in W/K. The difference between

35

Johnson noise and phonon noise is that one arises from the thermal motion of electrons whereas phonon noise arises from the exchange of phonons.

### 3.3.4  Shot Noise

The constant nature of DC current presents fluctuations in the arrival of the discrete electron flow which creates shot noise. Although these fluctuations are random in occurrence, its variability is minimal in comparison to the average value of a current flow [109]. When electrons "hop" over a region such as the barrier between a p-n junction in a diode, the observable variability increases thus increasing shot noise. Therefore, this uptick in shot noise is not present in resistors as there is no junction in the material. Shot noise, as with any statistical variation, is seen as random and wide ranging during short observation, becoming a small yet constant measurable variation over larger bandwidths. Shot noise is defined by Equation 3.15:

$$V_n = R\sqrt{2qI\Delta B} \qquad\qquad \textbf{3.15}$$

where $R$ is the resistance, $q$ is the electronic charge, $I$ is the DC bias current and $\Delta B$ is the bandwidth.

### 3.3.5  Noise Equivalent Power

Noise equivalent power (NEP) in a microbolometer pixel is defined as the incident power that generates an output signal that is equal to the *rms* noise output which results in a signal to noise ratio of unity. The NEP indicates how sensitive the detector is, if the microbolometer is biased with a constant current source, the NEP is expressed in W/√Hz and is defined as [110]:

$$NEP = \frac{V_{rms}}{R_v} \qquad\qquad \textbf{3.16}$$

where $R_v$ is the responsivity of the detector and $V_{rms}$ is the square root of the quadratic sum of uncorrelated noise sources also known as noise spectral density (NSD). $V_{rms}$ is expressed in V/√Hz and is defined as:

$$V_{rms} = \sqrt{\left[V_{1/f}^2 + V_J^2 + V_{ph}^2 + V_n\right]} \qquad\qquad \textbf{3.17}$$

where $V_{1/f}$ is the 1/f noise voltage, $V_J$ is the Johnson noise voltage, $V_{ph}$ is the phonon noise voltage and $V_n$ is the shot noise (only related to diodes). A detector that has a greater detecting ability has a smaller NEP and a detector that produces a greater output voltage (from a given radiation signal) has a greater responsivity.

# 3.4 Atmospheric Absorption of Terahertz

Detectors are designed to absorb or resonate at a specific frequency depending on the application. An absorption spectrum displays the intensity at which the detector absorbs the incident radiation over a range of frequencies or wavelengths. The absorption spectra is typically characterised by radiating the sample and measuring either the transmitted energy or reflected energy over the terahertz spectrum. The frequency dependent absorption, $A$, is defined as 3.18:

$$A(\omega) = 1 - R(\omega) - T(\omega) \qquad \textbf{3.18}$$

where $R$ is the reflection and $T$ is the transmission. The wavelength is calculated using Equation 3.19:

$$\lambda = cT = \frac{c}{v} \qquad \textbf{3.19}$$

where $c$ is the speed of light (299,792,458 m/s $\approx$ 3x10$^8$ m/s), $T$ is the period, and $v$ is the frequency.

As previously mentioned, the terahertz spectrum is considered to be the wavelength region between 30 μm and 3 mm, but not all wavelengths are ideal for imaging purposes due to attenuation in atmosphere. Atmospheric attenuation and scattering in varying conditions, such as fog and humidity, are two major concerns in the development of focal plane array imagers for the terahertz spectral region. As the frequency increases there is more diffuse scattering and higher attenuation of the signal that limits the range of detection [8]. The attenuation is also dependent on height but above 16 km the effect of moisture is negligible, therefore the attenuation is insignificant which has enabled the development of inter-satellite communication [111].

This aspect is particularly important for stand-off imaging as it will limit the target distances and imaging performance of the imaging system. Fortunately, there are certain low atmospheric attenuation windows in the terahertz region investigated by the Submillimeter Wave Technology Laboratory in the University of Massachusetts [112]. Figure 3.5 shows the variation of atmospheric attenuation as a function of frequency and relative humidity (RH). It indicates the existence of five distinct terahertz window regions between 0.3 and 4 THz. The atmospheric terahertz spectral transmission is normalized to 1 (100% attenuation) at 0.3 THz and the RH ranges from 5% (top red line) to 58% (bottom orange line). The five window regions are centred around 1.488 THz, 1.979 THz, 2.11 THz, 2.52 THz, and 3.42 THz [112]. The attenuation was calculated over a distance of 50 m. The window with the lowest attenuation is 1.488 THz over all humidity. In this

Thesis the terahertz window used is 2.52 THz which has an attenuation of -13.5 dB at 6.4% RH and -78 dB at 58 % RH.
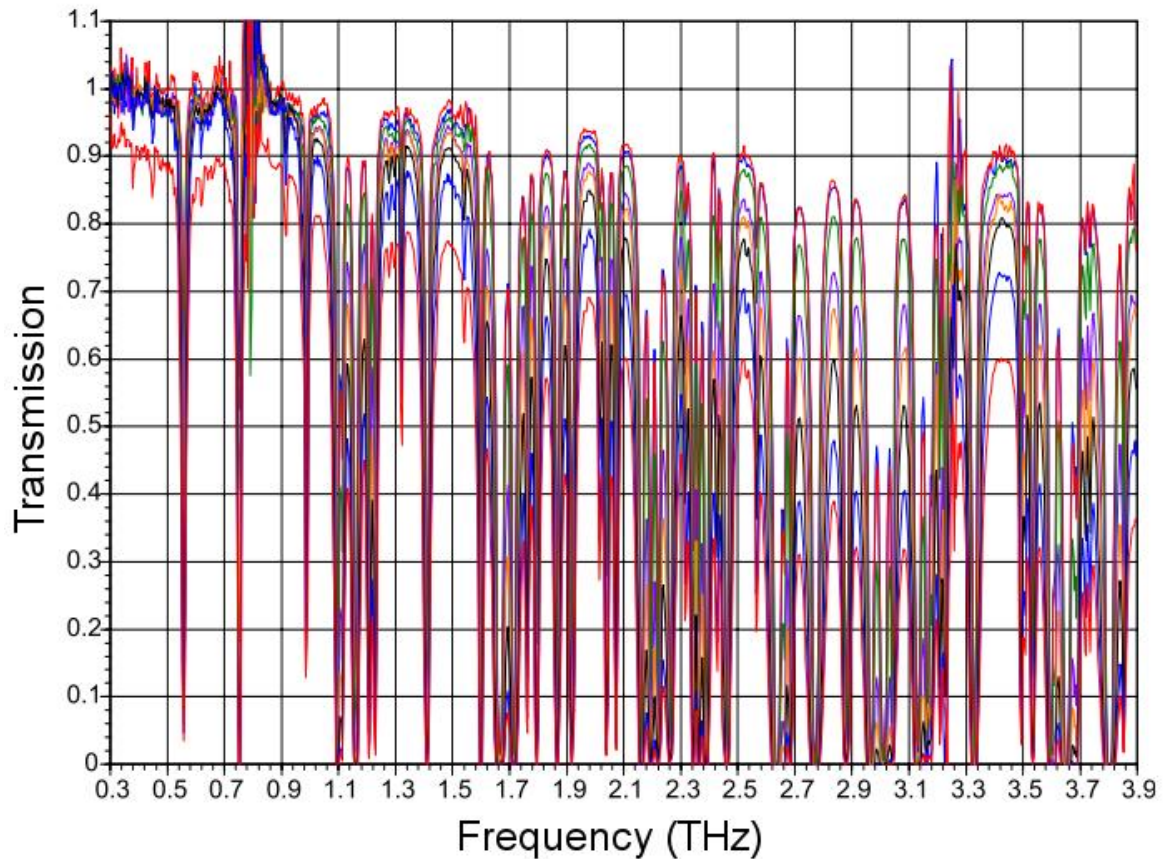


**Figure 3.5 - Terahertz atmospheric windows from 0.3 to 4 THz varying the relative humidity from 5% (top red line), 6.4% (blue line),11.8% (green line), 25.9% (purple plot), 39.4% (black line), 52% (bottom blue line), and 58% (bottom orange plot). The atmospheric window of interest is 2.51 to 2.55 THz. Reproduced with permission: [Linden, K.J.; Neal, W.R.; Waldman, Jerry; Gatesman, A.J.; Danylov, A., "Terahertz laser based standoff imaging system," in 34th Proceedings of Applied Imagery and Pattern Recognition Workshop, pp.-14 © 2005 IEEE [112]]**

# 3.5 Metamaterial Absorbers

The application of MM absorbers is very important in the terahertz spectrum due to the difficulty to find strong frequency selective terahertz absorbers. Such MM absorbers naturally lend themselves to terahertz detection applications such as thermal sensors with the integration of microbolometers creating complete terahertz detectors. The advantage of the MM structure arrays is their ability to absorb wavelengths larger than the actual size of a single MM cell. MMs can also be used to create resonant absorber structures where the radiation is absorbed in a device thickness significantly smaller than the wavelength of radiation, overcoming the thickness limitation of common quarter wavelength antenna structures [113]. MM absorbers have previously been fabricated in research facilities at the

University of Glasgow (James Watt Nanofabrication Centre) exploring the use of different materials, geometric shapes and layer thicknesses [114]–[116]. These previous studies have effectively shown that by manipulating the inter-metal dielectric layer thickness, refractive index, and MM geometric shape the terahertz narrowband absorption magnitude and resonance frequency can be customised [115].

The geometry investigated for this Thesis is a cross-shaped MM absorber shown in Figure 3.6 where (a) shows the pixel's top view and (b) shows the pixel's cross-section dimensions. The MM absorber consists in an electric ring resonator (ERR) built in a metallic layer, paired with a metallic ground plane and separated by an insulating layer. The ERR structure couples strongly to uniform electric fields but negligibly to magnetic fields. By pairing the ERR with a ground plane, the magnetic component of the incident terahertz wave induces a current parallel to the direction of the E-field [114]. The result is that at the resonant frequency the electric and magnetic component of the incident terahertz wave is absorbed by the MM structure giving rise to local heating creating a narrowband resonant response in a MM thickness of approximately λ/50. The electric response can be tuned by altering the geometry of the ERR, and the magnetic response is tuned by changing the spacing between the ERR and the ground plane.
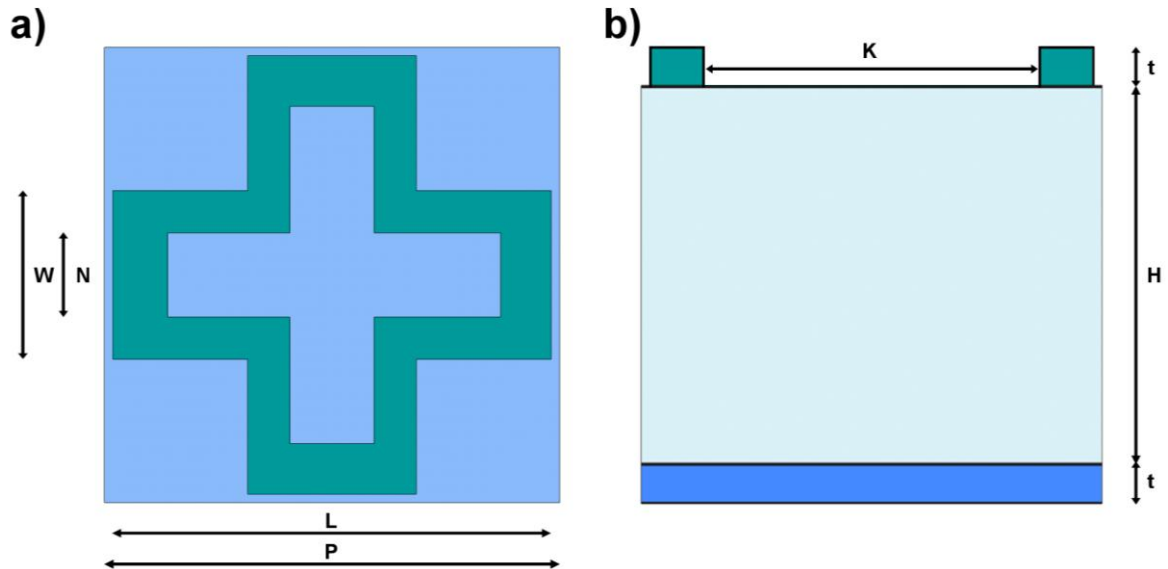


**Figure 3.6 – Metamaterial absorber showing the a) top view with the cross-shaped electric ring resonator (ERR) and b) cross-section showing the metal and insulating layers.**

Terahertz MM absorbers have a narrow absorption bandwidth that is typically 20% of the centre frequency. To calculate the theoretical MM resonance frequency the single pixel structure is evaluated using the effective inductance (*L*) and capacitance (*C*) in an equivalent *LC* circuit, shown in Figure 3.7, exhibiting a magnetic resonance response of the form $\omega = 1/\sqrt{LC/2}$ according to Ye *et. al.* where they use a similar cross-shaped structure [117]. When pairing a metallic ERR with a metallic ground plane, the capacitance

can be calculated as a two plate capacitor if the source is incident to the $z$ direction. The effective capacitance is calculated using Equation 3.20:

$$C = \frac{\varepsilon_r \varepsilon_0 A}{H}$$
<div align="right">**3.20**</div>

where $\varepsilon_r$ is the dielectric relative material permittivity, $\varepsilon_0$ is the vacuum permittivity constant, $A$ is the metallic plate area and $H$ is the thickness of the dielectric in between the metallic plates. Additional capacitance, not taking into consideration here, is added from the side walls to the neighbouring structures in an array setting. The effective inductance ($L$) is calculated by adding the total inductance introduced by the width of the cross ($L_W$) and the length ($L_L$) according to Ding *et. al.* (Equation 3.23) [118]. The inductance expressions are shown in Equations 3.21 and 3.22. These expressions used to calculate the inductances were derived from the *LC* equivalent circuit and the proposed cross-shaped stacked structure for a single MM cell shown in Figure 3.6.

$$L_W = \frac{\mu_0 W_1 H}{W_2}$$
<div align="right">**3.21**</div>

$$L_L = \frac{\mu_0 W_1 H}{L_1}$$
<div align="right">**3.22**</div>

$$L = L_W + L_L$$
<div align="right">**3.23**</div>

where $\mu_0$ is the permeability of free space constant, $L_1$ is the length of the cross and $W_1$ is the arm width, and $H$ is the thickness of the dielectric in between the metallic plates. Due to the symmetry of the single cell $W_1 = W_2$ and $L_1 = L_2$.
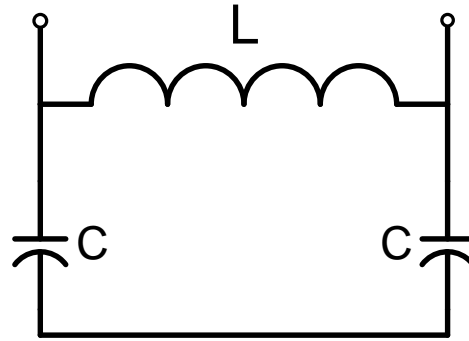


**Figure 3.7 – Effective inductance (L) and capacitance (C) in an equivalent LC circuit for a cross-shaped MM absorber with an insulating layer separating two metallic layers.**

The characterisation of MMs is done through retrieval techniques of the effective material parameters which consists in simulating the scattered waves such as the complex transmission and reflection coefficients better known as scattering (S) parameters [119]. According to Smith *et. al.* the MM effective parameters, electric permittivity $\varepsilon$ and the magnetic permeability $\mu$, can be found by simulating the inversion of the *S* parameters obtained from the transmission and reflection propagating waves on the MM structure

[120]. The EM properties of materials can be determined by using Maxwell's equations where uniform and single frequency plane waves propagating in a medium, $\eta$, along the $z$ direction and normal to the material slab interfaces are related to the transmission and reflection spectra.

Figure 3.8 shows a homogeneous one dimension slab with thickness $d = z_2 - z_1$, with fields propagating between two positions in space. The transmitted wave is S$_{21}$ and the reflected wave is S$_{11}$. This structure is used for simplicity in explaining the EM parameter retrieval technique for MMs.
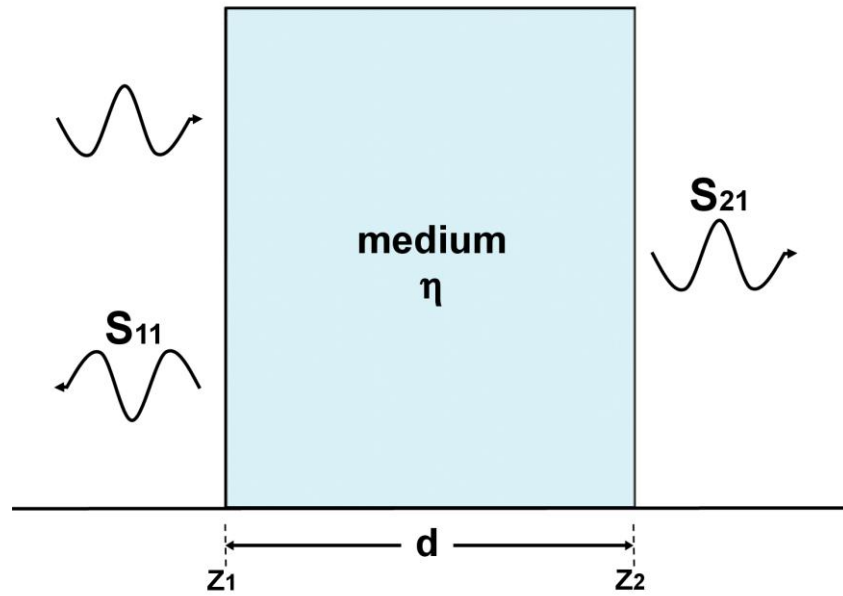


**Figure 3.8 – Scattering parameters on a homogeneous one dimensional slab with fields propagating between two positions in space.**

The *S* parameters relate the transmission waves to the reflection waves on the MM structure using Equations 3.24 and 3.25 respectively [120]:

$$S_{21} = \frac{1}{\cos(nkd) - \frac{i}{2}\left(z + \frac{1}{z}\right)\sin(nkd)} \qquad \textbf{3.24}$$

$$S_{11} = \frac{i}{2}\left(\frac{1}{z} - z\right)\sin(nkd) \qquad \textbf{3.25}$$

where *n* is the refractive index and *z* is the wave impedance of the MM, they are related to $\varepsilon$ and $\mu$ by these relations: $\varepsilon = n/z$ and $\mu = nz$. The inversion of the S parameters provides the refractive index and the wave impedance for a homogeneous material expressed in Equations 3.26 and 3.27 respectively:

$$n = \frac{1}{kd}cos^{-1}\left[\frac{1}{2S_{21}}(1 - S_{11}^2 + S_{21}^2)\right] \qquad \textbf{3.26}$$

$$z = \sqrt{\frac{(1 + S_{11})^2 - S_{21}^2}{(1 - S_{11})^2 - S_{21}^2}}$$ **3.27**

The retrieved parameters for a MM absorber are displayed in Figure 3.9 as an example. The real parts of the optical constants cross close to zero, a condition required for zero reflection, while, whenever the real part of the permittivity is positive, the real part of the permeability is negative and vice versa (a condition required for zero transmission). For a heterogeneous structure with a continuous metallic ground plane, the transmission will be nearly zero across the entire frequency range [121]. At the frequency of maximum absorption, $\omega_0$, there is a peak of the imaginary component of the permeability, implying high absorption [114].
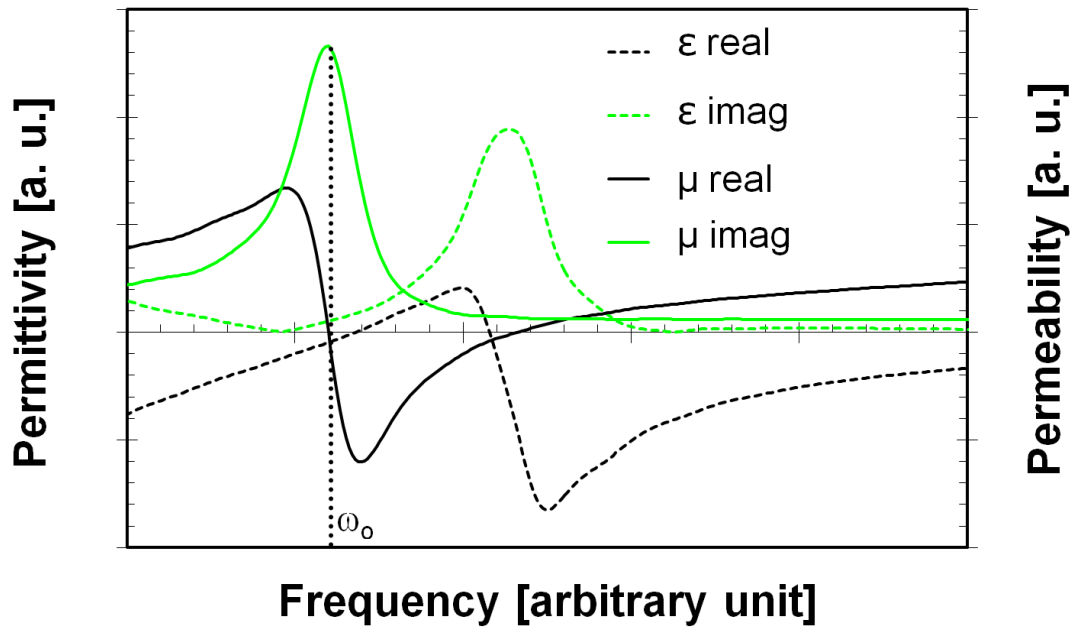


**Figure 3.9 – Example of effective permittivity and permeability parameters.**

## 3.6 Summary

The relevant figures of merit for the characterisation of terahertz detectors were discussed in this chapter. Detector performance is evaluated in terms of the responsivity, NEP, TCR for resistive detectors or TCV for diodes detectors, and $\tau$. An ideal detector has a high responsivity, high TCR/TCV, low NEP and short $\tau$. The figures of merit depend on the physical characteristics of the detectors such as the physical layout and material composition. High responsivity can be achieved by choosing a material with a high temperature coefficient, small thermal conductance from the supporting arm structure, and larger bias current. However a larger bias current means that the 1/f noise will increase, therefore responsivity and noise are a trade-off in the design of detectors. A short $\tau$ is also

desired, this can be achieved by reducing the membrane thickness (volume of the pixel) to reduce $C_{th}$.

Due to the lack of natural materials that selectively absorb terahertz radiation, MMs were introduced in the interest of their relevant function as terahertz absorbers. The characterisation techniques were explained using the retrieval methods by $S$ parameter inversion. For simplicity it was assumed that the MM structure was a homogeneous, one dimensional structure. It was concluded that the parameter extraction and effective inductance and capacitance is just an approximation to understand the working mechanism of terahertz MM absorbers.

# Chapter 4 Design of a Single Pixel Terahertz Detector and Metamaterial based Focal Plane Array

The design of a MM absorber and readout electronics for a terahertz FPA is thoroughly described in this chapter. The MM absorber previously fabricated at the University of Glasgow is explained for a better understanding of the background and original idea that led to the monolithic integration of the terahertz absorber into a CMOS process. The integrated readout electronics with VOx microbolometer pixel arrays had 4 main prototypes: a 5 x 5 array, an 8 x 8 array, a 64 x 64 array-serial readout and a 64 x 64 array-parallel readout. This chapter will focus on the design and simulation of a single pixel, 5 x 5 array with serial readout and 64 x 64 array with parallel readout integrated with VOx microbolometer pixels. Additionally, the idea to implement a p-n diode microbolometer was investigated by designing single diode pixels and a 64 x 64 array with parallel output readout electronics. The concept of integrating a MM absorber, microbolometer sensor and readout electronics presents a significant progression towards the creation of a camera for terahertz applications.

## 4.1 Pixel Design

The ability of MMs to function as terahertz absorbers was investigated at the University of Glasgow where single and broadband absorbers were created and characterised by Dr. James Grant from the Microsystems Technology Group (MST) [113]–[116]. This concept was investigated due to the difficulty of finding strong frequency selective terahertz absorbers for integration with terahertz detectors for imaging applications.

The single band MM absorber design consisted of an array of sub-wavelength elements integrated into two metallic layers separated by a dielectric. The top metallic layer consisted of a symmetric cross-shaped ERR and the bottom metallic layer was a continuous ground plane. Due to the unique EM properties of MMs, the absorption

frequency and amplitude can be customised independently. The tuning of the electric and magnetic responses can be determined by the size, shape, and thickness of the terahertz MM absorber.

The first fabricated prototype consisted of a single band absorber containing one continuous metal layer acting as a ground plane separated from a metallic cross-shaped resonator by an insulating material [114]. Figure 4.1a-b shows top and cross-sectional views of the MM absorber fabricated on site in the James Watt Nanofabrication Centre (JWNC). This design was used to characterise the absorption frequency and amplitude of the MM by modifying design variables such as the use of different insulating materials, thicknesses and cross-shape dimensions. For this particular example the materials of the absorber's metallic sections were Titanium/Gold (Ti/Au) and the insulating layer was polyimide dielectric.
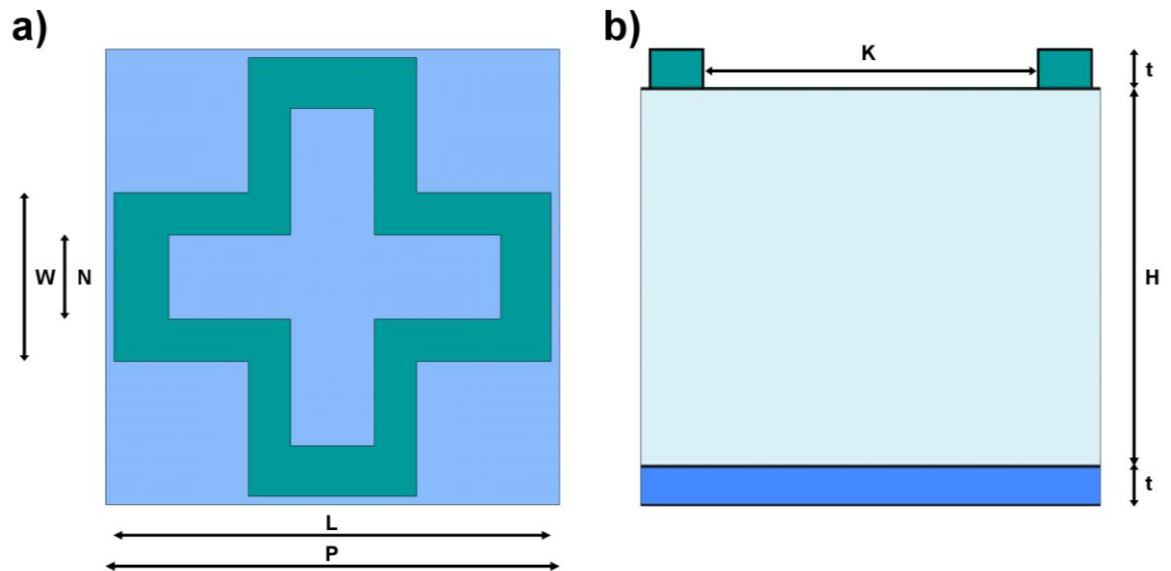


**Figure 4.1 – Cross-shaped MM absorber a) top view and b) middle cross-section. The MM structure had a calculated absorption frequency of approximately 1.99 THz based on Equations 3.20 and 3.23.**

| Parameter | Value |
|-----------|-------|
| $\varepsilon_r$ | 3.4 |
| H | 3.1 μm |
| t | 230 nm |
| K | 10.0 μm |
| L | 26.0 μm |
| W | 10.0 μm |
| N | 5.0 μm |
| P | 27 μm |

**Table 4.1 – MM absorber simulation parameters**

The absorption frequency for this design was analytically estimated using Equations 3.20 and 3.23 based on the cross-shaped ERR dimensions listed in Table 4.1. The calculations resulted in an absorption frequency of 1.99 THz. Then, the MM structure was numerically simulated using finite-difference time-domain (FDTD) with Lumerical Inc. software. The three dimensional simulations were performed with a plane wave source incident in the $z$ direction on the metal/dielectric/metal substrate unit cell. Periodic boundary conditions were used for the x-y plane, along with a mesh step size of $\Delta x = \Delta y = 0.2$ µm and $\Delta z = 0.05$ µm. The metallic sections of the absorber were modelled as Au with a frequency independent conductivity of $4 \times 10^7$ Sm$^{-1}$. Reflection and transmission spectra were recorded at planes 100 µm above and 100 µm below the ERR. Figure 4.2 shows the transmission, absorption and reflection simulated spectra based on the frequency dependant absorption expression, shown in Equation 3.18, indicating absorption of around 80% at 2.12 THz. This result compares well with the analytical calculations where an absorption of approximately 2.0 THz was calculated. The transmission is very close to zero due to the continuous metallic ground plane in the MM absorber.
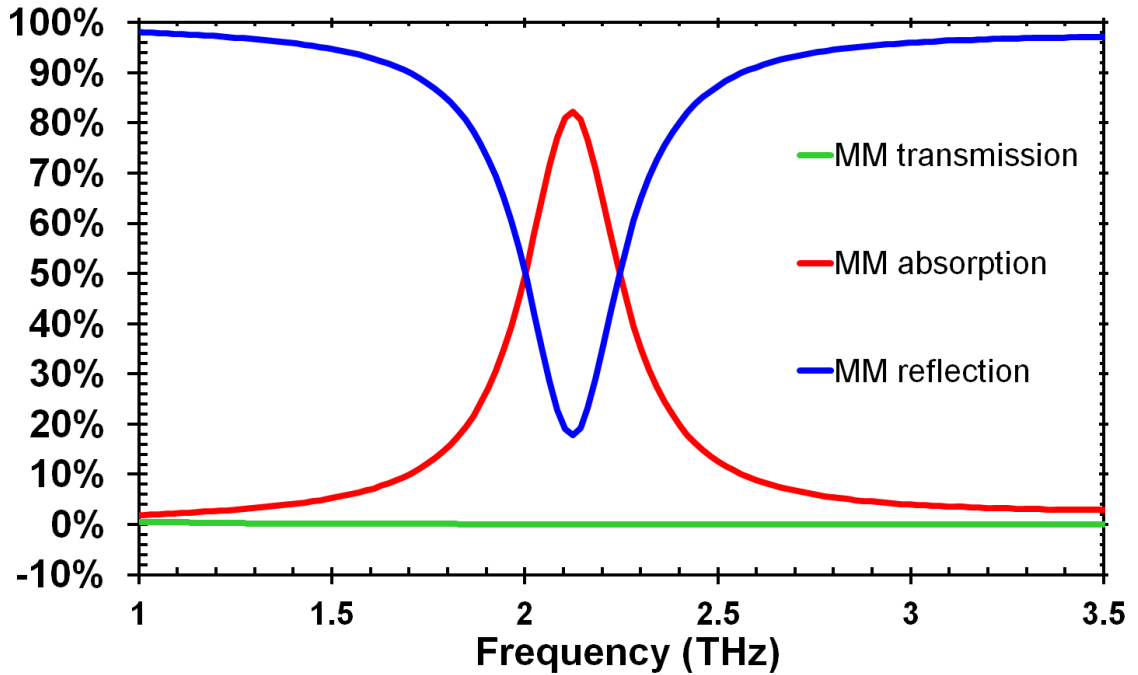


**Figure 4.2 - Simulation data of the MM absorber with a polyimide thickness of 3.1 µm showing a frequency dependant absorption and reflection of 2.12 THz. The transmission is close to zero due to the metallic ground plane. [Simulations done by Dr. James Grant].**

The simulated power absorption distributions for the ERR, dielectric spacer, and the ground plane layers are shown in Figure 4.3a-c while a cross-section of the power distribution in the x-z plane at $y = 3$ µm is shown in Figure 4.3d. The power distribution graphs shows that the majority of the energy is dissipated as ohmic loss in the ERR layer and as dielectric loss in the first 500 nm of polyimide below this layer.
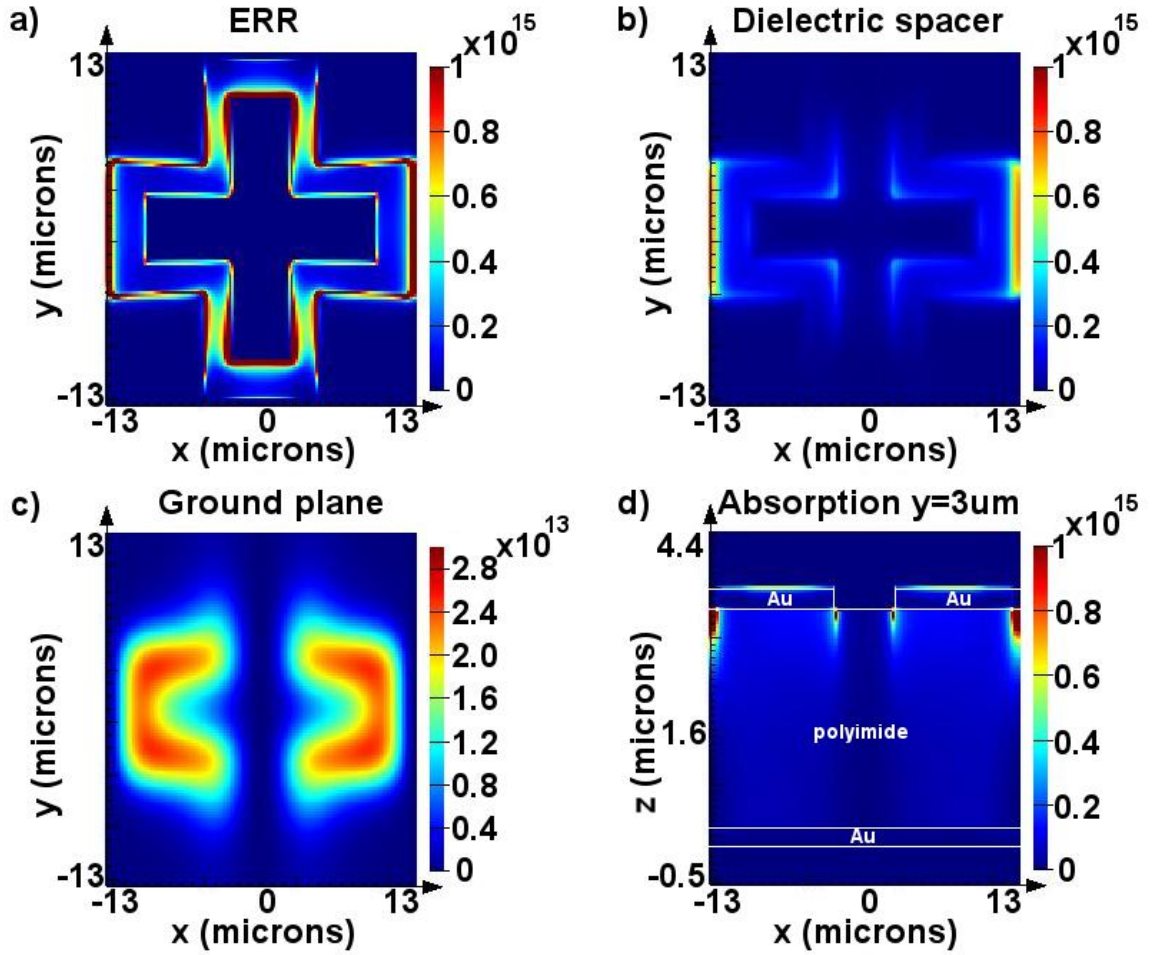
**Figure 4.3 - Power distribution in a single MM absorber structure with a 3.1 μm thick polyimide spacer at a frequency of 2.12 THz. Energy dissipation in a) the ERR layer, b) the dielectric spacer, c) the ground plane, and d) *x-z* plane at *y* = 3 μm. [Simulations done by Dr. James Grant].**

The effective permittivity and permeability were extracted via inversion of the simulated *S* parameters as explained in Section 3.5. The retrieved parameters for the MM absorber, including real and imaginary $\varepsilon$ and $\mu$, are shown in Figure 4.4. This figure shows the real parts of the optical constants crossing close to zero which is a condition for zero reflection. To fulfil the condition of zero transmission, the real part of the permittivity has to be positive and the real part of the permeability has to be negative or vice versa. The high absorption is illustrated by the peak of the maximum absorption frequency, $\omega_0$, at the imaginary component of the permeability. For this particular example the absorption frequency is 2.12 THz.
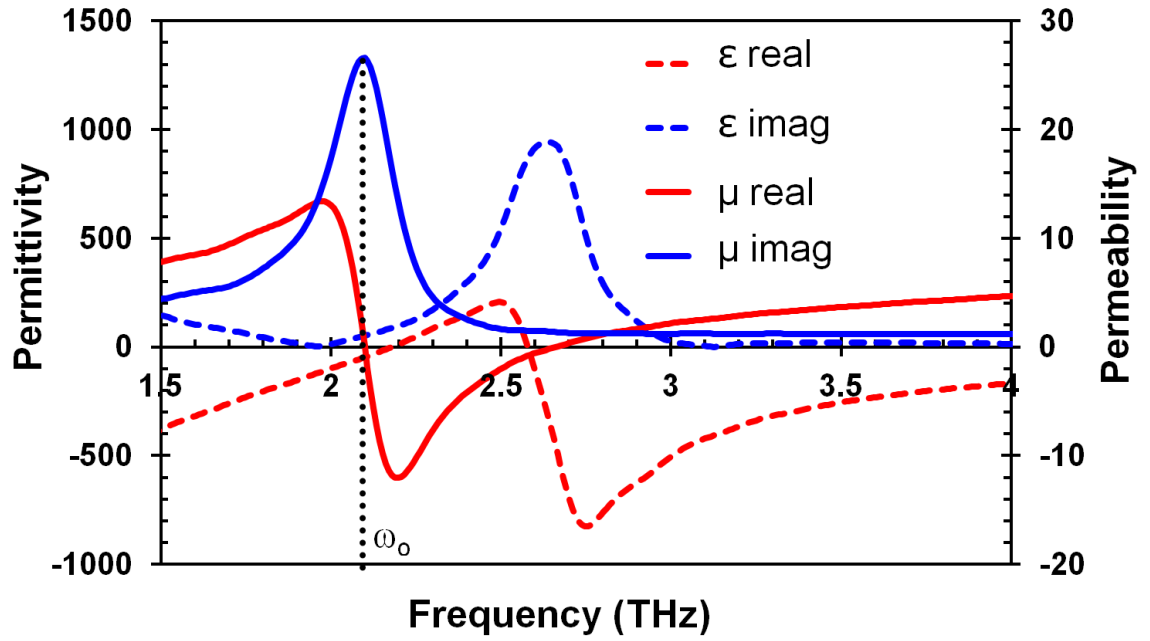
**Figure 4.4 - Simulation of the effective permittivity and permeability parameters via the inversion of the S parameters. [Simulations done by Dr. James Grant].**

According to Equations 3.20 and 3.23 the absorption characteristics of a MM absorber are dependent on the geometric shape of the ERR and the distance between the two metallic layers. Additionally, the frequency absorption peak shifts depending on the width and length of the ERR. Several cross-shaped MM absorbers with different parameters were simulated for comparison of the shift in frequency absorption peak. Figure 4.5 shows the simulation results for a MM absorber with a closed cross-shape with a 3.1 μm thick polyimide dielectric where both variables, *W* and *L*, were swept from 5 to 20 μm. The original absorption spectra (blue line) from the first MM absorber with an open cross-shape is shown as a reference for comparison to the other absorption peaks. The original dimensions of the open cross-shaped MM absorber are listed in Table 4.1. The open symbols represent the change in frequency absorption peak when the length is changed and the width is fixed at 5 μm. The lines represent the change in frequency absorption peak when the width is changed and the length is fixed at 26 μm. There is a marked blue shift in the absorption peak position from 2.12 THz to 8.1 THz as the cross arm length is varied from 26 μm to 5 μm. Furthermore, there is 1 THz redshift in the absorption peak position when the cross arm width is 26 μm compared to 5 μm. Figure 4.6 shows the original MM with a polyimide dielectric thickness ranging from 1 to 7.5 μm thicknesses compared with a 3 μm thick $SiO_2$ dielectric. The graph illustrates the increasing peak absorption in relation to thickness between 1 and 3.1 μm, and the slight peak absorption value reduction at greater thicknesses. There is also a distinct redshift of

0.25 THz throughout the increasing polyimide thickness. From this, an optimal polyimide thickness where maximum absorption is obtained can be seen. Also studied were absorbers with $SiO_2$ dielectrics. For these, a maximum absorption of 65% at 1.90 THz was measured with 3 μm thickness.
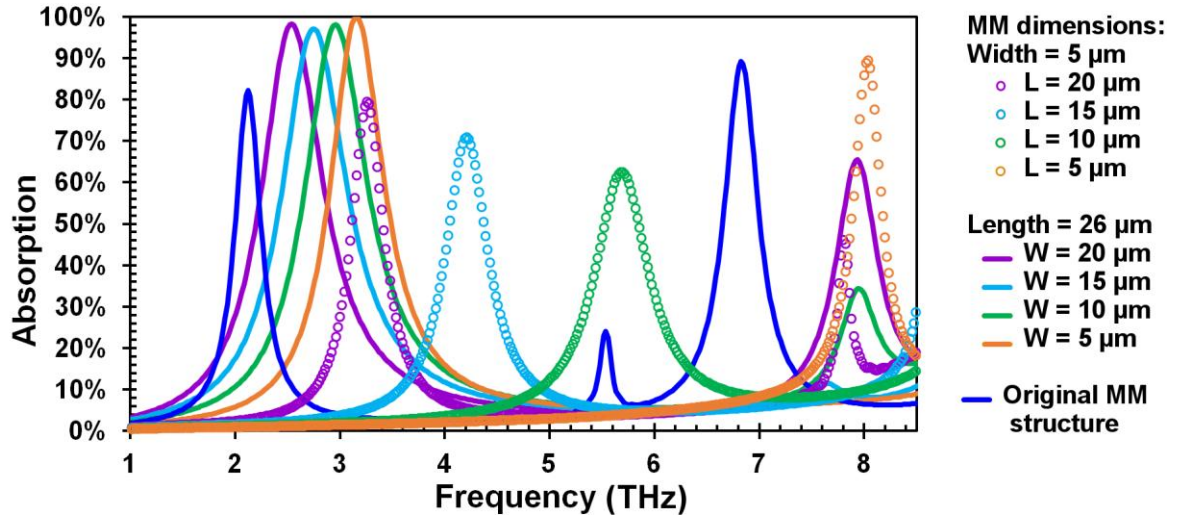


**Figure 4.5 - Simulation results displaying the effect in the absorption characteristics when modifying the width and length of the cross shaped ERR. The open symbols represent the change in frequency absorption peak when the length is changed and the width is fixed to 5 μm. The lines represent the change in frequency absorption peak when the width is changed and the length is fixed to 26 μm. [Simulations done by Dr. James Grant].**
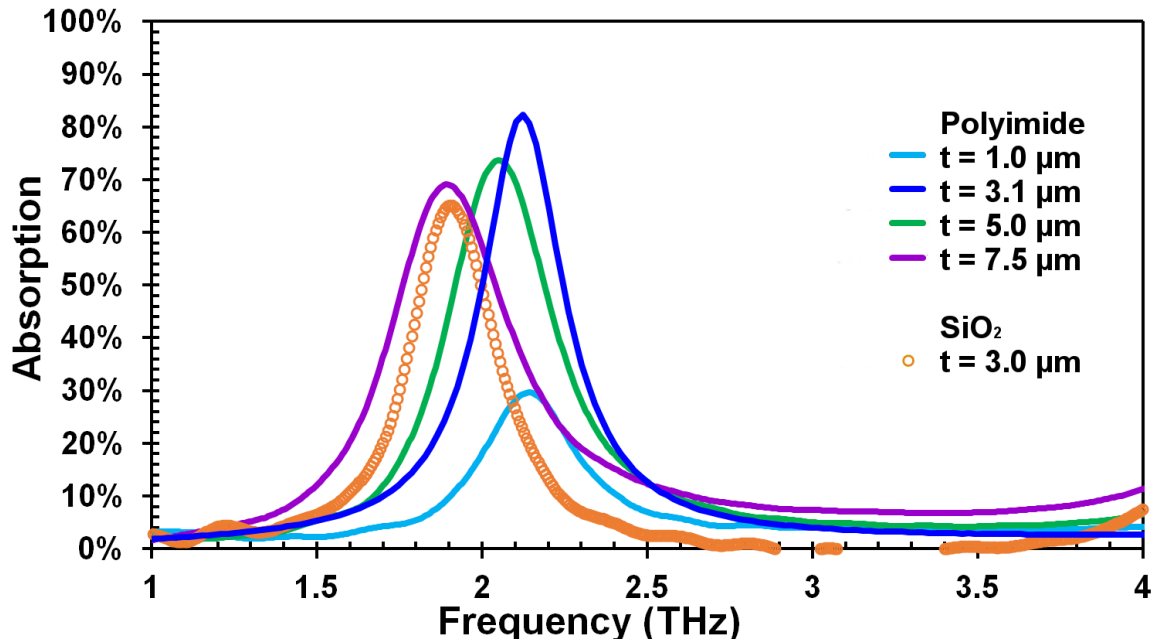


**Figure 4.6 – Effect of modifying the dielectric thickness and material of the MM absorber. [Simulations done by Dr. James Grant].**

A broadband MM absorber was previously investigated by the MST group to create wideband absorbers using multiple stacked cross-shaped ERRs [116]. The device consisted of alternating stacks of metallic ERRs and dielectric layers on top of a metallic ground

49

plane. The design of the crosses was based on the results from the single band absorber where it was concluded that the resonant frequency of the absorption peak was mainly determined by the arm length of the cross that is parallel to the electric field. Therefore, each layer was designed to have crosses of differing lengths ($L_1$-$L_3$) in order to support several resonant modes closely positioned together in the absorption spectrum. Additionally, by tuning the dielectric thickness ($H_1$-$H_3$), the multilayer structure can be impedance-matched to free space at each resonant frequency and broadband absorption thus obtained. The width of each cross arm was 6 μm and the thickness of each metallic layer was 200 nm. A top view and middle cross-section of the broadband absorber is shown in Figure 4.7 with the respective parameter values listed in Table 4.2.
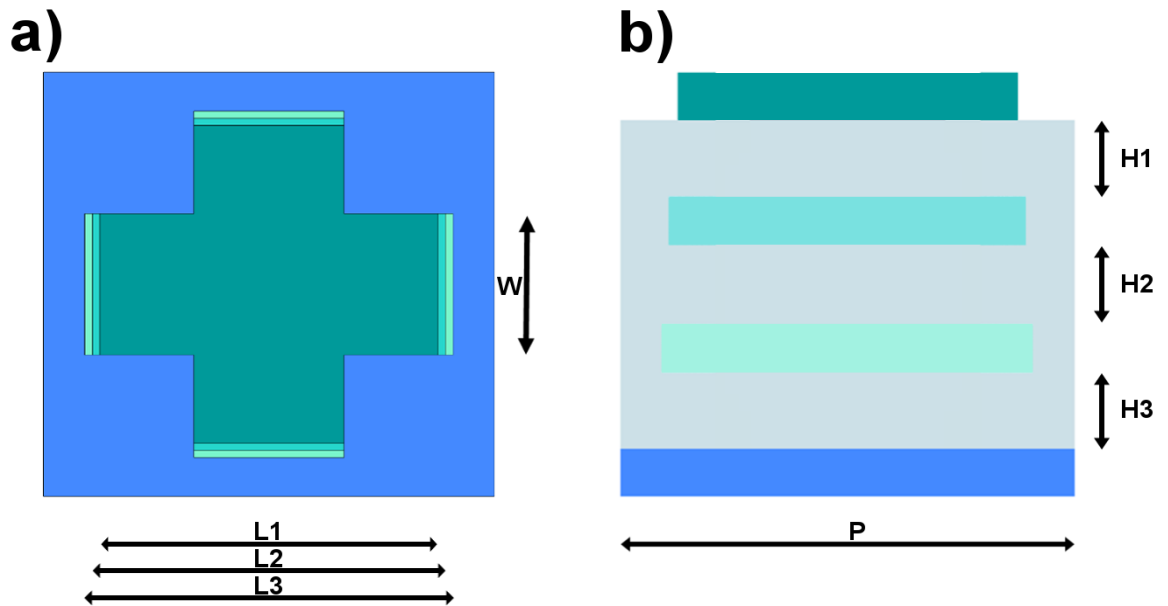


**Figure 4.7 – Broadband MM absorber with 3 stacked cross-shaped ERRs separated by dielectric layers a) top view and b) middle cross-section.**

| Parameter | Value |
|-----------|-------|
| $\varepsilon_r$ | 3.4 |
| $H_1$ | 0.7 μm |
| $H_2$ | 1.2 μm |
| $H_3$ | 2.0 μm |
| $L_1$ | 17 μm |
| $L_2$ | 15.4 μm |
| $L_3$ | 15 μm |
| P | 22 μm |

**Table 4.2 – MM absorber simulation parameters**

The simulation parameters were repeated from the single band absorber method using FDTD simulations. The simulated data for the multilayer MM absorber is shown in Figure 4.8. The broadband absorber was compared to a single band absorber and a 5 μm thick polyimide sample with no ERR structure. The sample without an ERR structure had

minimal absorption from the polyimide layer validating that the high absorption in the other samples is a consequence of the MM structure and not of the absorption of the dielectric. The single band absorber had a single frequency absorption peak at 5.42 THz with 78 % absorption. This absorber had an arm length of 17 µm and dielectric thickness of 2 µm. Finally, the broadband absorber had three resonances at 4.32 THz, 5.31 THz, and 5.71 THz with absorption magnitudes of 66%, 77%, and 80% respectively. Owing to these three closely position resonant peaks, a wide absorption band was obtained from 4.08 THz to 5.94 THz with an absorption greater than 60%. Taking the central frequency of the three-layer structure to be 5.01 THz, the FWHM of the absorption is 48% of the central frequency. Compared to the 20% of a single layer MM absorber, this is almost two and a half times the FWHM.
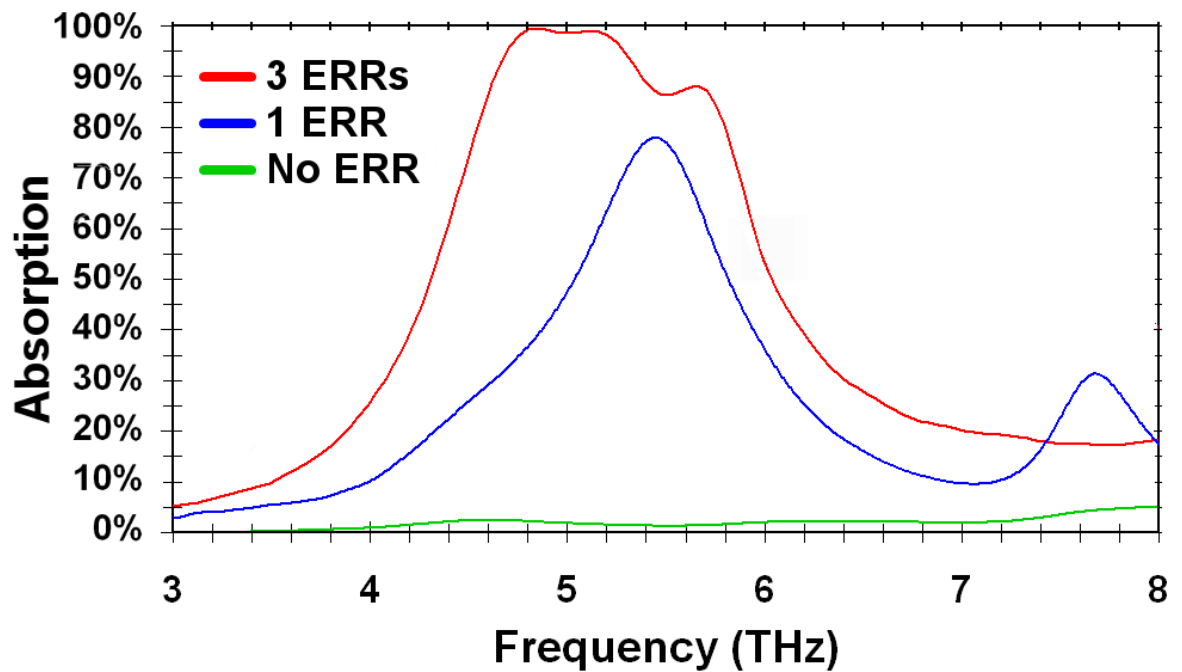


**Figure 4.8 – Absorption spectra from the broadband absorber compared to a single band absorber and a sample without ERR. The single band absorber had one frequency absorption peak at 5.42 THz and the broadband absorber had three peaks at 4.32, 5.31, and 5.71 THz with absorption magnitudes of 66%, 77%, and 80% respectively. [Simulations done by Dr. James Grant].**

The power distribution was simulated in the x-z plane to demonstrate the origin of the broadband spectral characteristics. The three resonances are shown in Figure 4.9a-c. The resonance at 4.84 THz is primarily associated with excitation of the bottom ERR layer, while the resonances at 5.16 and 5.70 THz are mainly a consequence of excitation of the middle and top ERR layers, respectively. These distributions clearly reveal that each ERR contributes to the broadband absorption.
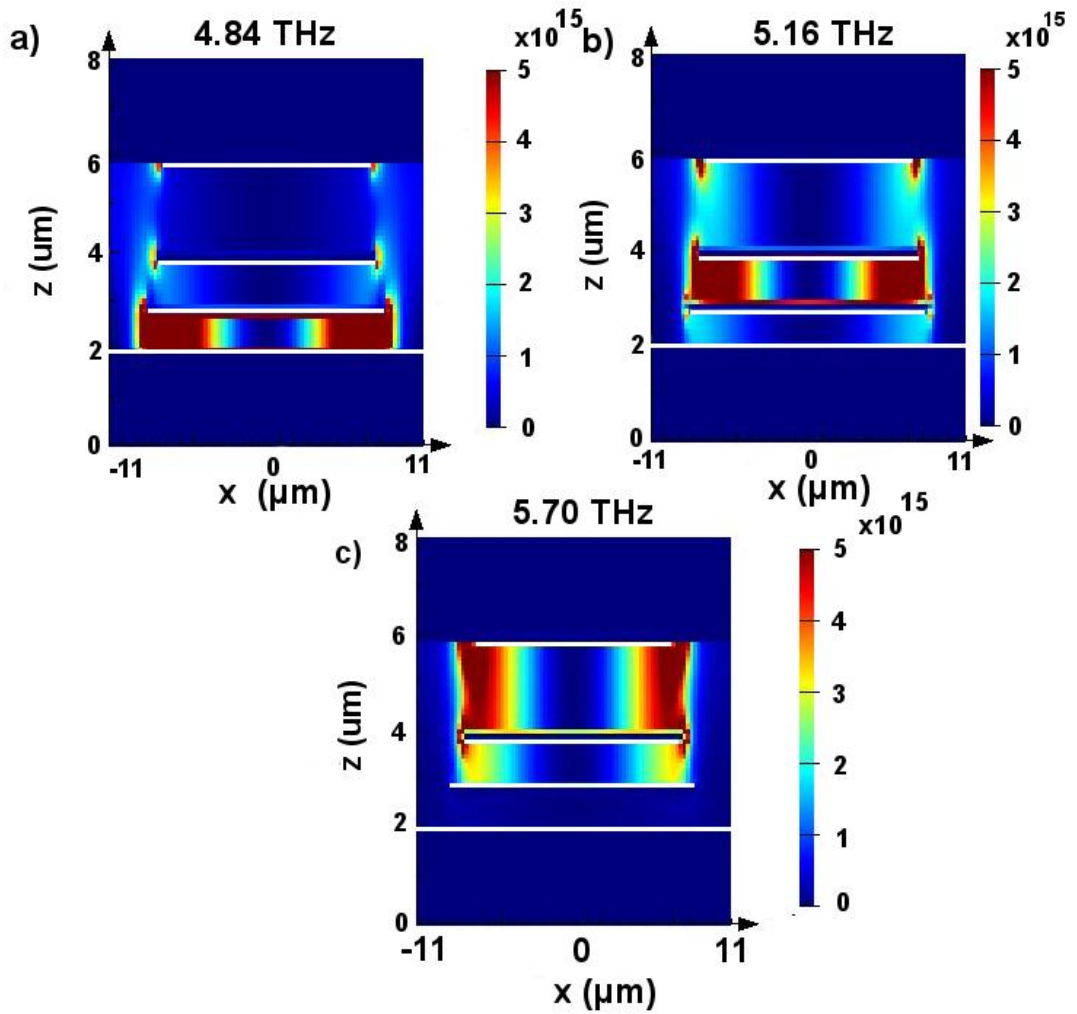
**Figure 4.9 - Power distribution of the broadband MM absorber. a) Resonance at 4.84 THz from the excitation of the bottom ERR layer, b) resonance at 5.16 THz from the ERR middle layer and c) resonance at 5.70 THz from the top ERR layer. [Simulations done by Dr. James Grant].**

# 4.2 CMOS Technology 180 nm Process

Based on the prototypes previously presented it can be concluded that the ability of MMs to be built in metallic and insulating layers to function as terahertz absorbers there is great potential to integrate them into a standard CMOS process. The available metallic and insulating layers in CMOS technologies can be used to create sub-wavelength arrays of single or broadband terahertz absorbers. This reduces the need for costly full-custom chip processing which helps to create a cost effective terahertz FPA with integrated readout circuit electronics.

The design kit used for the design of the readout electronics was the CMOS9t5V process from Texas Instruments (TI, formerly National Semiconductor). It is a 180 nm CMOS process based on the Taiwan Semiconductor Manufacturing Company (TSMC)

process with low voltage (1.8 V) and high voltage (5 V) capabilities. The transistor characteristics are shown in Table 4.3.

| Device | Lmin | Wmin | Vt typ. | Vds max. |
|---|---|---|---|---|
| 1.8 V NMOS | 180 nm | 220 nm | 0.469 V | 2.0 V |
| 1.8 V PMOS | 180 nm | 220 nm | -0.509 V | -2.0 V |
| 5.0 V NMOS | 600 nm | 450 nm | 0.714 V | 5.5 V |
| 5.0 V PMOS | 600 nm | 450 nm | -0.908 V | 5.5 V |

**Table 4.3 - Transistor characteristics**

The CMOS9t5V process has six metallic layers with its respective insulating layers. The material properties and sizes of the layers are process dependent and due to a non-disclosure agreement they cannot be discussed in detail. But, an example of this process cross-section is shown in Figure 4.10 where the six metallic layers are labelled as M1 to M6, the insulating layers in between metals are in light blue colour and the vias 1 to 5 inter-connecting the metallic layers are shown in yellow.
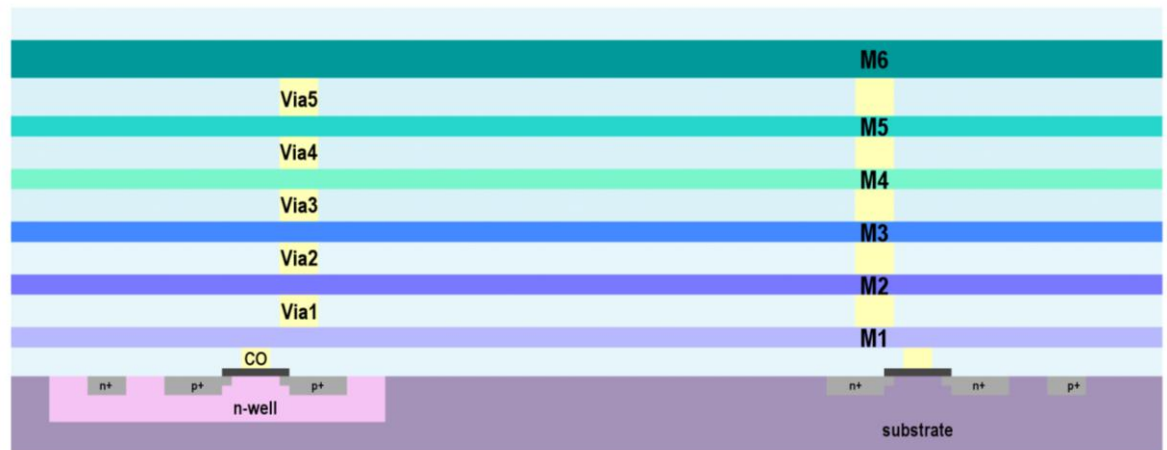


**Figure 4.10 – Example of a CMOS process (CMOS9t5V) with six metallic and insulating layers with respective vias for inter-layer connections for routing of the metallic layers.**

# 4.3 Chips Fabricated

Seven chips were fabricated in this project under the TI University Support Program using the CMOS9t5V process. This section explains the details of each chip named as Chip A to Chip F as described in Table 4.4. The Thesis will only focus on the results from Chip A, B, C, F & G. The rest of the chips were not fully tested due to time limitations.

**Table 4.4 – Description of each fabricated chip**

| Chip Name | Microbolometer Pixel Type | Characteristics |
|---|---|---|
| Chip A | VOx<br>30 μm x 30 μm | Five MM array designs with the purpose of determining that the resonant absorption occurred at the frequency of interest. Testing of single pixels and the 5 x 5 readout electronics:<br>• Design 1 - Single band absorber & 5 x 5 FPA with readout electronics<br>• Design 2 – Broadband absorber & 5 x 5 FPA with readout electronics<br>• Design 3 – Six single broadband absorber pixels routed to external pads for characterisation<br>• Design 4 – No absorbers, only a ground plane<br>• Design 5 – Broadband absorbers & 5 x 5 FPA with readout electronics<br>Single circuit blocks:<br>• Operational Transconductance Amplifier<br>• 5 bit Current DAC<br>• Decoder |
| Chip B | VOx<br>30 μm x 30 μm | Six single broadband absorber pixels routed to external pads for characterisation in a 5 x 5 mm$^2$ array used to measure absorption at 2.5 THz using a spectrometer |
| Chip C | VOx and p-n diode<br>30 μm x 30 μm | Two microbolometer designs:<br>• Design 1 – 8 x 8 FPA with broadband absorbers and VOx microbolometers<br>• Design 2 – Six single broadband absorbers with P-N diode microbolometers |
| Chip D | VOx<br>30 μm x 30 μm | 64 x 64 FPA with broadband absorbers and integrated readout electronics with serial output architecture |
| Chip E | VOx and p-n diode | Copy of Chip C with a modification of the ESD pad ring |
| Chip F | VOx<br>40 μm x 40 μm | 64 x 64 FPA with broadband absorbers and integrated readout electronics with parallel output architecture |
| Chip G | p-n diode<br>40 μm x 40 μm | 64 x 64 FPA with broadband absorbers and integrated readout electronics with parallel output architecture |

# 4.4  Chip A

## 4.4.1  Pixel Designs

Chip A contained five arrays with three different MM designs, three 5 x 5 arrays with readout electronics, individual pixels, and single circuit blocks for characterisation purposes. It was sent for fabrication to TI on January 2012. According to the MM simulation results presented in Section 4.1, the absorption frequency position of the single band and broadband absorbers is sensitive to the refractive index of the dielectric insulator. Since the refractive index of the inter-layer dielectric of the CMOS9t5V process is not known at terahertz frequencies, different pixel designs were included to maximise the chances that one of the pixels would absorb at 2.5 THz. Each array covered an area of 1.5 mm x 1.5 mm and had a pixel size of 30 μm x 30 μm. The total area of Chip A was 6014.83 μm x 7484 μm as shown in Figure 4.11.

The design of the three MM absorbers was based on the simulation results of the stacked cross-shaped ERRs detailed in Section 4.1. The pixels in Design 1 had single band absorbers with an ERR in M6 and continuous ground plane in M5 (Figure 4.12e). The pixels in Designs 2 and 3 were identical and were composed by a broadband absorber with three ERRs in M4, M5 and M6 and continuous ground plane in M3 (Figure 4.12f,c) . This design was simulated without the passivation layer on top of M6. The reason behind such simulations was that eventually the passivation layer would have had to be removed to expose the top metal M6 stud and connect the microbolometer sensor to it. Therefore, it was necessary to simulate the absorption response without the passivation. The pixels in Design 4 did not have ERRs, only a continuous ground plane in M5 (Figure 4.12d). This was done as a precaution in case that none of the designs would absorb at the desired frequency. If that was the case, the MMs could have been added in our fabrication facilities (JWNC). The pixels on Design 5 were composed of a broadband absorber identical to Designs 2 and 3, but with the main difference of keeping the passivation layer on top of M6 (Figure 4.12a). The readout electronics were in Design 1, 2, and 5 and the individual pixels connected to pads were in Designs 3 and 4. A summary of the designs is presented in Table 4.5. It details the description of the MM absorbers and summarises the characteristics and differences between the arrays. The ERR parameters for each Design are listed in Table 4.6.
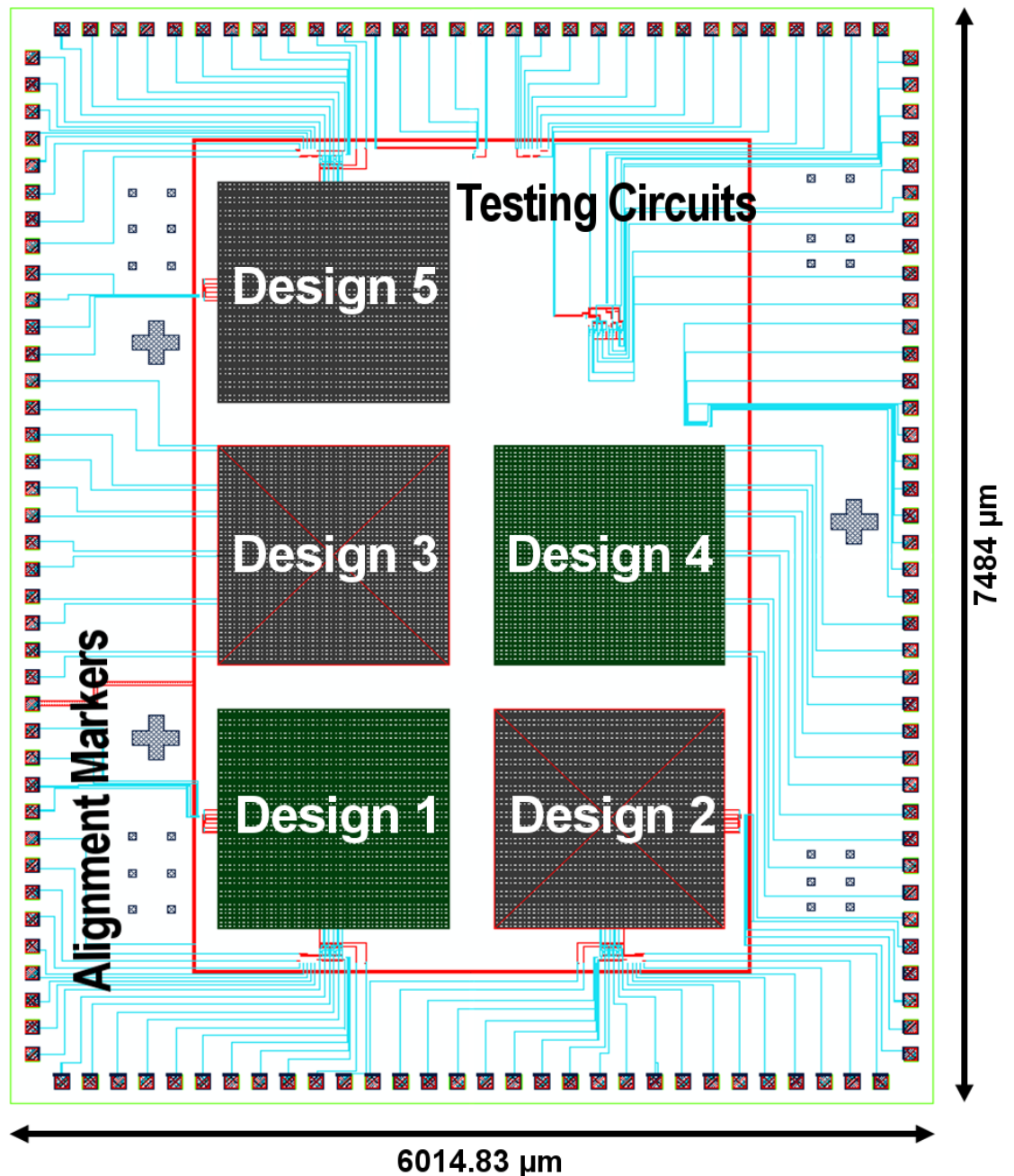
**Figure 4.11 - Chip A layout containing five MM arrays with three different MM designs, three 5 x 5 arrays with readout electronics, individual pixels, and single circuit blocks for characterisation purposes.**

| Array Design No. | Readout Electronics | Passivation Layer | Ground Plane Metal Layer | ERRs in Metal Layers |
|---|---|---|---|---|
| 1 | Yes | Yes | Metal 5 | 1 ERR in Metal 6 |
| 2 | Yes | No | Metal 3 | 3 ERRs in Metals 4,5,6 |
| 3 | No | No | Metal 3 | 3 ERRs in Metals 4,5,6 |
| 4 | No | Yes | Metal 5 | No ERRs |
| 5 | Yes | Yes | Metal 3 | 3 ERRs in Metals 4,5,6 |

**Table 4.5 - Detailed description of the five arrays on Chip A**
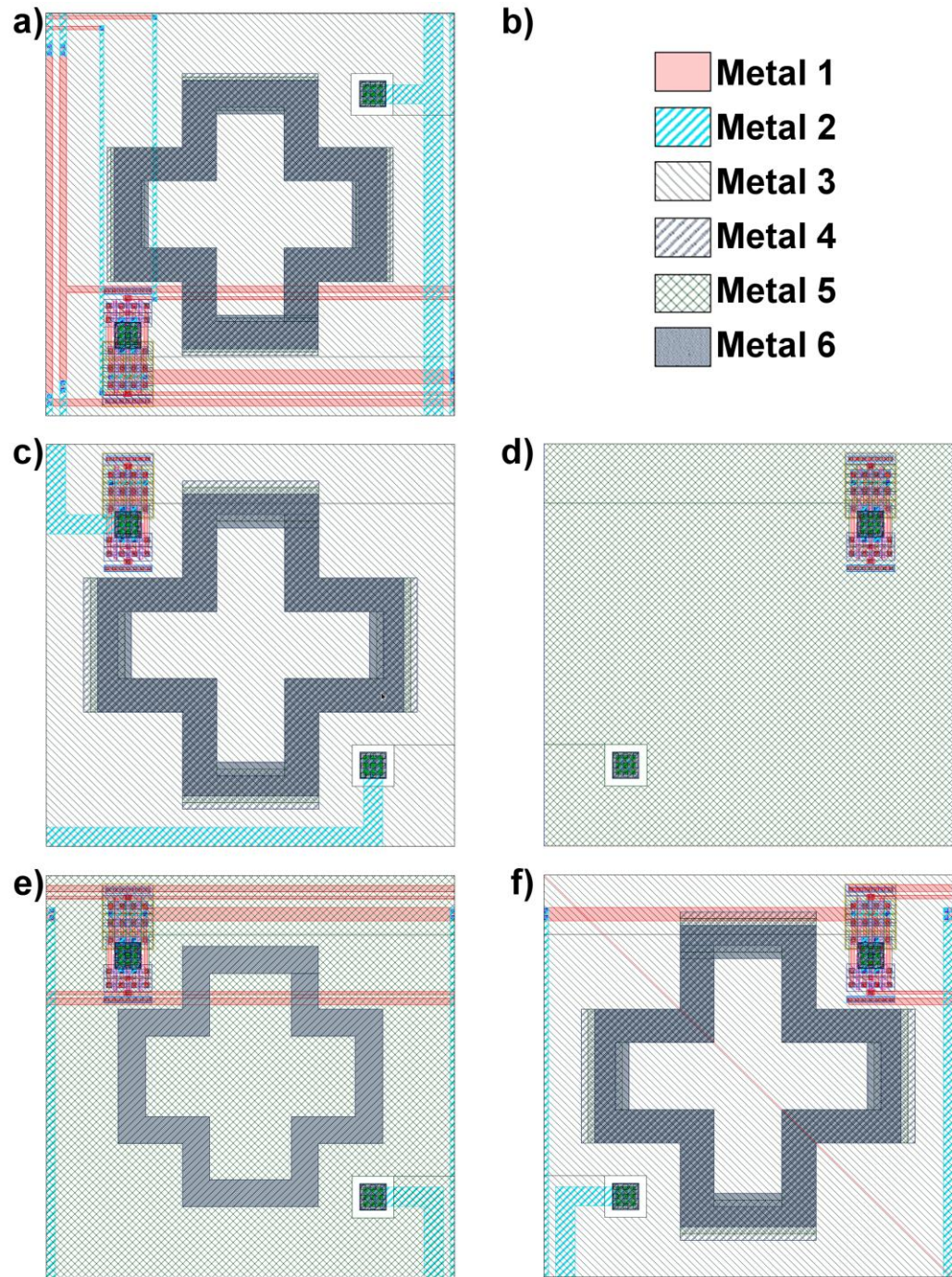
**Figure 4.12- Pixel MM Absorbers: a) Design 5 broadband MM pixel, b) metals colour coding, c) Design 3 broadband MM pixel, d) Design 4 without MMs, e) Design 1 single band MM pixel, and f) Design 2 broadband MM pixel.**

| Parameter | Design 1 | Design 2 & 3 | | | Design 5 | | |
|---|---|---|---|---|---|---|---|
| | M6 | M4 | M5 | M6 | M4 | M5 | M6 |
| K [µm] | 15.4 | 19.5 | 18.5 | 17.5 | 16.0 | 15.5 | 15.0 |
| L [µm] | 19.4 | 24.5 | 23.5 | 22.5 | 21.0 | 20.5 | 20.0 |
| N [µm] | 6.0 | 5.0 | 5.0 | 5.0 | 5.0 | 5.0 | 5.0 |
| W [µm] | 10.0 | 10.0 | 10.0 | 10.0 | 10.0 | 10.0 | 10.0 |

**Table 4.6 – Electric ring resonator parameters for the single and broadband absorbers in Designs 1, 2, 3, and 5**

The optimised MM absorber structures were simulated using 3D FDTD (Lumerical Inc) software. The simulation steps were identical to the ones previously mentioned for the single band MM absorber in Section 4.1. In this case, the mesh step size was $\Delta x = \Delta y = 0.1$ μm and $\Delta z = 0.05$ μm for better accuracy. The three absorber designs in Chip A had an absorption magnitude of at least 50% at 2.5 THz as shown in Figure 4.13. The pixels in Design 1 were single band absorbers and had an absorption magnitude of 70% (blue line). The broadband pixels without passivation on top of M6 on Design 2 and 3 had an absorption magnitude of 50% (green line). The pixels on Design 5 were identical to the ones in Design 2 and 3, but had passivation on top of M6 and had an absorption magnitude of 72% (red line).
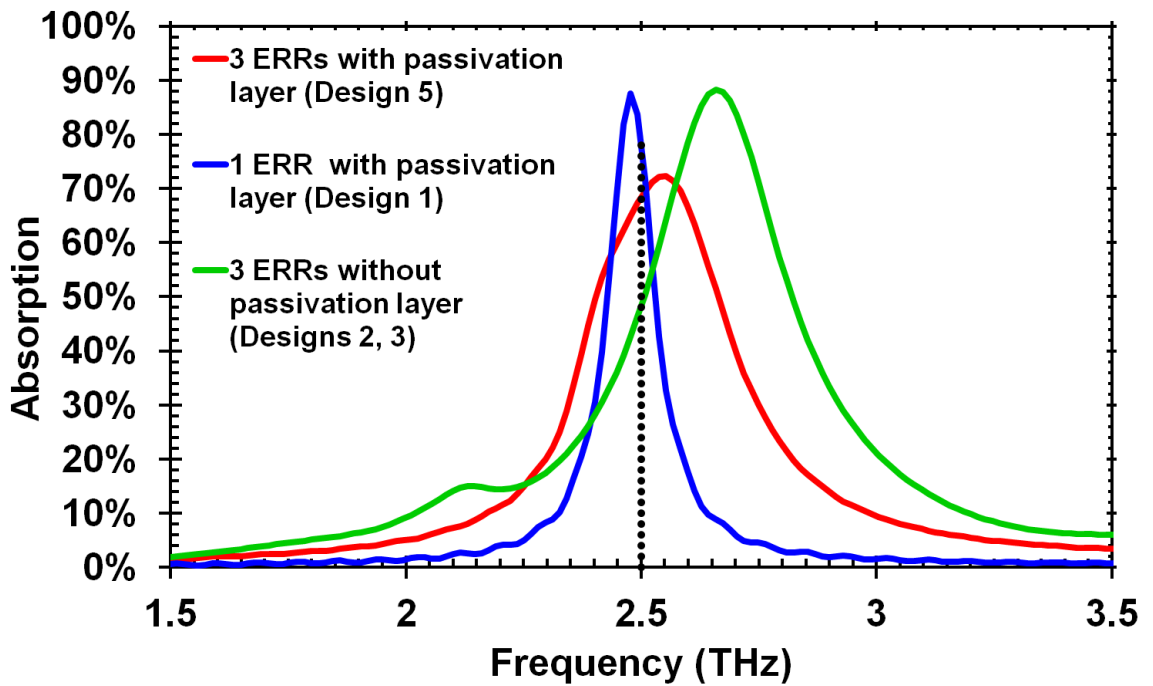


**Figure 4.13 – Absorption simulation data for the three MM absorbers in Chip A. The pixels in Design 1 have one ERR and an absorption magnitude of 70% (blue line). The pixels in Designs 2 and 3 have 3 ERRs without the top most passivation layer and have an absorption magnitude of 50% (green line). The pixels in Design 5 have the same ERR structure as Designs 2 and 3 but have passivation on top; they have an absorption magnitude of 72%. [Simulations done by Dr. James Grant].**

The optical constants were extracted via the inversion of the $S$ parameters. The retrieved parameters, including real and imaginary $\varepsilon$ and $\mu$, for the MM absorber in Designs 2 and 3 are shown in Figure 4.14. The dashed lines indicate the real and imaginary permittivity and the solid lines indicate the real and imaginary permeability. The vertical points indicate the frequency ($\omega_0$) of the maximum absorption at 2.5 THz, at the imaginary component of the permeability. The real parts of the optical constants both cross zero at $\omega_0$ which is required for zero reflection. The real part of the permittivity is negative and the

real part of the permeability is positive as required for zero transmission across the frequency range.
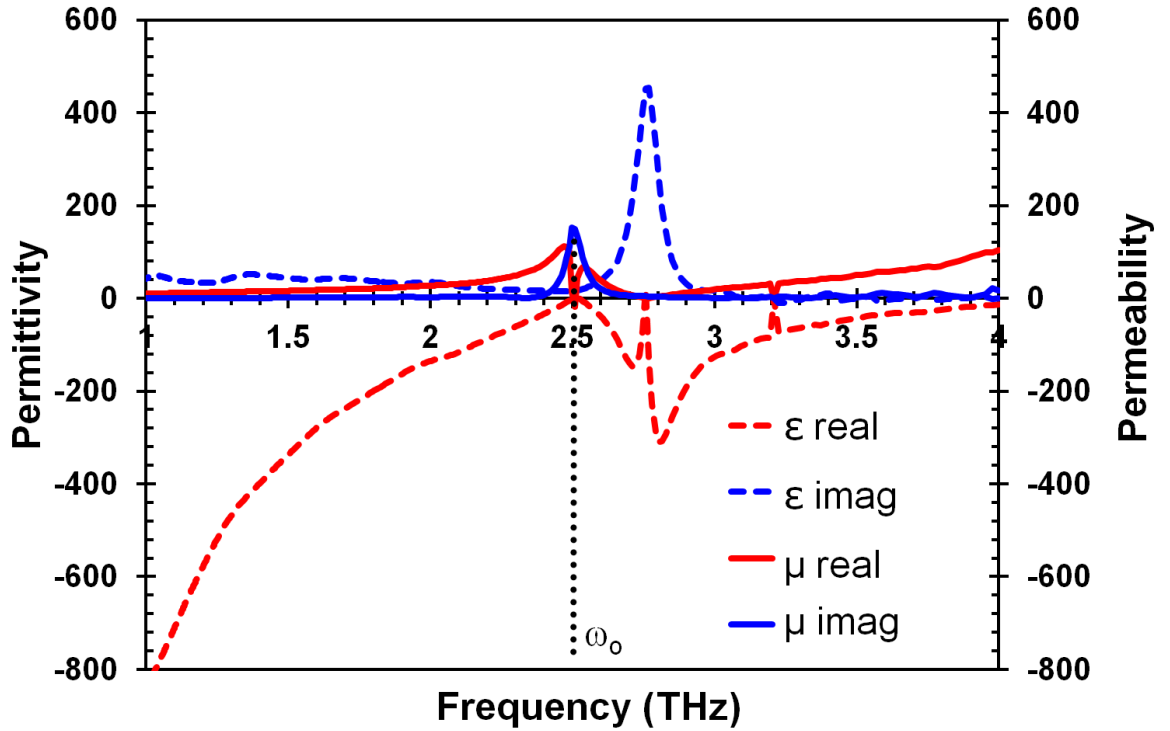


**Figure 4.14 - Chip A simulated effective parameters showing the real (red) and imaginary (blue) *μ* in dashed lines and real (red) and imaginary (blue) *ε* in solid lines. [Simulations done by Dr. James Grant].**

Figure 4.15a shows the refractive index of the materials that compose the MM absorber. The metallic layers are shown in red and the dielectric insulating layers in blue. The simulated absorption distribution in the x-z plane shown in Figure 4.15b reveals that the majority of the terahertz radiation is absorbed within the first micrometre of the metallic layer and also in the first 200 nm of inter-metal dielectric beneath the M6 ERR. Therefore, placing the VOx microbolometer above M6 is the right approach to obtain higher response. Figure 4.15c shows the simulated terahertz absorption distribution below the M6 ERR in the x-y plane. Due to the inherent symmetry of the MM absorber device the FDTD simulations show how the absorption properties change with angle of incidence of the EM wave. Figure 4.15d shows that the absorption magnitude at 2.5 THz is not sensitive to the angle of incidence for up to an angle of 45°.This means that even when the incident angle for the pixels at the edges of the array is different from the pixels on the centre, the absorption magnitude of all the pixels will be constant.
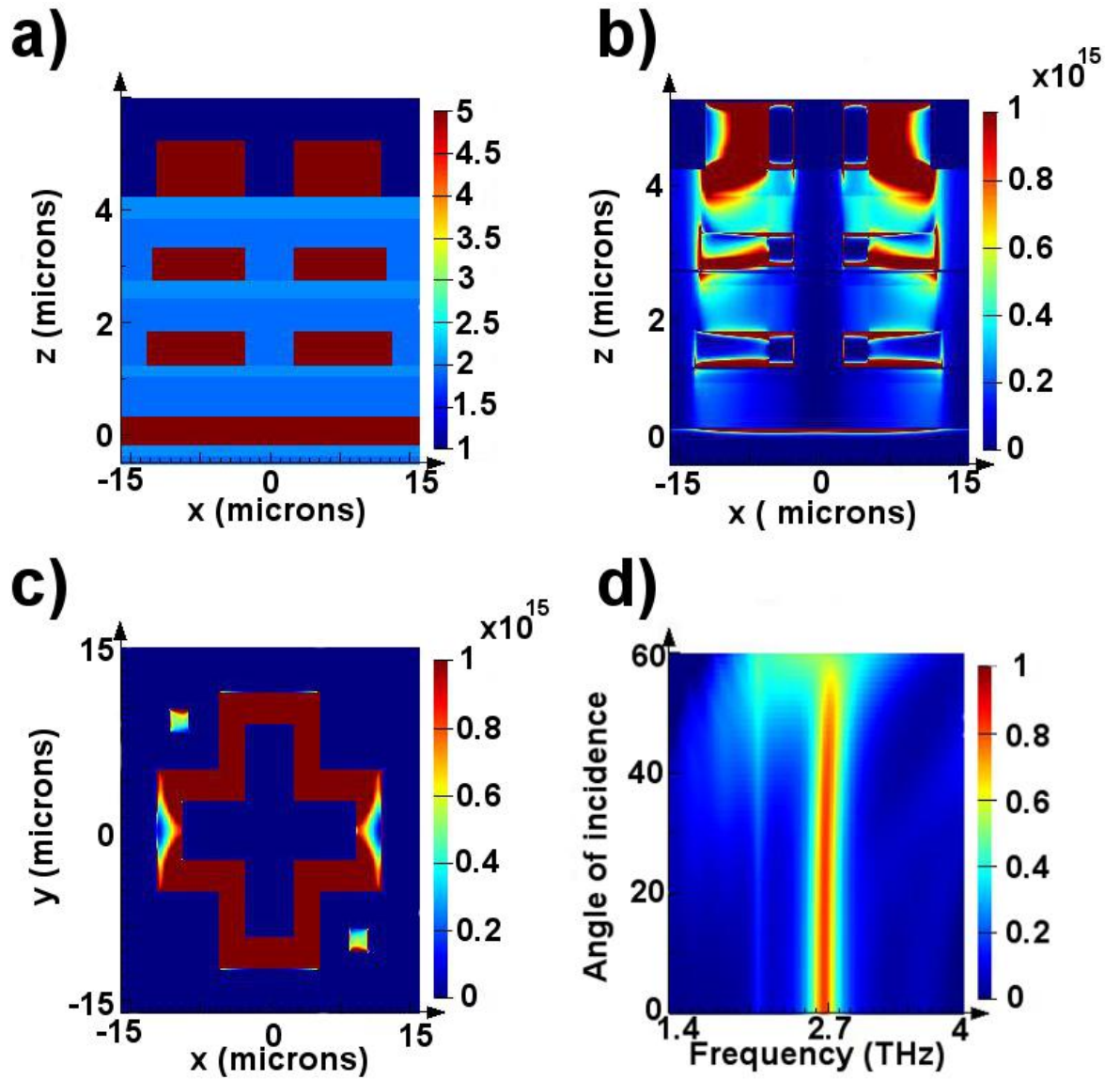
**Figure 4.15- Power distribution simulations of Chip A. a) Cross-section showing the colour-coded refractive index of the materials that comprise the metamaterial absorber. b) Simulated Terahertz absorption distribution plot in the x-z plane at y = 5 µm. c) Simulated x-y absorption distribution in the insulator immediately beneath the M6 layer and d) simulated spectral absorption response as a function of incident angle. [Simulations done by Dr. James Grant].**

# 4.5 Readout Electronics for the Focal Plane Array

Designs 1, 2, and 5 of Chip A had on-chip readout electronics for a two-dimensional 5 x 5 pixel matrix. The CMOS FPAs were developed using Cadence design tools and the TI-CMOS9t5V design kit. The readout of two-dimensional arrays of resistive microbolometers requires the change in resistance to be measured by an output voltage or current. The change in resistance is caused by the changes in incident terahertz radiation. The magnitude of the change is also dependant in the bias voltage or current applied to the

microbolometer. All these factors and requirements were taking into consideration while designing the readout circuit.

The readout circuit block diagram for the 5 x 5 array is shown in Figure 4.16. The readout circuit is identical for the three arrays. This integrated circuit is composed of one row and column decoder, switches for selecting pixels, a 5-bit current DAC, and five operational amplifiers (op amp). The design kit available only contained basic electronic component such as transistors, resistors, diodes, etc. Therefore each circuit, including the digital logic gates, were designed from transistor level and their respective layouts were done. The design of each circuit block will be explained throughout this section followed by an explanation of how the readout electronics function.
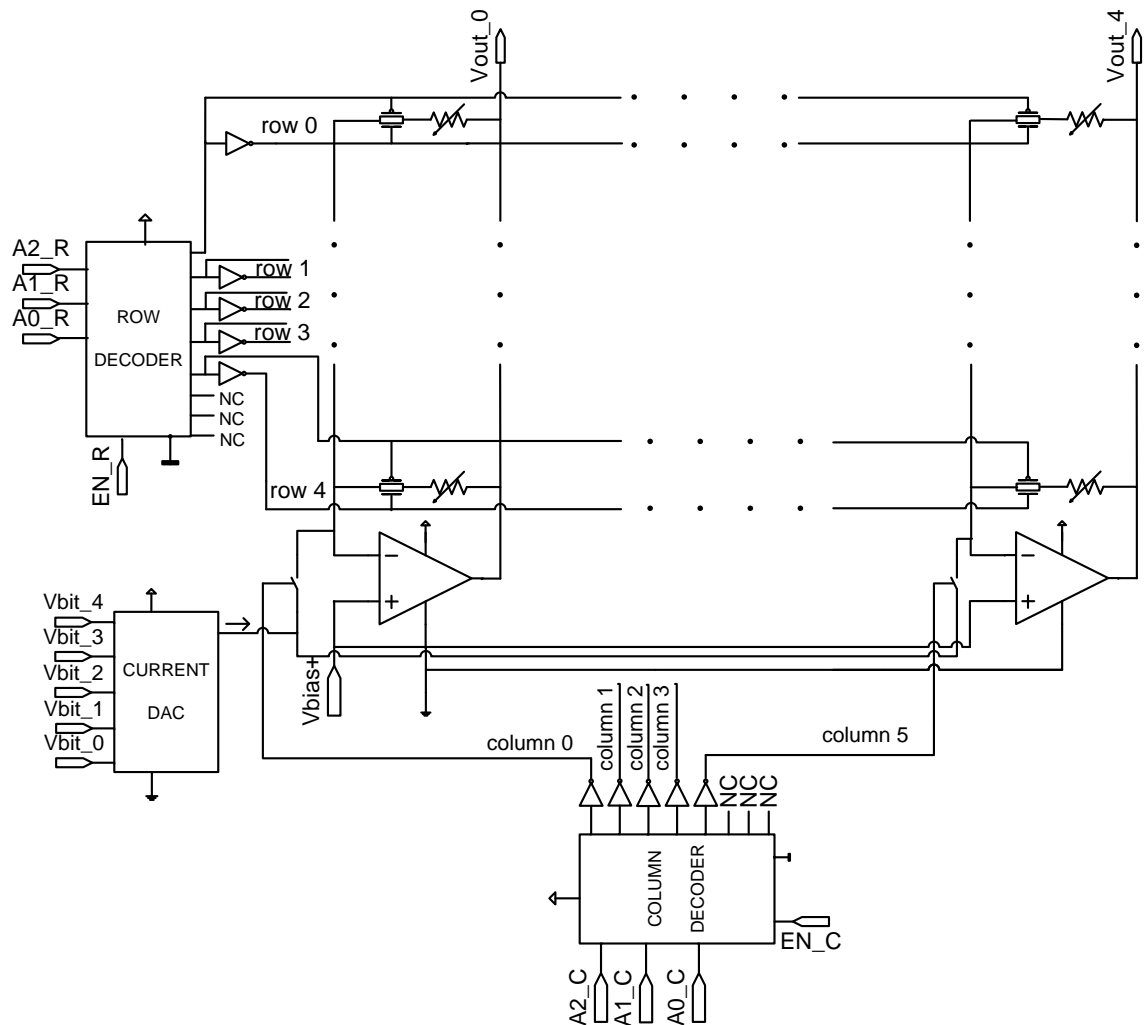
**Figure 4.16 - Serial output 5 x 5 focal plane array readout circuit block diagram.**

## 4.5.1 Decoders

The individual selection of pixels is dependent on the use of one row and one column decoder at a time. For the 5 x 5 pixel array selection two identical 3 to 8 decoders with enable functions were designed. The decoder functions as follow: when enable (EN) is low

(0 V) it decodes the 3-bit input on the A2_R, A1_R, A0_R input lines for the row decoder and A2_C, A1_C, A0_C  for the column decoder. This enables the corresponding word-line for the row decoder and column decoder meaning that only one pixel is selected at a time.

The decoder was designed with four inverters and five 4 input NAND gates as shown in Figure 4.17. These basic logic gates were made from minimum width NMOS (280 nm/ 180 nm) and 3 times minimum width PMOS (640 nm/ 180 nm) transistors. Half the truth table is shown in Table 4.7, the other half is not shown because when the EN signal is high all outputs are disabled. For the 5 x 5 array only switches 0 to 4 (SW0 to SW4) were used.
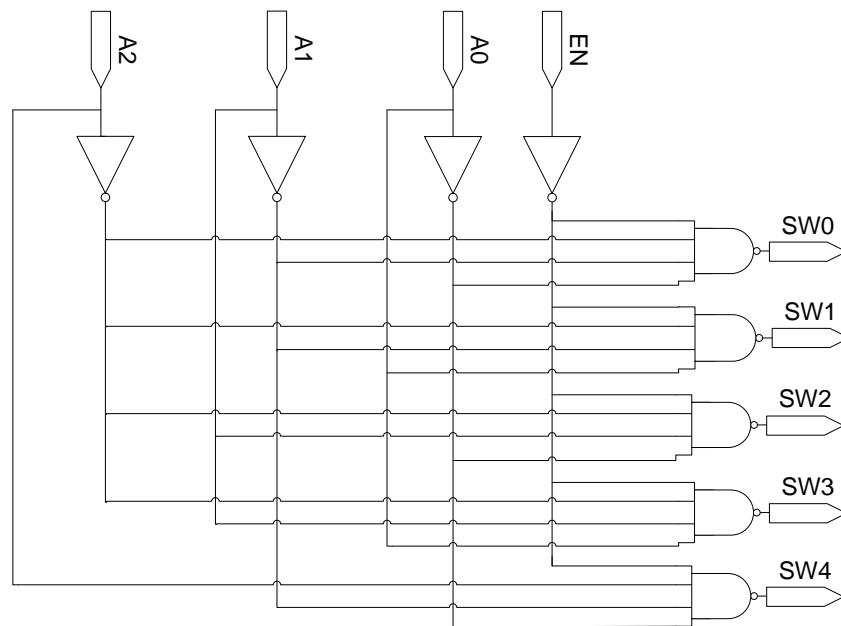


**Figure 4.17 - Decoder schematic.**

| ENABLE | A2 | A1 | A0 | Y |
|--------|----|----|----|----|
| 0 | 0 | 0 | 0 | SW0 |
| 0 | 0 | 0 | 1 | SW1 |
| 0 | 0 | 1 | 0 | SW2 |
| 0 | 0 | 1 | 1 | SW3 |
| 0 | 1 | 0 | 0 | SW4 |
| 0 | 1 | 0 | 1 | SW5 |
| 0 | 1 | 1 | 0 | SW6 |
| 0 | 1 | 1 | 1 | SW7 |

**Table 4.7 - Decoder half truth table**

The decoder simulation results for the selection of 5 pixels are shown in Figure 4.18. The input signals (A2, A1, A0) and EN are shown in purple and the output signals (SW0 to SW4) are shown in blue. The input signals start with the word line 000 and progress to 111 for 2 cycles. A2 is the most significant bit (MSB) and A0 is the least

significant bit (LSB). The simulation results show that in the first cycle, when EN is low, only one output is activated per pulse starting with SW0 until SW4. When EN is high, all the outputs are disabled. The pulse width is adjusted depending on the readout speed, for this example each pulse is 50 µs.
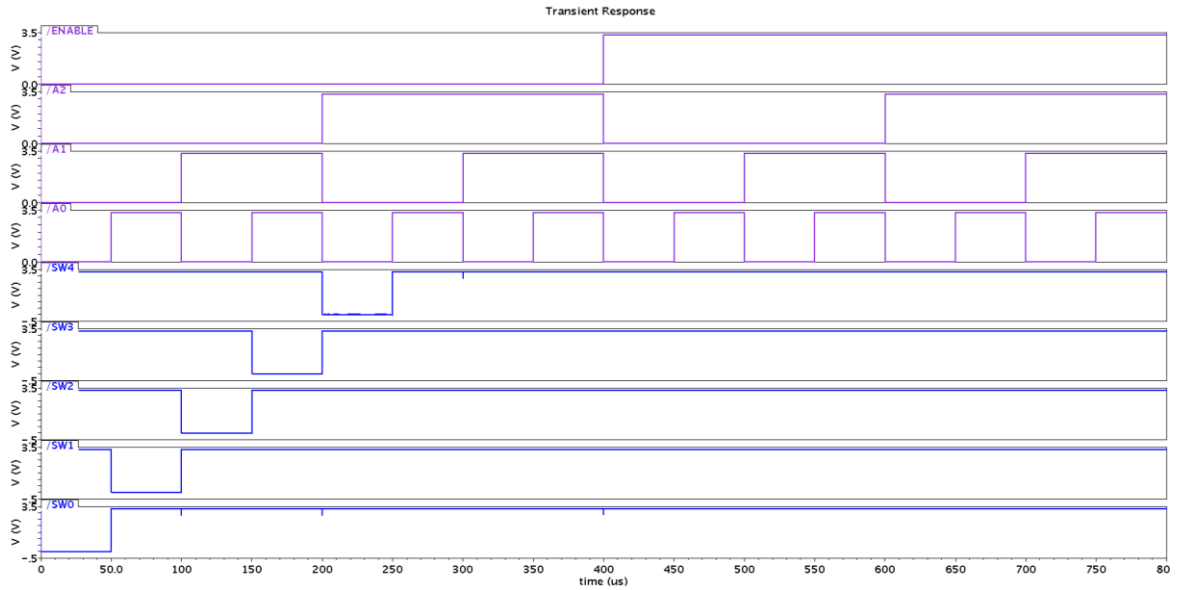


**Figure 4.18 – Decoder simulation results. Input signals in purple (EN, A2, A1, A0) and output signals in blue (SW0 to SW4). When EN is low only one output is decoded depending on the input word-line, when EN is high all the outputs are disabled.**

### 4.5.2 Transmission Gates

The transmission gates (TGs), also known as switches, were designed to access and to readout every pixel of the array. The TGs were connected to the outputs of the row and column decoders to access only one pixel at a time. The main specifications for the design of TGs are speed and low resistance. They have to provide a low ON resistance ($R_{ON}$) compared to the microbolometer resistance of more than 100 times difference while still maintaining reasonable on and off times. The TG circuit design and the respective transistor's sizes are shown in Figure 4.19. The p-channel and n-channel transistors are connected in parallel to avoid dynamic range limitations. The bulk of the NMOS is connected to 0 Volts (GND) and the PMOS to 3.3 Volts (VDD). A pair of dummy transistors with their source and drain connected together were used to reduce feedthrough effects [122]. These dummy transistors acting as capacitors are connected to the output signal of the TG.
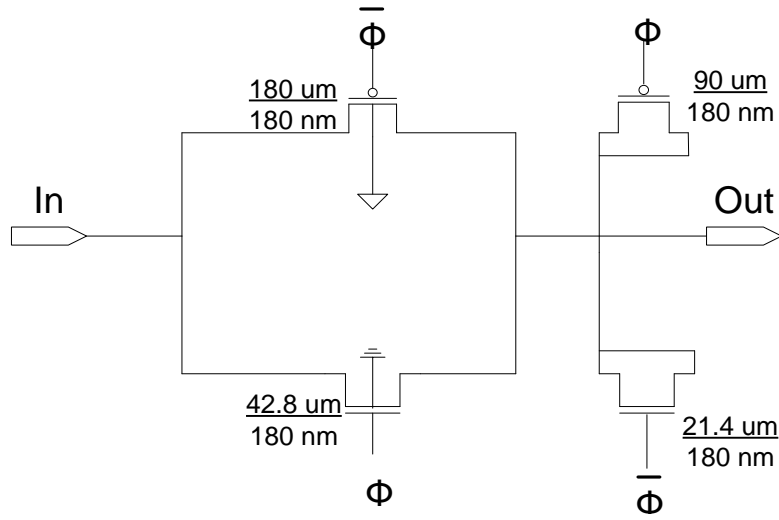
**Figure 4.19 - Transmission Gate schematic.**

The TG simulation results are shown in Figure 4.20. The $R_{ON}$ is below 13 Ω for a maximum current of 3 μA and maximum bias voltage of 3.3 V. The NMOS is dominant when passing lower voltages and the PMOS passes higher bias voltages. This behaviour is noted in Figure 4.20a where $R_{ON}$ changes its resistance depending on the input voltage, although the resistance change is minimum (<3 Ω). The TGs are enabled by complementary signals ($\Phi$ and $\overline{\Phi}$) from the row and column decoder's outputs. The TG is activated when the NMOS gate has 0 V and the PMOS gate has 3.3 V. When the TG is on, the input signal is equal to the output signal as shown in Figure 4.20b and c.
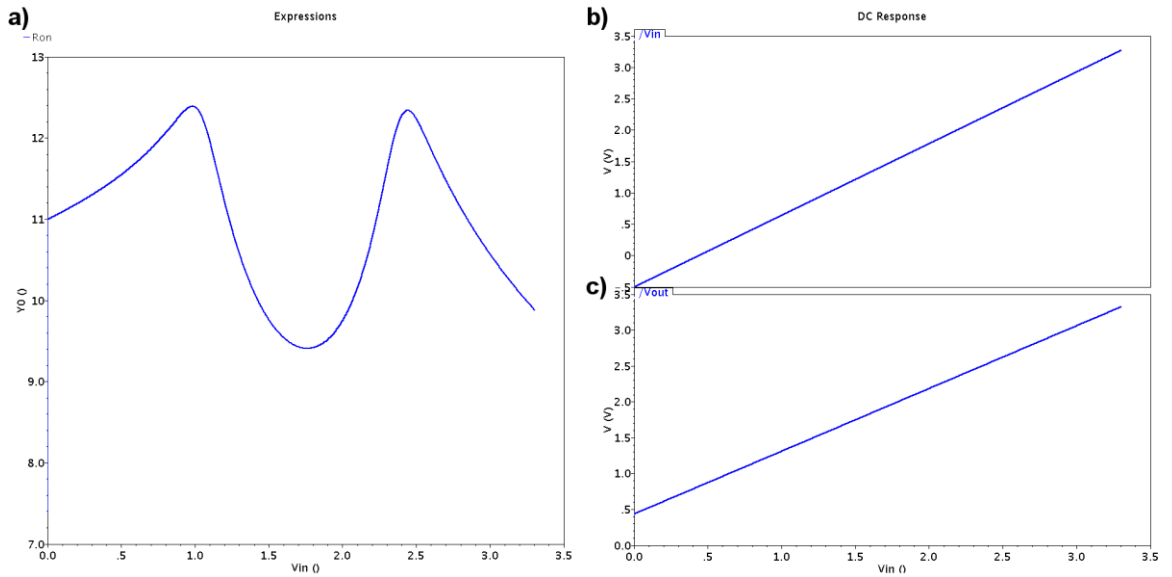


**Figure 4.20 - a) Transmission gate ON resistance and b) Input signal equal to c) output signal.**

## 4.5.3 5-bit Current Digital-to-Analogue Converter

A current DAC was designed to bias the microbolometers. The design of the single output DAC was based on the basic R-2R ladder topology. The R-2R ladder is a binary

weighted current source which is relatively easy to design and implement on-chip by utilizing accurate layout techniques such as common-centroid and unit-matching. Due to the high resistance of the $VO_x$ microbolometers, the current bias had to be on the range of nanoAmpers to avoid saturation of the output amplifier with an output range of 0.3 V to 3.3 V. Therefore, large values of resistors in the range of megaohms were needed to obtain such small currents on the ladder network. This approach could not be implemented in the integrated circuit due to the significant increase of chip area and layout mismatch. The solution was to replace the resistors with PMOS transistors operating in the linear region to perform as an R-2R ladder. All the transistors had the same width and length (440 nm/900 nm) in each branch of the 5-bit current DAC as shown in Figure 4.21.
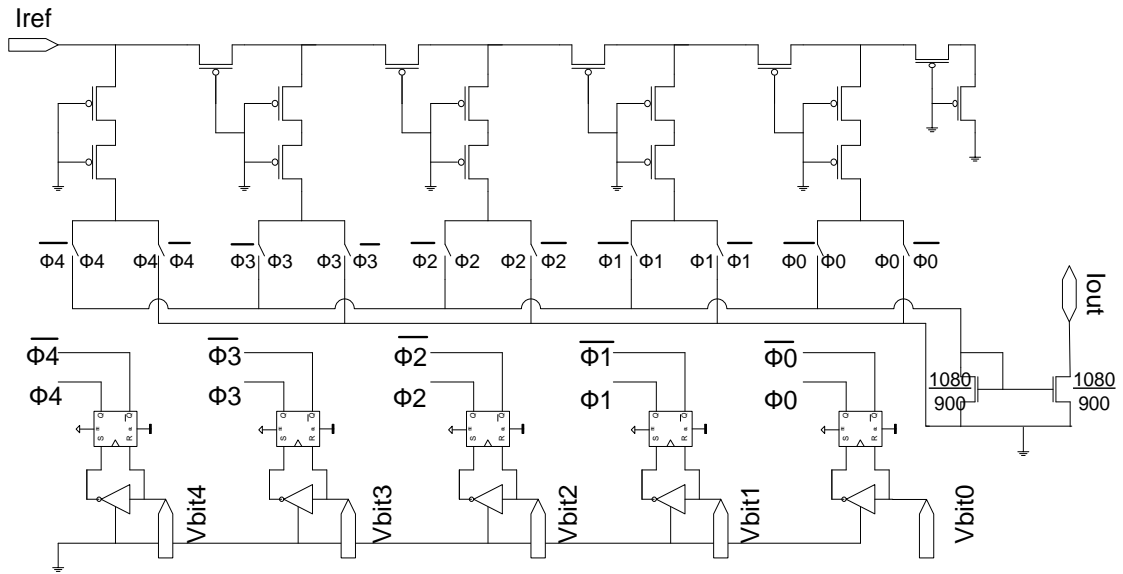


**Figure 4.21 - 5 bit current DAC schematic.**

The minimum current value of the ladder had to be chosen at least one order of magnitude higher than the transistor leakage current. In the CMOS9t5V technology, the leakage current for the PMOS is 30 pA/µm, thus 100 nA was an appropriate value. The external reference current, $I_{ref}$, was determined using $2^n$ times the LSB current of the ladder [123]. For the 5 bit DAC ($2^5$=32), therefore 100 nA * 32 = 3.2 µA. The 5-bit current DAC provides a single mirrored current output from 100 nA to 3 µA using a reference current of 3.2 µA as shown in the simulation results in Figure 4.22.
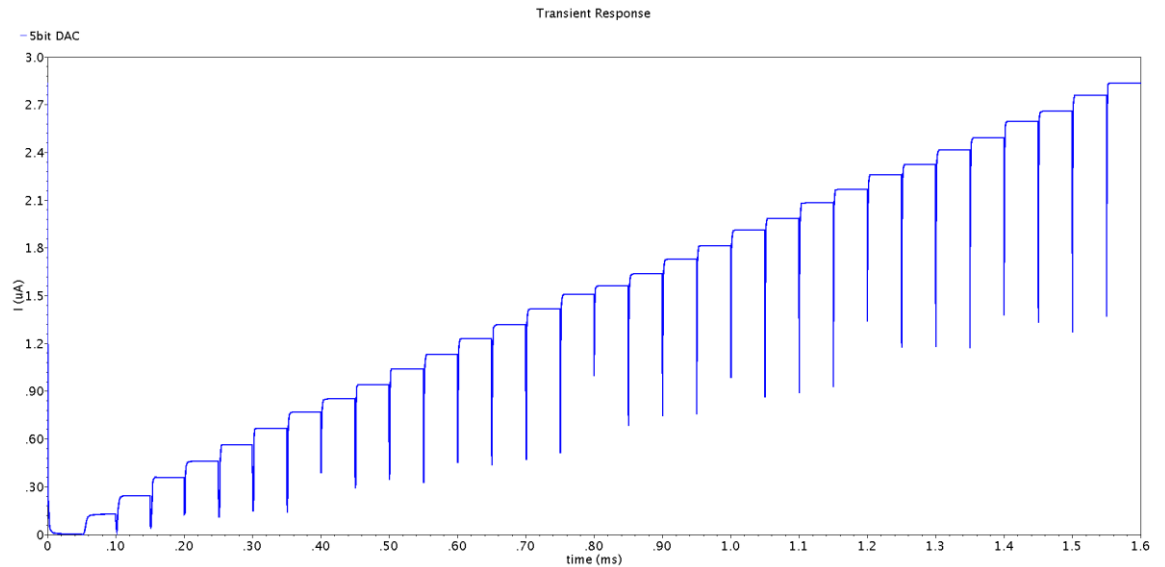
**Figure 4.22 – Simulation results from the 5-bit current DAC showing a minimum current of 100 nA to 3µA.**

The current value is proportional to the input digital word provided by external pads. The bits control the differential switches of each ladder leg with complementary overlapping signals provided by a Set-Reset (SR) latch shown in Figure 4.23 where the inputs are S=1, R=0, and Q=1 therefore the function is considered to be 'setting' the outputs to the controlling signals of the DAC. The use of the SR latch ensures that the current source does not switch off completely to avoid large glitches when switching taking only 4 ns [124]. The current in each ladder leg has two available paths through the differential switches so that the current source always delivers current [125]. When the particular branch is not selected by the input word, the current is dumped to ground. On the other hand, if it is selected, the current is steered to the DAC output and is mirrored by a basic current mirror and fed only to the column of the pixel being readout.
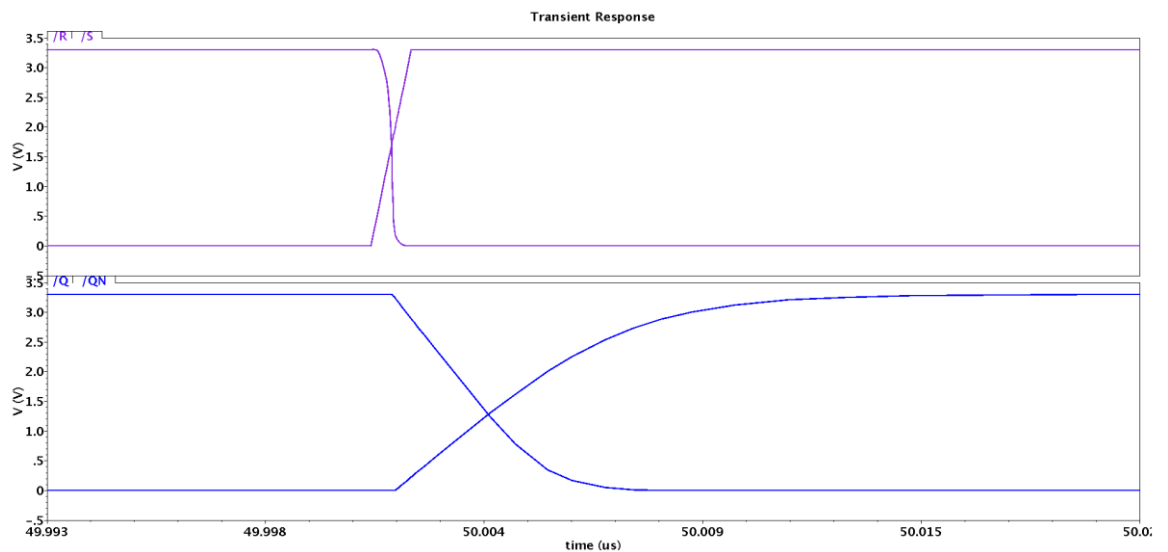


**Figure 4.23 - Set-Reset latch simulation results where the input signals (purple) are S=1 and R=0 therefore the outputs (blue) are set to Q=1 and QN=0.**

66

## 4.5.4 Operational Amplifier

The topology of the amplifier is based on a basic operational transconductance amplifier amplifier (OTA). The amplifier is composed of two stages: differential input stage and single-ended output stage. The input stage is composed of a PMOS differential pair, loaded by a PMOS current mirror. The differential pair transistors are sized to drive 12.5 µA in each branch provided by a basic cascoded current mirror load. The output stage consists of a source follower and a current-sink load.

Figure 4.24 shows the schematic and transistor sizes of the amplifier. The open-loop characteristics versus frequency are shown in Figure 4.25a. It shows an open loop gain (OLG) of 88dB, a 3dB frequency of 1.66 kHz, a BW of 19.7 MHz and a phase margin of 61.26°. Figure 4.25b shows the transient response in an open loop configuration with a differential input signal of 10 $\mu V_{p-p}$ and the resulting single ended output signal with an OLG of 25000 V/V.

The amplifier is used at the end of each column with the purpose of producing a voltage dependent on the resistance value of the microbolometer depending on the terahertz incident radiation power. There are five amplifiers in the array, one per column. The microbolometer is connected in a feedback configuration to the output amplifier. As the current biases the microbolometer, the amplifier reads a potential between 0.3 V and 3.0 V depending on the microbolometer's resistance value. The process is repeated for every pixel until a voltage map is created.
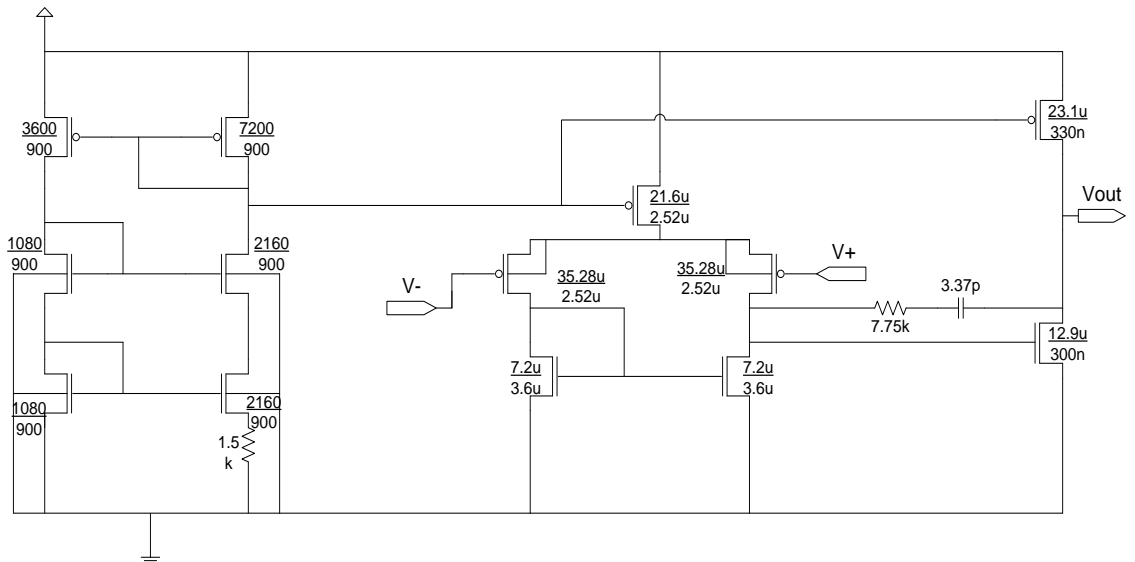


**Figure 4.24 - Operational Amplifier schematic with an integrated cascaded current source.**
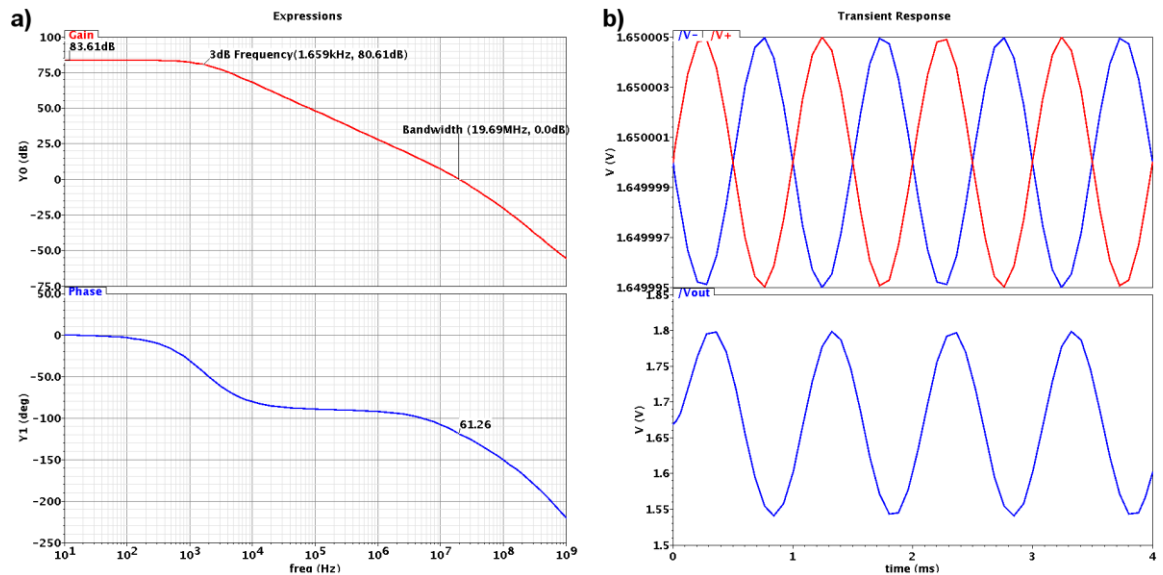
**Figure 4.25 – a) Open loop versus frequency characteristics showing a gain of 83.61 dB, 3dB frequency of 1.66 kHz, a BW of 19.7 MHz and a phase margin of 61.26°. b) Transient response showing a differential input signal of 10 $\mu V_{p-p}$ and an output signal with the respective gain of 25000 V/V.**

### 4.5.5  5 x 5 Readout Process

The readout process will be explained in this section. First, the microbolometers are properly biased by the 5-bit current DAC to provide voltage outputs within the power-supply range of the operational amplifier (0V - 3.3 V). The bias current depends on the resistance value of the microbolometer. After the current has been binary weighted with the external 5 bits of the digital input word, the readout process begins by selecting one pixel at a time controlled by the row and column decoder. The first column is selected by closing a switch that connects the current DAC to the respective column; each row from the selected column is read. Then, the process repeats to read every pixel in every column. Only one column at a time is biased with current to reduce the power consumption and output load for the DAC. The amplifier then reads the output voltage of every pixel depending on the microbolometer resistance and bias current. The schematic of a single pixel readout is shown in Figure 4.26 and the complete schematic of the 5 x 5 array is shown in Figure 4.16.
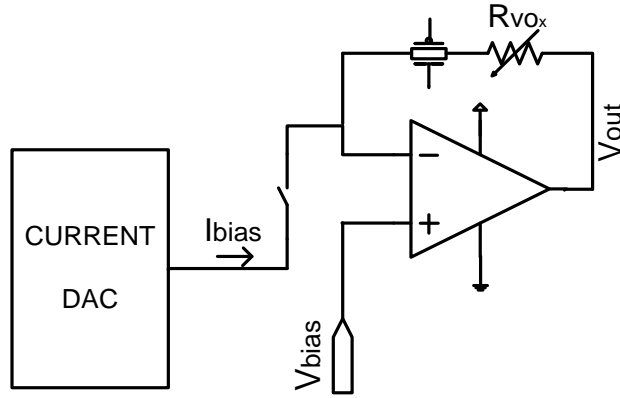
**Figure 4.26 - Single pixel readout schematic.**

The row decoder and column decoder signals are shown in Figure 4.27. The row decoder signals are A2_R, A1_R and A0_R and the column decoder signals are A2_C, A1_C and A0_C. The row decoder allows single pixels to be selected while the column decoders allow the current to flow from the DAC to pixels in the particular column selected. For this example, the pixels are read at 10 KHz (A0_R sets the frequency), then every column switches at 1/5 of that frequency since 5 pixels are being read per column. Therefore, the total readout timing for a 5 x 5 array would be 1.25 ms per frame.
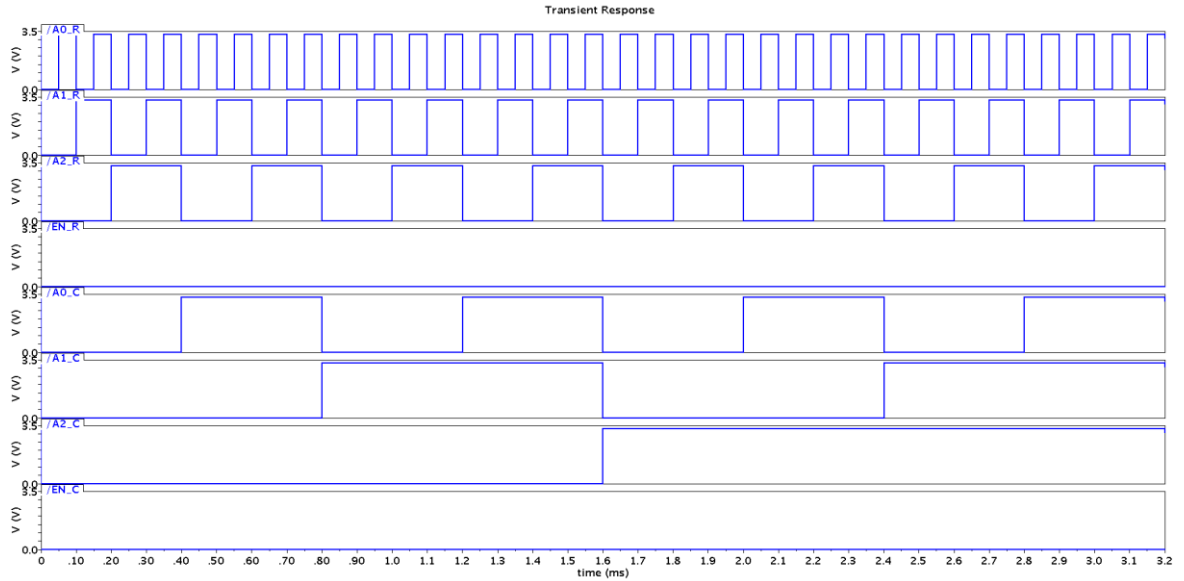


**Figure 4.27 - Row and column decoder signals.**

Figure 4.28 shows the simulation results from the 5 x 5 serial readout schematic. In this particular example, the microbolometers were simulated as ideal resistors ($R_{VOx}$). The bias current was 1.3 μA and the bias voltage was 0.3 V. The values of the resistors and respective output voltages are listed in Table 4.8. The output voltages were obtained using Equation 4.1 which was derived from the schematic in Figure 4.26.

$$V_{out} = I_{bias} * R_{VOx} + V_{bias} \qquad \textbf{4.1}$$

69

where $V_{out}$ is the amplifier's output voltage, $I_{bias}$ is the bias current from the DAC, $R_{VOx}$ is the microbolometer's resistance, and $V_{bias}$ is the amplifier's bias voltage connected to the non-inverting input. The simulation results were in agreement with the calculated values corresponding to the output voltage depending on the $R_{VOx}$.
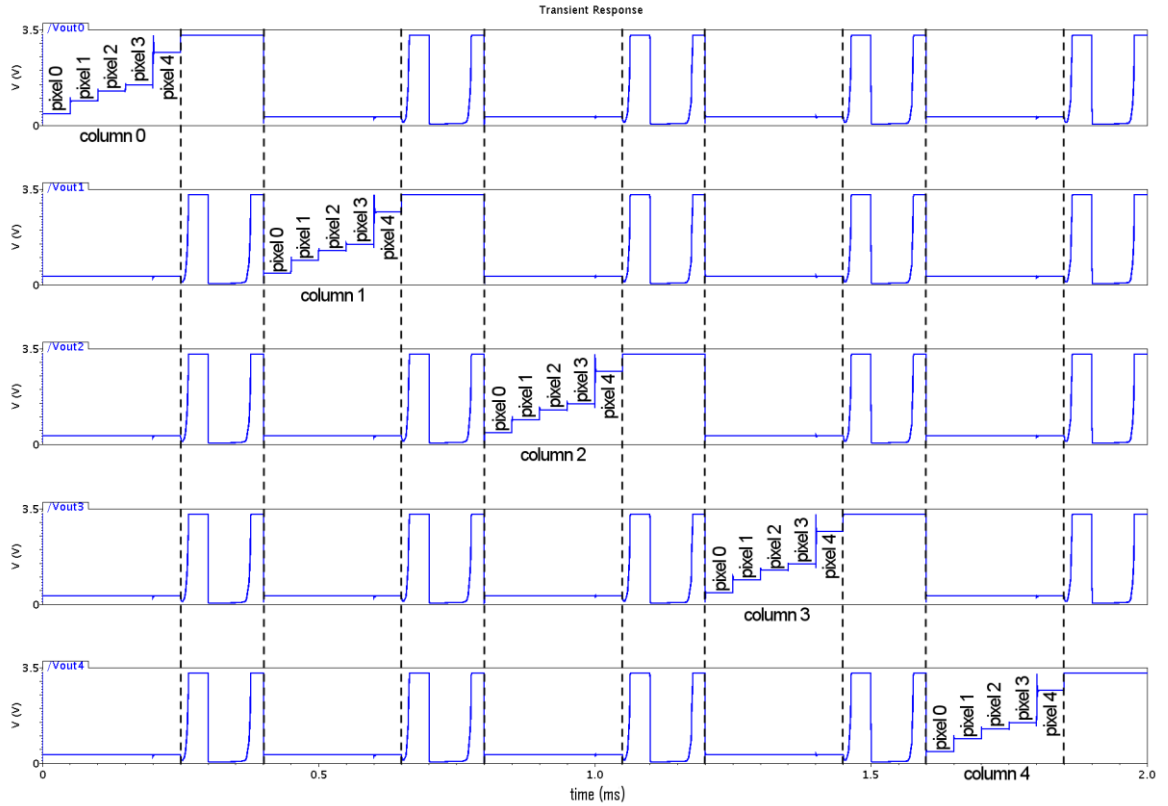


**Figure 4.28- FPA output signals from every pixel on the 5 x 5 array.**

| Resistance [Ω] | Pixel Output Voltage [V] |
|---|---|
| 100 k | 0.42 |
| 500 k | 0.89 |
| 800 k | 1.24 |
| 1 M | 1.48 |
| 2 M | 2.66 |

**Table 4.8 – Readout output voltages**

# 4.6 Chip B

Chip B was fabricated to characterise the absorption response using a Fourier Transform Infrared (FTIR) spectrometer. The pixel design on this chip was identical to Design 2 and 3 from Chip A containing 3 ERRs in M4, M5 and M6, a continuous ground plane in M3, insulating layers, no passivation, and VOx microbolometers. Due to the continuous ground plane on the MM array, there is no transmission therefore the reflection was simulated to calculate the MM absorption. The absorption response was 50% at 2.5 THz as previously shown in Figure 4.13 (green line). The FTIR spot diameter is 4 mm,

thus a sample area larger than the spot diameter was needed to measure the reflection at a 30° angle. Chip B had an array area of 5 x 5 mm$^2$ with six pixels routed to external pads. The total area of Chip B was 6731.92 μm x 6731.92 μm as shown in Figure 4.29.
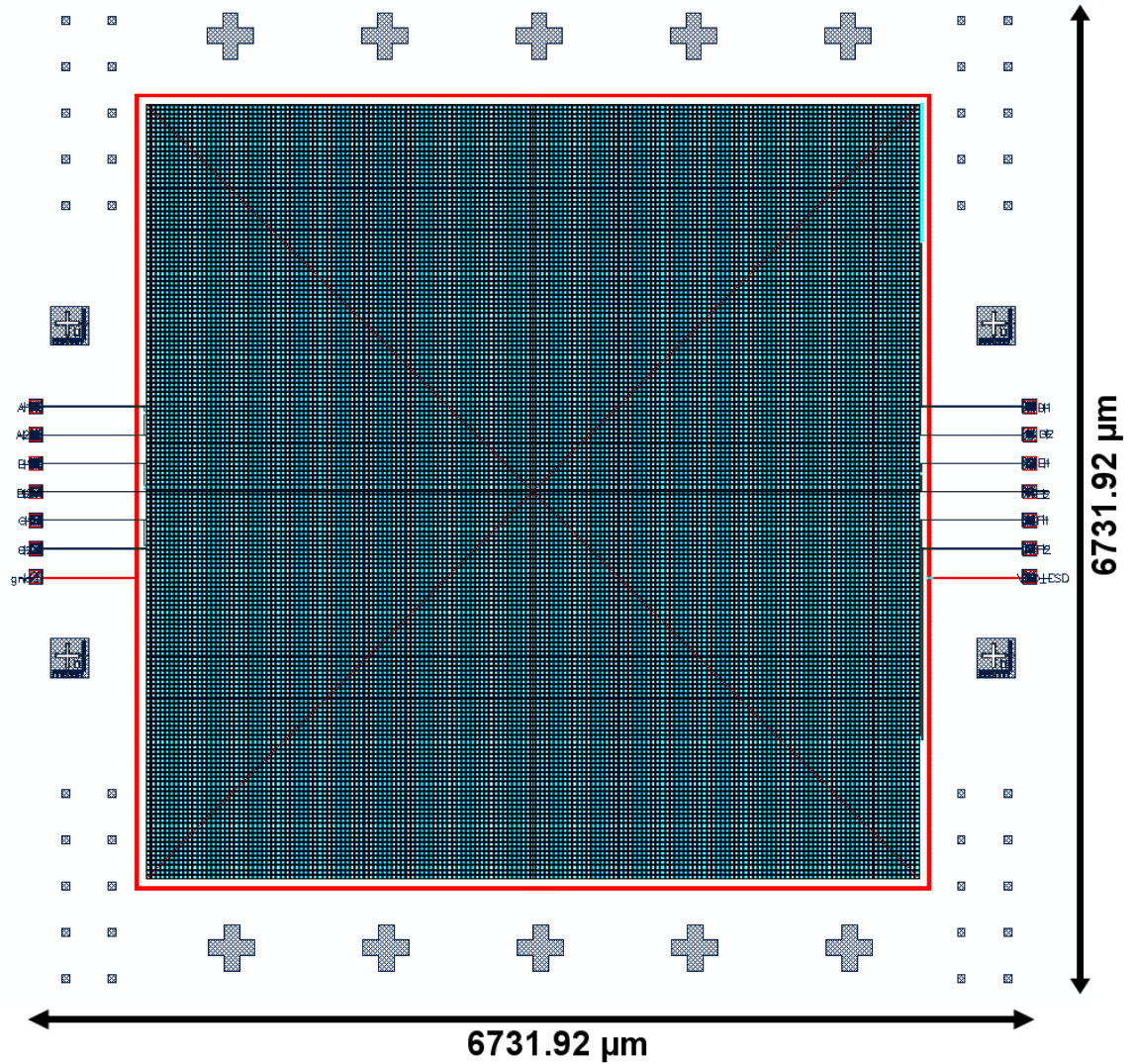


**Figure 4.29 - Chip B layout with a total area of 6731.92 μm x 6731.92 μm.**

## 4.7 Chip C

Chip C was composed of two arrays with broadband absorbers and different microbolometers. Figure 4.30 show the layout of Chip C with an area of 3112.90 μm x 5280.68 μm. The top design was a diode microbolometer array with six pixels routed to external pads. The bottom design was an 8 x 8 VOx microbolometer FPA with electrostatic discharge (ESD) protected pads. Originally, the CMOS9t5V kit did not contain a library with ESD protected pads, therefore Chip A and B had minimal ESD protection (only guard rings surrounding the electronics). It was from Chip C that the ESD pads were added only to the 8 x 8 FPA. The pixels on both arrays contain broadband absorbers identical to the ones in Chip A-Design 2 with 50% absorption at 2.5 THz.
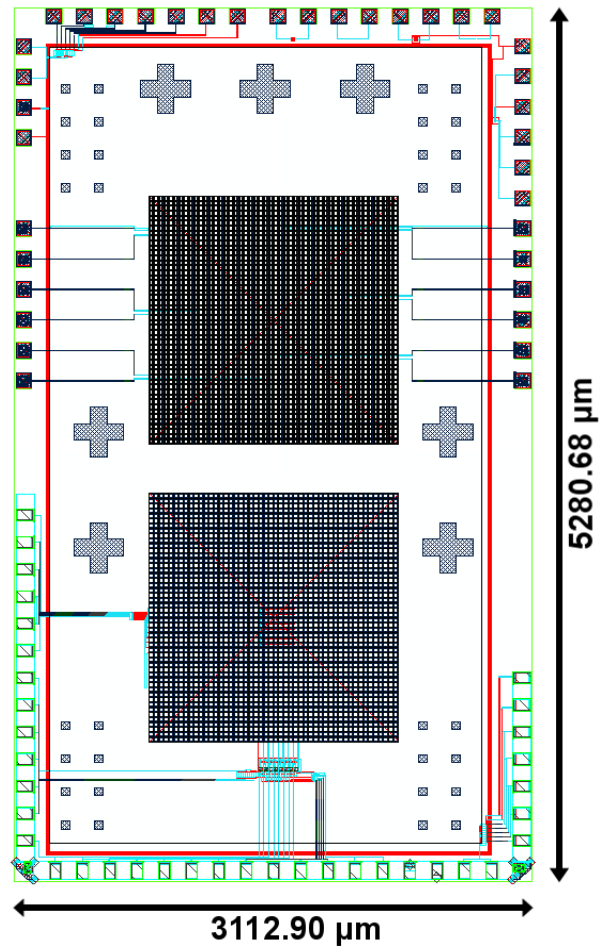
**Figure 4.30 – Layout of Chip C with a total area of 3112.90 μm x 5280.68 μm. The top array has 6 diode pixels routed to external pads for characterisation. The bottom array has an 8 x 8 VOx FPA with ESD pad ring.**

The 8 x 8 VOx FPA worked identically to the 5 x 5 FPA with serial readout electronics as explained in Section 4.5.5; hence the focus of this section will be on the diode array. The common use of silicon diodes in uncooled IR detectors led to the idea of designing terahertz sensors with the principle of using the integrated p-n diodes as microbolometers in combination with terahertz MM absorbers. Silicon diodes are ideal for imaging systems due to their temperature sensing characteristics and existing integration in the standard CMOS process. Diodes reside on the bottom layers of the CMOS process in contrast to the VOx microbolometers that are deposited on top of the MM absorbers. The use of p-n diode sensors was worth investigating due to simpler post-processing etching steps, better sensor uniformity, lower noise and reduced self-heating.

Ideal diodes have a forward voltage of 0.7 V and a TCV of -0.2 %/K resulting in a voltage change per degree of temperature of -2 mV/K. The sensitivity is low compared to VOx microbolometers but can be improved by adding diodes in series to increase the TCV. The simulated I-V characteristics for one diode and three diodes in series are shown in

Figure 4.31a-b respectively where the forward voltage for one diode was 0.7 V and for three diodes was approximately 2.0 V.
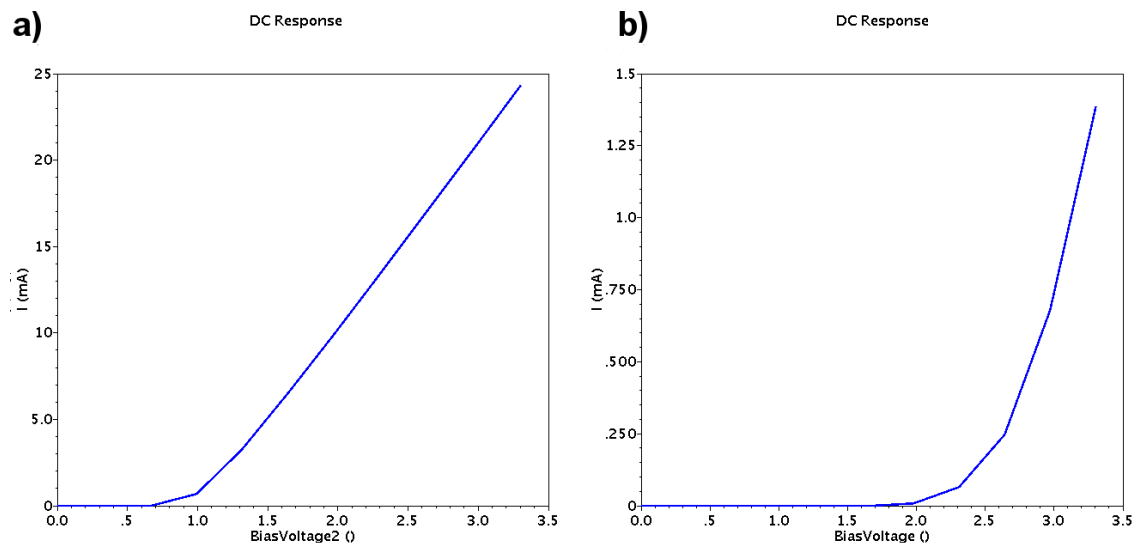


**Figure 4.31 – I-V characteristics of a) single diode and b) three diodes.**

In order to increase the sensitivity of the pixel, it was necessary to add more than one diode per pixel. The number of diodes per pixel was decided based on two constraints: pixel size and maximum power supply voltage. The maximum number of diodes able to fit in a 30 μm x 30 μm following the Design Rule Check (DRC) rules was three diodes in series where each diode measured 4.85 μm x 12.6 μm. Figure 4.32 shows the layout of a single pixel with three diodes covered by the continuous ground plane.
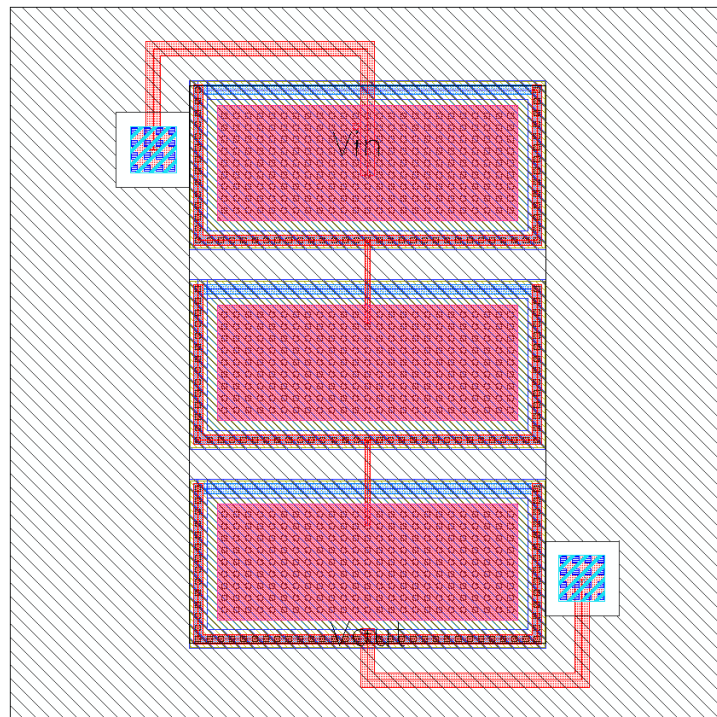


**Figure 4.32 - Chip C single pixel layout showing three diodes in series.**

The sensitivity was simulated by sweeping the temperature from 10°C to 70°C and measuring the diode voltage change at different bias currents (100 nA to 200 μA). Figure

4.33a-b show the diode simulation results where the sensitivity was calculated by measuring the slope as -2 mV/°C for one diode and -6 mV/°C for three diodes in series respectively. The circuit schematics are shown as insets of Figure 4.33a-b for one and three diodes respectively.
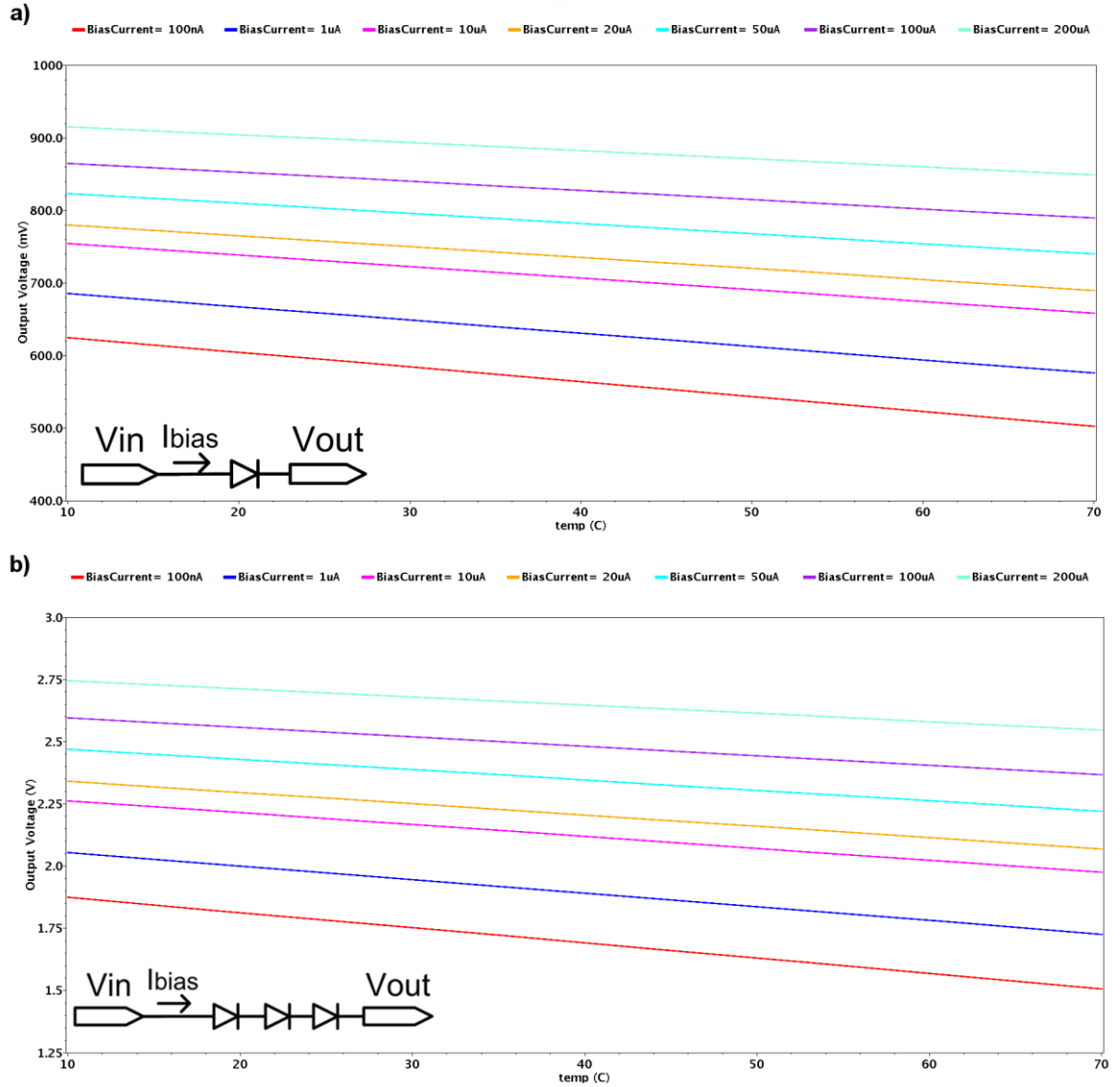


Figure 4.33 – a) Sensitivity of a single diode and b) three diodes.

# 4.8 Chip D

The advantage of scalable technology and the design of three previous chips with smaller arrays gave us the experience and confidence to create a FPA with a larger number of pixels. Chip D was designed to be a 64 x 64 pixel array with serial readout electronics and ESD protected pads. The design and readout architecture was identical to the 5 x 5 FPA resulting in one problem: readout speed. The serial readout of a 64 x 64 array reading at 50 μs per pixel would take 0.2 s per frame restricting the FPA to operate at video rate speed of at least 25 fps. Furthermore, Chip D needed 90 pads for testing the readout

electronics requiring additional equipment for the testing set-up. Therefore, Chip F was created to be a 64 x 64 array with parallel readout electronics architecture. The layout of Chip D is shown in Figure 4.34.
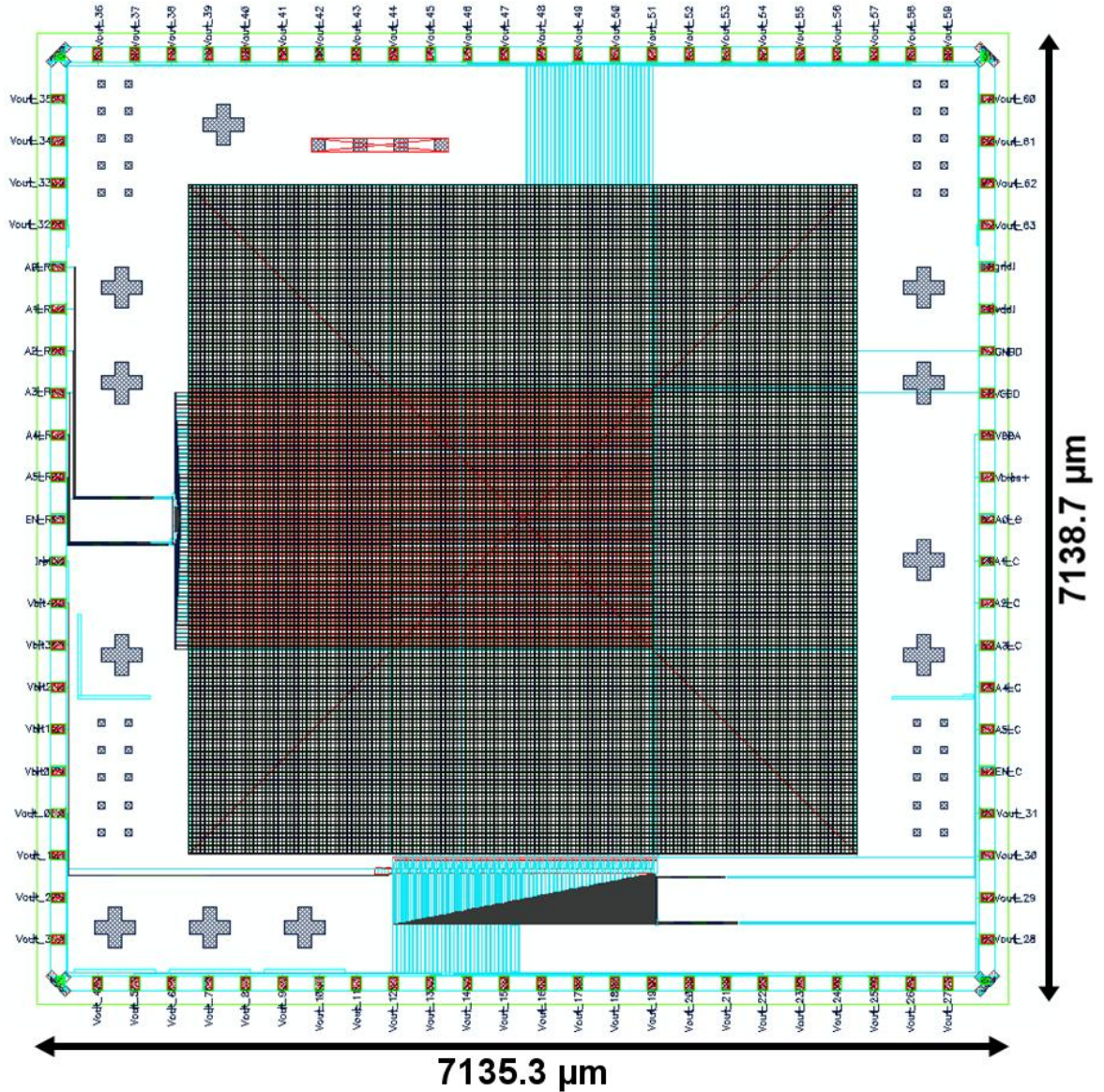


**Figure 4.34 - Chip D 64 x 64 focal plane array layout with a total area of 7135.5 µm x 7138.7 µm.**

# 4.9 Chip F

Chip F was designed as a 64 x 64 FPA with broadband terahertz absorbers containing two ERRs in M5 and M6, and the ground plane in M3. The layout of the pixels changed slightly from Chip A due to the post-processing steps required for pixel isolation where M4 was used as a sacrificial etching layer. The ERR in M4 was substituted by a metal square with an area of 26 µm x 26 µm. The post-processing was necessary to decrease the response time and reduce cross-talk. The post-processing steps will be explained in Chapter 5. The total size of the chip was 8027.33 µm x 8033.78 µm with the

array covering an area of 5920 µm x 5920 µm and each pixel being 40 µm x 40 µm as shown in Figure 4.35a-b respectively. The dimensions of the ERRs in M5 and M6 were identical to the Chip A Design 2 and their parameters are listed in Table 4.9.
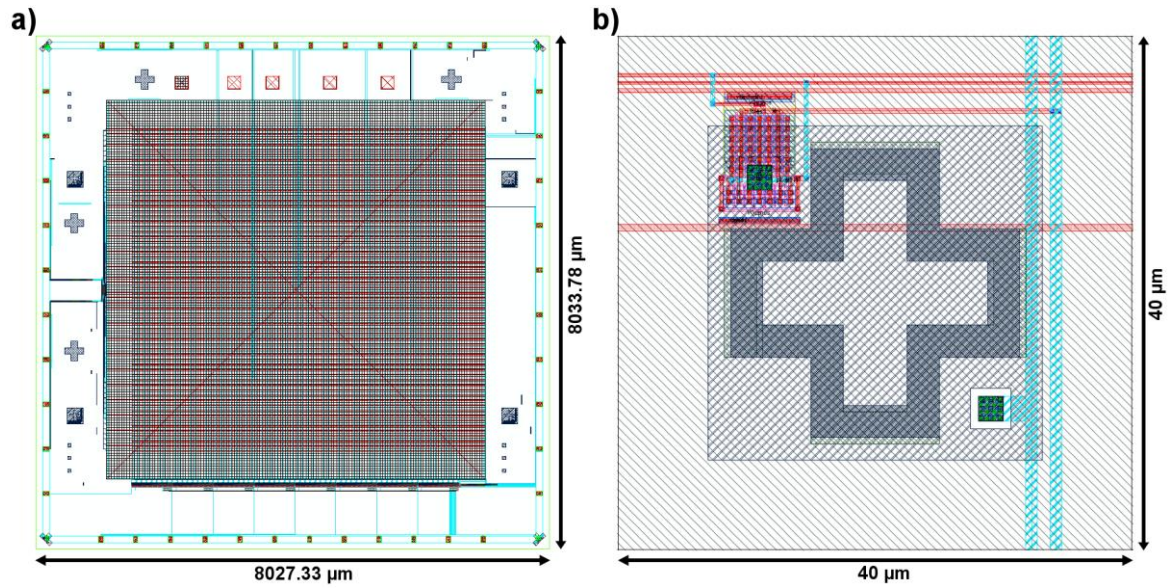


**Figure 4.35- a) Layout of Chip F with an area of 8027.33 µm x 8033.78 µm and b) single pixel layout with two ERRs in an area of 40 µm x 40 µm. The pixel shows the electronics routing to the transmission gate.**

| Parameter | M6 ERR | M5 ERR |
|-----------|--------|--------|
| K | 17.5 µm | 18.5 µm |
| L | 22.5 µm | 23.5 µm |
| N | 5.0 µm | 5.0 µm |
| W | 10.0 µm | 10.0 µm |

**Table 4.9 – Electric ring resonator parameters for Chip F**

The absorption characteristics of Chip F were simulated using Lumerical Inc. software. Based on previous simulation results, it was assumed that this design would absorb at 2.5 THz, but would only have two absorption peaks directly related to the two ERRs. The broadband pixels had an absorption magnitude of 97% at 2.5 THz and 93% at 2.8 THz as shown in Figure 4.36. The simulation showed the two peaks as expected, due to the use of two ERRs in the MM absorber.
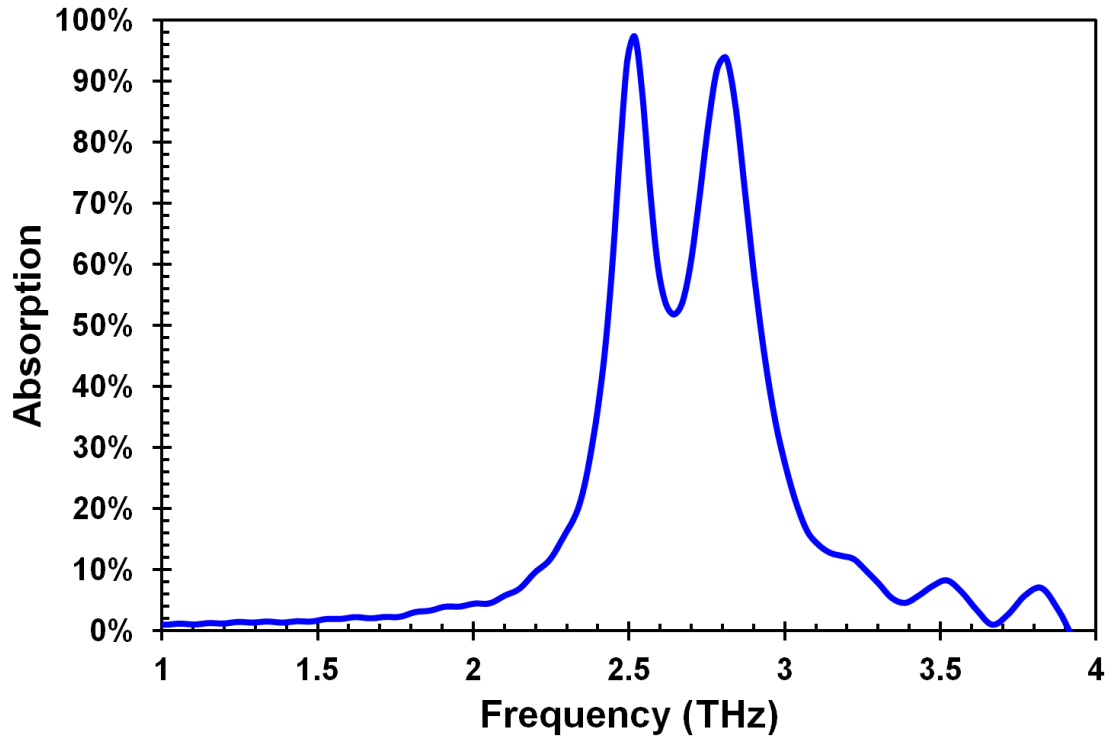
**Figure 4.36 - Chip F frequency absorption from two ERRs at 2.5 and 2.8 THz with 97% and 94% absorption. [Simulations done by Dr. James Grant].**

### 4.9.1  VOx 64 x 64 array Parallel Readout

The parallel readout architecture was based on the 5 x 5 array readout design. The parallel readout architecture has the major advantage of increasing readout speed. The array was designed using the same electronic components from the 5 x 5 array including the 5-bit DAC, 3 to 8 decoder, and amplifiers. In order to select 64 rows a 6 to 64 bit decoder with EN function was used. This decoder was built using nine 3 to 8 decoders where eight decoders give 64 outputs. In order to enable the eight decoders, eight EN functions were needed. These EN functions were obtained from the ninth 3 to 8 decoder. Each one of the 3 to 8 decoders shared the external 3 LSBs (A0, A1, and A2) except the main one, which was controlled by the external 3 MSBs (A3, A4, and A5). This single decoder controlled the EN functions of the 8 decoders allowing for the proper selection of 64 rows. The schematic of the 6 to 64 decoder is shown in Figure 4.37.
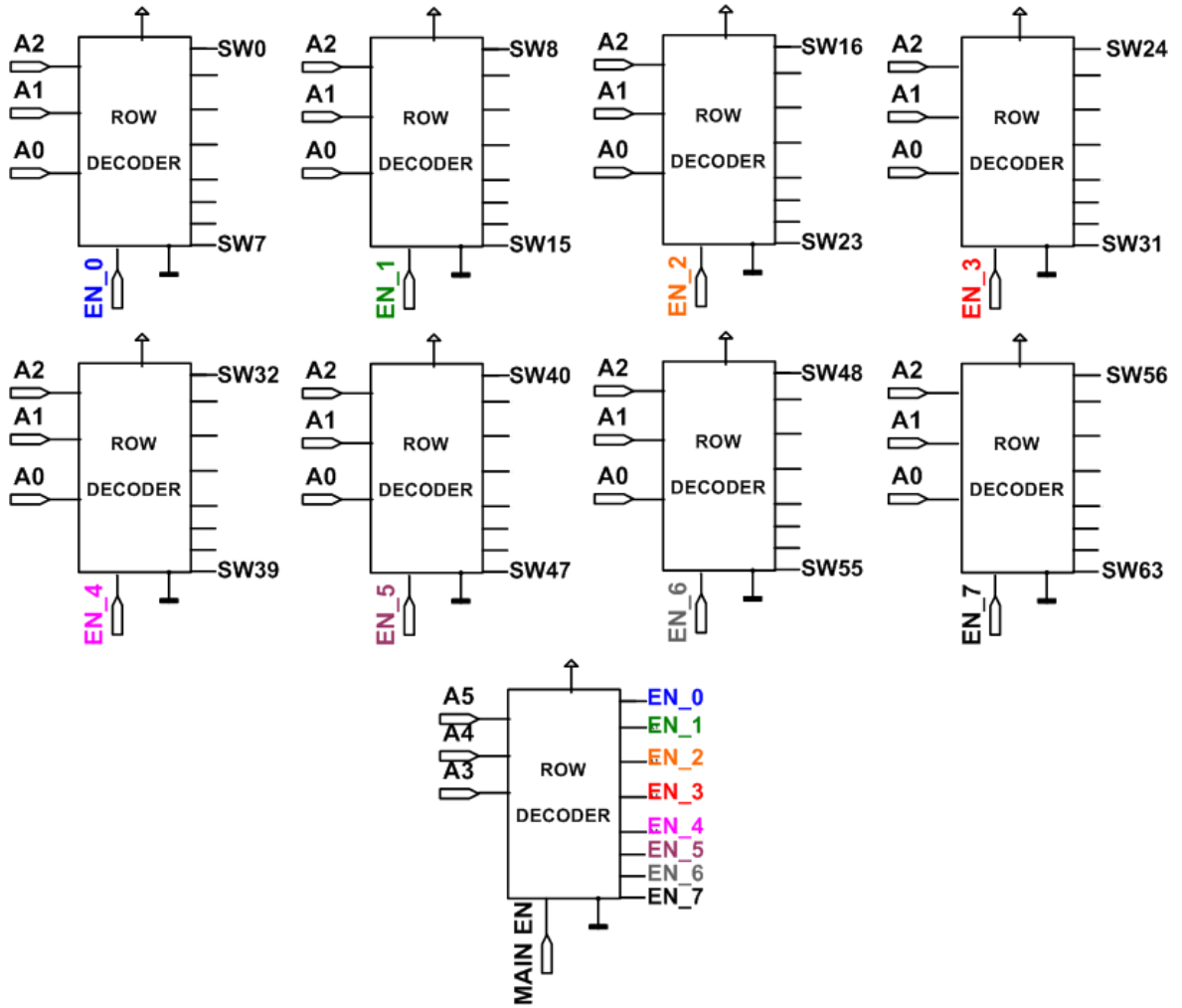
**Figure 4.37 - Schematic of 6 to 64 decoder created with nine 3 to 8 decoders.**

The parallel readout process starts with properly biasing the VOx microbolometers using the 5-bit current DAC. The external bias current selected depends on the resistance value of the microbolometer. It is necessary to check the output voltages are within the maximum voltage rails of the OTA. After the current has been binary weighted with the external 5 bits of the digital input word, the readout process begins by selecting eight columns at the same time and one row of each one of those columns. This means that instead of having only one current DAC, the array has eight current DACs that bias eight columns at the same time. Therefore, the reading time is reduced by 8 times compared to the serial readout architecture. Each one of the 64 columns has an OTA connected in a transimpedance feedback configuration to the microbolometer. As the current biases the microbolometer, the amplifier reads a voltage between 0.3 V and 3.0 V depending on its microbolometer's resistance value. In order to read the 8 columns simultaneously, each output from the OTA is connected to a switch and to one of the eight output amplifiers used as buffers. Lastly, all the voltages are read out to create a voltage map. The single pixel readout schematic is shown in Figure 4.38.

The simulation results from the VOx 64 x 64 array with parallel readout architecture are shown in Figure 4.39. The simulation shows the simultaneous reading of 8 output channels labelled as VOUT0 to VOUT7. Each pixel was readout at 25 µs resulting in 12.8 ms per frame and 320 ms for 25 frames.
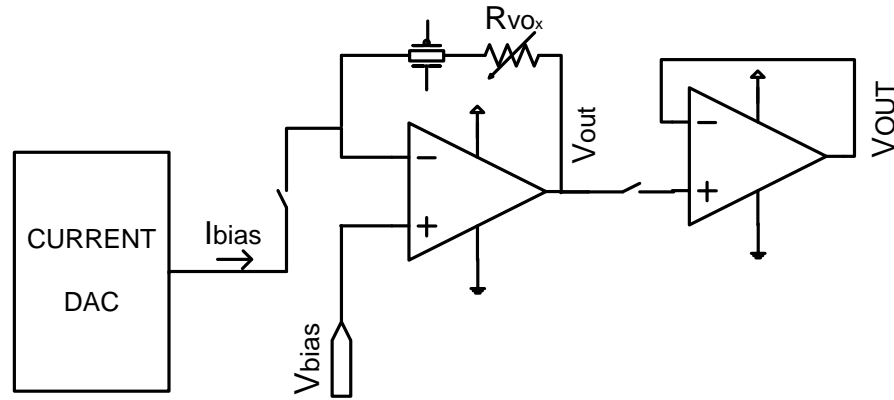


**Figure 4.38 - Single pixel schematic of the VOx 64 x 64 focal plane array.**
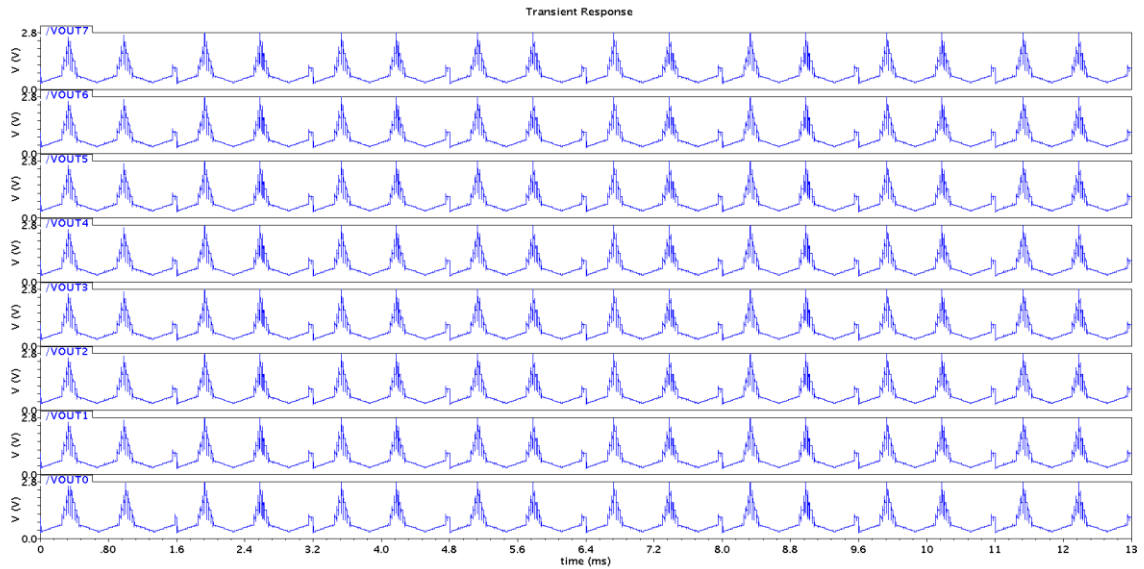


**Figure 4.39 – Schematic simulations from 64 x 64 focal plane array with parallel readout architecture, each graph shows simultaneous reading of 8 columns (VOUT0 to VOUT7).**

For this simulation the DAC was externally biased with a 24 µA constant current source and the bit word was 00100. The output current measured from the DAC was 368 nA. Each pixel was simulated with a different resistance value to measure the respective output voltages and to prove that the amplifier reads a different voltage output depending on the resistance. In this case, the resistances are ideal, but once the VOx microbolometers are added to the CMOS chip, the resistance will change only -2 %/K to -3 %/K when exposed to the laser. Figure 4.40 shows the output of only one column and 64 rows where the output voltages change from 0.33 to 2.14 V depending on the resistance values of 100 kΩ to 5 MΩ. The output voltages were also calculated using Equation 4.1

and the results are listed in Table 4.10. The calculated values properly match the simulation results.
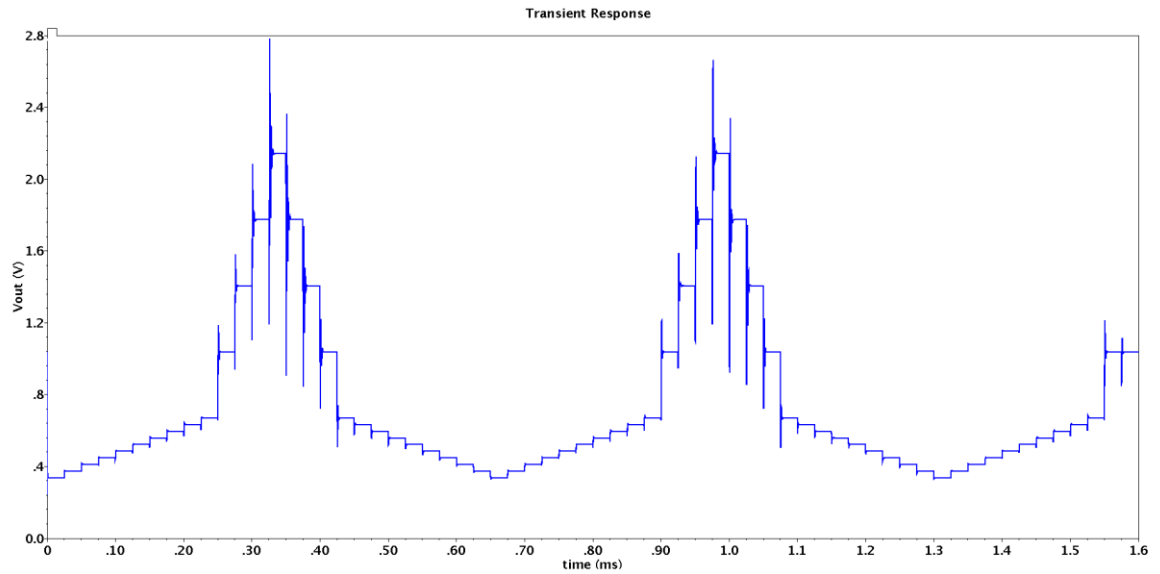


**Figure 4.40 – Readout simulation for 1 column and 64 rows with resistance values from 100 kΩ to 5 MΩ. The output voltage changes depending on the resistance value.**

| Resistance [Ω] | Pixel Output Voltage [mV] |
|---|---|
| 100 k | 0.3376 |
| 200 k | 0.3743 |
| 300 k | 0.4112 |
| 400 k | 0.4479 |
| 500 k | 0.4848 |
| 600 k | 0.5217 |
| 700 k | 0.5585 |
| 800 k | 0.5954 |
| 900 k | 0.6322 |
| 1 M | 0.6691 |
| 2 M | 1.0375 |
| 3 M | 1.4059 |
| 4 M | 1.7743 |
| 5 M | 2.1424 |

**Table 4.10 - Calculated output voltages from different resistance values**

# 4.10 Chip G

Chip G was composed of a 64 x 64 array with p-n diode microbolometers and single band terahertz absorbers. The layout of Chip G had a total area of 8033.78 μm x 7377.74 μm with the array covering an area of 5920 μm x 5920 μm and each pixel being 40 μm x 40 μm as shown in Figure 4.41a-b respectively. Due to post-processing requirements, the layout of the pixel looks different to the previous designs and only contains one ERR. The reason being that the diodes exist underneath all the metal layers, therefore deep etching of the inter-metal dielectric and metal layers was required to isolate

the pixels. Additionally, etching of the underlying silicon is required to create thinner pixel membranes. The rest of the metal layers are used as a mask to protect the ERR. Additionally, having a continuous ground plane is no longer possible due to etching through the entire CMOS stack to isolate the pixels. The layout of the pixel shows the surroundings of the pixels covered by metals which are used to protect the routing metals (M1 and M2) and to create the supporting arms of the pixel membrane. The pixel is composed of one ERR in M5, with the dimensions listed in Table 4.11, to create a resonance at 2.5 THz. The M6 on top of the ERR is used as a mask to protect the ERR during the etching process with M3 used as ground plane. Both metals are square shape with areas of 26 μm x 26 μm each. The pixel layout also shows one diode measuring 4.85 μm x 12.6 μm and one transmission gate used for row selection in the readout process.
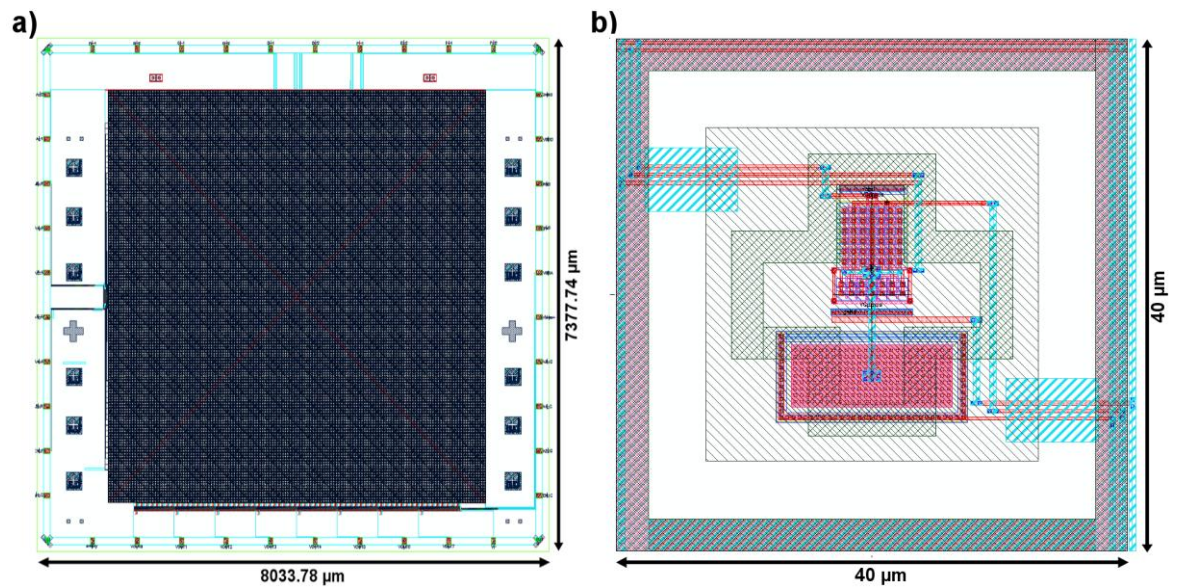


**Figure 4.41 - a) Layout of Chip G with an area of 8033.78 μm x 7377.74 μm and b) single pixel layout with one ERRs in an area of 40 μm x 40 μm.**

| Parameter | M5 ERR |
| :---: | :---: |
| K | 17.0 μm |
| L | 22.0 μm |
| N | 5.0 μm |
| W | 10.0 μm |

**Table 4.11 – Electric ring resonator parameters for Chip G**

The MM structure was simulated using FDTD with Lumerical Inc. software as discussed in Section 4.1. Figure 4.42 shows the simulation results from a single ERR in M5, it has an absorption of 76% at 2.5 THz. Compared to the rest of the broadband MM absorber arrays, the single layer MM absorber has a narrowband absorption peak.
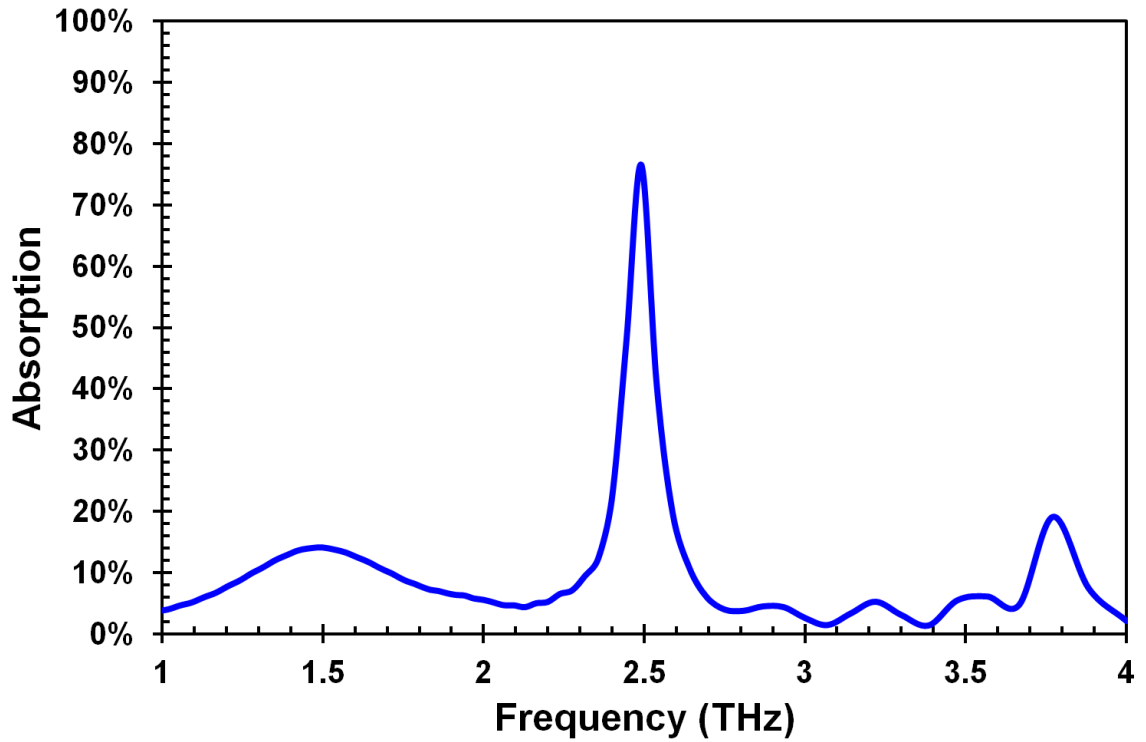
**Figure 4.42 – Simulation results from Chip G showing absorption of 76% at 2.5 THz. [Simulations done by Dr. James Grant].**

## 4.10.1 Diode 64 x 64 array with Parallel Readout

The readout schematic was designed using the same electronic components as the VOx arrays. In this array, a current DAC was not used to bias the pixel; instead an external voltage source connected to an active resistor was used for biasing. This was done due to time constraints when submitting Chips F and G to the final fabrication run. Figure 4.43 shows the schematic of a single pixel readout. The parallel readout follows the same procedure as described in Section 4.9.1.
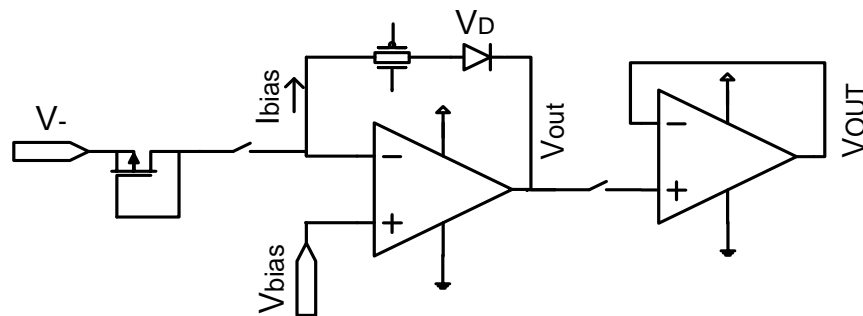


**Figure 4.43 – Single pixel readout schematic for the 64 x 64 diode array.**

An example of the simulation results from the p-n diode array is shown in Figure 4.44. For this simulation the pixels were biased at 50 μA by setting the external voltage supply (*V-*) to 3.3V and *Vbias* to 1.7 V. The simulation results show an average TCV of ─1.4 mV/°C in a temperature range of 10°C to 70°C.
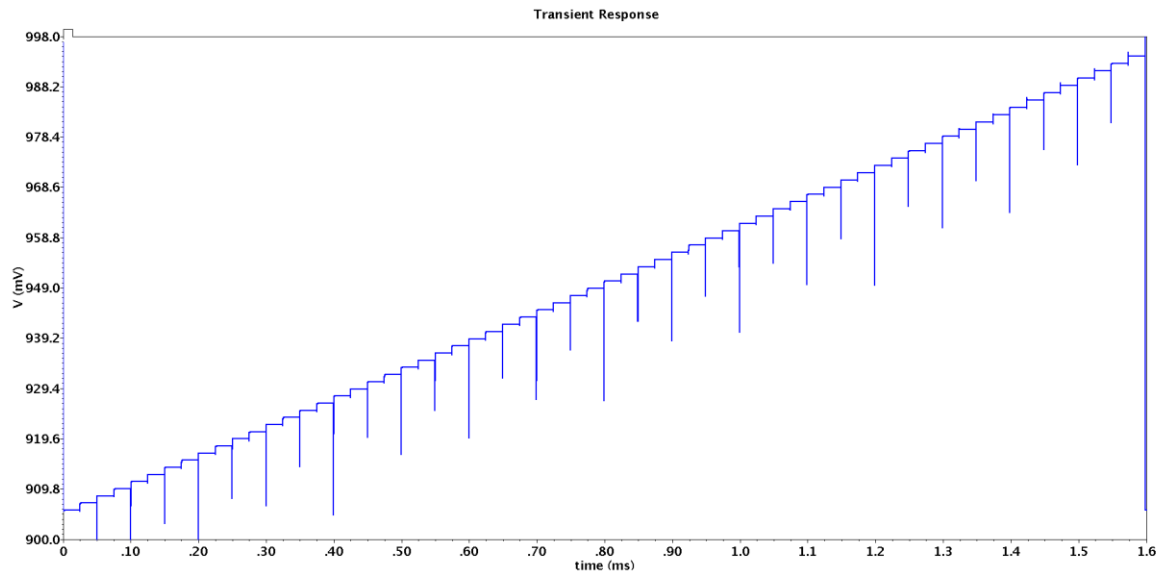
**Figure 4.44 – Simulation results for one column and 64 rows showing the increase of voltage per degree of temperature.**

# 4.11 Summary

The design of terahertz MM absorbers, microbolometers and readout electronics was thoroughly described in this chapter. The simulation results for ERRs proved the concept of obtaining single and broadband spectral responses depending on the number of stacked resonators. The MMs can be manipulated to absorb at the required frequency by changing the shape of the resonator. The simulation results were used to integrate MM structures and microbolometers to obtain terahertz sensors sensitive to temperature. The capability of MM structures to be integrated into the CMOS process presented a major advantage towards the creation of low-cost terahertz FPAs. Once the MMs were integrated in the CMOS process, the FPAs were created using serial and parallel readout electronic architectures. Two microbolometer materials were investigated: VOx and silicon p-n diode. Both of them were used to build different FPAs namely: VOx 5 x 5 array, VOx 64 x 64 array with serial readout, VOx and p-n diode 64 x 64 array with parallel readout electronics. Both sensors are capable of producing images at video rate speed, although the VOx is more sensitive to temperature compared to the p-n diode sensor, but the p-n diode already exists in the CMOS process. It was worth investigating both options because they have distinct and unique advantages towards the creation of terahertz FPAs.

# Chapter 5 Focal Plane Array Experimental Characterisation

This chapter will describe the FPA experimental characterisation techniques and detail the results obtained from the fabricated chips. The experimental results will be compared to the simulation results presented in the previous chapter including important FOMs such as $Rv$, TCR, TCV, NEP, and $\tau$. The fabricated chips were packaged and post-processed by Dr. James Grant. The post-processing steps were needed to add the resistive microbolometers and to create membranes in the FPAs. VOx microbolometers were patterned on top of the MM absorbers and three membrane thicknesses were investigated for Chip A, B, and F. For Chip C and G, p-n diode microbolometers were characterised with three membrane thicknesses. The experimental results from the post-processed chips will be presented in the following sections starting from the characterisation of single circuit blocks, absorption characteristics of the MM arrays, single VOx and p-n diode pixels, 5 x 5 VOx FPA, and 64 x 64 FPAs. The MM based terahertz FPA with VOx microbolometers was employed in both a transmission and reflection mode imaging experiment to demonstrate its imaging capabilities using the CW FIR gas laser operating at 2.5 THz.

## 5.1 CMOS Characterisation

The first CMOS chips received from the foundry were Chip A. This chip contained five arrays with three different MM designs, three 5 x 5 FPAs, individual pixels routed to output pads and single circuit blocks needed for characterisation purposes. The individual electronics circuits did not require post-processing procedures in order to be evaluated; therefore each circuit was tested to verify proper functioning of the readout electronics. The individual circuits in Chip A were a 3 to 5 decoder, 5-bit current DAC and OTA. Custom designed hi-resolution printed circuit boards (PCBs) made in the School of Engineering workshop were used to test every circuit. The PCBs were designed using Easily Applicable Graphical Layout Editor (EAGLE) software and were made from thin layers of copper foil (1 oz) laminated to both sides of an FR4 (flame retardant) glass epoxy

panel. After the post-processing of the CMOS chips was complete, the FPAs were characterised. The experimental results obtained from Chip A will be explained in the following sections.

## 5.1.1 Packaging

Fifty dies were fabricated in the foundry and the ones ready to be tested were packaged in Ceramic Pin Grid Array (CPGA) packages from the company Spectrum, Semiconductor Materials, Inc. The 100 CPGA through-hole mount package has a ceramic substrate for enhanced thermal heat dissipation and a cavity of 11 mm x 11 mm. It contains 100 gold-plated pins, with a 2.54 mm pitch, brazed in a matrix pattern to the bottom of the ceramic substrate. Figure 5.1a and b show the top and bottom view of the 100 CPGA package respectively. The bottom right corner of Figure 5.1b shows an extra pin which is used for orientation guidance when placing the package into a socket. After the chips were glued into the 100 CPGA package, they were bonded following the specifically designed bonding diagrams. The bonding was done using the Hesse and Knipps 710 ultrasonic wire bonder located in the School of Physics and Astronomy at the University of Glasgow.
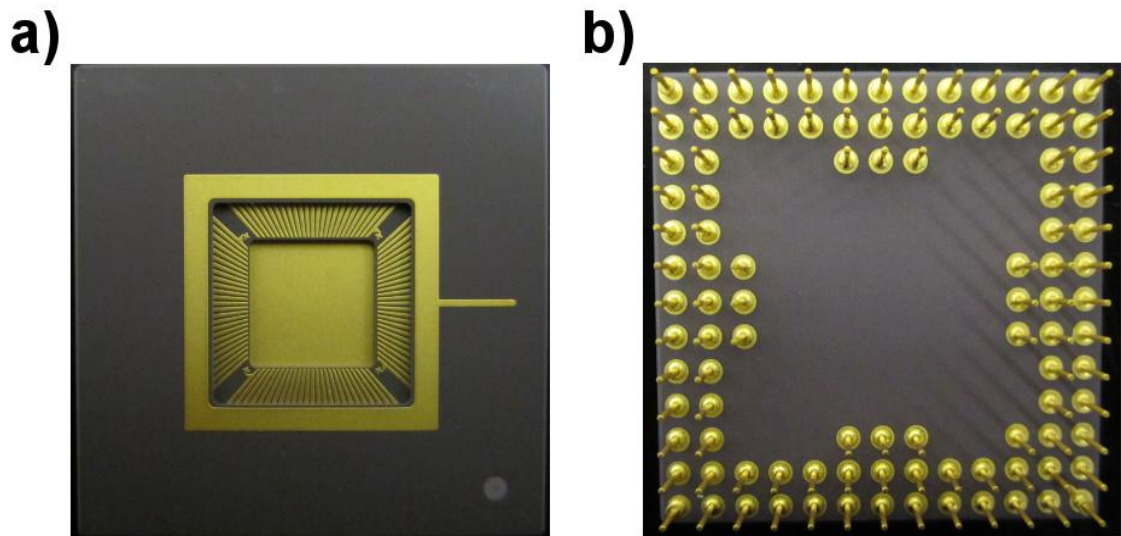


**Figure 5.1 - 100 CPGA package a) top view showing the 11 x 11 mm$^2$ cavity and b) bottom view showing the pin grid array in the ceramic substrate and the extra pin in the right corner used for orientation.**

## 5.1.2 3 to 5 bit Decoder

The 3 to 5 bit decoder was tested using a simple test set-up consisting of a DC voltage source used to bias all the input bits (EN, A2, A1, and A0) to 3.3 V (high) or 0 V (low). Sliding switches were used to manually select the digital input word and an oscilloscope was used to measure the output voltages or digital output word (Y0 to Y4).

Figure 5.2a shows the PCB used for testing which corresponds to the schematic shown on Figure 5.2b. The 3 to 5 decoder was designed as a 3 to 8 decoder, but only five outputs were enabled. When EN is low, the 3-bit input word decodes the corresponding output. When EN is high, none of the outputs are decoded. The DC experimental results shown in Table 5.1 demonstrate that the input word 0000, which corresponds to the decimal number 0, enables the first output $Y0 = 0$ V while maintaining the other outputs in a high state. The decimal input 1 enables the second output, $Y1$, and the process continues to sequentially select the corresponding output.
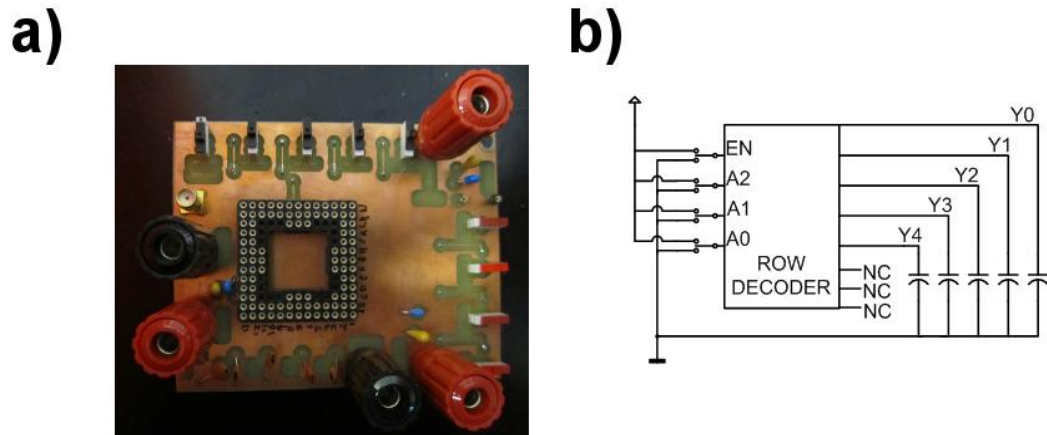


**Figure 5.2 – a) PCB fabricated to test the decoder and b) PCB equivalent schematic.**

| Inputs [V] | | | | | Outputs [V] | | | | |
|---|---|---|---|---|---|---|---|---|---|
| **Decimal** | **EN** | **A2** | **A1** | **A0** | **Y0** | **Y1** | **Y2** | **Y3** | **Y4** |
| 0 | 0 | 0 | 0 | 0 | **0.003** | 3.3 | 3.3 | 3.3 | 3.3 |
| 1 | 0 | 0 | 0 | 3.3 | 3.3 | **0.004** | 3.3 | 3.3 | 3.3 |
| 2 | 0 | 0 | 3.3 | 0 | 3.3 | 3.3 | **0.003** | 3.3 | 3.3 |
| 3 | 0 | 0 | 3.3 | 3.3 | 3.3 | 3.3 | 3.3 | **0.003** | 3.3 |
| 4 | 0 | 3.3 | 0 | 0 | 3.3 | 3.3 | 3.3 | 3.3 | **0.004** |

**Table 5.1 - DC experimental results for a 3 to 5 bit Decoder**

## 5.1.3 Operational Amplifier

The amplifier was composed of a differential input stage (V+ and V-) and single-ended output stage ($V_{out}$). The PCB was designed to verify the DC and AC performance of the amplifier. The PCB contains the configurations shown in Figure 5.3a, b, and c which correspond to unity gain test, offset-voltage test, and inverting configuration with a set gain respectively. The PCB is shown in Figure 5.3d and contains the test benches mentioned previously which can be formed by using jumper sockets to form the desired configurations. The external bias voltages are applied using banana connectors.

The unity gain or buffer configuration was tested in the closed-loop gain configuration shown in Figure 5.3a where $V$- is connected to $V_{out}$ in a feedback loop and it follows the input voltage $V+$. The test set-up consisted in sweeping $V+$ from 0 V to 3.3 V and $V_{out}$ was measured using a voltmeter. Figure 5.4a shows the simulation results compared to the experimental results where $V$- is equal to $V_{out}$ and $V+$ for the voltage range of 0.2 V to 3.1 V.

The input offset voltage was measured following the configuration in Figure 5.3b where $V+$ was set to 1.65 V and $V$- was swept from 1.64 to 1.67 V with 1 mV increments. This test measures the voltage difference between the inputs, $V+$ and $V$-, to set the output voltage to the same potential, in this case 1.65 V. The simulation results compared to the experimental results are shown in Figure 5.4b. The simulation results are ideal, therefore at 1.65 V the input voltages are equal to the output voltage. In the experimental results there is a 0.23 μV offset voltage amplified by the open loop gain to 6 mV. This small voltage can be compensated by injecting an offset voltage into the non-inverting input to match both inputs. The input offset voltage is small enough to measure the minimum voltage expected of 0.3 V in the experiments.

The inverting configuration is shown in Figure 5.3c where the closed loop gain was measured with external feedback resistors ($R1$ and $R2$). The gain for this configuration is dependent on the value of the resistors by the relationship: $V_{out}/V_{in} = -R2/R1$. The input common-mode signal was set to 1.65 V and the AC signal was set to 200 mV$_{p-p}$. The gain was set to 10 V/V by setting R1 to 1 kΩ and R2 to 10 kΩ. The frequency was swept from 10 Hz to 20 MHz. The experimental results are shown in Figure 5.4c where the gain stays constant until 400 kHz, then it stops amplifying showing a bandwidth (BW) of 18 MHz which compare well to the simulation results showing a BW of 19.6 MHz. Figure 5.4d shows an oscilloscope image displaying a gain of 10 V/V at 100 KHz.
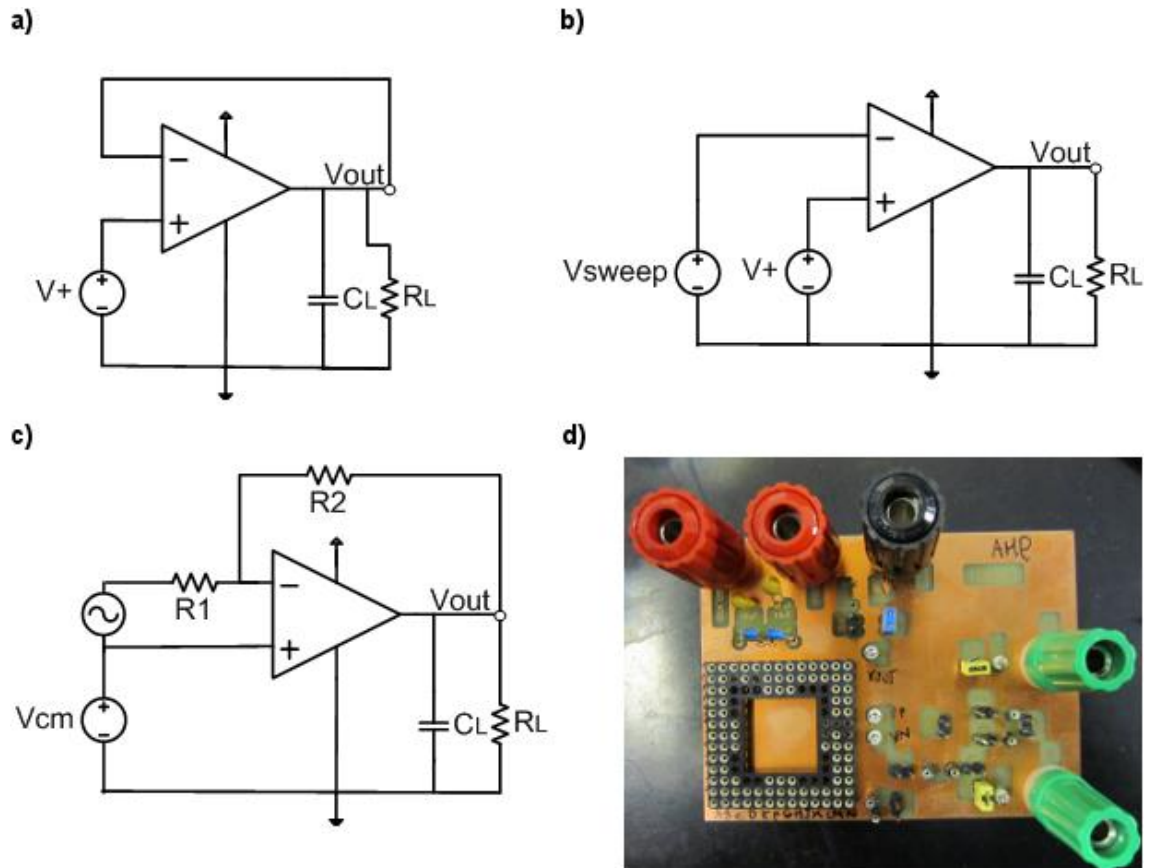
**Figure 5.3 - Equivalent schematics to test a) unity gain, b) offset-voltage, c) inverting configuration with a set gain, and d) printed circuit board used for testing the amplifier.**
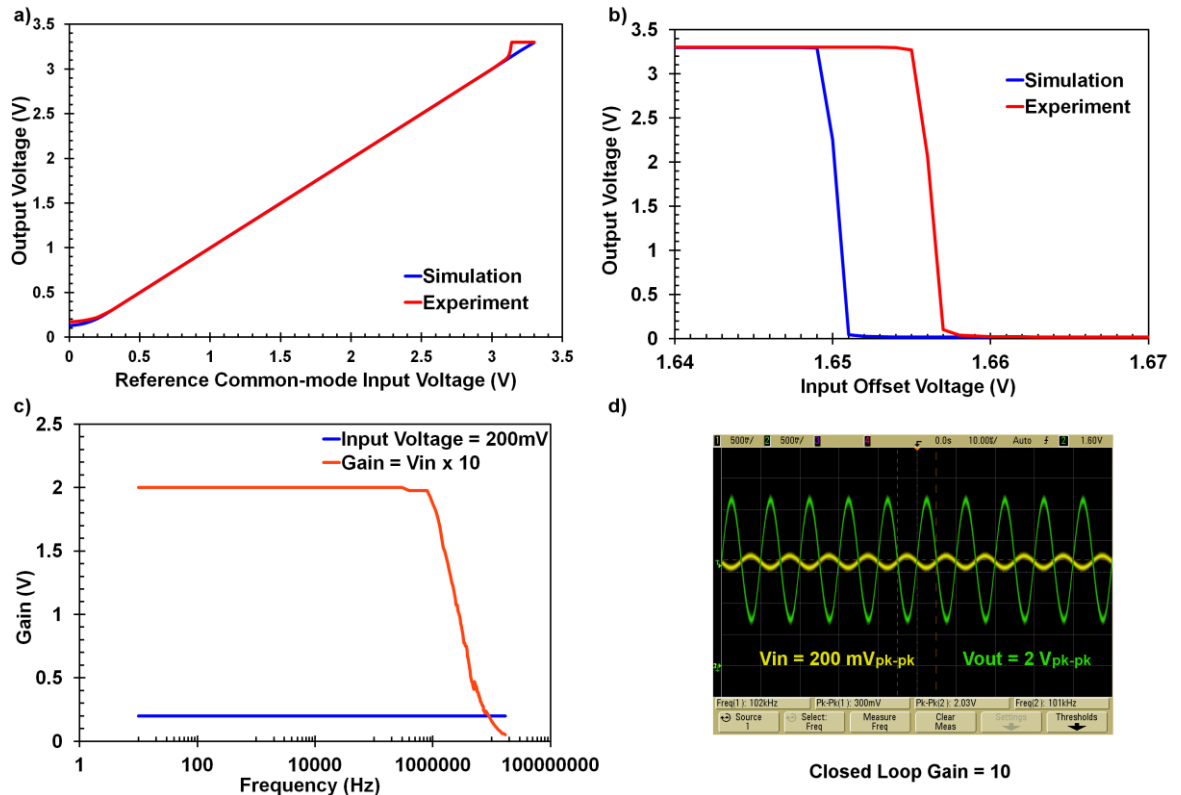


**Figure 5.4 – Operational amplifier simulation results compared to experimental results. a) Unity gain, b) input offset voltage, c) inverting configuration with a gain of 10 V/V in response to frequency and d) oscilloscope image showing a gain of 10 V/V at 100 kHz.**

### 5.1.4 5-bit Current Digital-to-Analogue Converter

The 5-bit current DAC was tested using the PCB shown in Figure 5.5a which represents the schematic shown on Figure 5.5b. The DAC had five input voltages ($V_{bit\_0}$ to $V_{bit\_4}$), one external current source ($I_{source}$), and one output voltage ($V_{out}$). The test set-up consisted of a DC voltage source used to bias $V_{bit\_0}$ to $V_{bit\_4}$ and $V_{bias}$. Sliding switches were used to manually select the five input bits to 3.3 V or 0 V and a voltmeter was used to measure $V_{out}$. $V_{bias}$ was used as a reference voltage and a load resistor ($R_L$) connected in series with $V_{out}$ and $V_{bias}$ was used to measure the output current. The current was calculated using Equation 5.1.

$$I_{out} = \frac{V_{out} - V_{bias}}{R_L} \qquad \textbf{5.1}$$

where $V_{out}$ is the voltage from the DAC output, $V_{bias}$ is the external bias voltage, and $R_L$ is an ideal load resistor.
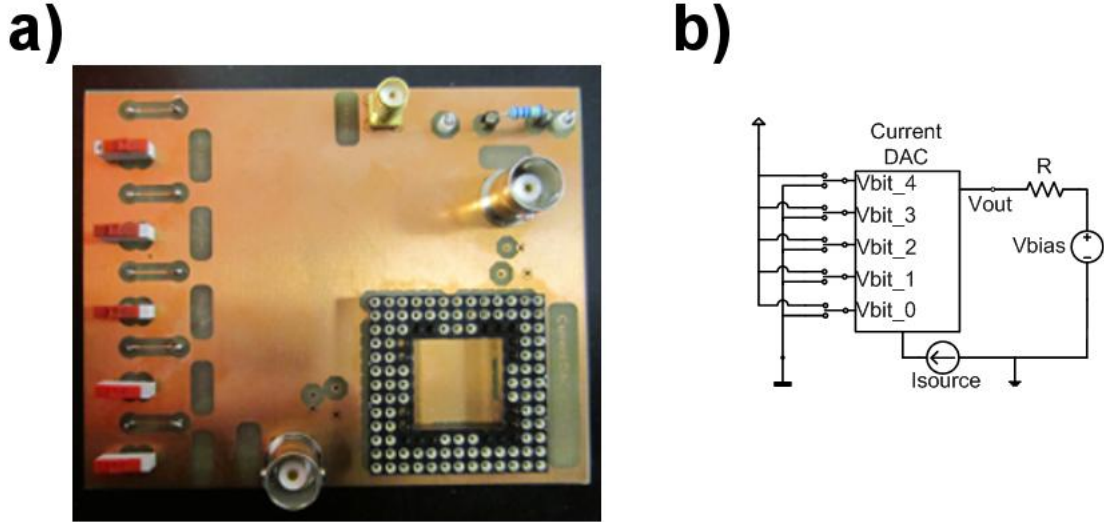


**Figure 5.5 - Schematic to test the 5-bit current DAC.**

The test set-up followed the simulation parameters from Section 4.5.3 where $I_{source}$ was set to 3.2 µA, $V_{bias}$ was 3.3 V, and the load $R$ was 1 MΩ. The simulation results (blue symbols) were compared to the experimental results (red symbols) shown in Figure 5.6. The proportional increase in current dependent on the input binary code is observed in both graphs, although the experimental results show a larger output current than expected. This is probably due to leakage current or layout mismatch introduced in the transistors. The 5-bit current DAC provided a current from 330 nA to 2.89 µA, if a smaller current than the minimum is needed, $I_{source}$ can be set to a lower bias current.
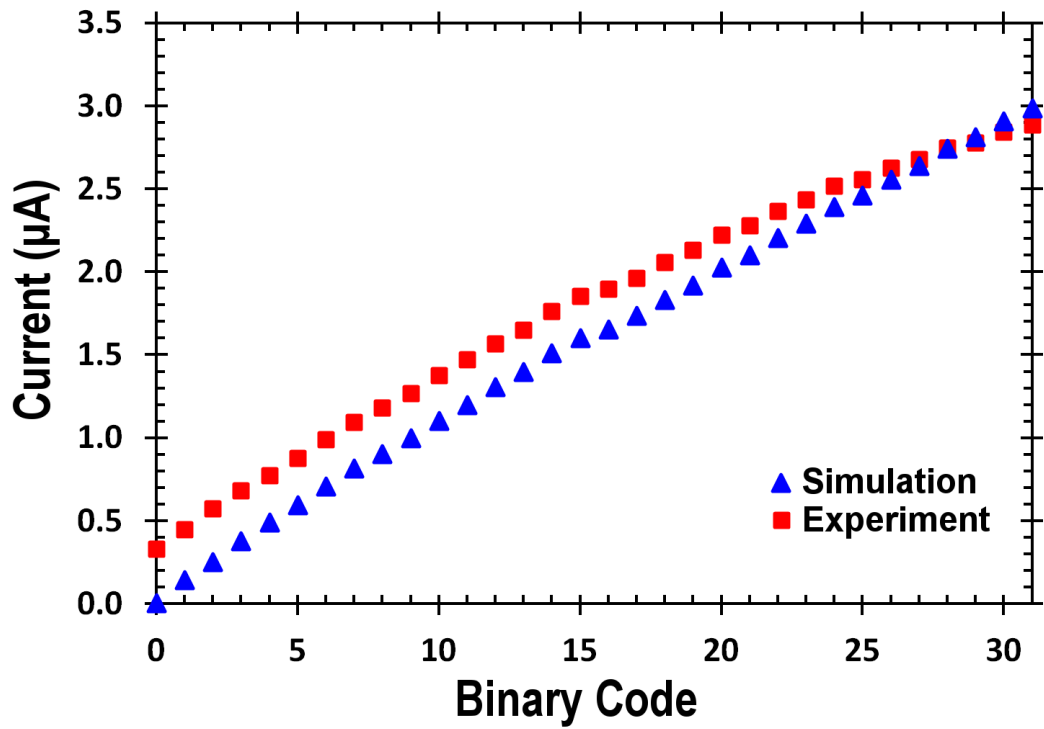
**Figure 5.6 - 5-bit Current DAC simulation results (blue symbols) compared to experimental results (red symbols) showing a proportional amount of current dependent to the binary input code.**

### 5.1.5 Spectral Response

It was imperative that the MM absorber structure designed for chip A absorb at 2.5 THz, the output frequency of the source used to evaluate the detector responsivity. To evaluate the absorption spectrum characteristics a Bruker IFS 66v/S FTIR spectrometer was used. However, it was found that the minimum usable spot size of the spectrometer was 4 mm diameter and since the size of each array on Chip A was 1.5 x 1.5 mm it was not possible to obtain an accurate measurement of the spectral response. Therefore it was necessary to fabricate a second CMOS chip, Chip B, which had an array size of 5 mm x 5 mm. Chip B was composed of a ground plane in M3 and a broadband MM absorber with three ERRs in M4, M5, and M6. Chip B was characterised under vacuum in the FTIR spectrometer in transmission mode at normal incidence and in reflection mode at 30° incidence. The set-up consisted of an Hg source, 6 μm multi-layer Mylar beamsplitter and DLaTGS pyroelectric detector. The measured transmission spectra were normalised with respect to the signal measured from a 4 mm diameter open aperture and the reflection spectra were normalised to that of a gold mirror. The experimental and simulation absorption spectra were calculated using Equation 3.18. The reflection is the only factor limiting absorption as explained in Section 4.1 due to the ground plane being thicker than the typical skin depth in the terahertz regime.

Figure 5.7 shows the comparison between the simulation (blue line) and experimental (red line) absorption spectra. The experimental results of the stacked ERRs have two broad absorption peaks at 2.78 THz and 2.5 THz with an absorption magnitude of 71.4 % and 56.4 % respectively. These results confirm that the MM structure fabricated in the CMOS chips absorbs at the required frequency of 2.5 THz. The MM absorber simulation and experimental results differ due to the assumed values in simulation of the inter-metal dielectric refractive index and potential thickness non-uniformity of the three inter-metal dielectric layers.
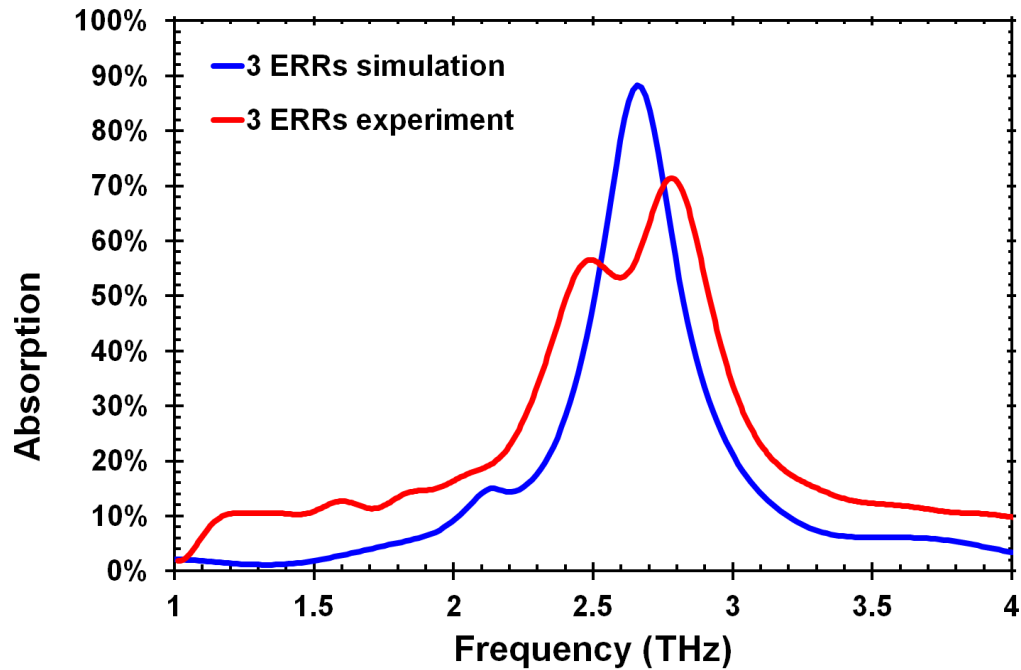


**Figure 5.7 – Chip B absorption spectra simulated results (blue line) compared to experimental results (red line) showing two absorption peaks at 2.78 THz and 2.5 THz with an absorption magnitude of 71.4 % and 56.4 % respectively. [Simulation and measurement done by Dr. James Grant].**

# 5.2 VO$_x$ Microbolometer Post-processing Steps

The post-processing steps of the CMOS chips differed for the VOx sensor and the p-n diode sensor. In this section the four post-processing lithographic steps performed after receiving the CMOS chips from the foundry that were to be functionalised with VOx microbolometers will be explained. These steps were necessary to add the VOx microbolometers to the MM array and to create thin pixel membranes in the FPA. On receiving the chips from the foundry the approximately 2 µm thick silicon oxynitride passivation layer had been removed over the array. This was to facilitate easy access to the M6 studs and enable connection to the VOx microbolometers. The 4 key post processing steps performed and developed by Dr. James Grant were:

1. Deposition of an insulator: a 100 nm spacer layer of $Si_3N_4$ was deposited to separate the MM structure from the microbolometer.

2. Definition and deposition of VOx sensor: the microbolometer pattern was defined in a bi-layer of Polymethyl Methacrylate (PMMA) and a 200 nm thick VOx layer deposited by reactive sputtering under the conditions of: 500 W RF power, 10 μbar pressure, 95%/5% $Ar/O_2$ partial pressure and for 2 hours. After deposition, the VOx film was annealed in an Ar environment at 300ºC for 30 minutes in order to reduce the sensor resistance.

3. Definition of the connecting tracks from the M6 studs to the microbolometers: the second lithographic step involved defining a PMMA mask and etching the 100 nm thick $Si_3N_4$ above the bond pads and M6 studs using a reactive ion etch chemistry of $CHF_3/Ar$. A bi-layer of PMMA and lift-off procedure was subsequently used to deposit the 20 nm Ti/ 1000 nm Al connecting tracks between the VOx sensor element and the M6 studs.

4. Etching of silicon underneath the microbolometer to leave a membrane structure: the CMOS chip was back etched down to the pre-metal dielectric layer using an ICP Si dry etch process. A 14 μm thick layer of AZ4562 was used as the photomask. For the thicker membrane samples the CMOS chip was back etched leaving silicon and dielectric underneath the chip to maintain the readout electronics

Figure 5.8a shows an optical micrograph of a section of the unprocessed chip as received from the foundry. Figure 5.8b shows an optical micrograph of the post-processed chip with the M6 ERR layer and the VOx microbolometer sensor connected to the M6 studs using Ti/Al tracks. The tracks connect the microbolometer to the electronics placed in the bottom two layers of the CMOS process. Figure 5.8c shows a Scanning Electron Micrograph (SEM) picture of a section of the post-processed chip. Figure 5.8d shows an SEM picture of the cross-section of one pixel showing the VOx microbolometers, Ti/Al tracks and metal layers. The cross-section was done using a Focused Ion Beam (FIB) tool.
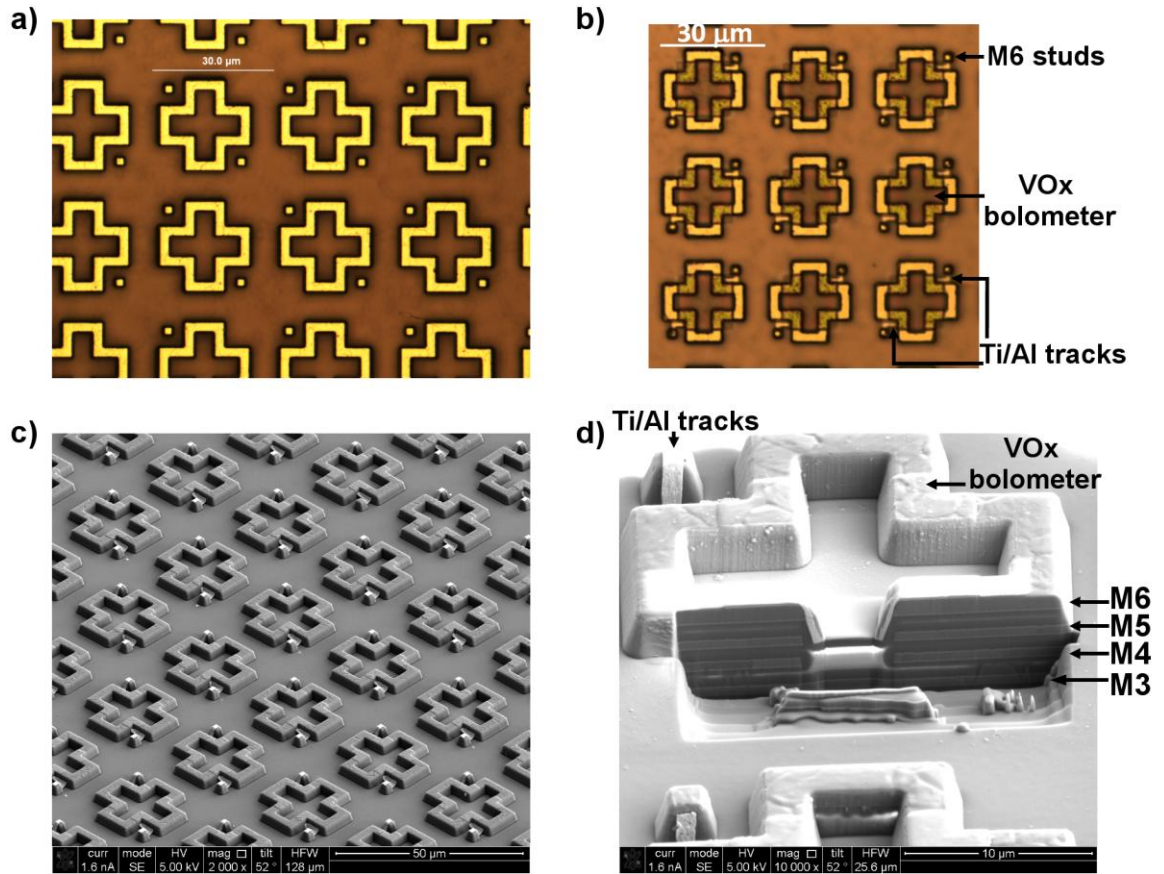
**Figure 5.8 – a) Chip A as received from the foundry showing the ERR and vias in M6. b) Post-processed chip with VOx microbolometers and Ti/Al tracks. c) SEM picture of post-processed chip and d) SEM picture showing the pixel's cross-section. [Pictures taken by Dr. James Grant].**

# 5.3 Terahertz Laser

Terahertz detectors are characterised with terahertz sources such as gas or optically pumped lasers. These are the most conventional sources for CW imaging due to their high output power in the range of 1 mW to 150 mW. Optical pumped lasers consist of a terahertz laser cell, containing a low pressure molecular gas, which is pumped by a grating tuned $CO_2$ laser. The output frequency is determined by the gas pumped into the cavity having several discrete emission lines [1]. The operational characteristics of these terahertz sources were described in Section 2.3.4.

The terahertz source used for the characterisation of our terahertz detector was bought from the company Edinburgh Instruments. The laser is a $CO_2$ pumped $CH_3OH$ (methanol) vapour laser operating at 2.5 THz. The laser mechanism works as follows: first, the $CO_2$ mid-infrared laser produces a laser beam of 40 W at a wavelength frequency of 10.6 μm. Second, the IR laser beam is transformed into a terahertz laser beam by directing it through pressured methanol. The resulting terahertz laser has a maximum output power

of 150 mW when using the emission line 9P36 that corresponds to a wavelength of 118.8 μm. Figure 5.9 shows a picture of the terahertz laser, the $CO_2$ laser is on the left and the methanol is introduced in the cavity from the laser on the right.
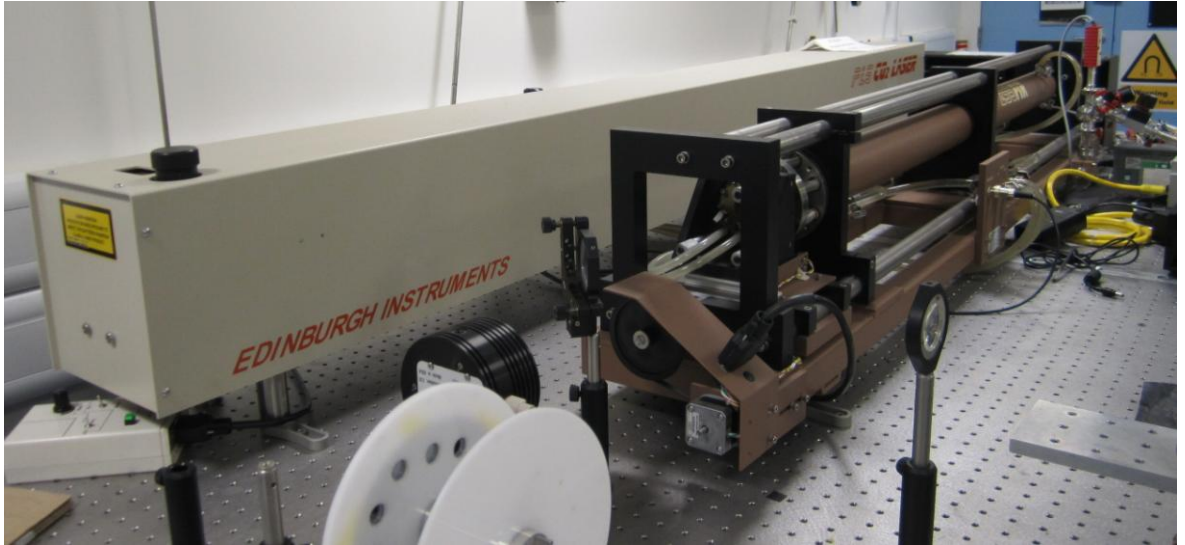


**Figure 5.9 - Terahertz laser composed of a $CO_2$ laser (left) and the methanol is introduced in the cavity from the laser on the right.**

The laser beam spot size was measured at the focus point using a commercial IR camera (Photon 320) from FLIR Inc. The Photon camera is an uncooled microbolometer sensor array with 324 x 256 pixels and each pixel is 38 x 38 $\mu m^2$. The spot size was measured using the software Image J by inputting the total size of the array as a reference and then measuring the spot diameter. The focused beam shown in Figure 5.10 had a diameter of approximately 1.8 mm and therefore an area of 2.83 $mm^2$.
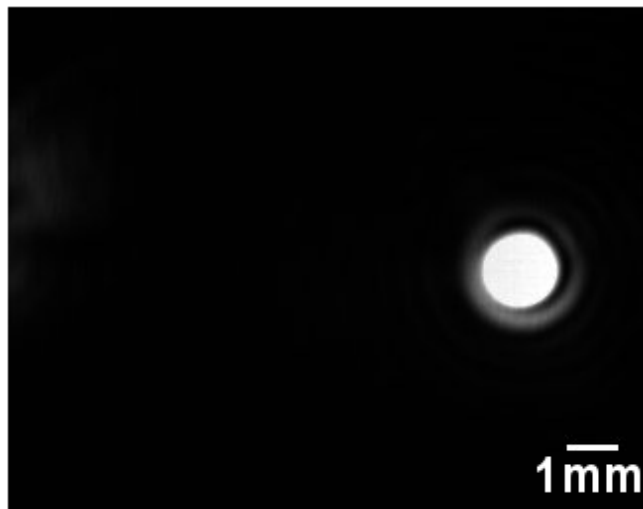


**Figure 5.10 – Focused terahertz laser beam spot showing a 1.8 mm diameter captured using a commercial infrared focal plane array (Photon 320).**

# 5.4 Experimental Characterisation of VOx Microbolometers

Electrical and optical tests were performed to experimentally characterise the terahertz FPA. The performance was determined by measuring the figures of merit explained in Chapter 3 including $R_v$, TCR, NEP, and $\tau$. The first experiments were done in Chip A due to the confirmed absorption at 2.5 THz. Single pixels with VOx microbolometers were tested from Chip A-Design 3 as well as the VOx 5 x 5 FPA from Chip A-Design 2.

## 5.4.1 Responsivity

The resistance and responsivity of the post-processed pixels from Chip A with their respective VOx microbolometers were measured using a Parameter Analyser (Keithley 4200-SCS). The parameter analyser was used for I-V characterisation and 4 point probe measurements. The parameter analyser has 4 high precision Source Measure Unit (SMU) used for sourcing voltage or current and simultaneously measuring voltage or current as required. The resistance and responsivity of single pixels were measured using the PCB shown in Figure 5.11a. Its respective equivalent circuit is shown in Figure 5.11b. The PCB has six double dip switches to select one of the six pixels and four Bayonet Neill–Concelman (BNC) connectors on each side to connect to the SMUs. The PCB has access to three pixels on the left side and three on the right side, therefore eight BNC coaxial connectors were needed in total. The resistance of the six pixels routed to external pads was measured by applying a ground reference and sweeping a bias voltage from 0 to 6 V. The current was simultaneously read and the average resistance was measured as 41 MΩ with a variation of 30%.

The pixel's DC response, in terms of V/W, from the single pixels in Chip A-Design 3 was measured at different bias currents ranging from 10 to 600 nA. The responsivity was calculated using Equation 3.6 where the differential voltage was obtained when the laser was on and off. According to the same equation, it is expected that the responsivity increases as the current increases and as the thermal capacitance of each pixel is reduced. Therefore, the underlying silicon underneath the pixels was etched in three samples to create membranes of differing thickness. Four samples from Chip A were tested: Chip A7 was left unetched i.e. 300 µm of silicon and 8 µm inter-metal dielectric remaining, Chip

A8 had a 58 μm thick membrane, Chip A9 had a 34 μm thick membrane and Chip A10 had a 8 μm thick membrane. Table 5.2 summarises the characteristics of each sample.
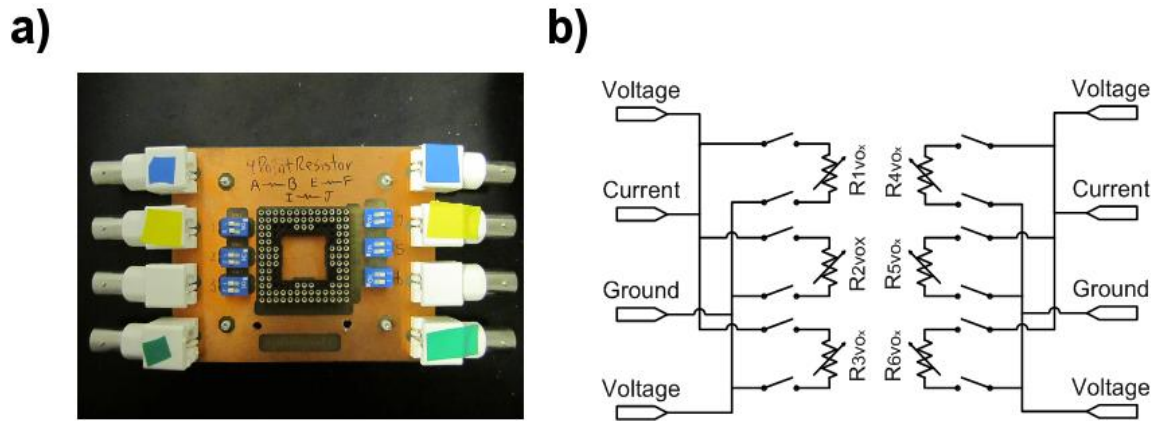


**Figure 5.11 – a) PCB used for testing single VOx pixels and b) its equivalent circuit.**

| Chip A samples | Membrane characteristics |
|---|---|
| A7 unetched | 300 μm silicon + 8 μm dielectric |
| A8 etched | 50 μm silicon + 8 μm dielectric |
| A9 etched | 26 μm silicon + 8 μm dielectric |
| A10 etched | 0 μm silicon + 8 μm dielectric |

**Table 5.2 - Chip A samples description**

The responsivity was experimentally characterised by measuring the area of the laser beam and incident power at the array. The incident power at the FPA was measured by a Scientech AC2500 power meter at the focus point. Once the power per $\mu m^2$ was determined, the incident power at a single 30 μm x 30 μm pixel was calculated as 26 μW per pixel. The terahertz beam was directed by a mirror onto a Tsurpurica lens of 11 cm focal length and 50% transmission that focused the beam onto the FPA. The FPA was placed at the focus point and mounted in an x-y-z motorised translation stage. The detector was current biased using the Keithley 4200-SCS and the transient voltage was measured simultaneously while the terahertz beam was on and off ($V_{ON/OFF} = V_{ON} - V_{OFF}$). The voltage difference was measured and the responsivity was calculated. Figure 5.12 shows the experimental set up for the characterisation of DC responsivity.
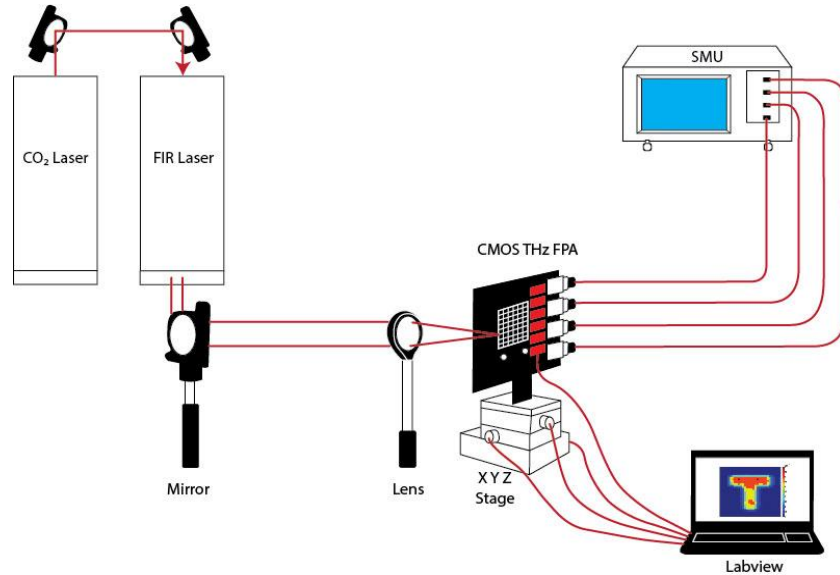
**Figure 5.12 - Experimental set up for the characterisation of DC responsivity.**

Figure 5.13 shows the DC responsivity of the four Chip A samples at different bias currents. The graph shows the lowest responsivity from Chip A7 as expected (green line) owing to having the thickest membrane. The largest responsivity of 32.65 kV/W was attained with a bias current of 600 nA for Chip A10 (blue line). However, it should be noted that for Chip A10 there is no silicon remaining, therefore, there is no means to address the pixels when employed in a FPA. Chip A9 (red line) shows a large responsivity of 21.98 kV/W with a bias current of 600 nA. This chip has 26 μm of silicon remaining making it possible to address the 5 x 5 array.
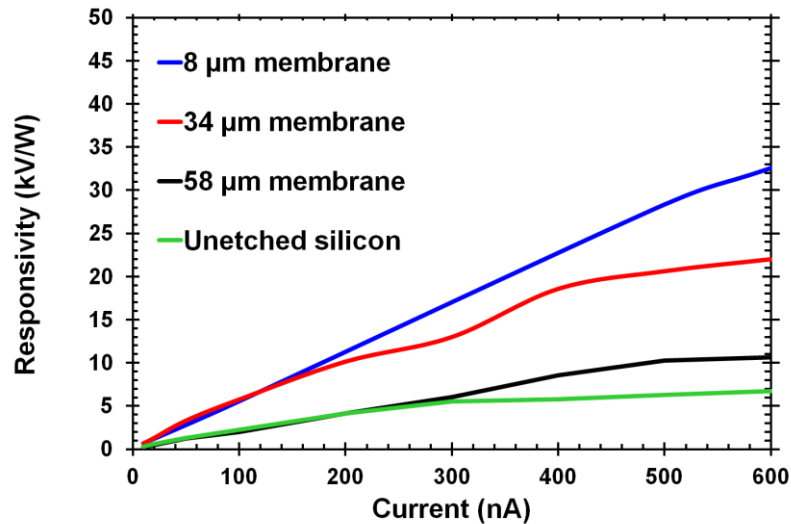


**Figure 5.13 - Responsivity comparison at DC for an unetched pixel (green line) and three etched pixels: 8 μm (blue line), 34 μm (red line), and 58 μm (black line) membrane thickness.**

## 5.4.2  Responsivity as a Function of Modulation Frequency

The measurement was repeated in order to characterise the responsivity as a function of frequency. An optical chopper (Thor Labs) used to modulate the terahertz beam

at a fixed frequency was introduced into the terahertz beam path in front of the focusing lens as shown in Figure 5.14. The microbolometers were current biased to 100 nA using the 5-bit DAC and the $V_{ON/OFF}$ signal detected from the readout electronics was measured by a lock-in amplifier (EG&G Model 5210) synchronised to the beam chopper.
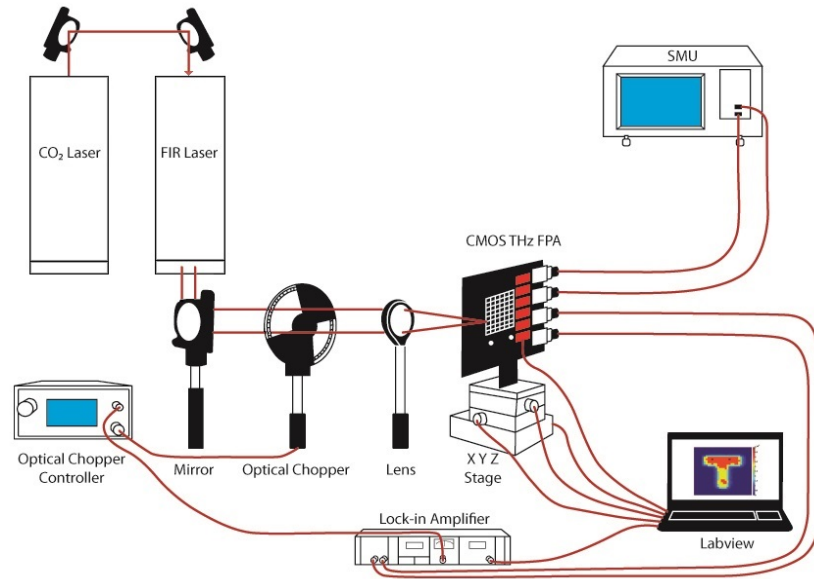


**Figure 5.14 - Experimental set up to characterise responsivity as a function of frequency.**

Chip A9 and A10 were used to determine the response at different frequencies. The responsivity of Chip A9 in the range of 1 to 15 Hz at room temperature is shown in Figure 5.15 (red triangles). The highest responsivity at 1 Hz is 235 V/W compared to the DC responsivity of 5722 V/W at 100 nA. The thermal time constant was found from the responsivity versus frequency data to be 194 ms at a bias current of 100 nA. Since the responsivity increases with a thinner membrane, Chip A10 was characterised from 1 Hz to 50 Hz at the same bias current as shown in Figure 5.15 (blue squares). The graph shows a significant increase in responsivity from 235 V/W to 5620 V/W at 1 Hz. Moreover, increasing the bias current from 100 nA to 2 μA gave a responsivity of 59 kV/W and an extracted thermal time constant of 68 ms for Chip A10 (black circles). The decrease in thermal capacitance (thinner membrane) from Chip A9 to Chip A10 proved to reduce the thermal time constant of the sensor from 194 ms to 68 ms.
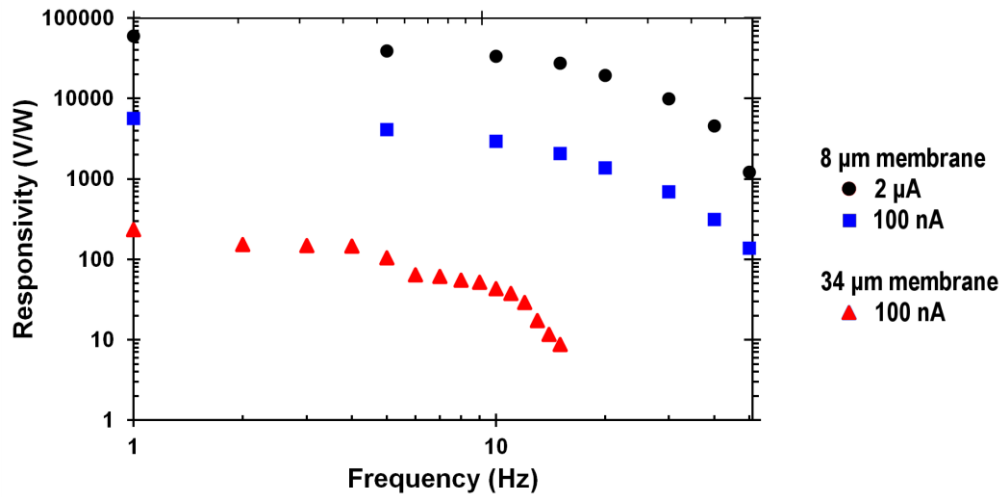
**Figure 5.15 - Responsivity as a function of modulation frequency for Chip A9 biased at 100 nA (red triangles), Chip A10 biased at 100 nA (blue squares), and Chip A10 biased at 2 μA (black circles). The 8 μm membrane pixel on Chip A10 biased at 2 μA has the largest responsivity since there is smaller thermal capacitance.**

### 5.4.3 Voltage map

The functionality of the readout circuit was demonstrated by measuring the DC output voltage of every pixel in the 5 x 5 array at room temperature with and without laser radiation. Every pixel in the array of Chip A9 was sequentially selected and the output voltages were measured to create a reference voltage map, to produce the 'OFF-frame'. The second 'ON-frame' was recorded when the FPA was illuminated by the terahertz laser. For alignment purposes the middle pixel output voltage was monitored to ensure the terahertz beam was focused in the centre of the array. The measured voltage on a pixel decreases with increased brightness because the VOx TCR is negative. Good alignment was necessary to detect the lowest voltage on the pixel thus enabling the measurement of a larger voltage difference between the two frames ($V_{ON/OFF}$). The PCB used to test the 5 x 5 FPA is shown in Figure 5.16. The pixels were selected using sliding switches to set 0 V or 3.3 V as inputs for the row and column decoders. The FPA was current biased using an external current source and the 5-bit current DAC to 100 nA to ensure the absolute output voltages remained within the output amplifier minimum and maximum voltages (0.3 V to 3.0 V). The bias voltages (0.3 V) and power supplies (0 V to 3.3 V) were connected to external voltage supplies through SubMiniature version A (SMA) coaxial connectors and the output voltages were measured through SMA coaxial connectors as well.
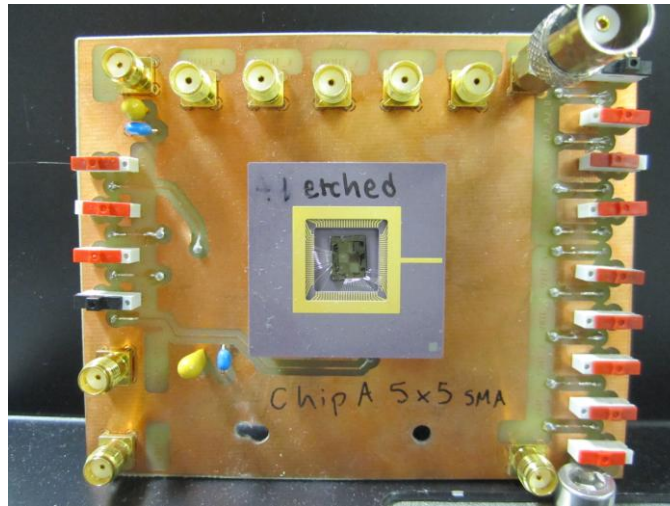
**Figure 5.16 - PCB used to test the 5 x 5 FPA.**

The differential $V_{ON/OFF}$ detector voltages of all the pixels in the 5 x 5 FPA are shown in Figure 5.17. They are in the range of 0.1 V to 0.8 V owing to the VOx nonuniformity changing the microbolometer resistance from pixel-to-pixel in the array. For an imaging system this effect would appear as fixed pattern noise that can be minimised by taking differential measurements consisting in recording alternate frames with and without laser radiation, where the first frame measurement would be used as a reference.
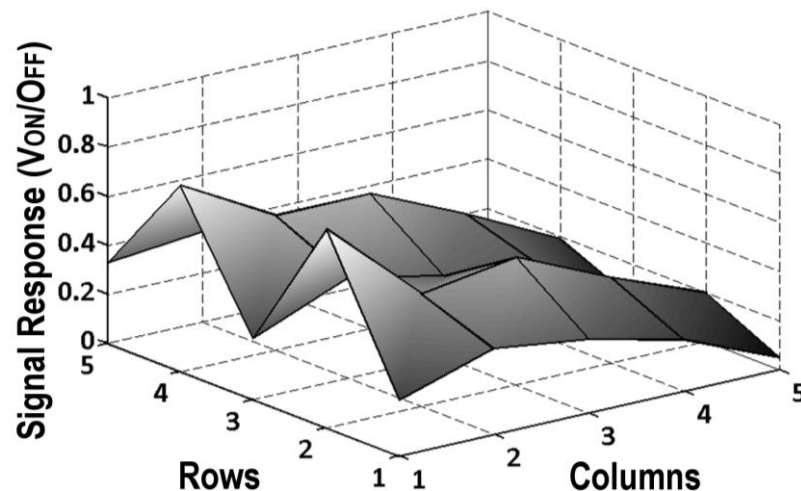


**Figure 5.17 - Differential signal response ($V_{ON/OFF}$) voltage map of Chip A9 5 x 5 FPA biased at 100 nA.**

## 5.4.4  Temperature Coefficient of Resistance

The TCR was determined by placing Chip A9 in an environmental chamber. It was DC current biased using the Keithley 4200-SCS and the 5-bit current DAC. The TCR was evaluated by measuring the change in output voltage as a function of temperature ranging from 10°C to 40°C with one degree steps. Labview was programmed to input the digital code into the row and column decoders thus selecting each pixel of the array every second. The current DAC was controlled externally to select currents from 20 nA to 80 nA. All the

output voltages from the 5 x 5 array were recorded to determine the current at which the FPA did not saturate the output amplifiers within the temperature range. The largest and most appropriate current was 60 nA at which all the output voltages were within the limits of the output amplifier voltage at all temperatures. Figure 5.18 shows the TCR for every pixel in the array at 25 °C. The average TCR was -2 %/K and the average microbolometer resistance was 24 MΩ for this chip.
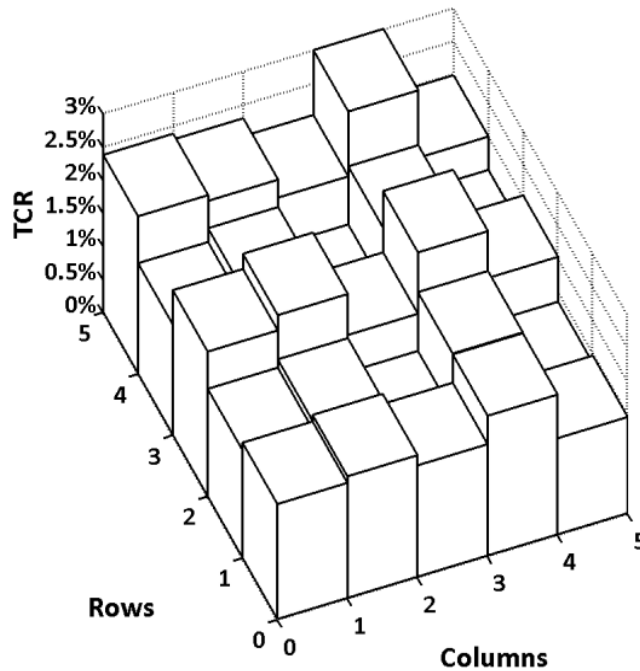


**Figure 5.18- Chip A9 TCR in 5 x 5 VOx FPA at 25 °C with an average TCR of -2 %/K and average pixel resistance of 24 MΩ.**

## 5.4.5  Noise Spectral Density

The NSD measurement setup consisted in current biasing the detector and measuring the voltage noise using a dynamic signal analyser (Agilent 35670A). The FPA was placed in a Faraday cage to reduce the influence of external noise. The *rms* voltage noise per square root unit bandwidth was measured from 1 Hz to 10 kHz at 25°C for the VOx 5 x 5 FPA in chip A9 (red line) and single VOx pixel in chip A10 (blue line) at 100 nA as shown in Figure 5.19. The noise spectrum reveals that the dominant noise source is *1/f* in nature. The higher noise from Chip A9 is attributed to additional noise from the readout electronics.

101
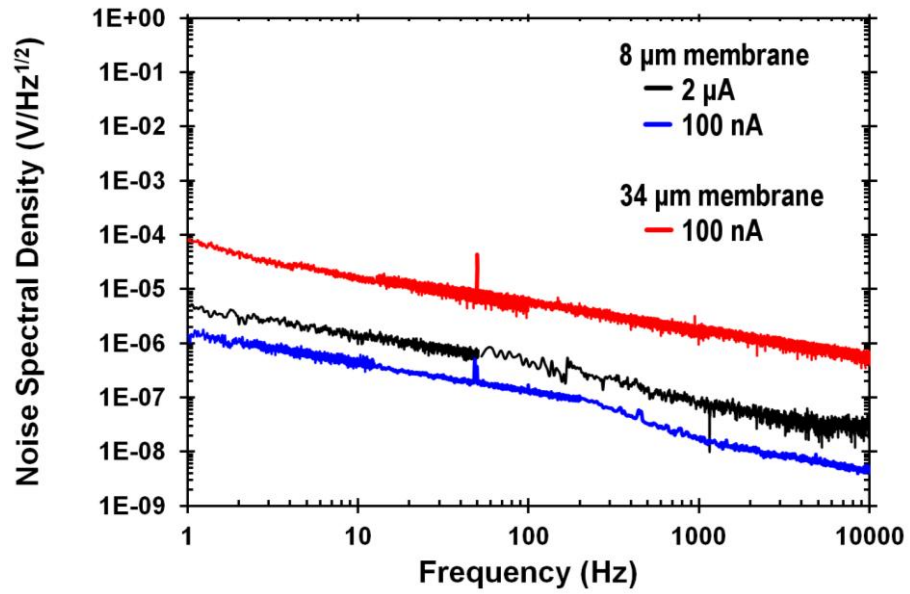
**Figure 5.19 - Noise spectral density for the 5 x 5 array in Chip A9 bias at 100 nA (red line), single pixel in Chip A10 bias at 100 nA (blue line) and 2 μA (black line).**

The NEP per square root unit bandwidth was calculated using Equation 3.16. The responsivity data at modulation frequencies from 1 Hz to 50 Hz used to calculate the NEP of the 5 x 5 array and the single pixel was previously shown in Figure 5.15. Additionally, the NEP was determined using the NSD data from both chips as shown in Figure 5.19. Figure 5.20 shows the minimum NEP for the Chip A9 and A10 devices biased at 100 nA and 2 μA. The minimum NEP for the 5 x 5 array on Chip A9 biased at 100 nA was 173.26 nW/√Hz at 4 Hz (open red triangles). This can be compared to the single pixel noise in Chip A10 with a minimum NEP of 108 pW/√Hz at 15 Hz biased at 100 nA (open blue squares) and a minimum NEP of 37 pW/√Hz at 15 Hz biased at 2 μA (open black circles). According to the *1/f* noise equation (3.13), the noise is dependent on the bias current, therefore it can be seen that the noise increases with increasing bias current. Additionally, the thinnest membrane of Chip A10 had lower noise and higher responsivity as expected.
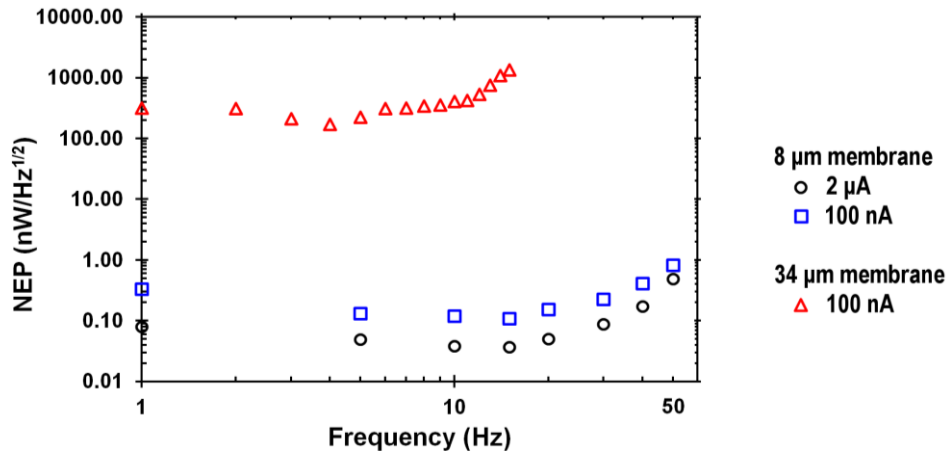
**Figure 5.20 – Noise Equivalent Power (NEP) as a function of frequency for the 5 x 5 array in Chip A9 biased at 100 nA (red triangles), single pixel in Chip A10 biased at 100 nA (blue squares) and 2 μA (black circles). The 8 μm membrane pixel (Chip A10) biased at 2 μA has a minimum NEP of 37 pW/√Hz at 15 Hz.**

# 5.5 Experimental Characterisation of Diode Microbolometers

The diode microbolometers from Chip C were characterised using the single pixels routed to external pads. Electrical characterisation was done as soon as the chips were received due to the advantage that no post-processing had to be done because the diodes were already integrated in the CMOS process. The performance was determined by measuring the $R_v$, TCV, and NSD. The same testing procedures and post-processing techniques were followed to create pixel membranes.

### 5.5.1 Diode Microbolometer Post-processing

Chip C was composed of a 1.5 mm x 1.5 mm array with p-n diode microbolometers and no readout electronics as described in Section 4.7. Six pixels, randomly selected in the array, were routed to external pads for single pixel characterisation. The integration of diode microbolometers in the CMOS process eased and reduced the post-processing steps compared to the VOx array making this option worth exploring. The post-processing had the purpose to create pixel membranes which was achieved by only one step: back etching the silicon substrate. Two membrane thicknesses were created leaving 1 μm and 50 μm of silicon remaining after etching.

Figure 5.21a shows an optical micrograph of a section of the unprocessed chip as received from the foundry. The picture shows the ERRs in the top layer (M6), via studs and surrounding metal structures intended to be used during post-processing to isolate each

individual pixel although this step was not a priority for initial tests. The visible metal studs connected all the metal layers to connect down to the anode and cathode of the diodes. Since the array did not have readout electronics, M1 and M2 were used to connect the diode microbolometers to the output pads. It is important to mention that the thickness of the pixels can be reduced by only using M1 and M2 for routing electronics, M3 for ground plane and M4 for the cross-shaped MM. Figure 5.21b shows an optical micrograph of the bottom section of a post-processed chip showing the thinner pixel membrane with 3 diodes in series in each pixel and their respective input and output contacts.
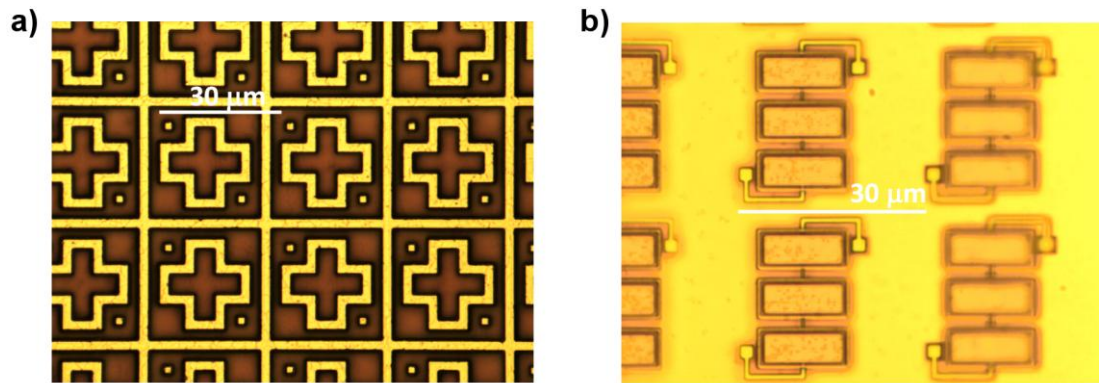


**Figure 5.21 – a) Optical micrograph of the unprocessed chip showing a section of the array with the respective ERRs and vias in M6. b) Post-processed chip showing the 3 diodes in series in each pixel after back etching the underlying silicon to create a thinner membrane. [Pictures taken by Dr. James Grant].**

## 5.5.2 Responsivity

The responsivity of the pixels from Chip C was measured using a Parameter Analyser (Keithley 4200-SCS). The parameter analyser was used for I-V characterisation and 4 point probe measurements as described in Section 5.4.1. The responsivity of the single pixels was measured using the PCB shown in Figure 5.22a. Its respective equivalent circuit is shown in Figure 5.22b. This PCB functions exactly as the one used for the VOx pixels where the pixel selected is current biased and has a reference ground, meanwhile the input and output voltages are measured using a total of 4 coaxial BNC connectors.
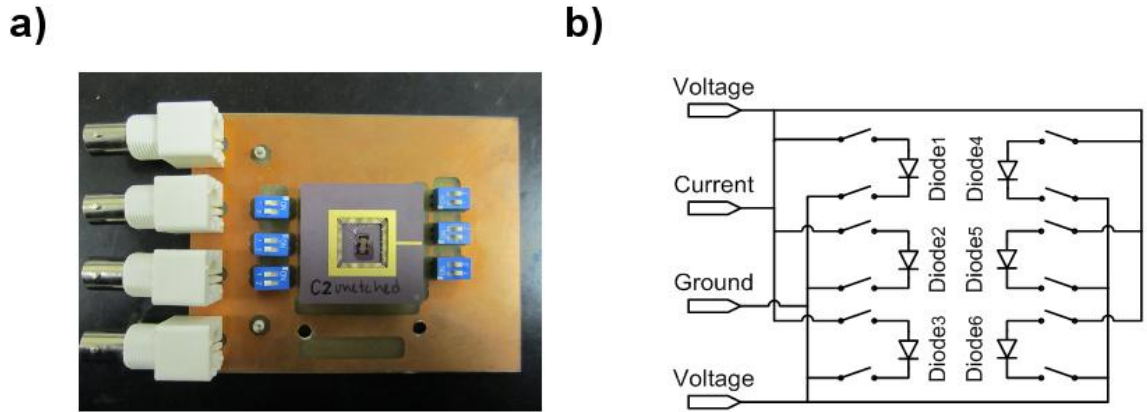
**Figure 5.22 – a) Chip C PCB used to characterise 6 single diodes and b) its equivalent circuit.**

The same principle of etching the silicon underneath the detectors used in the VOx chips was applied to increase the responsivity. Figure 5.23 shows the responsivity of a single diode detector at three stages of etching and at different bias currents ranging from 10 nA to 200 μA. It can be seen from these results that the lowest responsivity resulted from the unetched device, as expected from Equation 3.7, due to having the largest thermal capacitance (more volume). Successive measurements were made from diode pixel membranes with 1 μm and 50 μm of silicon remaining after etching. It can be seen that the highest responsivity, 1800 V/W at 20 μA, was achieved on the sample with the thinnest membrane due to the reduced thermal capacitance meaning that a device with less volume allows for faster heating or cooling of the pixel. The responsivity is approximately 12 times lower compared to the VOx detectors due to the difference in temperature coefficients of the microbolometer materials.
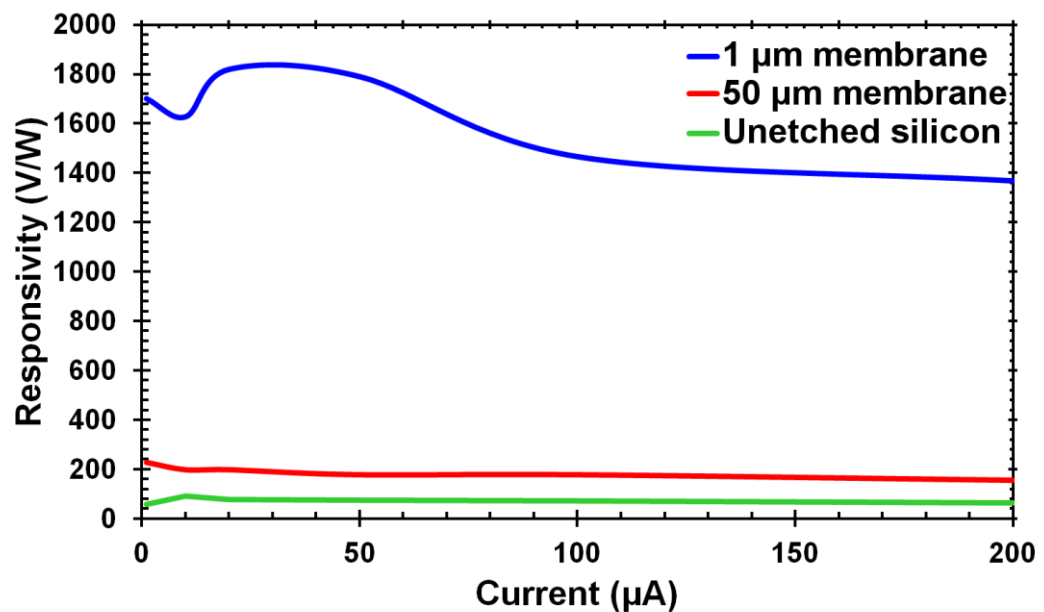


**Figure 5.23 - Responsivity from unetched (green line) and etched pixels with 50 μm (red line) and 1 μm (blue line) membranes. The 1 μm membrane had the highest responsivity, 1800 V/W at 20 μA, due to the reduced thermal capacitance.**

### 5.5.3 Temperature Coefficient of Voltage

The p-n diode sensor thermal characterisation procedures were identical to those of the VOx sensor mentioned in Section 5.4.4. The TCV of the diode pixels was measured using the environmental chamber in conjunction with a Keithley 4200-SCS parameter analyser used for current biasing. The TCV was determined by measuring the slope created by the change in output voltage as a function of temperature in the range of 10°C to 70°C. Figure 5.24 shows a comparison of the simulation and experimental TCV results. The simulation graph shows a TCV of -6mV/K as a result of the three diodes in series while the experimental results from the etched diodes only show an average TCV of -1.54 mV/K at 25°C. The results from the unetched devices shared the same experimental TCV characteristics.
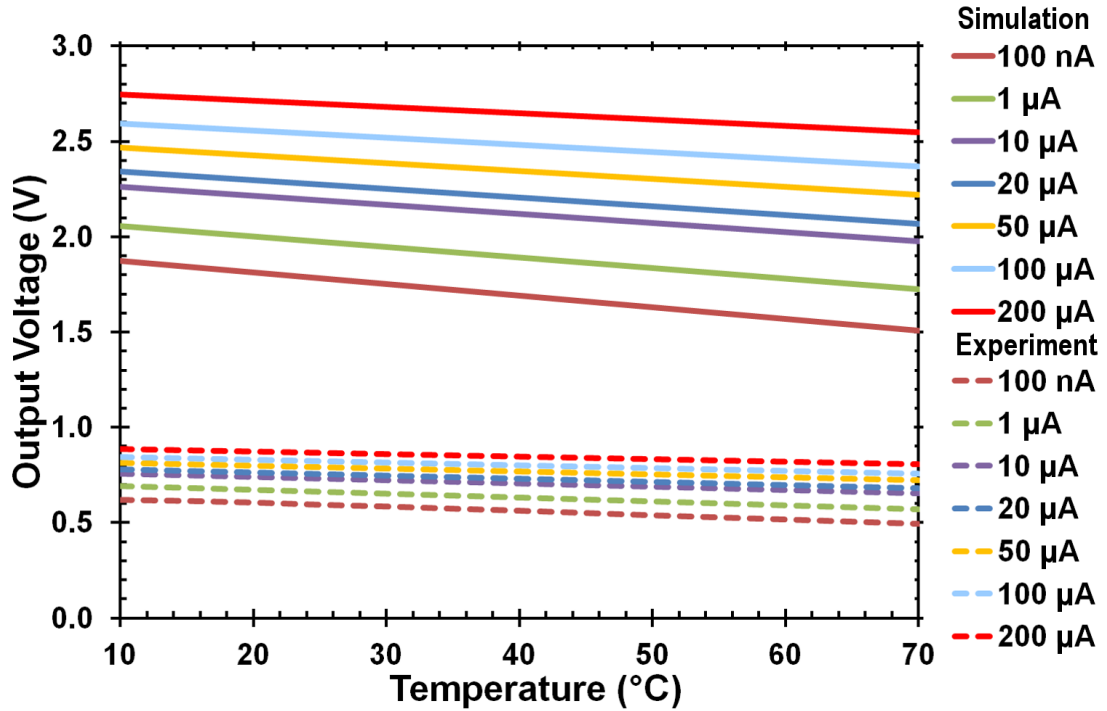


**Figure 5.24 - Simulation and experimental characterisation of the temperature coefficient of voltage (TCV) for a single pixel with 3 diodes in series. The simulation results show a TCV of -6 mV/K in all currents in contrast with the experimental results only showing an average TCV of -1.54 mV/K for the unetched (not shown in the graph) and etched devices.**

### 5.5.4 Noise Spectral Density

The NSD measurement setup consisted in current biasing the detector and measuring the voltage noise using a dynamic signal analyser (Agilent 35670A). Chip C was placed in a Faraday cage to reduce the influence of external noise. The *rms* voltage noise per square root unit bandwidth was measured from 1 Hz to 10 kHz at 25°C for the unetched chip (green line) and etched chip with 1 μm membrane thickness (blue line)

biased at 10 µA as shown in Figure 5.25. The noise spectrum for the unetched chip shows both *1/f* and thermal noise components. The *1/f* noise is dominant at the lower frequencies and the thermal noise makes the noise constant at larger frequencies. The etched chip shows a *1/f* noise behaviour even at higher frequencies. This behaviour is assigned to the introduced defects while post-processing the chip. The NEP could not be calculated due to the low responsivity which did not allow for the responsivity as a function of frequency to be measured.
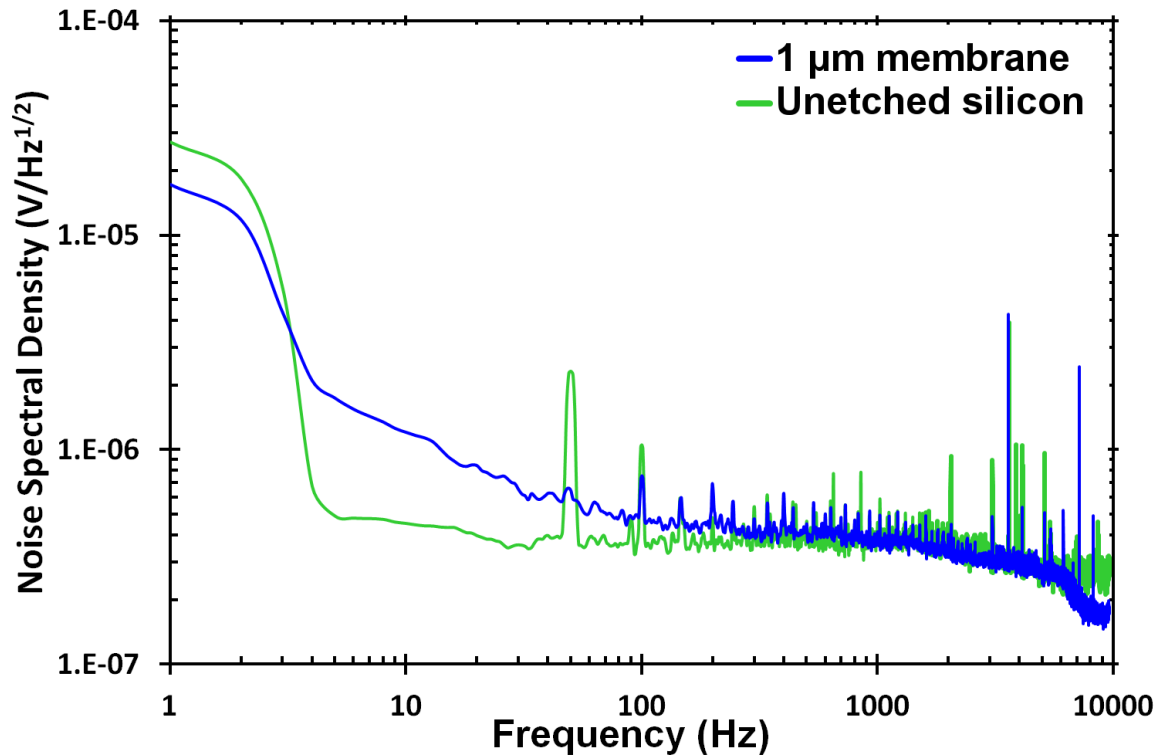


**Figure 5.25 - Noise spectral density at 10 µA from the unetched chip (green line) and etched chip with 1 µm thickness membrane (blue line).**

# 5.6 64 x 64 Focal Plane Arrays

## 5.6.1 VOx Chip F Characterisation

Chip F was designed as a 64 x 64 FPA with VOx microbolometers. It included broadband terahertz absorbers containing two ERRs in M5 and M6 and the ground plane in M3. The dimensions of the ERRs in M5 and M6 were identical to Chip A Design 2 listed in Table 4.9. The rest of the physical characteristics of Chip F were described in Section 4.9. The layout of the pixels changed slightly from Chip A due to the anticipated post-processing steps required for pixel isolation where M3 was intended to be used as a sacrificial etching layer. For easier access to isolate the pixels, the distance between the ERRs was increased by 5 µm on each side of the pixel resulting in a pixel pitch of 40 µm.

The post-processing steps for Chip F were similar to that for Chip A as described in Section 5.2. The steps included the addition of the VOx microbolometers and Ti/Al tracks to connect the microbolometers to the M6 studs. However instead of back etching the underlying silicon the intermetal dielectric between the pixels was etched down to the M3 aluminium layer and then this layer was sacrificially etched in order to isolate every pixel and minimise the thermal cross-talk and also to decrease the membrane thickness in order to reduce the thermal time constant and improve the pixel response time. This final etching step of the intermetal dielectric oxide and subsequent sacrificial aluminium etch is a non-trivial step and was not completed at the time of writing. However it is still a goal for the future of this project.

Figure 5.26a shows an optical micrograph of a section of the unprocessed chip as received from the foundry. The image shows the ERRs in M6 and the respective M6 studs used to connect the VOx microbolometer to the readout electronics. Figure 5.26b shows an optical micrograph of the post-processed chip with the ERRs in M6 and the VOx microbolometer sensors connected to the M6 studs using Ti/Al tracks. The tracks connect the microbolometer to the electronics placed in the bottom two layers of the CMOS process. In contrast with Chip A, the VOx was placed in an L shape due to complications during the deposition of the material creating contact problems when the VOx was placed directly on top of the cross shaped ERR. Figure 5.26c shows an SEM picture of a section of the post-processed chip showing the same features as Figure 5.26b. Figure 5.26d shows a 3D SEM picture of one pixel showing the VOx microbolometer in an L shape and Ti/Al tracks connecting the microbolometer to the M6 studs.
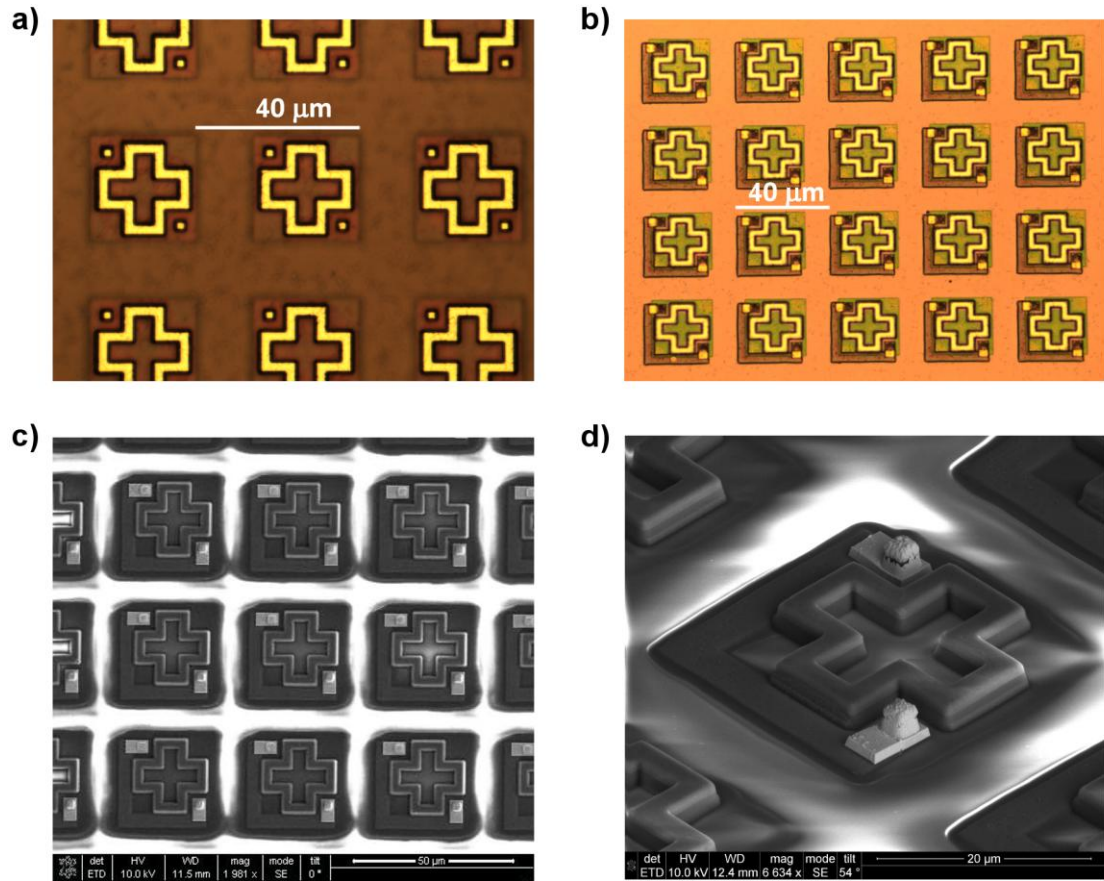
**Figure 5.26 - a) Chip F as received from the foundry showing the ERR and vias in M6 with a pixel pitch of 40 μm. b) Optical micrograph of post-processed chip with VOx microbolometers and Ti/Al tracks. c) SEM picture of post-processed chip and d) SEM pixel picture showing the VOx microbolometer and Ti/Al tracks connecting to the M6 studs. [Pictures taken by Dr. James Grant].**

The absorption characteristics of Chip F were obtained following the techniques to measure the spectral response described in Section 5.1.5. Figure 5.27 shows the comparison between the simulation (blue line) and experimental (red line) absorption spectra. According to the simulation results, the absorption spectra had two narrowband peaks, caused by the two stacked ERRs, at 2.5 THz and 2.8 THz with an absorption magnitude of 97% and 94% respectively. The experimental results show a broadband absorption peak centred around 2.5 THz with an absorption magnitude of 62%. This results confirmed absorption at the required frequency. The difference between simulation and experimental results may be to the assumed values in simulation of the inter-metal dielectric refractive index and the non-continuity in the ground plane allowing for some transmission.
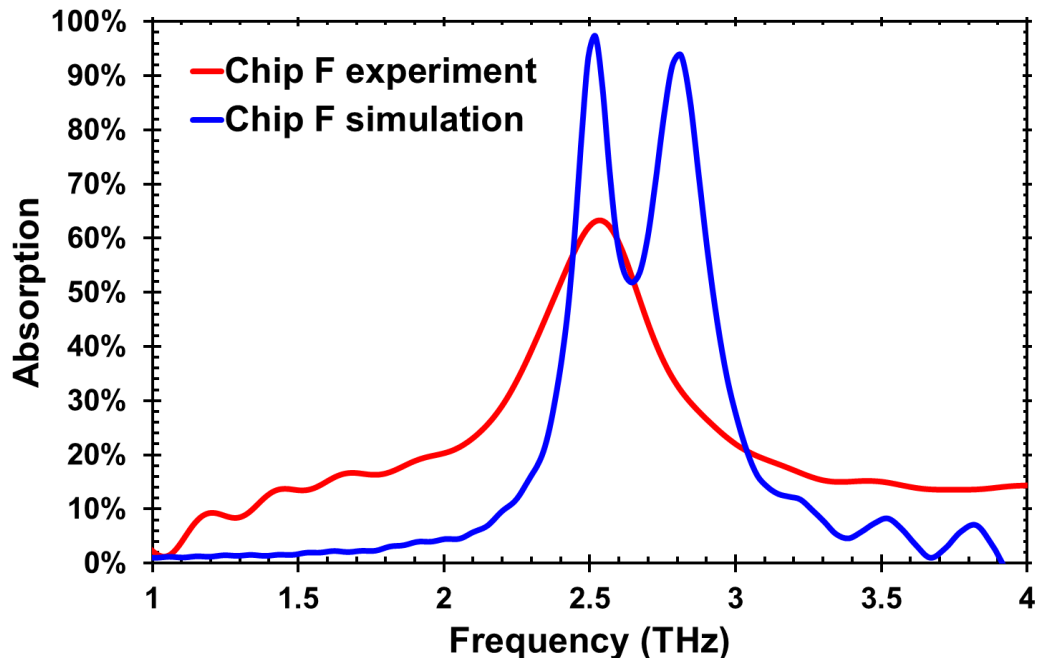
**Figure 5.27 - Chip F absorption characteristics showing a broadband absorption peak at 2.5 THz with an absorption magnitude of 62 %(red line) compared to the simulation results (blue line) showing two absorption peaks at 2.5 THz and 2.8 THz with 97% and 94% absorption respectively. [Simulation and measurement done by Dr. James Grant].**

## 5.6.2 Chip G Characterisation

Chip G was designed as a 64 x 64 FPA with p-n diode microbolometers. The layout of the pixels was composed of one ERR in M5, one p-n diode microbolometer and a ground plane in M3 as described in Section 4.10. The diodes exist in the bottom layers of the CMOS process, therefore it was necessary to etch all the inter-metal dielectric and metallic layers to isolate the pixels. Taking this into consideration, M6 was used as a mask to protect the M5 ERR during the deep etching process. Metal layers from M3 to M6 were used to protect the routing metals, M1 and M2, which were carefully positioned in the perimeter of each pixel as shown in the optical micrograph in Figure 5.28a. The image shows a section of the unprocessed chip with the M6 layer on top of the ERR and in the perimeter of the pixels covering the routing metals. The post-processing steps, performed and developed by Dr. James Grant, to isolate the pixels were:

1. Etch 8 μm of $SiO_2$ from the top of the chip
2. Etch 15 μm into the silicon from the top of the chip
3. From the back of the chip etch approximately 295 μm to create membranes. This step required a 35 μm thick photomask.

Figure 5.28b shows an SEM picture of the post-processed chip where the first 23 μm of the surrounding $SiO_2$ dielectric and Si were etched as M6 was used as a mask. The last

SEM picture in Figure 5.28c shows a milled out section of the pixel used to study the etch depth into the silicon. The image shows the metal layers surrounding the perimeter of the pixels (M3, M4, M5 and M6) covering the routing tracks in M2. Additionally, the image shows the 8 μm of $SiO_2$ and the 15 μm of silicon etched. The only step missing to complete the full post-process was to back etch the chip to create thin membranes.
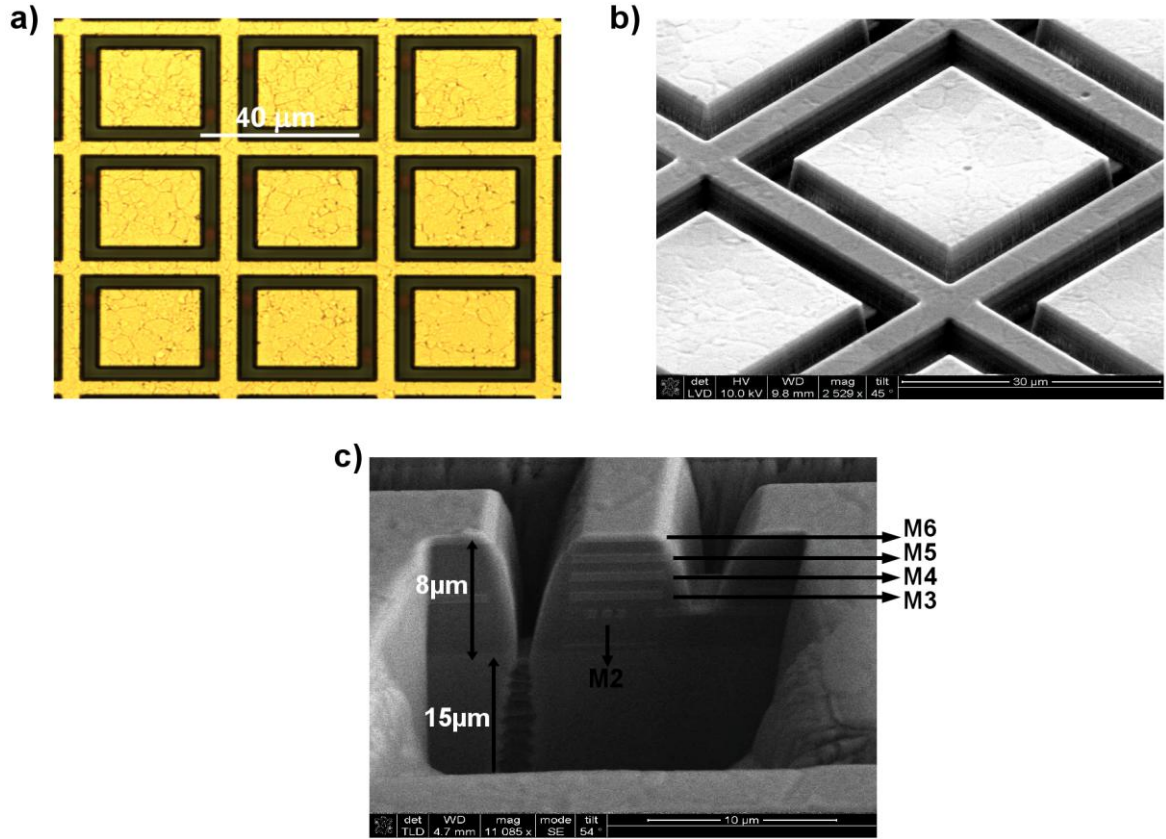


**Figure 5.28 – a) Optical micrograph showing a section of the unprocessed Chip G with M6 covering the ERR and the routing tracks on the perimeter of the pixels. b) SEM picture showing a close up of one pixel with the surrounding 23 μm of silicon and insulator etched. c) Post-processed chip showing a section of the array milled out to examine the etched depth into the $SiO_2$ (8 μm) and the silicon (15 μm). [Pictures taken by Dr. James Grant].**

Ideally the pixels would be isolated by removing all the material surrounding the microbolometer and only the metals connecting to the routing tracks would hold the pixel membranes. Due to the misalignment when back etching the chip, the last step was not completed. The problems associated with die level post-processing could be overcome by wafer-level fabrication where the yield would improve significantly.

The absorption characteristics of Chip G were not experimentally characterised due to the non-continuous ground plane which allows the underlying silicon to absorb terahertz radiation. Therefore, this makes an inaccurate measurement of the absorption response from the MM structure. Previous measurements have shown absorption spectra similar to the simulation results, therefore it was safe to assume appreciable absorption at 2.5 THz in Chip G.

The electronics of Chip G were tested as the chip was received from the foundry without the necessity to post-process the chip. The chip was bonded into a 100 CPGA package and the readout electronics were tested by reading the voltage of each pixel in the 64 x 64 array and creating the voltage map shown in Figure 5.29. The voltage map shows an average output voltage of 1.21 V. The data was taken using a Labview program which will be described in the next section.
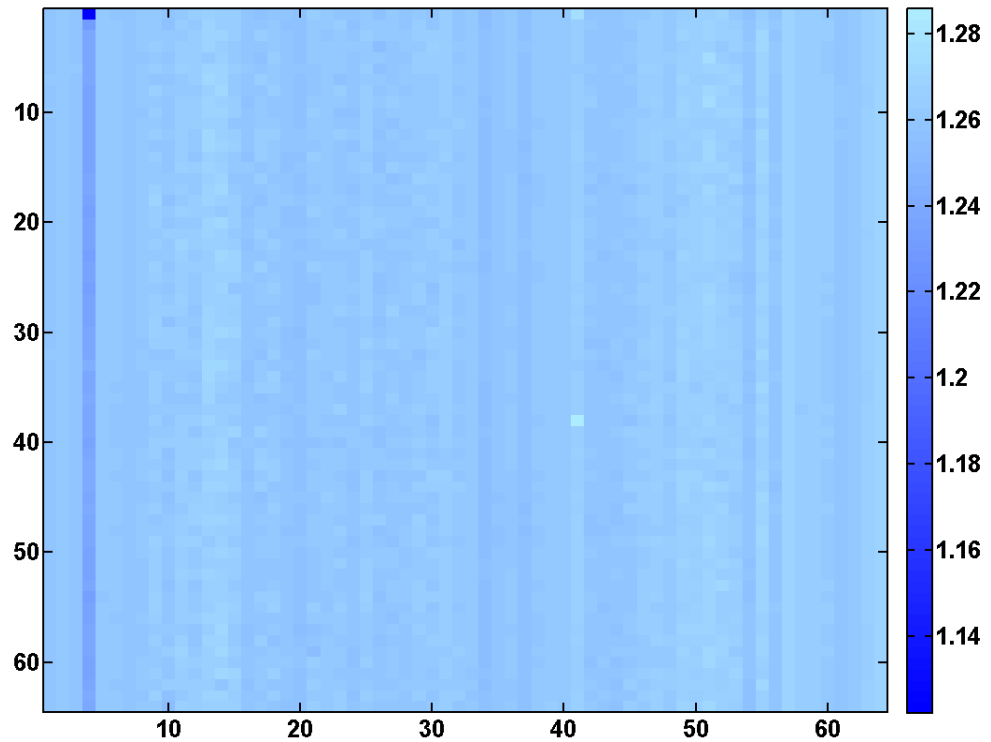


**Figure 5.29 - Chip G 64 x 64 pixel array voltage map.**

# 5.7 Labview for 64 x 64 FPA Readout

Labview was used as the interface to readout every voltage in the 64 x 64 FPA. The front panel used as the user interface is shown in Figure 5.30 where the user inputs the information required in each path and the real time data can be seen in the 'data' window.

1. Rate: this refers to the rate in Hertz in which 1 frame is taken (ideally 1 second per frame).
2. Digital Addresses File Path: this is an external text file that contains all the digital addresses as binary codes to select each pixel on the array. The file path where the text file is saved is entered here. The text file starts with [000000000] and ends with [111111111] and it contains 512 binary addresses.
3. Results File Patch: the readout voltages are saved as a .tdms file which can be opened with excel. The user selects the location and name of the file to be saved.
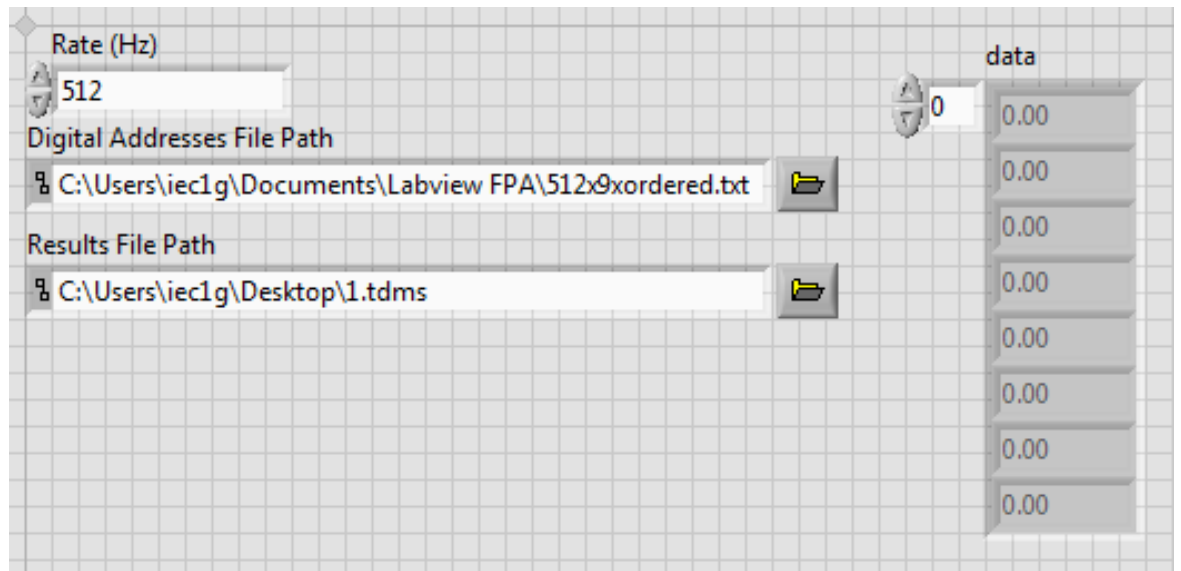
**Figure 5.30 - Front Panel window use as the user interface to select the rate, delay, input addresses and output file.**

The Labview block diagram is shown in Figure 5.32. Chip F and G had the same requirements for digital inputs and analogue outputs. Each chip required 9 digital inputs to select 8 columns and read 8 analogue outputs simultaneously. The readout circuits are explained in Sections 4.9.1 and 4.10.1. The block diagram is split in sections from 1 to 10 for easier understanding. The program follows these steps:

1. The 9 digital and 8 analogue channels are created

2. Set timing parameters: 512 x 8 samples are read at the specified rate in the front panel

3. Synchronization parameters: the digital and analogue data is synchronised by setting an external reference clock at a rate of 100 MHz

4. Trigger delay: the delay was introduced to take the readout measurement after the detector reaches a constant voltage. This time depends on the $\tau$ of the microbolometers. The default delay is set to trigger at 50 % of the pulse width.

5. Digital addresses: the text file is read and the 512 digital addresses are stored in the memory of the computer before the readout process starts.

6. Logging data: the .tdms file is configured and the data will be saved in the file and read in the front panel.

7. Events structure palette: this structure set the tasks to start in order, the readout will only start after all the previous steps have been accomplished

8. The readout process starts: the addresses are sent to the chip at the set rate (Figure 5.31) and the 8 voltages are read and logged. The data is shown in the front panel in real time.

9. After 512 samples are acquired, the data acquisition stops

10. If there is any error while running the program, a dialog box will pop up

The .tdms file contains all the information to create the voltage map shown in Figure 5.29.
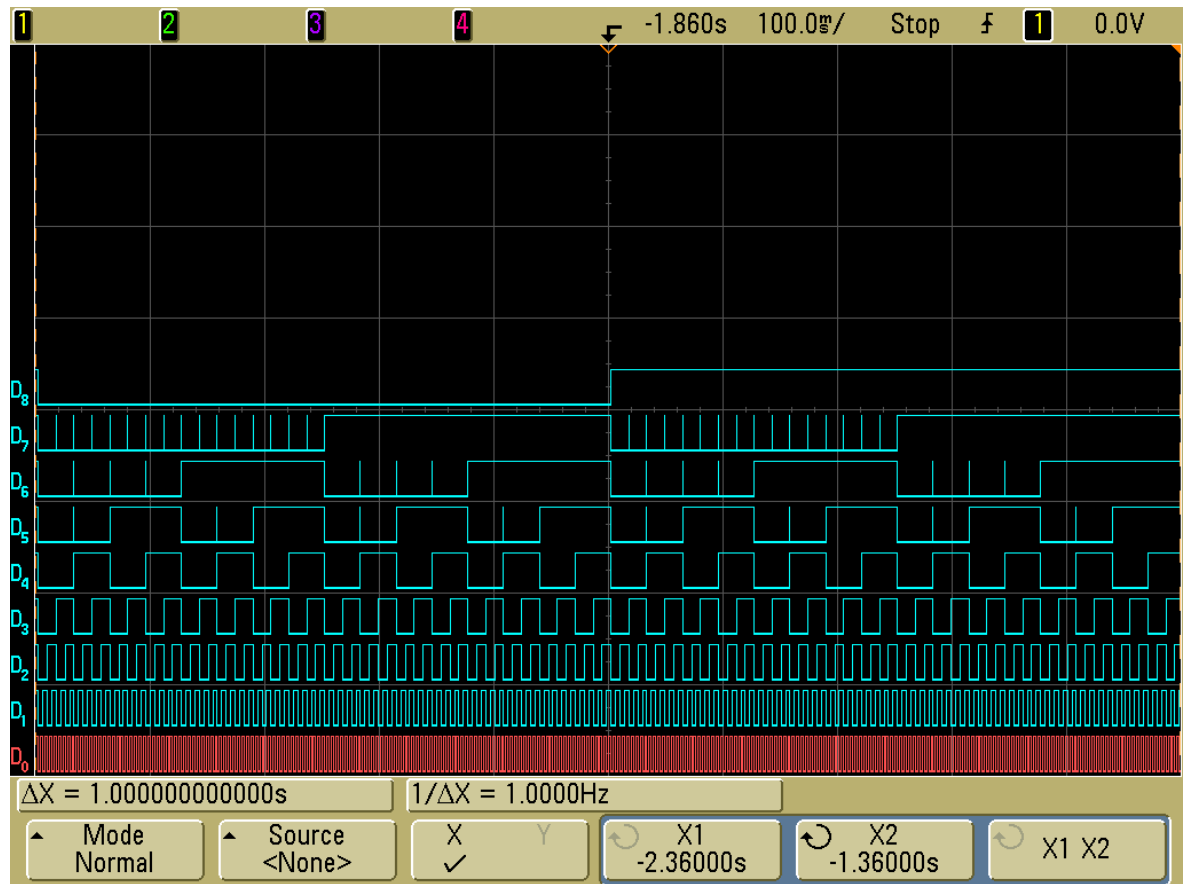


**Figure 5.31 – Digital signals created by Labview to select 8 columns and 8 rows simultaneously. The oscilloscope image shows a frame rate of 1 Hz.**
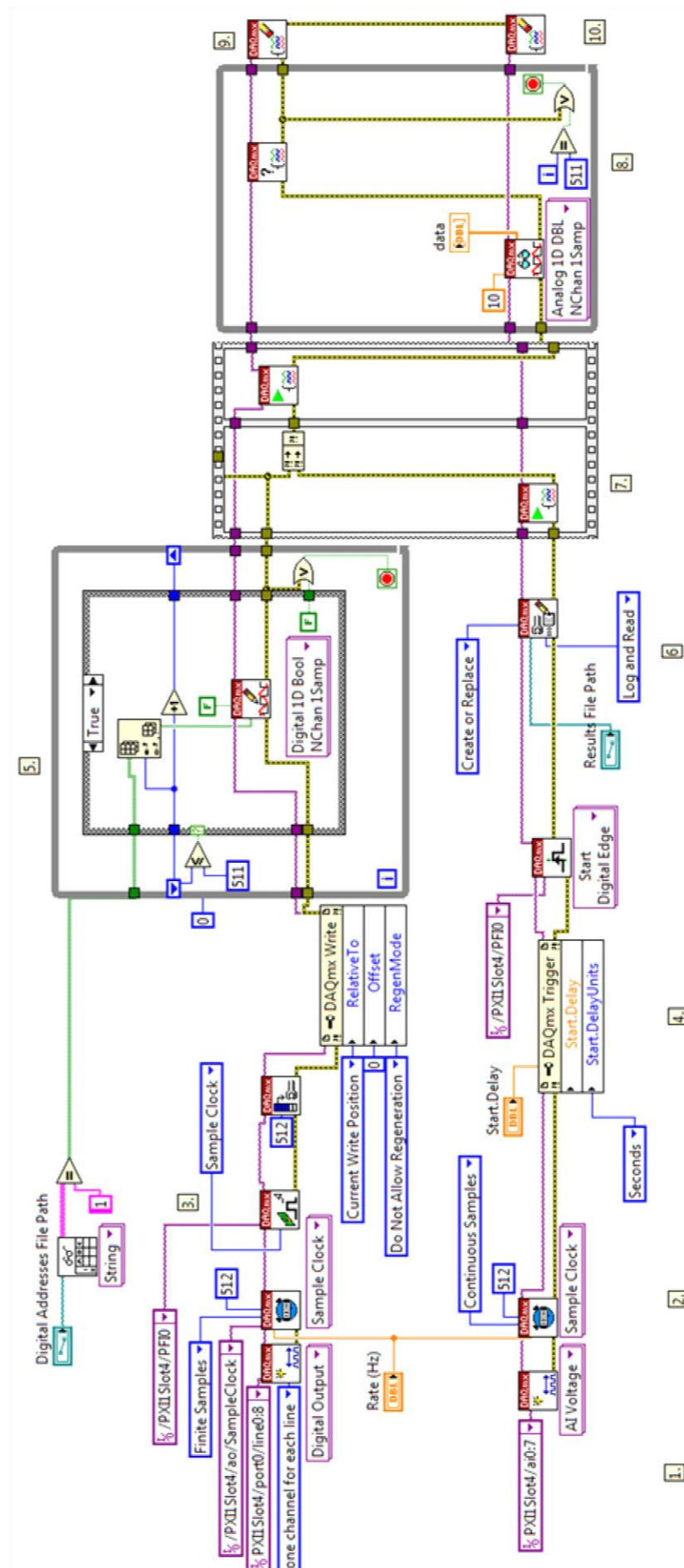
**Figure 5.32 – Labview block diagram used to readout each voltage on the 64 x 64 array.**

115

# 5.8 Terahertz Imaging Experiments

The MM based terahertz FPAs with VOx microbolometers were employed in both a transmission and reflection mode imaging experiments to demonstrate their imaging capabilities using the CW FIR gas laser operating at 2.5 THz as the source. The VOx FPA was chosen for the imaging experiments because the responsivity was approximately twelve times higher than the diode sensor as discussed in Section 5.5.2. Therefore, the VOx detectors were prioritised for the imaging experiments. Only one pixel was used for the experiments due to the unsuccessful isolation of each pixel in the array and as a consequence it was necessary to raster scan the object to form an image.

## 5.8.1 Transmission mode imaging

The first experiment was the transmission mode imaging using the device with the highest response (Chip A10). The set up for this experiment is shown in Figure 5.33 where an aluminium object in a 'T' shape and the rest of the components were aligned to the terahertz beam path. The 'T' shape was attached to a holder and placed on the translation x-y-z motor stage. The object was located at the focus distance of a Tsupurica lens (11 cm), separated by the same distance from a polymethylpentene (TPX) lens. The terahertz FPA was placed at the TPX lens focal length (6.5 cm). The transmission of terahertz radiation propagating through the object was the output detected by the FPA as the incident beam was modulated using an optical chopper set to 1 Hz. The FPA was current biased at 100 nA by a Keithley 4200-SCS. The beam was focused onto the CMOS terahertz FPA and the differential output voltages were measured at the same frequency by the lock-in amplifier. The lock-in amplifier separated the signal from noise by taking differential measurements. It acquired the data of every pixel while being scanned to build a two-dimensional image.
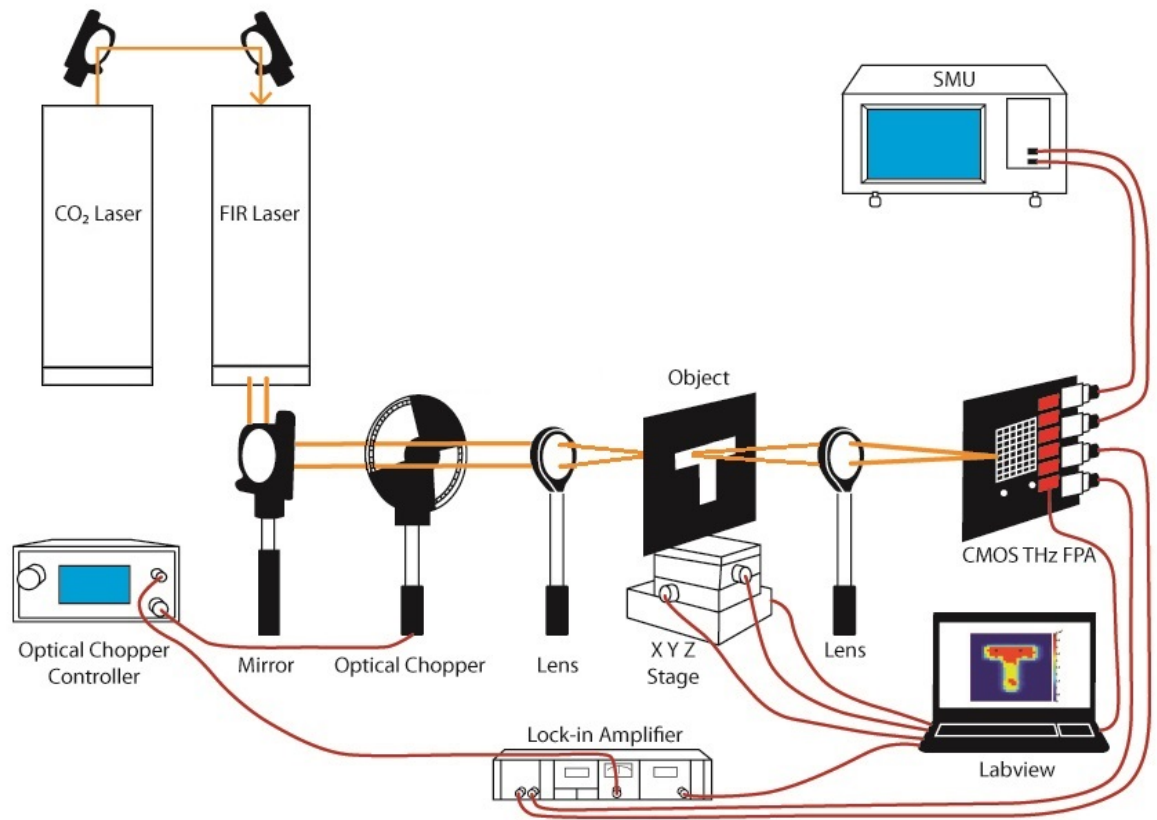
**Figure 5.33 – Set up for the single pixel imaging transmission mode experiment using the CMOS terahertz FPA.**

The object used in the imaging experiment was an aluminium square with the following dimensions: length = width = 20 mm and thickness = 2 mm. It had a cut out 'T' shape with a length of 10 mm, height of 15 mm and arm widths of 3 mm. The optical image is shown in Figure 5.34a. The readout area was set to 20 x 20 mm in the x-y plane and the first image had 1 mm x 1 mm pixel resolution. The output power from the laser was 89 mW. The resulting terahertz image from the first imaging experiment using the 8 μm membrane thickness device (Chip A10) is shown in Figure 5.34c showing a clear image of the aluminium T shape and the surrounding background. The transmission experiment was repeated to increase the image resolution. The readout area was set to 25 x 25 mm with 0.5 mm x 0.5 mm resolution and the clear image of the 'T' shape is shown in Figure 5.34e.

In order to prove the capability of non-invasive detection and the transparent characteristics of terahertz waves, the object was hidden in a manila envelope as shown in Figure 5.34b. The transmission mode experiment was repeated under the same conditions first with a resolution of 1 mm x 1 mm and then with a resolution of 0.5 mm x 0.5 mm. Due to the instability of the laser power for these experiments the power had increased to 125 mW. Figure 5.34d shows the captured terahertz image of the object when covered by

the manila envelope in the first resolution and Figure 5.34f shows the terahertz image for the second resolution. Both images show a clear outline of the 'T' shape object.
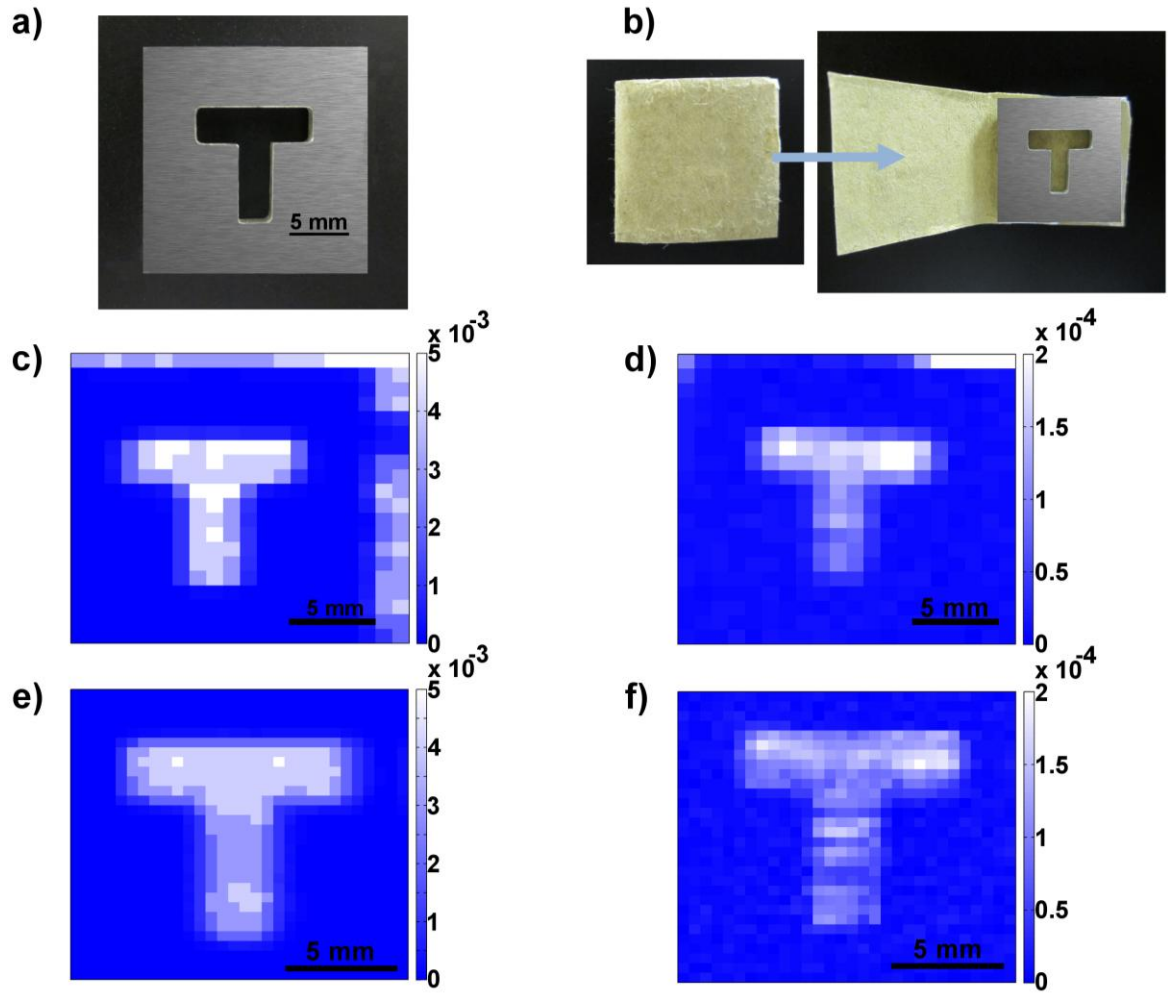


**Figure 5.34 - Transmission mode imaging pictures using the 8 μm membrane thickness device (Chip A10) at 2.5 THz. a) Optical image of the aluminium 'T' shape uncovered and b) covered object. c) Transmission mode image with 1 mm x 1mm resolution of uncovered object and d) covered object. e) Transmission mode image with higher resolution of 0.5 mm x 0.5 mm from uncovered object and f) covered object.**

The device with a 34 μm thick membrane containing the 5 x 5 pixel array was also used as the detector in the transmission mode imaging experiment. The experiment was repeated under the same circumstances with a readout area of 25 x 25 mm and 0.5 mm x 0.5 mm resolution. The laser's output power for this experiment was 115 mW. Figure 5.35a shows the optical image of the aluminium 'T' shape used for this experiment. This object had the following dimensions: length = width = 45 mm and thickness = 0.5 mm. The cut out 'T' shape had a length of 19 mm, height of 21 mm and arm widths of 5 mm. Figure 5.35b shows the transmission image obtained. The experiment was repeated but the aluminium object was hidden in a manila envelope as shown in Figure 5.35c. The resulting image is shown in Figure 5.35d. The image is barely discernible due to the difference in responsivity from Chip A9 to Chip A10. Chip A9 had a responsivity of 24 times lower

than Chip A10 at 1 Hz. Another reason can be the output power of the laser that can dramatically drop after hours of use.
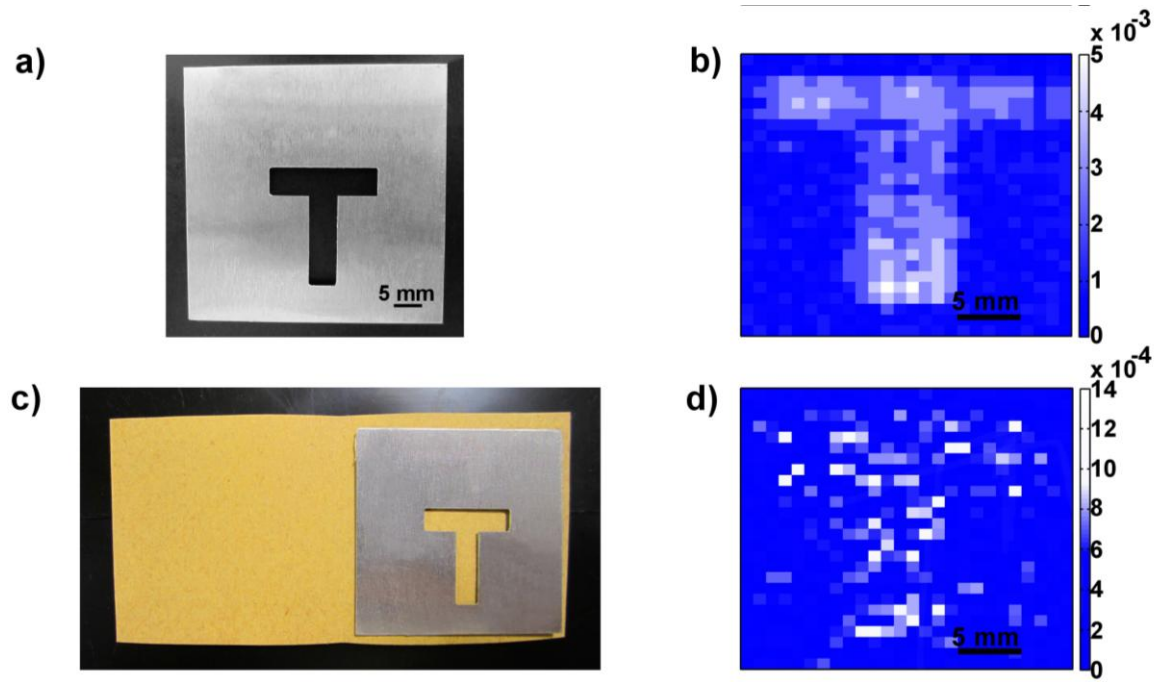


**Figure 5.35 - Transmission mode imaging pictures using the 34 μm membrane thickness device (Chip A9 – 5 x 5 array) at 2.5 THz. a) Optical image of the aluminium 'T' shape. b) Transmission mode image with 0.5 mm x 0.5 mm resolution of uncovered object. c) Optical image of the aluminium 'T' shape covered by a manila envelope. d) Transmission mode image with a resolution of 0.5 mm x 0.5 mm from the covered object.**

## 5.8.2 Reflection mode imaging

The reflection mode imaging experiment was made using the 8 μm thick membrane of Chip A10. The experiment set up is shown in Figure 5.36. The terahertz source, current biasing, terahertz beam modulation and lock-in detection method were identical to that used for the transmission mode imaging experiment shown in the previous section. This imaging experiment consisted in reflecting the focused terahertz beam from the surface of an aluminium object and refocusing it onto the terahertz detector at an angle of 15°. The object used had the same characteristics as the one described and shown in Figure 5.35a. The same figure is used for easier comparison in the reflection mode images as shown in Figure 5.37a. The readout area was set to 25 x 25 mm and 0.5 mm x 0.5 mm resolution. The laser's output power was 95 mW. The captured image from the reflection experiment is shown in Figure 5.37b. Once again, the experiment was repeated by covering the object with a manila envelope as shown in Figure 5.37c and its respective terahertz image is shown in Figure 5.37d. The stand-off distance was 20 cm.
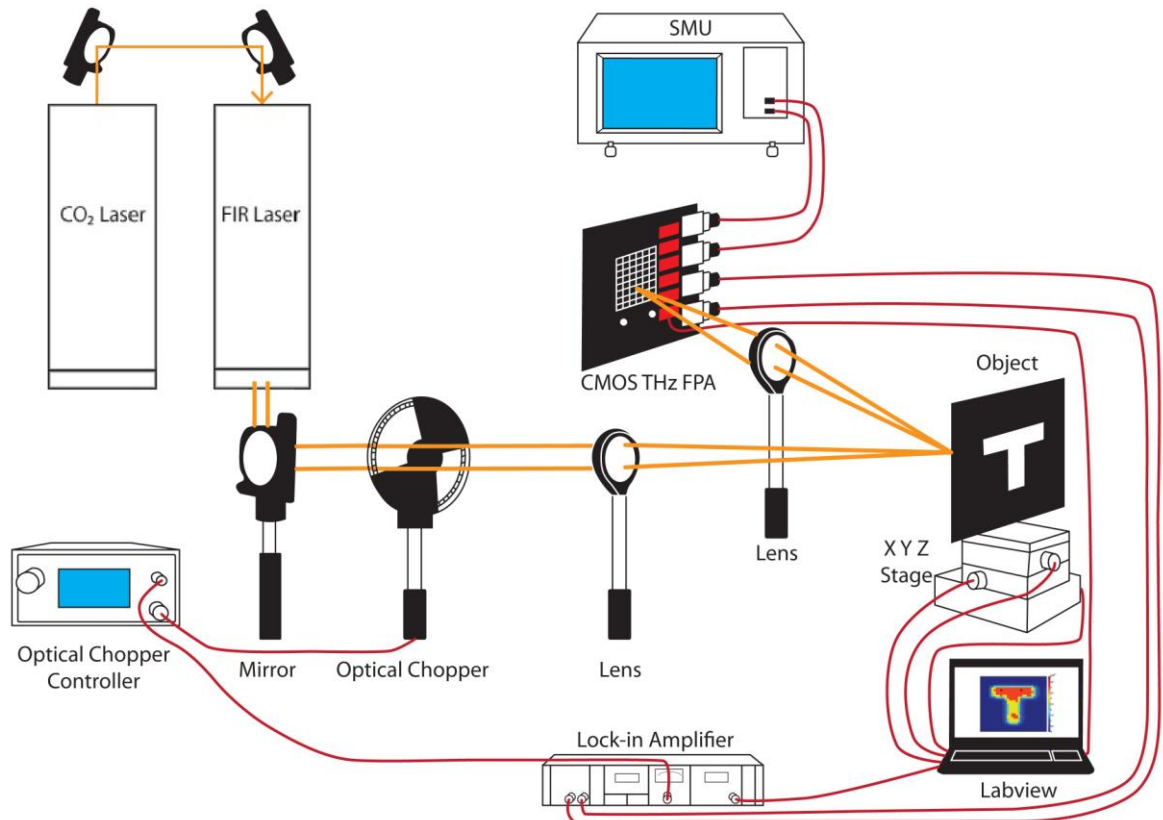
**Figure 5.36 - Set up for the single pixel imaging reflection mode experiment using the CMOS terahertz FPA.**
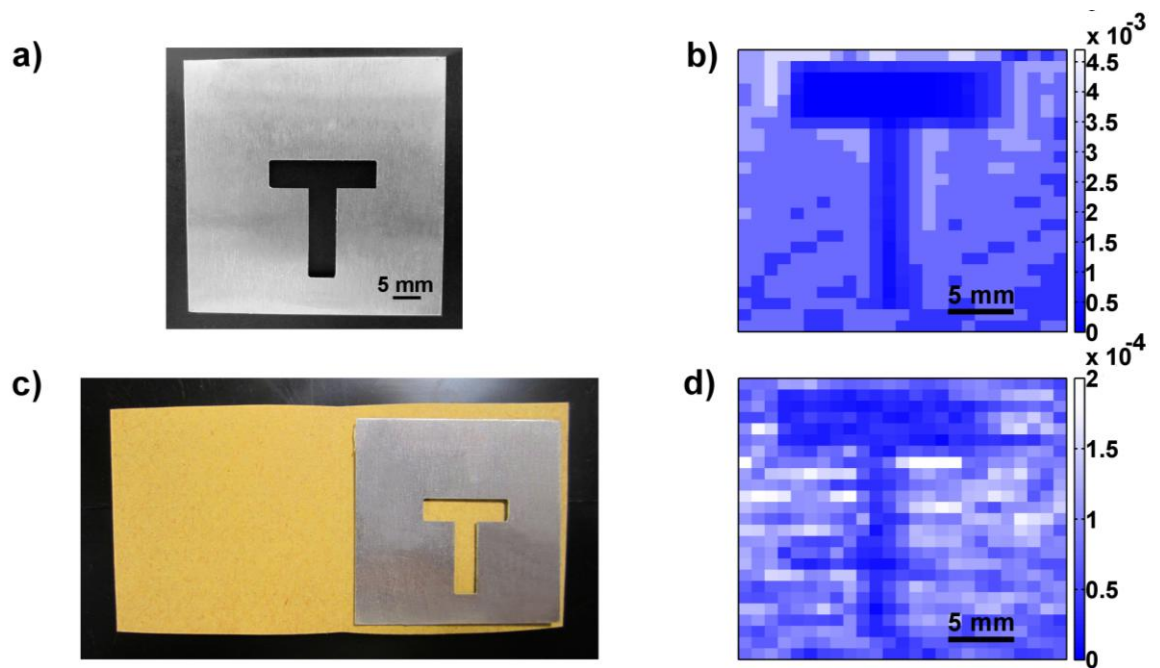


**Figure 5.37 - Reflection mode imaging pictures using the 8 µm membrane thickness device (Chip A10) at 2.5 THz. a) Optical image of the aluminium 'T' shape. b) Reflection mode image of uncovered object. c) Optical image of the aluminium 'T' shape covered by a manila envelope. d) Reflection mode image from the covered object.**

# 5.9 Summary

The experimental results obtained from the fabricated chips were presented in this chapter. The first set of dies (Chip A) fabricated by TI contained single circuit blocks that were individually tested to compare their performance to the simulation results. The chips were packaged upon receipt into a 100 pin CPGA package and were bonded by Dr. James Grant. Individual PCBs were designed to test the 3 to 5 bit decoder, OTA and 5-bit current DAC. The experimental results obtained from the circuit blocks compared well to the simulation results presented in Chapter 4. Chip B was used to test the spectral response of the MM absorbers. The minimum usable spot size of the FTIR spectrometer was 4 mm diameter, making it impossible to measure the spectral response from Chip A as the arrays were 1.5 mm x 1.5  mm. Therefore, Chip B was designed and fabricated to have the same MM structure as Chip A but with an array size of 5 mm x 5 mm. The spectral response had two broad absorption and confirmed absorption at the required frequency of 2.5 THz.

The FOMs described in Chapter 3 were measured from Chip A (VOx microbolometers) and Chip C (p-n diode microbolometers) including $Rv$, TCR, TCV, NEP, and $\tau$. The post-processing procedure to pattern the CMOS chips with VOx microbolometers was described. Due to the difficulty in post-processing single dies as opposed to wafers, the pixels on the arrays were not isolated; therefore it was only possible to evaluate single pixel performance and establish the effect of membrane thickness on the responsivity and NEP. Both microbolometer types showed that thinner membranes result in higher responsivity due to the reduced thermal capacitance meaning that a device with less volume allows for faster heating or cooling of the pixel. It is also concluded that the P-N diode microbolometers have approximately 12 times lower responsivity compared to the VOx detectors due to the difference in temperature coefficients and as a consequence the VOx detectors have shorter thermal time constants.

Higher resolution FPAs with both types of microbolometers were fabricated with their respective readout integrated circuits. The 64 x 64 arrays had a parallel readout process to increase readout speed and achieve video rate imaging depending in the thermal time constant. The MM based terahertz FPA with VOx microbolometers was employed in both a transmission and reflection mode imaging experiment to demonstrate its non-invasive imaging capabilities by imaging objects enveloped in paper.

# Chapter 6 Conclusions and Future Work

The development of terahertz imaging technologies has been hindered due to the lack of high sensitivity and low-cost sources and detectors. Therefore, it is necessary to develop uncooled and cost-effective detectors compatible with CMOS technology to bring terahertz imaging on par with their EM neighbours. The purpose of this work has been to develop a room temperature terahertz detector for imaging applications by monolithically integrating terahertz MM absorbers, uncooled microbolometer sensors and readout electronics into a commercial 180 nm CMOS process.

The Thesis explains the design, simulation, fabrication and characterisation of two types of terahertz FPAs composed of broadband MM absorbers built directly in the metallic and insulating layers of the CMOS process, VOx or p-n diode microbolometers and custom made readout integrated circuits in serial and parallel mode. The main conclusions derived from the characterisation of the two types of detectors, readout electronics performance and suggestions of future work are presented in this chapter.

The main achievements of this work are:

- The design of cross-shaped MM absorbers for single band and broadband absorption working in the terahertz atmospheric window of 2.51 THz to 2.55 THz with specific absorption at 2.5 THz. The operating frequency of 2.5 THz corresponds to a wavelength of 118.8 μm. Operating at shorter wavelengths enables better spatial resolution, compared to mm waves, in imaging applications.

- The characterisation of two types of uncooled microbolometer sensors: VOx and p-n diode. Single pixels routed to output pads were used to characterise the performance of both microbolometers after being integrated in each pixel of the CMOS FPA.

- Fully customised ROICs were designed, layout, simulated, tested and fabricated in a six metal layer 180 nm CMOS process from TI. The initial ROIC was designed as a 5 x 5 VOx array with serial readout. In order to increase the readout speed, a parallel readout architecture was designed for the chips containing the VOx and p-n diode microbolometers in the 64 x 64 FPAs.

- The monolithic integration of the MM absorbers, microbolometer sensors and ROICs in a commercial CMOS process creating the first high sensitivity room

temperature MM based terahertz FPA with the potential of scalability to high resolution imaging systems and low-cost manufacture.

- Transmission and reflection mode imaging was demonstrated by imaging a covered and uncovered metallic object using a raster scanner method where individual VOx pixels were used as detectors.

The feasibility to design single band and broadband terahertz absorbers realised directly in the metallic and insulating layers of the CMOS process was demonstrated by creating MM absorbers composed of cross-shaped ERRs. The MM absorbers were integrated into three metallic layers separated by a dielectric. These subwavelength MM structures demonstrated that the absorption frequency changes by manipulating the size, thickness and shape of the MM absorber. In order to realise broadband absorbers it was necessary to stack ERRs created in the top metallic layers of the six metal CMOS process separated by the respective dielectric. The FWHM of the broadband absorbers increased to 48% of the central frequency compared to the 20% of a single layer MM absorber. These structures were investigated due to the lack of selective, strong terahertz absorbers in nature. The MM absorbers described throughout the Thesis had an absorption magnitude of more than 50% at a frequency of 2.5 THz.

Two uncooled microbolometer materials were investigated: VOx and silicon p-n diode. Both options were investigated because of their sensitivity to temperature changes and wide use in IR imaging systems. The fabricated chips were packaged and post-processed by Dr. James Grant. The post-processing steps were required to add the VOx microbolometers and to create membranes in the FPAs. The VOx microbolometer was patterned above the M6 ERR structure and the p-n diode had the great advantage of being already integrated in the lower layers of the CMOS process. The respective ROICs were designed for a VOx 5 x 5 array with serial readout and VOx and p-n diode 64 x 64 array with parallel readout electronics.

## 6.1.1 Vanadium Oxide Microbolometer

Single pixels were used to characterise the VOx microbolometer terahertz detector from Chip A containing a broadband MM absorber in a 5 x 5 FPA. One unetched FPA and three membrane thicknesses were investigated for this microbolometer type:

- Chip A7 unetched: 300 µm silicon + 8 µm dielectric
- Chip A8 etched: 50 µm silicon + 8 µm dielectric
- Chip A9 etched: 26 µm silicon + 8 µm dielectric
- Chip A10 etched: 0 µm silicon + 8 µm dielectric

Chip A10 had the largest responsivity of 32.65 kV/W with a bias current of 600 nA. However as the membrane had no silicon remaining therefore there were no means to address the pixels when employed in a FPA. The responsivity from Chip A9 was compared to A10 and showed a responsivity of 21.98 kV/W with a bias current of 600 nA. Chip A9 had 26 μm of silicon remaining allowing it to be addressed in a FPA format. The lowest responsivity was obtained from A7 due to having the thickest pixel volume.

The responsivity as a function of frequency was measured in the range of 1 Hz to 50 Hz. The highest responsivity at 1 Hz was 235 V/W from Chip A9 compared to the DC responsivity of 5722 V/W at 100 nA. The thermal time constant was extracted from the responsivity versus frequency data to be 194 ms at a bias current of 100 nA. Since the responsivity increases with a thinner membrane, Chip A10 was characterised at the same bias current and it showed a significant increase in responsivity from 235 V/W to 5620 V/W at 1 Hz. Moreover, increasing the bias current from 100 nA to 2 μA gave a DC responsivity of 59 kV/W and an extracted thermal time constant of 68 ms. The decrease in thermal capacitance (thinner membrane) from Chip A9 to Chip A10 proved to reduce the thermal time constant of the sensor from 194 ms to 68 ms.

The minimum NEP was measured from the 5 x 5 array on Chip A9 biased at 100 nA resulting in 173.26 nW/√Hz at 4 Hz. This result was compared to the single pixel NEP in Chip A10 which showed a minimum NEP of 108 pW/√Hz at 15 Hz biased at 100 nA and a minimum NEP of 37 pW/√Hz at 15 Hz biased at 2 μA. The VOx microbolometers in the array had an average TCR of -2 %/K.

## 6.1.2 PN Diode microbolometer

Chip C was composed of an array with broadband MM absorbers and p-n diode microbolometers where single pixels were routed to external pads to characterise an unetched device and devices of two membrane thicknesses:

- 1 μm of silicon + 8 μm dielectric
- 50 μm of silicon + 8 μm dielectric

The DC responsivity was measured from 10 nA to 200 μA on all three devices showing the highest responsivity of 1800 V/W at 20 μA from the device with 1 μm of silicon remaining. The device with 50 μm of silicon remaining had a responsivity of 198 V/W at the same bias current. The lowest responsivity resulted from the unetched device due to it having the largest thermal capacitance (more volume). The experimental results from the etched p-n diodes showed an average TCV of -1.54 mV/K at 25°C.

The material with higher responsivity and higher thermal coefficient was used for the imaging experiments. The VOx detectors proved to have a responsivity approximately 12 times higher compared to the p-n diode detectors due to the larger temperature coefficient. Therefore VOx detectors were employed in both a transmission and reflection mode imaging experiment. A CW FIR gas laser operating at 2.5 THz with a maximum power of 150 mW was used for the experiment. In the transmission mode experiment, the detector collected the radiation passing through the metallic object. In the reflection mode experiment, the detector collected the radiation being reflected from the metallic object. In both modes, the first detector (Chip A10) was raster scanned as only one pixel was used for these experiments. The non-invasive imaging capabilities of the MM based terahertz detector were demonstrated as the metallic objects were covered by manila envelopes and the detector successfully created a discernible image of the object. The central pixel of the 5 x 5 FPA (Chip A9) was also used for the imaging experiments in transmission and reflection mode by raster scanning the array. The transmission experiments successfully created an image of the metallic object, but in the reflection experiment, the image was barely discernible due to the lower responsivity of Chip A9.

As the main conclusion, this Thesis presented a new method for terahertz imaging technology by successfully demonstrating the technology in both transmission and reflection mode imaging. The device was monolithically integrated into a commercial 180 nm CMOS process. This technology presents a high sensitivity room temperature technology that is capable of scaling and low-cost manufacture.

## 6.2 Future Work

The presented Chip G and Chip F described in Section 5.6.1 and 5.6.2 contained 64 x 64 MM based FPAs with p-n diode microbolometers and VOx microbolometers respectively. Due to the complications in the post-processing procedures when working with the single dies, the pixel isolation was not completed by the time this Thesis was written. Therefore, the natural progression of the work presented would be the realisation of individual membranes and pixel isolation to eliminate cross-talk and enable high resolution and real-time imaging. The company Kelvin Nanotechnology Ltd (KNT) at the University of Glasgow was subcontracted to develop a suitable process to post-process the chips.

The design of MM based terahertz FPAs relied on exploiting the novel integration of MM structures into a commercial CMOS technology. It was demonstrated that the design of single band and broadband terahertz MM absorbers and their operating frequency

was extremely flexible by modifying the unit cell size (pixel pitch), ERR dimensions and number of ERR built in metal layers separated by the respective insulating layer. Therefore MMs can be scaled to other wavelengths from IR to microwave, potentially providing a compact and powerful method for building CMOS integrated image sensors in every relevant spectral band. Additionally, the possibility to create detectors in different bands is now feasible by positioning different MM absorber arrays in one single chip. Each area of the array would detect different frequency bands.

Absorption at different frequency bands has already been demonstrated by McCrindle *et. al.* where visible plasmonic filter technology was combined with MM structures into a CMOS chip to create a device capable of rendering images at visible and terahertz frequencies [126]. The integration of co-axial mid IR and terahertz MM absorbers is feasible by inserting a sub-array of appropriately sized IR ERRs into the layers that compose the THz MM absorber (metal/dielectric/metal). It has been demonstrated that these structures produce resonant absorption peaks in two distinct frequency bands; one at 4 µm and one at 2.67 THz [127]. The exploitation of such hybridised MM and plasmonic structures would result in a low-cost and compact multispectral camera integrated in a commercial CMOS technology where simultaneous rendering of images in three or more EM spectrums would be possible. Combining the information detected by the multispectral camera would result in a more informative and data rich image.

# References

[1] P. Nezih and A. N. Abbas, "Terahertz Technology for Nano Applications," in *Encyclopedia of Nanotechnology*, B. Bhushan, Ed. Springer, 2012, pp. 2653–2666.

[2] F. Simoens and J. Meilhan, "Terahertz real-time imaging uncooled array based on antenna- and cavity-coupled bolometers.," *Philos. Trans. A. Math. Phys. Eng. Sci.*, vol. 372, no. 2012, pp. 1–12, 2014.

[3] X.-C. Zhang, "Terahertz wave imaging: horizons and hurdles," *Phys. Med. Biol.*, vol. 47, no. 21, pp. 3667–3677, 2002.

[4] Y. Xiaoxia, D. Abbott, and B. W.-H. Ng, *Terahertz Imaging for Biomedical Applications: Pattern Recognition and Tomographic Reconstruction*. Springer, 2012.

[5] R. M. Woodward, V. P. Wallace, R. J. Pye, B. E. Cole, D. D. Arnone, E. H. Linfield, and M. Pepper, "Terahertz pulse imaging of ex vivo basal cell carcinoma," *J. Invest. Dermatol.*, vol. 120, no. 1, pp. 72–78, 2003.

[6] X.-C. Zhang and J. Xu, *Introduction to THz wave photonics*. Springer, 2010.

[7] P. H. Siegel, "Terahertz Technology in Biology and Medicine," *IEEE Trans. Microw. Theory Tech.*, vol. 52, no. 10, pp. 2438–2447, 2004.

[8] P. Mukherjee and B. Gupta, "Terahertz (THz) Frequency Sources and Antennas - A Brief Review," *Int. J. Infrared Millimeter Waves*, vol. 29, no. 12, pp. 1091–1102, 2008.

[9] K. Kawase, Y. Ogawa, Y. Watanabe, and H. Inoue, "Non-destructive terahertz imaging of illicit drugs using spectral fingerprints," *Opt. Express*, vol. 11, no. 20, pp. 2549–2554, Oct. 2003.

[10] J. E. Bjarnason, T. L. J. Chan, A. W. M. Lee, M. A. Celis, and E. R. Brown, "Millimeter-wave, terahertz, and mid-infrared transmission through common clothing," *Appl. Phys. Lett.*, vol. 85, no. 4, pp. 519–521, 2004.

[11] T. May, G. Zieger, S. Anders, V. Zakosarenko, M. Starkloff, H.-G. Meyer, G. Thorwirth, and E. Kreysa, "Passive stand-off Terahertz imaging with 1 Hertz frame rate," *Proc. SPIE, Terahertz Mil. Secur. Appl. VI*, vol. 6949, pp. 69490C–1–8, 2008.

[12] P. H. Siegel, "Terahertz technology," *IEEE Trans. Microw. Theory Tech.*, vol. 50, no. 3, pp. 910–928, Mar. 2002.

[13] T. May, H.-G. Meyer, and J. Popp, "Candid Cameras," *SPIE Professional*, Jul-2010.

[14] N. Karpowicz, H. Zhong, J. Xu, K.-I. Lin, J.-S. Hwang, and X.-C. Zhang, "Comparison between pulsed terahertz time-domain imaging and continuous wave terahertz imaging," *Semicond. Sci. Technol.*, vol. 20, no. 7, pp. S293–S299, 2005.

[15] P. Shumyatsky and R. R. Alfano, "Terahertz sources.," *J. Biomed. Opt.*, vol. 16, no. 3, pp. 033001–1–9, Mar. 2011.

[16] D. Pardo, J. Grajal, C. G. Pérez-Moreno, and S. Pérez, "An Assessment of Available Models for the Design of Schottky-Based Multipliers Up to THz Frequencies," *IEEE Trans. Terahertz Sci. Technol.*, vol. 4, no. 2, pp. 277–287, 2014.

[17] M. Henry, B. Ellison, P. Aryathilaka, N. Brewster, P. Huggard, G. Yassin, S.

Withington, and D. Maier, "Local oscillator development for focal plane array and Supra-THz astronomy receivers," *Proc. SPIE, Millimeter, Submillimeter, Far-Infrared Detect. Instrum. Astron. VII*, vol. 9153, pp. 91530O–1–9, Jul. 2014.

[18]  A. Maestrini, J. Bruston, D. Pukala, S. Martin, and I. Mehdi, "Performance of a 1.2 THz Frequency Tripler using a GaAs Frameless Membrane Monolithic Circuit," in *Microwave Symposium Digest, IEEE MTT-S International*, 2001, vol. 3, pp. 1657–1660.

[19]  A. G. Davies, E. H. Linfield, and M. B. Johnston, "The development of terahertz sources and their applications," *Phys. Med. Biol.*, vol. 47, no. 21, pp. 3679–3689, Oct. 2002.

[20]  B. F. Levine, "Quantum-well infrared photodetectors," *J. Appl. Phys.*, vol. 74, no. 8, pp. R1–R81, 1993.

[21]  J. Faist, F. Capasso, D. L. Sivco, C. Sirtori, A. L. Hutchinson, and A. Y. Cho, "Quantum Cascade Laser," *Science.*, vol. 264, pp. 553–556, 1994.

[22]  B. S. Williams, "Terahertz quantum-cascade lasers," *Nat. Photonics*, vol. 1, pp. 517–525, 2007.

[23]  Q. Y. Lu, N. Bandyopadhyay, S. Slivken, Y. Bai, and M. Razeghi, "Continuous operation of a monolithic semiconductor terahertz source at room temperature," *Appl. Phys. Lett.*, vol. 104, pp. 221105–1–5, 2014.

[24]  M. A. Belkin, F. Capasso, F. Xie, A. Belyanin, M. Fischer, A. Wittmann, and J. Faist, "Room temperature terahertz quantum cascade laser source based on intracavity difference-frequency generation," *Appl. Phys. Lett.*, vol. 92, no. 20, pp. 201101–1–3, 2008.

[25]  D. H. Auston and K. P. Cheung, "Coherent time-domain far-infrared spectroscopy," *J. Opt. Soc. Am. B*, vol. 2, no. 4, pp. 606–612, 1985.

[26]  J. W. Bowen, "Photoconductive Generation - The Auston Switch," in *Advances in Spectroscopy for Lasers and Sensing*, B. Di Bartolo and O. Forte, Eds. Springer, 2006, p. 112.

[27]  P. H. Siegel, "Terahertz Pioneer: David H. Auston," *IEEE Trans. Terahertz Sci. Technol.*, vol. 1, no. 1, pp. 6–8, 2011.

[28]  M. Inguscio, G. Moruzzi, K. M. Evenson, and D. A. Jennings, "A review of frequency measurements of optically pumped lasers from 0.1 to 8 THz," *J. Appl. Phys.*, vol. 60, no. 12, pp. R161–R191, 1986.

[29]  E. R. Mueller, "Optically-Pumped THz Laser Technology," *Coherent-DEOS*, 2001.

[30]  B. Ferguson and X.-C. Zhang, "Materials for terahertz science and technology," *Nat. Mater.*, vol. 1, pp. 26–33, 2002.

[31]  D. H. Auston, "Picosecond optoelectronic switching and gating in silicon," *Appl. Phys. Lett.*, vol. 26, pp. 101–103, 1975.

[32]  E. Castro-Camus, L. Fu, J. Lloyd-Hughes, H. H. Tan, C. Jagadish, and M. B. Johnston, "Photoconductive response correction for detectors of terahertz radiation," *J. Appl. Phys.*, vol. 104, pp. 053113–1–7, 2008.

[33]  M. J. E. Golay, "Theoretical Consideration in Heat and InfraRed Detection, with Particular Reference to the Pneumatic Detector," *Rev. Sci. Instrum.*, vol. 18, no. 5, pp. 347–356, 1947.

[34]  Y. S. Lee, *Principles of terahertz science and technology*. Springer, 2009.

[35]  Microtech Instruments, "THz Detectors – Golay Cells," *Microtech Instruments*.

[36] D. Dooley, "Sensitivity of broadband pyroelectric terahertz detectors continues to improve.," *Laser Focus World*, vol. 46, no. 5, pp. 49–53, May 2010.

[37] Center for Nanotechnology and Nanomaterials - Walter Schottky Institut, "An Introduction to Semiconductors." [Online]. Available: http://www.wsi.tum.de/Institute/Scientificbackground/AnIntroductiontoSemiconductors/tabid/65/Default.aspx. [Accessed: 23-Nov-2014].

[38] T. W. Crowe, W. L. Bishop, D. W. Porterfield, J. L. Hesler, and R. M. Weikle, "Opening the Terahertz Window with Integrated Diode Circuits," *IEEE J. Solid-State Circuits*, vol. 40, no. 10, pp. 2104–2110, 2005.

[39] J. L. Hesler and T. W. Crowe, "Responsivity and Noise Measurements of Zero-Bias Schottky Diode Detectors," in *18th International Symposium on Space Terahertz Technology*, 2007, no. 1, pp. 89–92.

[40] M. Dyakonov and M. Shur, "Shallow Water Analogy for a Ballistic Field Effect Transistor: New Mechanism of Plasma Wave Generation by dc Current," *Phys. Rev. Lett.*, vol. 71, no. 15, pp. 2465–2468, 1993.

[41] W. Knap, S. Nadar, H. Videlier, S. Boubanga-Tombet, D. Coquillat, N. Dyakonova, F. Teppe, K. Karpierz, J. Łusakowski, M. Sakowicz, I. Kasalynas, D. Seliuta, G. Valusis, T. Otsuji, Y. Meziani, A. Fatimy, S. Vandenbrouk, K. Madjour, D. Théron, and C. Gaquière, "Field Effect Eransistors for Terahertz Detection and Emission," *J. Infrared, Millimeter, Terahertz Waves*, vol. 32, no. 5, pp. 618–628, May 2011.

[42] A. Rogalski, "Semiconductor detectors and focal plane arrays for far-infrared imaging," *Opto-Electronics Rev.*, vol. 21, no. 4, pp. 406–426, 2013.

[43] M. I. Dyakonov, "Generation and detection of Terahertz radiation by Field Effect Transistors," *Comptes Rendus Phys.*, vol. 11, no. 413, pp. 1–10, 2011.

[44] A. Rogalski and F. Sizov, "Terahertz detectors and focal plane arrays," *Opto-Electronics Rev.*, vol. 19, no. 3, pp. 346–404, 2011.

[45] H. Sherry, J. Grzyb, Y. Zhao, R. Al Hadi, A. Cathelin, A. Kaiser, and U. Pfeiffer, "A 1kpixel CMOS camera chip for 25fps real-time terahertz imaging applications," in *IEEE International Solid-State Circuits Conference Digest of Technical Papers (ISSCC)*, 2012, pp. 252–254.

[46] R. Al Hadi, H. Sherry, J. Grzyb, N. Baktash, Y. Zhao, E. Ojefors, A. Kaiser, A. Cathelin, and U. Pfeiffer, "A broadband 0.6 to 1 THz CMOS imaging detector with an integrated lens," in *IEEE MTT-S International Microwave Symposium Digest (MTT)*, 2011, pp. 1–4.

[47] S. Ruan, J. Yang, and M. Zhang, "Real-time terahertz imaging using a 1.63 THz optically-pumped terahertz laser and a pyroelectric camera," *Proc. SPIE, 28th Int. Congr. High-Speed Imaging Photonics*, vol. 7126, no. 86, pp. 71261U–1–6, Nov. 2009.

[48] Ophir Photonics, "Pyrocam III & Pyrocam IV Series," 2014. [Online]. Available: http://www.ophiropt.com/user_files/laser/beam_profilers/Pyrocam.pdf. [Accessed: 01-Dec-2014].

[49] A. Dobroiu, M. Yamashita, Y. N. Ohshima, Y. Morita, C. Otani, and K. Kawase, "Terahertz imaging system based on a backward-wave oscillator," *Appl. Opt.*, vol. 43, no. 30, pp. 5637–5646, 2004.

[50] D. S. Tezcan, S. Eminoglu, O. S. Akar, and T. Akin, "An uncooled microbolometer infrared focal plane array in standard CMOS," *Proc. SPIE, Photodetectors Mater. Devices VI*, vol. 4288, no. 312, pp. 112–121, 2001.

[51] K. A. Hay, "Large format VOx microbolometer UFPA development at ITC," *Proc.*

*SPIE, Infrared Detect. Focal Pl. Arrays VIII*, vol. 6295, pp. 629505–1–6, Aug. 2006.

[52] F. Niklaus, C. Vieider, and H. Jakobsen, "MEMS-based uncooled infrared bolometer arrays - a review," *Proc. SPIE, MEMS/MOEMS Technol. Appl. III*, vol. 6836, pp. 68360D–1–15, Nov. 2007.

[53] M. Kohin and N. Butler, "Performance limits of uncooled VOx microbolometer focal plane arrays," *Proc. SPIE, Infrared Technol. Appl. XXX*, vol. 5406, pp. 447–453, Aug. 2004.

[54] T. Akin, "CMOS-Based Thermal Sensors," in *Advanced Micro and Nanosystems*, vol. 2, 2005, pp. 479–511.

[55] R. T. Rajendra Kumar, B. Karunagaran, D. Mangalaraj, S. K. Narayandass, P. Manoravi, M. Joseph, V. Gopal, R. K. Madaria, and J. P. Singh, "Room temperature deposited vanadium oxide thin films for uncooled infrared detectors," *Mater. Res. Bull.*, vol. 38, pp. 1235–1240, 2003.

[56] S. Eminoglu, S. D. Tezcan, M. Y. Tanrikulu, and T. Akin, "Low-cost uncooled infrared detectors in CMOS process," *Sensors Actuators, A Phys.*, vol. 109, pp. 102–113, 2003.

[57] E. Mottin, A. Bain, J. L. Martin, J. L. Ouvrier-Buffet, S. Bisotto, J. J. Yon, and J. L. Tissot, "Uncooled amorphous silicon technology enhancement for 25µm pixel pitch achievement," *Proc. SPIE, Infrared Technol. Appl. XXVIII*, vol. 4820, pp. 200–207, 2003.

[58] M. Almasri, B. Xu, and J. Castracane, "Amorphous silicon two-color microbolometer for uncooled IR detection," *IEEE Sens. J.*, vol. 6, no. 2, pp. 293–300, 2006.

[59] FLIR, "Uncooled detectors for thermal imaging cameras - Technical Note," 2008.

[60] G. C. Holst, *Common sense approach to thermal imaging*. SPIE Optical Engineering Press, 2000.

[61] S. P. Langley, "The Bolometer and Radiant Energy," *Proc. Am. Acad. Arts Sci.*, vol. 16, pp. 342–358, May 1880.

[62] E. F. Nichols and H. Rubens, *Heat Rays of Great Wave Length*. .

[63] C. Corsi, "TeraHertz: Quasi-optics or Submillimeter Waves? History, Actual Limits and Future Developments for Security Systems," in *TeraHertz and Security Applications*, C. Corsi and F. Sizov, Eds. Dordrecht: Springer, 2014, pp. 1–24.

[64] E. Öjefors, U. R. Pfeiffer, A. Lisauskas, and H. G. Roskos, "A 0.65 THz Focal-Plane Array in a Quarter-Micron," *IEEE J. Solid-State Circuits*, vol. 44, no. 7, pp. 1968–1976, 2009.

[65] R. Al Hadi, H. Sherry, J. Grzyb, Y. Zhao, W. Förster, H. M. Keller, A. Cathelin, A. Kaiser, and U. R. Pfeiffer, "A 1k-Pixel Video Camera for 0.7-1.1 Terahertz Imaging Applications in 65-nm CMOS," *IEEE J. Solid-State Circuits*, vol. 47, no. 12, pp. 2999–3012, 2012.

[66] A. Lisauskas, S. Boppel, V. Krozer, and H. G. Roskos, "Silicon CMOS-Based THz Detection," *IEEE Sensors*, pp. 55–58, Oct. 2011.

[67] F. Niklaus, A. Decharat, C. Jansson, and G. Stemme, "Performance model for uncooled infrared bolometer arrays and performance predictions of bolometers operating at atmospheric pressure," *Infrared Phys. Technol.*, vol. 51, pp. 168–177, 2008.

[68] R. Ambrosio, M. Moreno, J. Mireles, A. Torres, A. Kosarev, and A. Heredia, "An

overview of uncooled infrared sensors technology based on amorphous silicon and silicon germanium alloys," *Phys. Status Solidi C*, vol. 7, no. 3–4, pp. 1180–1183, 2010.

[69] M. Perenzoni and S. Domingues, "A diode-based bolometer implemented on micromachined CMOS technology for terahertz radiation detection," *Proc. SPIE, Silicon Photonics Photonic Integr. Circuits III*, vol. 8431, pp. 84311T–1–6, Jun. 2012.

[70] R. Han, Y. Zhang, Y. Kim, D. Y. Kim, H. Shichijo, E. Afshari, and K. K. O, "Active terahertz imaging using schottky diodes in CMOS: Array and 860-ghz pixel," *IEEE J. Solid-State Circuits*, vol. 48, no. 10, pp. 2296–2308, 2013.

[71] C. Chevalier, L. Mercier, F. Duchesne, L. Gagnon, B. Tremblay, M. Terroux, F. Généreux, J.-E. Paultre, F. Provençal, Y. Desroches, L. Marchese, H. Jerominek, C. Alain, and A. Bergeron, "Introducing a 384x288 pixel terahertz camera core," *Proc. SPIE, Terahertz, RF, Millimeter, Submillimeter-Wave Technol. Appl. VI*, vol. 8624, pp. 86240F–1–8, Mar. 2013.

[72] B. A. Munk, *Metamaterials: Critique and Alternatives*. John Wiley & Sons, Inc., 2008.

[73] V. G. Veselago, "The electrodynamics of substances with simultaneously negative values of ε and μ," *Sov. Phys. Uspekhi*, vol. 10, no. 4, pp. 509–514, 1968.

[74] Karlsruhe Institute of Technology, "Liquid with a positive index of refraction and a negative index of refraction." [Online]. Available: http://www.aph.kit.edu/wegener/264.php.

[75] J. B. Pendry, A. J. Holden, W. J. Stewart, and I. Youngs, "Extremely Low Frequency Plasmons in metallic microstructure," *Phys. Rev. Lett.*, vol. 76, no. 4773–6, pp. 1–12, 1996.

[76] J. B. Pendry, A. J. Holden, D. J. Robbins, and W. J. Stewart, "Magnetism from conductors and enhanced nonlinear phenomena," *IEEE Trans. Microw. Theory Tech.*, vol. 47, no. 11, pp. 2075–2084, Nov. 1999.

[77] R. A. Shelby, D. R. Smith, and S. Schultz, "Experimental verification of a negative index of refraction," *Science.*, vol. 292, pp. 77–79, 2001.

[78] T. J. Cui, D. R. Smith, and R. Liu, "Introduction to Metamaterials," in *Theory, design, and applications*, T. J. Cui, D. R. Smith, and R. Liu, Eds. Springer US, 2010, pp. 1–19.

[79] L. Butler, D. S. Wilbert, W. Baughman, S. Balci, P. Kung, S. M. Kim, M. S. Heimbeck, and H. O. Everitt, "Design, simulation, and characterization of THz metamaterial absorber," *Proc. SPIE, Terahertz Physics, Devices, Syst. VI Adv. Appl. Ind. Def.*, vol. 8363, pp. 83630J–1–8, May 2012.

[80] C. Rockstuhl, C. Menzel, S. Muhlig, and F. Lederer, "Theory of Optical Metamaterials," in *Encyclopedia of Nanotechnology*, B. Bhushan, Ed. Springer, 2012, pp. 2667–2679.

[81] A. Sihvola, "Metamaterials in electromagnetics," *Metamaterials*, vol. 1, no. 1, pp. 2–11, Mar. 2007.

[82] X. Zhang and Z. Liu, "Superlenses to overcome the diffraction limit.," *Nat. Mater.*, vol. 7, no. 6, pp. 435–441, Jun. 2008.

[83] N. I. Landy, C. M. Bingham, T. Tyler, N. Jokerst, D. R. Smith, and W. J. Padilla, "Design, theory, and measurement of a polarization-insensitive absorber for terahertz imaging," *Phys. Rev. B - Condens. Matter Mater. Phys.*, vol. 79, no. 12, pp. 125104–1–6, Mar. 2009.

[84]   C. M. Watts, X. Liu, and W. J. Padilla, "Metamaterial electromagnetic wave absorbers.," *Adv. Opt. Mater.*, vol. 24, pp. OP98–OP181, Jun. 2012.

[85]   D. Schurig, J. J. Mock, B. J. Justice, S. A. Cummer, J. B. Pendry, A. F. Starr, and D. R. Smith, "Metamaterial electromagnetic cloak at microwave frequencies.," *Science.*, vol. 314, no. 5801, pp. 977–980, Nov. 2006.

[86]   N. Fang and X. Zhang, "Imaging properties of a metamaterial superlens," *Appl. Phys. Lett.*, vol. 82, no. 2, pp. 161–163, Jan. 2003.

[87]   A. Orduña-Díaz, E. Castillo-Domínguez, A. Torres-Jacome, F. J. De la Hidalga-Wade, and C. G. Treviño-Palacios, "Design and fabrication of a bidimentional microbolometer array for Terahertz detection characterized at different temperatures," *J. Phys. Conf. Ser.*, vol. 274, pp. 012112–1–5, Jan. 2011.

[88]   P. W. Kruse, "Uncooled infrared focal plane arrays," *Proc. IEEE-ISAF*, pp. 643–646, 1994.

[89]   P. W. Kruse, "Principles of Uncooled Infrared Focal Plane Arrays," in *Uncooled Infrared Imaging: Arrays and Systems*, P. W. Kruse and D. D. Skatrud, Eds. Academic Press, 1997, pp. 17–40.

[90]   R. A. Wood, "Monolithic Silicon Microbolometer Arrays," in *Uncooled Infrared Imaging: Arrays and Systems*, P. W. Kruse and D. D. Skatrud, Eds. Academic Press, 1997, pp. 45–119.

[91]   R. A. Smith, F. E. Jones, and R. P. Chasmar, *The Detection and Measurement of Infrared Radiation*, Second. Oxford University Press, 1968.

[92]   R. A. Wood, "Uncooled thermal imaging with monolithic silicon focal planes," *Proc. SPIE, Infrared Technol. XIX*, vol. 2020, pp. 322–329, Nov. 1993.

[93]   S. Eminoglu, "Uncooled Infrared Focal Plane Arrays with Integrated Readout Circuitry using MEMS and Standard CMOS Technologies," Middle East Technical University, 2003.

[94]   R. K. Bhan, R. S. Saxena, C. R. Jalwania, and S. K. Lomash, "Uncooled infrared microbolometer arrays and their characterisation techniques," *Def. Sci. J.*, vol. 59, no. 6, pp. 580–589, 2009.

[95]   P. Eriksson, J. Y. Andersson, and G. Stemme, "Thermal Characterization of Surface- Micromachined Silicon Nitride Membranes for Thermal Infrared Detectors," *J. Microelectromechanical Syst.*, vol. 6, no. 1, pp. 55–61, 1997.

[96]   J. Nemarich, "Microbolometer Detectors for Passive Millimeter-Wave Imaging," 2005.

[97]   G. D. Boreman, "Detectors," in *Basic Electro-Optics for Electrical Engineers*, SPIE Optical Engineering Press, 1998, pp. 55–82.

[98]   J. B. Johnson, "Thermal agitation of electricity in conductors," *Phys. Rev.*, vol. 32, pp. 97–109, 1928.

[99]   H. Nyquist, "Thermal agitation of electric charge in conductors," *Phys. Rev.*, vol. 32, pp. 110–113, 1928.

[100]   D. V. Perepelitsa, "Johnson Noise and Shot Noise," *Analysis*, no. 2, pp. 1–4, 2006.

[101]   R. F. Voss, "1/f (Flicker) Noise: A Brief Review," *33rd Annu. Symp. Freq. Control*, 1979.

[102]   A. Van Der Ziel, "Unified Presentation of 1/f Noise in Electronic Devices: Fundamental 1/f Noise Sources," *Proc. IEEE*, vol. 76, no. 3, pp. 233–258, 1988.

[103]   D. A. Bell, "A survey of 1/f noise in electrical conductors," *J. Phys. C Solid State*

*Phys.*, vol. 13, no. 24, pp. 4425–4437, 1980.

[104] J. A. Jamieson, *Infrared physics and engineering*. McGraw-Hill, 1963.

[105] W. L. Wolfe and G. J. Zissis, *The infrared handbook*. Washington: The Office, 1978.

[106] P. W. Kruse, "Resistive Bolometers," in *Uncooled Thermal Imaging Arrays, Systems, and Applications*, SPIE Press, 2001, pp. 33–48.

[107] P. L. Richards, "Bolometers for infrared and millimeter waves," *J. Appl. Phys.*, vol. 76, no. 1994, pp. 1–24, 1994.

[108] J. C. Mather, "Bolometer noise: nonequilibrium theory.," *Appl. Opt.*, vol. 21, no. 6, pp. 1125–1129, 1982.

[109] P. W. Kruse, L. D. McGlauchlin, and R. B. McQuistan, *Elements of Infrared Technology: Generation, Transmission and Detection*. John Wiley & Sons, Inc., 1962.

[110] A. R. Luukanen and V.-P. Viitanen, "Terahertz imaging system based on antenna-coupled microbolometers," *Proc. SPIE*, vol. 3378. pp. 34–44, 1998.

[111] K. R. Jha and G. Singh, "Terahertz Sources and Antennas," in *Terahertz Planar Antennas for Next Generation Communication*, Springer International Publishing, 2014, pp. 1–22.

[112] K. J. Linden, W. R. Neal, J. Waldman, A. J. Gatesman, and A. Danylov, "Terahertz laser based standoff imaging system," *IEEE Proc. 34th Appl. Imag. Pattern Recognit. Work.*, p. -14, 2005.

[113] J. Grant, I. Escorcia-Carranza, C. Li, I. J. H. McCrindle, J. Gough, and D. R. S. Cumming, "A monolithic resonant terahertz sensor element comprising a metamaterial absorber and micro-bolometer," *Laser Photon. Rev.*, vol. 7, no. 6, pp. 1043–1048, Nov. 2013.

[114] J. Grant, Y. Ma, S. Saha, L. B. Lok, A. Khalid, and D. R. S. Cumming, "Polarization insensitive terahertz metamaterial absorber," *Opt. Lett.*, vol. 36, no. 8, pp. 1524–1526, Apr. 2011.

[115] Y. Ma, Q. Chen, J. Grant, S. C. Saha, A. Khalid, and D. R. S. Cumming, "A terahertz polarization insensitive dual band metamaterial absorber," *Opt. Lett.*, vol. 36, no. 6, pp. 945–947, Mar. 2011.

[116] J. Grant, Y. Ma, S. Saha, A. Khalid, and D. R. Cumming, "Polarization insensitive, broadband terahertz metamaterial absorber," *Opt. Lett.*, vol. 36, no. 17, pp. 3476–3478, Sep. 2011.

[117] Y. Q. Ye, Y. Jin, and S. He, "Omnidirectional, polarization-insensitive and broadband thin absorber in the terahertz regime," *J. Opt. Soc. Am. B*, vol. 27, no. 3, pp. 498–504, 2010.

[118] P. Ding, E. J. Liang, W. Q. Hu, Q. Zhou, L. Zhang, Y. X. Yuan, and Q. Z. Xue, "SPP-associated dual left-handed bands and field enhancement in metal-dielectric-metal metamaterial perforated by asymmetric cross hole arrays," *Opt. Express*, vol. 17, no. 4, pp. 2198–2206, 2009.

[119] F. J. Hsieh and W. C. Wang, "Full extraction methods to retrieve effective refractive index and parameters of a bianisotropic metamaterial based on material dispersion models," *J. Appl. Phys.*, vol. 112, no. 2012, 2012.

[120] D. R. Smith, D. C. Vier, T. Koschny, and C. M. Soukoulis, "Electromagnetic parameter retrieval from inhomogeneous metamaterials," *Phys. Rev. E*, vol. 71, no. 3, pp. 036617–1–11, Mar. 2005.

[121] X. Liu, T. Starr, A. F. Starr, and W. J. Padilla, "Infrared Spatial and Frequency Selective Metamaterial with Near-Unity Absorbance," *Phys. Rev. Lett.*, vol. 104, pp. 207403–1–4, May 2010.

[122] P. E. Allen and D. R. Holberg, *CMOS Analog Circuit Design*, 2nd ed. Oxford University Press, 2002.

[123] A. S. Sedra and K. C. Smith, *Microelectronic Circuits*. Oxford University Press, 2004.

[124] S. Domingues, L. H. C. Braga, and A. C. Mesquita, "A CMOS-only R-2R ladder D/A converter for image sensor applications," in *3rd International Conference on Signals, Circuits and Systems (SCS)*, 2009, pp. 1–6.

[125] J. J. Wikner, "Studies on CMOS digital-to-analog converters," Linköpings Universitet, 2001.

[126] I. J. H. McCrindle, J. Grant, T. D. Drysdale, and D. R. Cumming, "Multi-spectral materials: Hybridisation of optical plasmonic filters and a terahertz metamaterial absorber," *Adv. Opt. Mater.*, vol. 2, no. 2, pp. 149–153, 2014.

[127] J. Grant, I. J. H. McCrindle, C. Li, and D. R. S. Cumming, "Multispectral metamaterial absorber," *Opt. Lett.*, vol. 39, no. 5, pp. 1227–30, 2014.